Universidade de Aveiro Departamento de Engenharia de Materiais e Cerâmica
2016

Mirtha Alejandra de Oliveira Lourenço

Modificação de organossílicas mesoporosas periódicas para a separação de CO_2/CH_4

Tuning functionalized periodic mesoporous organosilicas for CO_2/CH_4 separation

Universidade de Aveiro
2016
Departamento de Engenharia de Materiais e Cerâmica

Mirtha Alejandra de Oliveira Lourenço

Modificação de organossílicas mesoporosas periódicas para a separação de CO_2/CH_4

Tuning functionalized periodic mesoporous organosilicas for CO_2/CH_4 separation

Tese apresentada à Universidade de Aveiro para cumprimento dos requisitos necessários à obtenção do grau de Doutor em Ciência e Engenharia de Materiais, realizada sob a orientação científica da Doutora Paula Celeste da Silva Ferreira, Investigadora FCT, Equiparada a Investigadora Principal do CICECO – Instituto de Materiais de Aveiro da Universidade de Aveiro e do Doutor José Richard Baptista Gomes, Investigador FCT, Equiparado a Investigador Principal do CICECO – Instituto de Materiais de Aveiro da Universidade de Aveiro.

Trabalho realizado com o apoio financeiro do projeto CICECO-Instituto de Materiais de Aveiro, POCI-01-0145-FEDER-007679 (FCT UID/CTM/50011/2013), financiado por fundos nacionais através da FCT/MEC e FEDER, no âmbito do Acordo de Parceria PT2020.

Trabalho realizado com o apoio da FCT sob a forma de bolsa individual de doutoramento com a referência SFRH/BD/80883/2011.

Para a minha família

o júri

presidente

Prof. Doutor José Carlos da Silva Neves
Professor Catedrático da Universidade de Aveiro

Prof. Doutor Alírio Egídio Rodrigues
Professor Emérito da Universidade do Porto

Prof. Doutor Fernando Manuel Bico Marques
Professor Catedrático da Universidade de Aveiro

Prof. Doutor João Carlos Matias Celestino Gomes da Rocha
Professor Catedrático da Universidade de Aveiro

Doutor Nicolas Bion
Chargé de Researche CNRS de Université de Poitiers

Prof. Doutor João Paulo Cristóvão Almeida Prates Ramalho
Professor Associado da Universidade de Évora

Doutora Paula Celeste da Silva Ferreira (orientadora)
Equiparada a Investigadora Principal da Universidade de Aveiro

Prof. Doutor João Manuel Pires da Silva
Professor Auxiliar com Agregação da Faculdade de Ciências da Universidade de Lisboa

agradecimentos

Gostaria de começar a agradecer à minha família por todo apoio, dedicação, amor incondicional e pelas muitas gargalhadas dadas. A eles dedico esta tese, porque sem eles nunca teria sequer chegado ao início desta etapa e é graças a eles que me fui mantendo positiva durante este processo de aprendizagem. Um abraço forte à minha mami, ao meu papi, à minha mana Mary, ao meu mano Leandro, ao meu namorido Nuno e ao mais novo "membro da família" *Heisenberg*. Amo-vos muito e obrigada por me fazerem feliz!

À minha orientadora Paula Ferreira e ao meu orientador José Richard Gomes, não só pela orientação, apoio e ensinamentos científicos, mas também pelas oportunidades que me proporcionaram e pela boa disposição, simpatia e motivação. Gostei muito de trabalhar convosco! Agradeço também a todos aqueles que colaboraram connosco durante estes últimos 4 anos, à Mariana Sardo, à Renée Siegel, à Maria Ferreira, ao Luís Mafra, ao Miguel Jorge, ao João Santos, ao Ricardo Silva, ao Rui Silva, ao Nicola Pinna e ao Stephane Pronier, e em especial ao Moisés Pinto e ao João Pires pela oportunidade e conhecimentos transmitidos na área da adsorção de gases.

Ao meu pessoal do CICECO, da *Cerâmica* e da *Química* que percorreram este caminho comigo, pela boa companhia à hora de almoço ou durante um café. Para eles esta citação do JJ:

"Quanto mais experiente a gente estejamos, mais conhecimento tamos, melhor também estamos."

Aos meus amigos de toda vida; aos que me acompanham desde a infância; aos que conheci durante as minhas jornadas em Coimbra e em Aveiro e à minha família do Caramulo, por me proporcionarem muitas gargalhadas e bons momentos.

A todos os técnicos, docentes e investigadores do CICECO, do departamento de Química e do departamento de Engenharia de Materiais e Cerâmica que me apoiaram durante estes 4 anos.

A todos espero ter a oportunidade de agradecer pessoalmente.

Um grande OBRIGADA!

palavras-chave

Organossílicas mesoporosas periódicas (PMOs), aminação, micro-ondas, catálise, adsorção, teoria do funcional da densidade (DFT), aproximação do modelo periódico.

resumo

Esta tese de doutoramento teve como principal objetivo a conceção de novas organossílicas mesoporosas periódicas (PMOs) para aplicação na separação de misturas gasosas de dióxido de carbono e metano. Materiais PMOs, com grupos fenileno e bifenileno bissililados, foram modificados por introdução de grupos funcionais amina, utilizando uma das seguintes metodologias:
i) reação de co-condensação;
ii) pós-modificação da ponte orgânica;
iii) "grafting".
O tamanho dos poros das PMOs funcionalizadas e não funcionalizadas foi definido pelo tamanho da cadeia alquilada da molécula molde (surfactante) utilizada na síntese do material poroso. Estudou-se o efeito do diâmetro dos poros na separação de CO_2/CH_4. Investigou-se também estratégias alternativas para modificar as propriedades físico-químicas dos materiais através de reações de superfície utilizando irradiação de micro-ondas; deposição de camada atómica (ALD) de óxido de alumínio; e carbonização dos materiais em atmosfera inerte.
A investigação experimental foi efectuada em paralelo com estudos computacionais. Realizou-se um estudo de simulação molecular recorrendo ao método de DFT, e usando um arranjo regular de grupos fenileno-sílica, para determinar as características ideais dos materiais para promover a separação de metano do dióxido de carbono em misturas destes gases. Foi utilizado um modelo simples, obtido pela repetição de uma célula unitária com 3 anéis fenileno, para simular a parede dos materiais PMOs e desta forma selecionar e avaliar as interações entre os gases e os grupos funcionais presentes na superfície dos materiais. A tendência do rácio entre energias de interação entre a estrutura da parede do fenileno - PMO e as moléculas de CO_2 e de CH_4 foi concordante com os rácios das constantes de Henry obtidos pela técnica de adsorção. Demonstrou-se uma boa sinergia entre tarefas experimentais e computacionais, o que permite a otimização de recursos, evitando a síntese desnecessária de materiais que se antecipem serem pouco eficazes para o processo de separação de misturas gasosas CO_2 e CH_4.
Assim, a abordagem seguida nesta tese para alcançar adsorventes eficazes foi baseada numa conjugação interdisciplinar envolvendo troca de informação entre as tarefas de síntese, modelação computacional e adsorção.

keywords

Periodic mesoporous organosilicas (PMOs), amination, microwave, catalysis, adsorption, density functional theory (DFT), periodic model approach.

abstract

The main objective of this PhD Thesis was the design of periodic mesoporous organosilicas (PMOs) for applications in carbon dioxide and methane separation. Novel PMOs were prepared by the modification of phenylene and biphenylene PMO materials with different amine functionalities through one of the three following synthetic strategies:

i) co-condensation reaction;

ii) organic bridge post-modification; or/and

iii) grafting.

The pore size of both functionalized and non-functionalized phenylene PMOs was regulated by the size of the alkyl-chain in the surfactant template. Materials with different pore sizes were used to understand the influence of the pore diameter on the CO_2/CH_4 separation. Additionally, it was aimed to explore alternative strategies to modify the physical-chemical properties of the materials such as microwave-assisted functionalization; atomic layer deposition (ALD) of aluminum oxide at the PMO surfaces; and carbonization of the PMO materials.

The experimental research was performed in parallel with computational studies. A molecular simulation study, using the DFT method and a regular arrangement of phenylene-silica groups, of the ideal characteristics of the adsorbent materials, for CO_2/CH_4 separation was performed. It was used a simple model of the wall of the PMO materials obtained by the repetition of a unit cell with 3 phenylene rings, to select and evaluate interactions between gases and functional groups in the surface of the materials. The tendency between the ratio of the interaction energies between the wall structure of the phenylene-PMO and the CO_2 and CH_4 molecules was in good agreement with the ratio of the Henry constants achieved by the adsorption technique. Therefore, a good synergy between experimental and computational tasks was implemented to optimize the resources, avoiding the synthesis of ineffective materials.

Thus, the strategy of this PhD Thesis to achieve effective adsorbents was based on an interdisciplinary approach and on the ability to link and interchange information between synthetic, computer modeling and adsorption experiments.

LIST OF FIGURES

LIST OF TABLES

ABBREVIATIONS AND ACRONYMS

ALD	Atomic layer deposition
APTMS	(3-aminopropyl)trimethoxysilane
ATR	Attenuated total reflectance
BET	Brunauer–Emmett–Teller theory
BJH	Barret–Joyner–Halenda
BLYP	Becke–Lee–Yang–Parr
BP86	Becke–Perdew 86
Bph	Biphenylene
BTEE	Bis(triethoxysilyl)ethene
BTEB	1,4-bis(triethoxysilyl)benzene
BTEBP	4,4′-bis(triethoxysilyl)-1,1′-biphenyl
BTET	2,5-bis(triethoxysilyl)thiophene
BTME	1,2-bis(trimethoxysilyl)ethane
BTMSPA	Bis[3-(trimethoxysilyl)propyl]amine
BzDMS	Benzyldimethylsilane
CC	Coupled cluster
CHTC	*cis*,*cis*-1,3,5-cyclohexanetricarboxamide precursor
CI	Configuration interaction
CP	Cross polarization
CT	Contact time
CTAB, C_{16}-TMA	Cetyltrimethylammonium bromide
DAB	Diaminobutane
DADD	Diaminododecane
DAH	Diaminohexane
DEA	Diethanolamine
DETA	Diethyltriamine
DFT	Density functional theory
DMSFc	Dimethylsilyl(ferrocene)
DTAB, C_{12}-TMA	Dodecyltrimethylammonium bromide
EA	Elemental analysis
EDA	Ethylenediamine
EDATMS	[3-(2-aminoethylamino)propyl] trimethoxysilane
EDS	Energy dispersive X-ray spectroscopy
EF	Energy filtered
EISA	Evaporation induced self-assembly
FTIR	Fourier transform infrared
GGA	Generalized gradient approximation
HF	Hartree-Fock

H-K	Hohenberg-Kohn
HMF	5-hydroxymethylfurfural
HR	High resolution
IAST	Ideal adsorbed solution theory
ICP	(3-triethoxysilylpropyl) isocyanate
ImTES	*N*-(3-Triethoxysilylpropyl) 4,5-dihydroimidazole
IR	Infrared
KJS	Kruk-Jaroniec-Sayari
LDA	Local density approximation
LSDA	Local-spin density approximation
MAC	Microwave activated carbon
MAS	Magic-angle spinning
MCM	Mobil composition of matter
MEA	Monoethanol amine
MD	Molecular dynamics
MDEA	Methyl diethanolamine
MOFs	Metal organic frameworks
MP	Møller-Plesset
MPTMS	3-mercaptopropyltrimethoxysilane
NMR	Nuclear magnetic resonance
N_2 isotherms	Nitrogen adsorption-desorption isotherms
ODTMA, C_{18}-TMA	Octadecyltrimethylammonium bromide
PAW	Projector-augmented wave
PBE	Perdew−Burke−Ernzerhof
Ph	Phenylene
PMO	Periodic mesoporous organosilica
PMS	Periodic mesoporous silica
PSD	Pore size distribution
PW-91	Perdew-Wang 91
PXRD	Powder X-ray diffraction
QSDFT	Quenched solid density functional theory
RD	Recycle delay
RPBE	Revised Perdew−Burke−Ernzerhof
SBA	Santa Barbara amorphous
SDA	Structure directing agent
SEM	Scanning electron microscopy
TDTMA, C_{14}-TMA	Tetradecyltrimethylammonium bromide
TEM	Transmission electron microscopy
TEOS	Tetraethoxysilane

TEPA	Tetraethylenepentamine
TGA	Thermogravimetric analysis
THF	Tetrahydrofuran
TLCT	True liquid-crystal templating
TMA	Trimethylamonium bromide or chloride
TMS	Trimethylsilane
UREDO	1-[3-(trimethoxysilyl)propyl] urea
vdW	Van der Waals
VTIR	Variable temperature infrared
XC	Exchange-correlation
XPS	X-ray photoelectron spectroscopy
ZIF	Zeolitic imidazolate framework

SYMBOLS

a	Unit cell parameter
a_0	Lattice constant
Å	Angstrom
°	Degree
b	Pore wall thickness
b	Langmuir surface affinity parameter
d	Inter-planar distance (from PXRD)
d_p	Pore diameter
$[H^+]$	Acid load
K_H	Henry constant
P	Pressure
q	Amount adsorbed
q_S	Langmuir saturation capacity
S	Selectivity
S_{BET}	BET Surface area
V_{micro}	Micropore volume
V_p	Pore volume
ν_R	Spinning rate

GREEK SYMBOLS

Θ	Bragg angle
δ	Chemical shift
ρ	Density
π	Pi number

INDEX

Chapter 1 – State of the art

1.1 Motivation and Objectives

The global objective of this PhD project was to tune the properties of periodic mesoporous organosilicas (PMOs) for biogas upgrading, *i.e.*, for CO_2/CH_4 separation.

The scientific activities, grounded on synergetic experimental and computational studies, were divided in five tasks according to the following specific aims:

Aim 1 – To prepare bissilylated organic precursors and novel PMOs with periodically ordered porous structure at the meso- and molecular-scales;

Aim 2 – To modify the pore size of the PMOs by changing the surfactant template and to evaluate its influence in the CO_2/CH_4 separation;

Aim 3 – To develop synthetic strategies to insert amine groups on the organic bridges of PMOs and to advance different methodologies to tune the properties of the PMOs.

Aim 4 – To calculate the energy of the interaction of CO_2/CH_4 molecules with the PMOs surface and to assess, at the atomic level, which functional groups enhance the properties of the materials for CO_2/CH_4 separation.

Aim 5 – To evaluate experimentally the developed PMOs for the adsorption of CO_2 and CH_4.

1.2 Biogas upgrading: the CH_4 purification problem

The human population is growing and at this moment we overpass the 7 billion of humans in the planet Earth. Several concerns have been associated to the expanding of the population which together with the strong economic progress leads to an increase of the world energy demand. Associated to the growth of the number of the humans there are also concerns associated with the rising production of organic waste and the intensive animal agriculture that all together foment the production of greenhouse gases. The emission of these gases to the atmosphere promotes the greenhouse effect and, consequently, leads to an increase of the temperature of our planet, promoting climate changes. Thus, a possible solution is to take advantage of these gases for energy production. Biogas is an alternative energy source, produced through the anaerobic digestion process of large variety of organic waste, such as sewage, animal byproducts, agricultural, industrial, and municipal solid wastes, Figure 1.1.[1–7] Biogas is mainly composed by methane (60-70%) and carbon dioxide (30-40%), and presents also trace gases such as H_2S, CO, H_2 and N_2, dust and dirt particles.

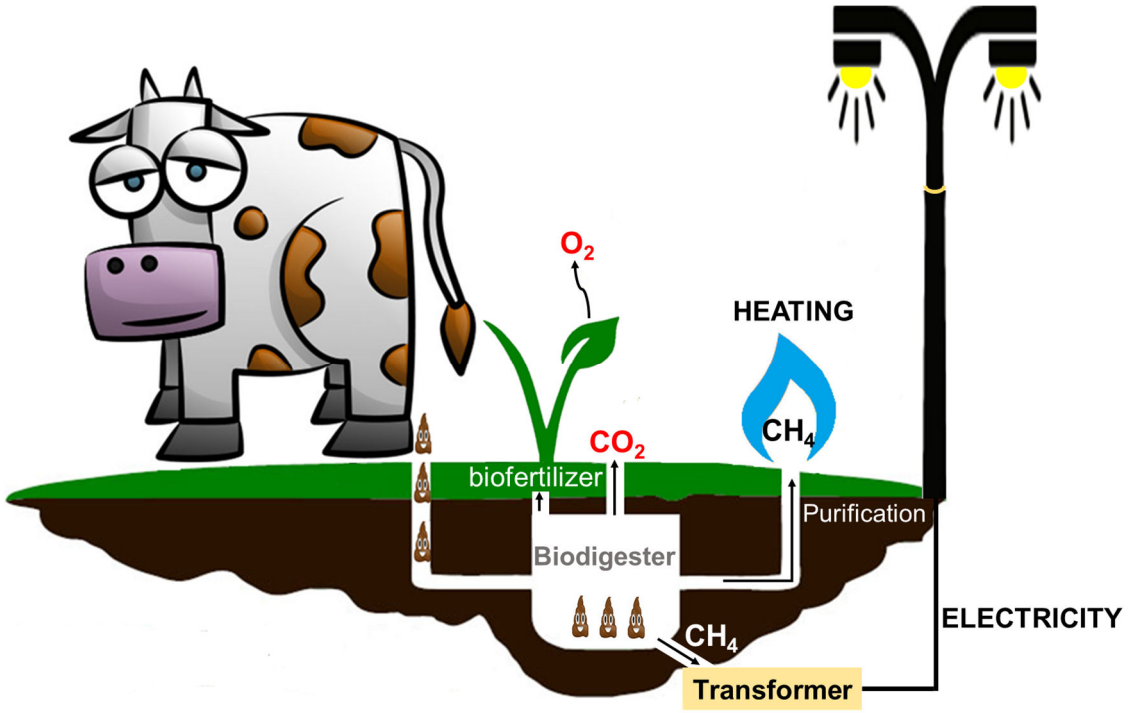

Figure 1.1. Biogas: a renewable energy.

Since impurities may cause corrosion, deposits and damage to equipment, it is required the complete removal of all the contaminant species in biogas to produce biomethane. Additionally, if the biogas is to be upgraded for household applications (standard natural

gas) or car fuel, it is also critical the removal of CO_2 since it reduces the energy content of biogas.[1–4,8,9] For example, to introduce the biogas at the natural gas pipelines, the methane gas needs to present a level of purification of 97%. Therefore, an energy efficient process to uptake CO_2 from CH_4 is required to spread the application of biogas, avoiding the corrosion of equipment and pipelines by the CO_2 acidic gas.[10,11] Moreover, up-taken CO_2 can be then used as refrigerant or at the agriculture production (through adsorption of CO_2 by the green plants) together with the biofertilizer obtained during the anaerobic digestion of the organic waste.[1,12] Current methodologies to purify off-gas (the effluent gas produced from the anaerobic digestion process of organic matter) and to increase its caloric value[1] are absorption, cryogenic distillation, membrane separation, and adsorption.[12,13] The main commercial solutions available for CO_2 uptake from biogas use absorption process through the use of amine based solvents able to react chemically with CO_2, such as monoethanol amine (MEA), diethanolamine (DEA), and methyl diethanolamine (MDEA), with chemical structures represented in Figure 1.2.

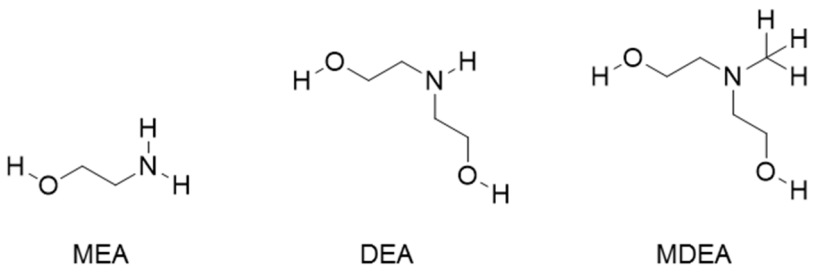

Figure 1.2. Chemical structures of MEA, DEA and MDEA.

Monoethanol amines are the most common solvents used due to their low cost. The available commercial technologies for CO_2/CH_4 separation present several drawbacks associated to the low CO_2 loading capacity of the solvent (0.40 kg CO_2 / kg MEA); degradation of the amine solvent in contact with NO_x, SO_x, O_2 gases; high cost of solution regeneration (concomitantly the CO_2 absorption capacity of the regenerated amine solution decreases); corrosion of the equipment by the amine solution and the scale up of the process. An alternative technology uses sterically hindered amines for CO_2 absorption. These have a low corrosive nature and less degradation from O_2 when compared to MEA as a solvent. However, the capacity to adsorb CO_2 is lower than the capacity observed for the MEA solution. Another process, aqua ammonia (NH_3), has been attracting attention due to the assumption that it could simultaneously remove NO_x and SO_x along with CO_2 from flue gases. This process presents high CO_2 loading capacity when compared to other absorption

processes (1.20 kg CO_2 / kg ammonia), and enables the control of several different pollutants at the same time. Additionally, it does not present equipment corrosion issues or absorbent degradation by oxygen. The resulting ammonium nitrate and ammonium sulfate (subproducts from the adsorption process) can be used as fertilizers. Although this process also presents some disadvantages, for instance i) the flue gas must be cooled to 15–27 °C due to volatility of ammonia, ii) additional equipment is necessary due to precipitates formation upon CO_2 capture and iii) high ammonia vapor losses occur during stripping.[13] Based on the limitations associated with the absorption technologies described above, the development of solid adsorbents to uptake CO_2 *via* adsorption separation has been thought as an alternative. The adsorption technology is a very attractive technique from small to medium-scale operations, but it relies on the availability of highly effective adsorbent materials, requiring the preparation of materials with different nature and structure.[14] Various mesoporous and microporous adsorbents, Figure 1.3, such as activated carbons[15–19], metal organic frameworks (MOFs)[15,20,21], zeolites and zeolitic imidazolate framework (ZIFs)[10,15,22–25], clays[26,27], and silica-based mesoporous materials[28,29] have been proposed for CO_2 adsorption/separation from biogas.

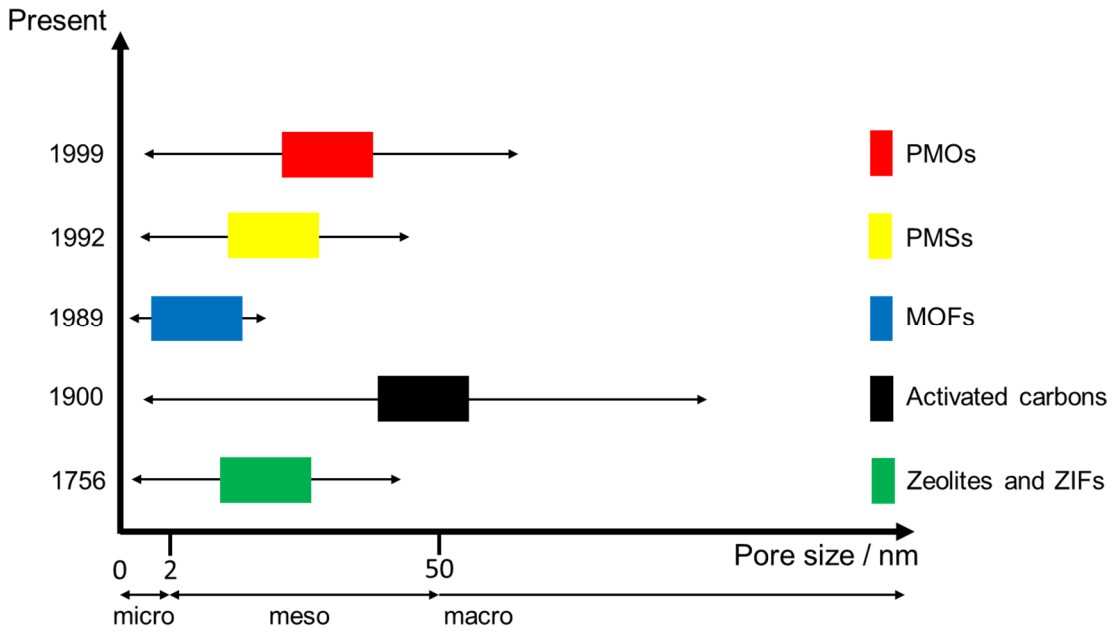

Figure 1.3. Development timeline of the porous material families according to the pore size.

The CO_2 capture capacities on several different materials, *e.g.* carbons, MOFs, zeolites and ZIFs, clays and silicas, have been reported in the literature.[30] Selected data for materials

used in the separation of CO_2/CH_4 are presented in Table 1.1. As it can be observed, all materials exposed adsorb more CO_2 than CH_4 at temperatures between 25 and 35 °C. In the case of the MAC (microwave activated carbon) material, the data were determined at different temperatures with concomitant effects on the values of the capacities. For instance, MAC shows a 20% reduction in the CO_2 capacity upon temperature increase from 25 to 35 °C. The CO_2/CH_4 adsorption capacity ratio also decreases with the increase of temperature. MOFs materials presenting Ni[31] or Mg[31] as metal centers adsorb higher amounts of CO_2 than MOFs prepared with Cu[32] or Al[33], but the ratio of the CO_2/CH_4 capacities is very low, when compared with the MOF with amine functionalities.

Zeolites and ZIFs adsorbents demonstrate CO_2 capacities inferior to those displayed by the MOFs CPO-27-Ni[31] and CPO-27-Mg[31], but the former also adsorb much smaller amounts of CH_4, giving rise to a larger ratio between the CO_2 and CH_4 capacities.

Table 1.1. Capacities of different adsorbents in the CO_2/CH_4 separation at 1 atm and their molar selectivity ratios.

Materials Type	**Materials**	**CO_2 capacity** ($mmol \cdot g^{-1}$)	**CH_4 capacity** ($mmol \cdot g^{-1}$)	**Ratio CO_2/CH_4**	**Temperature** (°C)
Carbons	a-MCMBs[17]	1.97	1.23	1.60	25
	MAC[19]	2.13	0.98	2.17	
		1.69	0.81	2.09	35
	Activated Carbon[34]	≈2.10	≈0.90	2.33	
MOFs	MOF-14(Cu)[32]	≈2.50	≈1.00	2.50	25
	CPO-27-Ni[31]	≈7.50	≈4.38	1.71	
	CPO-27-Mg[31]	≈8.75	≈4.29	2.04	
	amino-MIL-53(Al)[33]	1. 96	≈0.30	6.53	30
Zeolites and ZIFs	Hβ-zeolite[35]	1.76	0.38	4.63	
	Naβ-zeolite[35]	≈2.80	≈0.70	4.00	
	ZIF-7[4]	2.34	0.13	18.00	25
	T-type zeolite[36]	≈1.90	≈0.30	6.33	35
	LiX zeolite[34]	≈3.90	≈0.69	5.65	
	13X zeolite[22]	≈4.08	≈0.50	8.16	
	Chabazite zeolite (**r_2**KCHA)[37]	≈3.70	≈1.10	3.36	
Clays	PILC Al_w[27]	≈0.40	≈0.07	5.71	25
	PILC Al_B[27]	≈0.40	≈0.08	5.00	
Silicas	APTES@SBA-15[38]	≈1.29	≈0.44	2.93	
	APTES@STMB[38]	≈1.48	≈0.38	3.89	
	APTES@SHEPF[38]	≈2.39	≈0.31	7.70	
	APTES@STMBF[38]	≈1.87	≈0.06	31.17	
	MCM-41[39]	≈0.70	≈0.16	4.38	

In the case of clays, PILC Al_w[27] and PILC Al_B[27] show the smallest capacities for the adsorption of CO_2 and CH_4 from the selection of materials presented in Table 1.1, but the ratios between the CO_2/CH_4 capacities are similar to those displayed by other materials (*e.g.* zeolites).

Interestingly, despite the silica-based mesoporous materials present low CO_2 adsorption capacities, the ratios of the CO_2/CH_4 capacities of these materials are, in general, higher than in the case of the other adsorbents. A material showing high molar selectivity ratio is APTES@STMBF[38], which is an SBA-15 pore expanded silica prepared by condensation reaction of tetraethyl orthosilicate (TEOS) under the presence of P123 as structure directing agent, trimethylbenzene as swelling agent and ammonium fluoride as solubility enhancer, followed by grafting of aminopropyltriethoxysilane (APTES). Although, these adsorbents are still not ideal for CO_2 uptake from biogas mainly due to the following reasons: the ideal adsorbent needs to present the optimal features as high capacity, perfect selectivity, long-term durability, good mechanical stability, fast uptake processes, easy regeneration consistent with negligible capacity loss on multiple adsorption/desorption cycles and low toxicity.[40]

In order to attain these aims, the aromatic bridged-PMOs incorporating some modifications are proposed as adsorbents for CO_2/CH_4 gas separation. PMOs are easy to prepare and exhibit crystal-like walls, high specific surface areas, high pore volumes and high thermal stability.[41–43] Additionally, a good diffusion of the molecules can be achieved within the channels of the Ph-PMOs as the organic functions are an integral part of the walls of these materials. The control of the porosity of the PMOs is made through the use of template-assisted self-assembly method. Likewise on silica materials, the amine chemical modification of the Ph-PMO[44] can be done to improve the affinity of the materials to interactions with CO_2 without changing that with CH_4.

The novelty of the present PhD work is the tuning of the adsorption properties of PMOs through functionalization of their organic groups, using new synthetic strategies. Thus, the inclusion of different amino groups in PMOs is investigated for creating materials with high π-π conjugation and different hydrophobic/hydrophilic character. To the best of our knowledge, only a few examples of the preparation of amine-functionalized PMOs were reported in the literature and none of them were tested in the proposed applications. Moreover, all experimental work is performed in close synergy with the theoretical

calculations. Additionally, other non-conventional approaches were also used to improve the CO_2 adsorption properties of the PMOs and their selectivity for the CO_2/CH_4 separation.
The following section starts with a brief review of the history of how PMO materials emerged from silica, which organic functions were introduced in these materials, and which textural, physical and chemical properties were expected to be obtained with such modifications.

1.3 Ordered mesoporous silica materials

Nanostructured porous materials have been prepared by a bottom-up approach,[45–48] such as template-assisted self-assembly method,[46,48] in which the nanomolecular blocks are arranged around surfactant micelles *via* weak interactions.[49] This procedure allows the tuning of the pore shape, size and connectivity, as well as of the chemical composition.
In this PhD Thesis, the self-assembly methodology is extensively used to prepare organic-inorganic hybrid nanoporous material such as PMOs. These materials combine organic and inorganic properties and have received much attention in the last two decades.
PMOs, discovered in 1999[41–43], are mesoporous 2D structures formed by bissilylated organic bridges linked to each other by silica moieties,[50] which resemble periodic mesoporous silicas (PMS).[51–53] The M41S family of materials denoted as MCM (Mobil Composition of Matter)[54,55] and SBA (Santa Barbara amorphous)[54,55] materials are the most known PMSs.[50,55] PMSs and PMOs can have different shapes and pore sizes depending on the choice of the structured directing agent (SDA) and reaction conditions (pH, temperature, reaction time and precursors). Many similarities are found between the synthetic procedures of PMOs, SBAs and MCMs.[55] Their formation occurs through hydrolysis and condensation of the silica precursors around the supra-molecular assembly formed from a wide range of anionic and cationic surfactants, or gemini or triblock copolymers or oligomers under basic, acid or neutral conditions.[56,57] The porous material can be obtained by hydrothermal treatment or evaporation induced self-assembly (EISA),[50] and the free porosity is achieved through surfactant removal by solvent extraction in acidic media or calcination.[54] Two different mechanisms were proposed to explain the formation of these materials as presented in Figure 1.4. The first is a true liquid-crystal templating (TLCT) mechanism, which is observed in the absence of inorganic species under very high

concentrations of the surfactant (Figure 1.4a).[57–59] The second mechanism occurs at low concentration of template, and involves the formation of the lyotropic liquid-crystalline phase by self-assembly cooperation of the template and inorganic precursor. This one is designed as cooperative liquid crystal template (CLCT) mechanism (Figure 1.4b). The formation of the porous material *via* TLCT or CLCT is still a matter of scientific debate but recent computational studies support the latter (please refer to Ref. [60] and references therein).

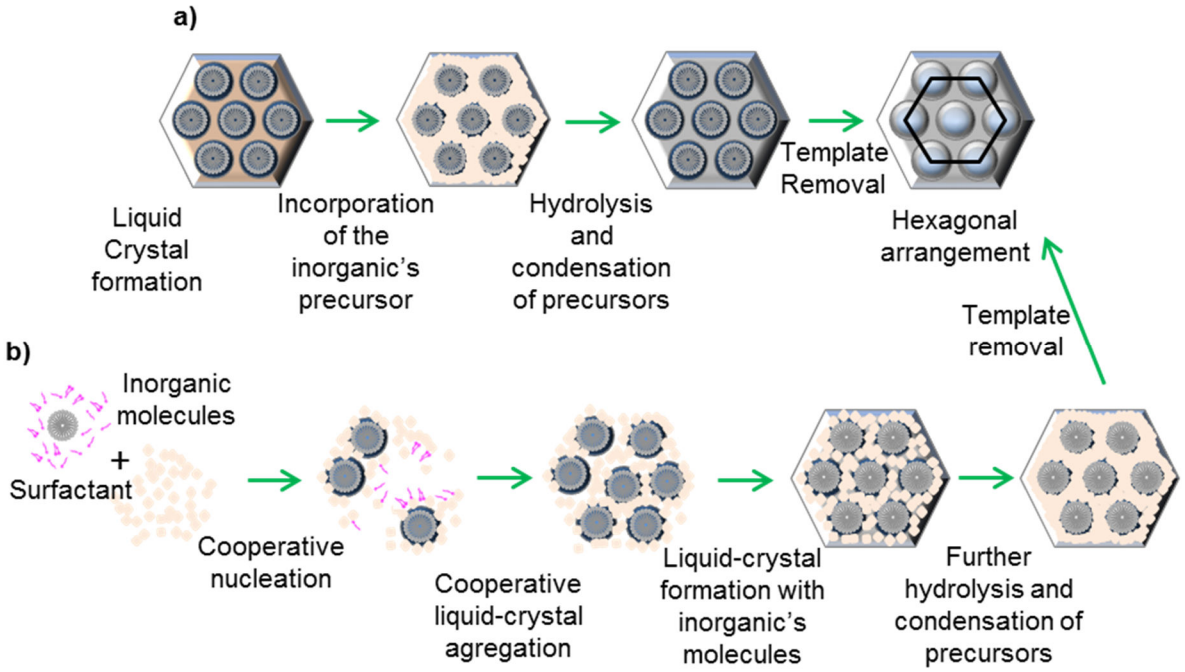

Figure 1.4. Preparation of periodic mesoporous materials in the presence of supramolecular structure-directing agents following a) TLCT or b) CLCT mechanisms. Adapted from reference [61].

Hexagonal, cubic, or laminar pore arrangements can be obtained, Figure 1.5.[57,62]

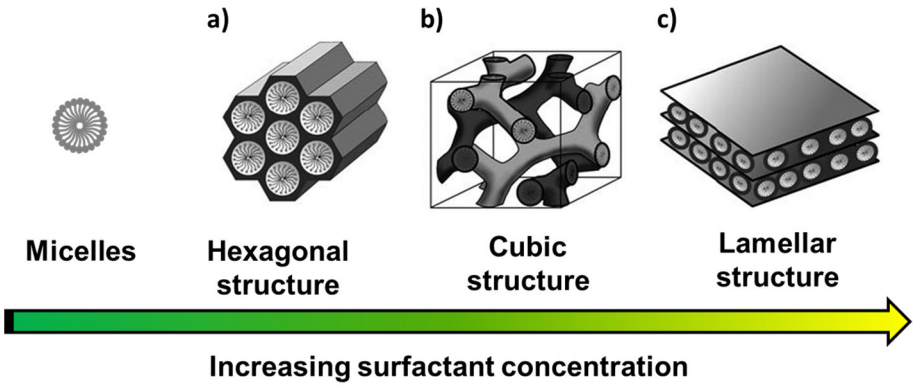

Figure 1.5. Hexagonal, cubic and laminar pore arrangements reported in the literature. Adapted from reference [57].

Besides a narrow distribution of the pore sizes and are higly ordered, PMSs present very interesting properties such as large specific surface areas, and as they possess a large number of free silanols, they can be easily modified to incorporate functional groups for the desired application.

1.3.1 Introduction of functional groups into porous materials

MCMs and SBAs have been largely applied in catalysis and adsorption, using polymeric, inorganic, organic and organometallic hosts into the pores.[41] The combination of inorganic and organic functionalities can be made through i) grafting or ii) co-condensation reaction.[63] In this way, the PMS materials can be tuned to obtain different polarities and/or new reaction centers.

1.3.2 Post-grafting functionalization of parent silica materials

The grafting[45] takes place when an organic silylated precursor (with a formula $(R'O)_3Si\text{-}R$) is added to the parent silica and reacts with the free silanols, Figure 1.6. Other precursors can be used to modify the silica materials, such as chlorosilanes ($ClSiR_3$), long-chain alcohols and silazanes ($HNSiR_3$).[57,58,63,64] Hence, a variety of organic groups, from acid to basic functionalities, can also be introduced inside the pores by changing the nature of the R groups in the material.

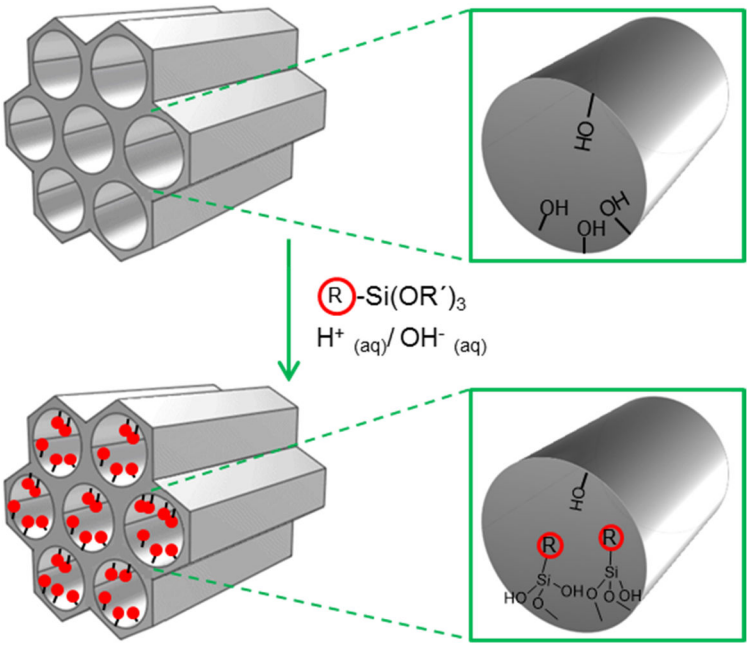

Figure 1.6. Functionalization of the PMS materials with terminal organosilanes using the grafting method. R is the organic function.

Although, the grafting typically leads to a decrease of specific surface area depending on both content and size of the group introduced. A drawback of the grafting technique is related with the diffusion of the species inside the pores since pore blockage may occur, especially when bulky species are used, reacting preferentially at the extremities of the channels. Moreover, heterogeneous distribution of the introduced organic moieties tends to arise from the grafting method[57] and the thermal stability of the materials is usually affected by the introduction of the organic moieties.

1.3.3 Co-condensation synthesis

An alternative process for the incorporation of functional groups into PMSs is the co-condensation reaction. The functionalities are introduced in the material during the synthesis by adding to the silica precursor a terminal trialkoxysilanes $(R'O)_3Si\text{-}R$, where R is the organic group. The hydrolysis and condensation of the two precursors takes place in the presence of SDA under basic, acid or neutral conditions.[57,58,63,64] The resulting material displays organic groups distributed along the pore walls, Figure 1.7. The advantages of the co-condensation reaction when compared to the grafting methodology are the absence of pore blocking and bulkier organic groups and higher loading of organics can be introduced in the material. As a result, functional groups are usually more homogeneously distributed in the framework.

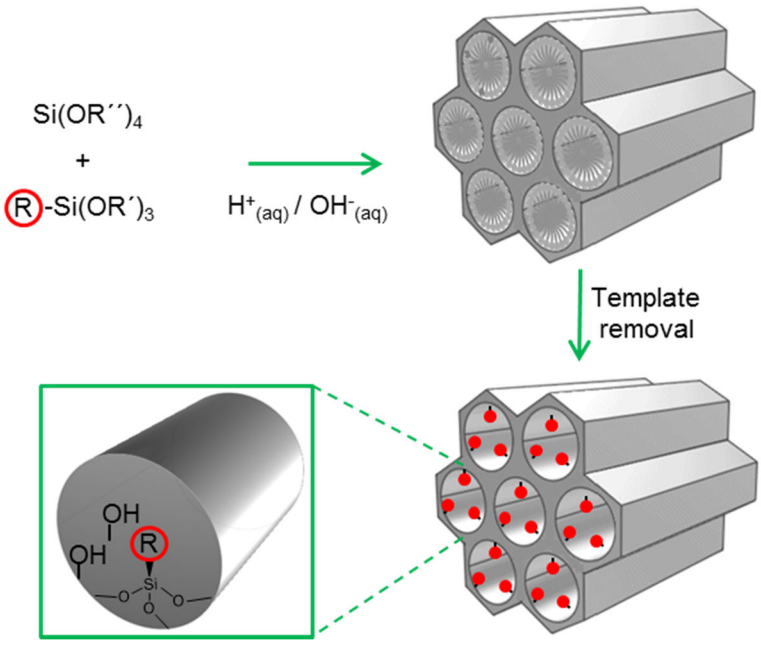

Figure 1.7. Co-condensation synthesis of $Si(OR'')_4$ with organosilanes precursors in the presence of SDA. R is the organic function.

However, the mesostructure order of the material is affected when the concentration of the organic precursors increases by more than 40 mol%. High contents of organic functions also can promote the reduction of the specific surface areas and originate broad pore-size distributions, which limit the shape, size and selectivity of these materials.[17] Moreover, a huge increase of the terminal organic silanes leads to different rates in the hydrolysis and condensations of different precursors favoring the homocondensation reaction of both precursors. [17] When this takes place the homogenous distribution of the precursor can be hardly achieved. In this synthetic approach the SDA removal must be done by extraction.[57] As in the case of the grafting, co-condensation method can be used to prepare organic-inorganic hybrid silicas incorporating a vast range of organic functionalities under well-chosen synthetic conditions.

1.4 Crystal-like periodic mesoporous organosilicas (PMOs)

As organic functionalized PMSs present several drawbacks, such as low organic content (less than 20%), reduced specific surface area, heterogeneity, potential leaching of organic species during application, PMOs appear as an interesting alternative to PMSs since the organic moieties are important elements of the skeleton of the material. The most dramatic change between the synthetic strategies of PMS and PMO materials is the use of a bissilylated organic precursor in the latter, instead of a pure inorganic silica source in the former. The organic moiety in the case of PMOs is strategically placed between the silicon atoms in order to directly integrate the wall of the material, keeping the pore channel free for potential applications.[41–43] Still, it is important to note that the distribution of functional groups in the walls of PMO materials is quite uniform while in the case of functionalized PMS materials, the functional groups essentially appear at the surface of the material.[41–43] Despite the high concentration of organic groups, PMOs usually present high thermal stability. This occurs due to the intercalation of organic/inorganic groups in the pore walls, enhancing the stability of the material.

A large number of bissilylated precursors has been used to prepare PMOs with different textural, physical and chemical characteristics with some examples being shown in Figure 1.8.

Studies in the field not only aim the synthesis of novel PMOs based on new bissilylated precursors, but also aspire the modification of the known precursors to improve properties

of these materials. Despite the appearance of numerous reports in the literature showing that PMOs bring important advantages when compared to other commercial materials, PMOs have not yet been introduced into the commercial market. The properties of these materials in some cases (for example for microelectronics) bring numerous advantages when compared to alternative products already under commercialization. However, the high price required to produce PMOs is a major drawback.

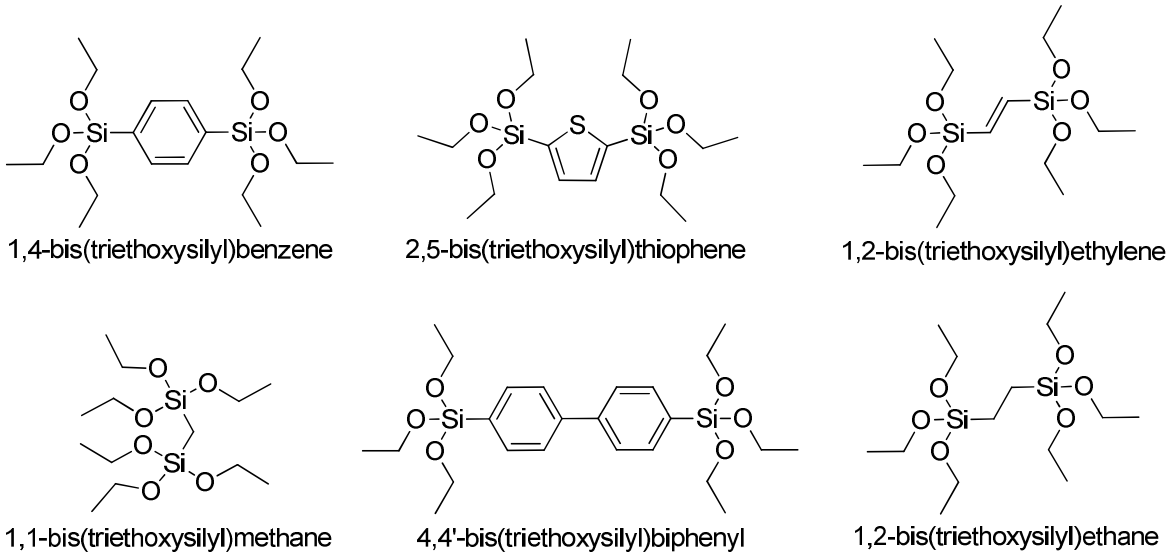

Figure 1.8. Structures of typical bissilylated precursors used to prepare PMOs.

For catalysis and adsorption applications, the properties of these materials are not yet the desirable ones having into account the high price when compared with those of alternative materials under use. Tuning the properties of PMOs for adsorption applications was the ultimate objective of this PhD Thesis. This was done by considering several synthetic procedures to introduce the desired functionalities into the materials, which were selected by previous analysis of the literature. A short review of the most remarkable advances in the field is provided below, together with suggested ways to improve the characteristics of PMOs, with special attention for materials prepared from nitrogen source precursors.

1.4.1 Single source precursor

Ozin *et al.*[41] described the synthesis of the ethene-PMO by hydrolysis and condensation of 1,2-bis(triethoxysilyl)ethene (BTEE) in the presence of cetyltrimethylammonium bromide (CTAB) under aqueous basic conditions. The free pores were obtained by solvent extraction. The ethene-PMO displayed well-ordered hexagonal mesostructure (Table 1.2) and high

surface area (637 $m^2 \cdot g^{-1}$). Then, the ethene bridge was brominated, rendering further chemical transformations readily accessible.

Inagaki *et al.*[42] reported the preparation of the ethane-PMO using as bissilylated precursor the 1,2-bis(trimethoxysilyl)ethane (BTME). The variation of the synthesis conditions (varying the proportion of the reagents, the ageing time and the hydrothermal time) led to the formation of two materials, one possessing 2D hexagonal mesophase and the other displaying 3D hexagonal mesophase, Table 1.2.[42]

Table 1.2. Structural properties of the selected PMOs.

PMO	mesostructure	S_{BET} ($m^2 \cdot g^{-1}$)	*d*p[a] (Å)	*a*[b] (Å)	*b*[c] (Å)
ethene-PMO[41]	2D *p6mm*	637	39.4	47.0	7-8
ethane-PMO[42]	2D and 3D *p6mm*	750 / 1170	31 / 27	57.0 / 88.6[d]	26 / 61.6[e]
ethane-PMO[43]	2D *p6mm*[g]	1234	22	47.3[g]	25
ethene-PMO[43]	2D *p6mm*[g]	897	24	48.5[g]	24
phenylene-PMO[51]	2D *p6mm*	-	38	52.5	-
biphenylene-PMO[65]	2D *p6mm*	869	35.4	48.3	12.9[e]
BTMSPA-PMO[66]	disordered	600	89.0	-	-
TMSEN-PMO[67]	disordered	310	107	-	-
BTEVA-PMO[68]	2D *p6mm*	900	28	47.8	19.8
CHTC-PMO[69]	2D *p6mm*	1079	31	62.0[h]	31[e]

[a]Pore width (*d*p) obtained from the Barret–Joyner–Halenda (BJH) method with the corrected Kelvin equation, *i.e.* Kruk-Jaroniec-Sayari (KJS)–BJH method at the maximum of pore size distribution calculated on the basis of adsorption data. [b]Unit cell parameter (*a*) calculated as ($2d_{100}/\sqrt{3}$). [c]Pore wall thickness (*b*) calculated as ($2d_{100}/\sqrt{3}$ - *d*p), where the first term is the unit cell parameter. [d]The 3D hexagonal material possesses a unit cell c = 55.4 Å. [e]This information is not given in the report. The *b* was calculated from the d_{100} and the *d*p provided in the report. [f]It is only observed the (100) reflection. The (110) and (200) reflection are expected for a hexagonal order material. [g]This information is not given in the report. The unit cell size was calculated from d_{100} reflection pattern obtained from the report. [h]Pore diameter calculated using classical density functional theory (DFT).

Stein *et al.*[43] also synthetized the ethane-PMO material but using different reaction conditions, such as pH, stirring time, reagents concentrations, and in the absence of hydrothermal treatment. The same authors also obtained the ethylene-PMO (*a.k.a.* ethene-PMO) with wormlike channels having uniform diameter.[43] Interestingly, the materials prepared by Stein and co-workers[43] were not as ordered as the materials prepared by Inagaki[42] and Ozin[41] groups, which suggests that the reaction conditions used to prepare these materials have huge influence in the mesostructures obtained. Ozin *et al.*[70] reported the preparation of phenylene- (Ph-), thiophene-, ferrocene-, bithiophene- and acetylene-PMOs. Despite the attempts in changing the synthetic conditions to obtain well-ordered materials, these authors could only prepare the Ph- and the thiophene-PMO with 2D hexagonal symmetry mesophase. The ferrocene- and the bithiophene-PMOs displayed poor

order, while the acetylene-PMO was difficult to control under aqueous media since it presented labile Si–C bonds.

In 2002, Inagaki and co-workers[51] synthetized, for the first time, a Ph-PMO showing meso- and molecular-scale periodicities. The Ph-PMO possesses a 2D *p6mm* symmetry lattice and a structural periodicity in the wall along the channel direction with a spacing of 7.6 Å, Table 1.2. In addition, these authors were able to sulfonate the aromatic benzene groups, paving the way for further synthetic modifications in these materials. In the same year, Inagaki *et al.*[65] also reported the preparation of *p*-biphenylene-PMO (Bph-PMO) using a similar synthesis procedure. Bph-PMO also displayed meso- and molecular-scale (interlayer spacing of 11.9 Å) periodicities and 2D hexagonal structure. Recently, Comotti *et al.*[71] demonstrated that this material stands out for its ability to present rotation motion. Through nuclear magnetic resonance (NMR) spectroscopy the authors proved the dynamic behavior and verified the existence of parallel and aligned molecular rotors along the mesochannel axes.

Ha and co-workers[66] synthetized a non-ordered PMO with basic functionalities by condensation of bis[3-(trimethoxysilyl)propyl]amine (BTMSPA) using P123 under acidic conditions, Table 1.2. The BTMSPA-PMO displayed hydrophilic silicate layers and it was tested, together with Ph-PMO and Bph-PMO materials, in the adsorption of lysozyme. They found that the amine moieties of the BTMSPA-PMO material did not interact with the lysozyme, and preferential lysozyme-PMO interaction was observed for the Ph-PMO and Bph-PMO, wich displayed hydrophobicity superior to BTMSPA-PMO. But, the interaction was suggested to be related also with the silanols groups as displayed by the different loading in each material. In fact, the BTMSPA-PMO only possesses 30% free silanols groups against about 70% of free silanols observed in the other PMOs. Therefore, in order to obtain additional information about the preferential interaction mechanism, the same authors[72] reported the use of these three materials in the adsorption of L-lysine (strong hydrophilicity), isoleucine (strong hydrophobicity) and glycine (intermediate character, *i.e.*, weak hydrophobic/hydrophilic properties). L-lysine was mainly adsorbed by BTMSPA-PMO, while isoleucine adsorbed more into Bph-PMO. Although, glycine was preferentially adsorbed by hydrophobic Ph- and Bph-PMOs in comparison to BTMSPA-PMO. The authors showed the importance of electrostatic interactions between PMOs and the adsorbed amino acids; they observed that the maximum amount of amino acid adsorbed occurs in the

isoelectric point of the amino acid. Furthermore, the pore size diameter of the materials also had significant contribution in the adsorption of the amino acids. More recently, Ha and co-workers[73] explored the capability of these three PMOs to adsorb nicotine from aqueous solution. The nicotine exhibits hydrophobic character being strongly adsorbed by Ph-PMO and, as in the case of the amino acids, it was observed a strong dependence between adsorption properties and isoelectric point and hydrophobicity of the PMOs.

Duan *et al*.[67] prepared a PMO material based on [3-(trimethoxysilyl)propyl]-ethylenediamine (TMSEN) precursor in the presence of non-ionic P123 surfactant and water. The disordered material presented a BET surface area of 310 $m^2 \cdot g^{-1}$ and an average pore diameter of 107 Å (*c.f.* Table 1.2). They tested the TMSEN-PMO material in heavy metal ion removal from water (ultra-pure water). The adsorbent showed high adsorption capacity for Cu^{II} (1.2 $mmol \cdot g^{-1}$) and Pb^{II} (1.3 $mmol \cdot g^{-1}$) ions and could be reused for several times without minimal loss of its capacity as an adsorbent. Additionally, high selectivity for Cu^{II} over Ni^{II} and Co^{II} was found, which turns this material a potential candidate for wastewater treatment, drinking water purification and soil remediation.

Beretta *et al*.[68] prepared divinylaniline organic bridging PMO (BTEVA-PMO) with 2D hexagonal mesostructure, with three reflections indexed having Miller indices (100), (110) and (200) and with a unit cell dimension of 47.8 Å, Table 1.2. Additionally to the meso-ordering of the pores, this PMO also presents crystal-like pore walls with a molecular-scale periodicity of 11.8 Å. This material has specific surface area of 900 $m^2 \cdot g^{-1}$ and a pore diameter of 28 Å. The access of the amino group in the aniline moieties of the BTEVA-PMO to further modifications was tested through chemical functionalization of the amine group with the amino-acid L-alanine by formation of an amide bond. Thus, the authors demonstrated that BTEVA-PMO is a good candidate for the formation of oligopeptides within the pores.

In 2015, Mizoshita and Inagaki[69] prepared a new PMO (CHTC-PMO) with *N*,*N*',*N*''-tris(3-triethoxysilylpropyl) *cis*,*cis*-1,3,5-cyclohexanetricarboxamide precursor (CHTC) in the presence of octadecyltrimethylammonium bromide (ODTMA) surfactant under basic conditions. The prepared functional material showed both meso- and molecular-scale orders. The authors only observed a strong (100) reflection in powder X-ray diffractometer (PXRD), but using transmission electron microscopy (TEM) they observed some PMO areas with 2D hexagonal packing and a lattice constant of 62.0 Å (d = 53.6 Å),

Table 1.2. The authors also observed the molecular-scale periodicity along the channel direction with a lattice constant of 16.5 Å (d = 14.3 Å). Thus, the CHTC-PMO presents both meso- and molecular-scale orders and this was possible due to the high self-assembly behavior of the precursor. Additionally, the authors found that the pore walls of this material could bind strongly silane-free guest molecules through H-bonded intercalation. This fact is very interesting due to the potential combination of H-bonded intercalation with chemical modification of silanol groups for constructing multifunctional PMOs.

Kuschel and Polarz[74] developed a new PMO with increased chemical versatility, containing brominated-phenylene moieties that can be accessible to further modification reactions. To prepare such material these authors started from a new precursor, 5-bis(triisopropoxysilyl)-3-bromobenzene, in the presence of Pluronic F123 triblock copolymer in ethanol under acidic conditions. Beside the efforts to obtain a material with ordered pores, they could only obtain a bromine-phenylene-PMO with worm-like ordering.

Bion *et al.*[75] considered different SDAs (alkyltrimethylammonium halides) to obtain Ph-PMO materials with 2D hexagonal mesostructure, but with different pore sizes. They observed that changing the alkyl-chain of the surfactant resulted in Ph-PMOs presenting different physical and textural properties. The alkyl-chain of the surfactants varied from fourteen to eighteen carbons. The surfactant with the biggest alkyl-chain promoted the formation of a Ph-PMO with large pore size, Table 1.3.

Table 1.3. Structural properties of the selected PMOs prepared with different bissilylated organic sources and SDAs.

PMO	SDA	S_{BET} ($m^2 \cdot g^{-1}$)	dp^a (Å)	a^b (Å)	b^c (Å)
phenylene-PMO[75]	TDTMA[e]	674	32	51.4	13
phenylene-PMO[75]	CTAB[f]	622	36	56.9	13
phenylene-PMO[75]	ODTMA[g]	653	39	62.2	15
thiophene-PMO[76]	P123	440	54	111	57
thiophene-PMO[76]	Brij 76	1020	33	62	29
phenylene-PMO[76]	P123	800	48	111	63
phenylene-PMO[76]	Brij 76	1110	33	65	32

[a]Pore width obtained from the BJH method with the corrected Kelvin equation, *i.e.* KJS–BJH method at the maximum of pore size distribution calculated on the basis of adsorption data. [b]Unit cell parameter calculated as ($2d_{100}/\sqrt{3}$). [c]Pore wall thickness calculated as ($2d_{100}/\sqrt{3}$ - dp), where the first term is the unit cell parameter. [e]TDTMA means tetradecyltrimethylammonium bromide. [f]CTAB means cetyltrimethylammonium chloride. [g]ODTMA means octadecyltrimethylammonium bromide.

Recently, Kalantzopoulos *et al.*[77] prepared ordered and disordered mesoporous phenylene-silica and tested their ability to uptake and storage hydrogen. The authors found that the

phenylene-PMO materials with 2D hexagonal pore order and varied pore sizes present a specific surface area between 640 and 782 $m^2 \cdot g^{-1}$, while the disordered phenylene-silica materials have specific surface areas between 650 and 910 $m^2 \cdot g^{-1}$. It was observed that the materials exhibit a reversible hydrogen excess surface adsorption capacity up to 2.10 wt% at 6 MPa and 77 K and the increase of the alkyl length of the surfactant seems to increase the hydrogen molecules on the adsorbent. Additionally, a direct correlation between physical properties of the prepared materials and the hydrogen adsorption behavior was found. For the case of the phenylene-PMOs, the authors observed an increase of the hydrogen capacity with the increase of the specific surface area, while the hydrogen capacity of the disordered mesoporous phenylene-silica adsorbents increases with the increase of pore volume and pore size.

Fröba *et al.*[76] also prepared the Ph- and the thiophene-PMO with different pore sizes but extremely ordered. The authors promoted the hydrolysis and the condensation of the precursors (1,4-bis(triethoxysilyl)benzene, BTEB, or 2,5-bis(triethoxysilyl)thiophene, BTET) in the presence of P123 and Brij 76 copolymers as SDA under acidic conditions. Ordered materials with 2D hexagonal (*p6mm*) mesoporous structures were formed. It was possible to control the pore sizes by changing the SDA. The P123 promoted the formation of PMOs with pore sizes larger than those obtained with Brij 76. P123 led to larger pore sizes when the organic moiety of the bissilylated precursor is changed from thiophene to phenylene, Table 1.3. With Brij 76, the size of the pores remained unchanged independently of the precursor used. So, the consideration of different bissilylated precursors, SDAs and reaction conditions (*e.g.* pH and temperature) allows the preparation of novel PMOs with different chemical, physical and textural properties.

Other developments to create PMOs with advanced functional bridges have been reported in the last few years.[50] These are the cases of the inclusion of heteroatoms such as N, S and P, or of moieties such as metal complexes, metal nanoparticles or chiral bridges for creating materials with high π-π conjugation and/or different hydrophobic/hydrophilic character, for adsorption and catalysis applications.[50]

There are three different methodologies to make possible the introduction of advanced functional groups into the channels of the PMOs: i) co-condensation, ii) organic bridge post-synthetic modification and iii) grafting reaction. These three approaches are described below.

1.4.2 Co-condensation reaction

Co-condensation synthesis allows the combination of two or more different mono- or bissilylated organic precursors to produce PMOs with functionalities well distributed into the matrix of the material, Figure 1.9.

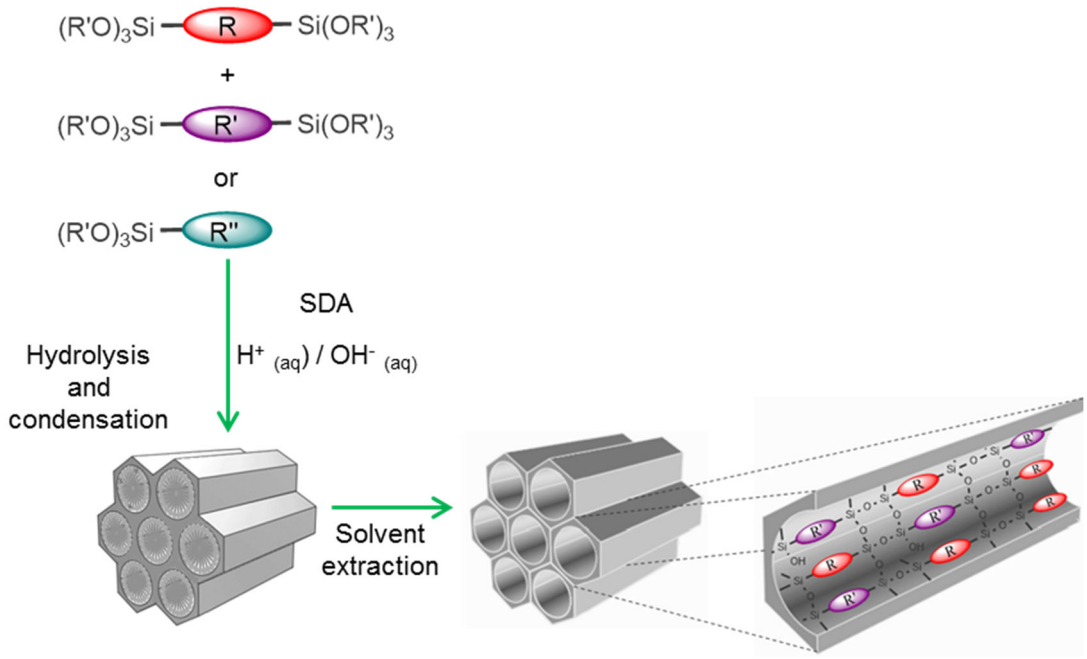

Figure 1.9. Schematic representation of functionalized-PMOs synthetized *via* co-condensation reaction. R, R', R'' represent different organic functions.

In 2002, Inagaki *et al.*[78] showed for the first time the preparation of a PMO with acidic functionalities using the co-condensation reaction. The novel material was obtained by combination of BTEB and 3-mercaptopropyltrimethoxysilane (MPTMS) in the presence of ODTMA under basic conditions. It presented the meso- and molecular-scale observed for Ph-PMO material. The authors varied the proportion of the precursors and found that, as the MPTMS amount increased, the degree of the mesoscopic order decreased. The 2D hexagonal arrangement of the pores was only well observed at 0.40 mol% of MPTMS, presenting 0.30 mmol·g^{-1} of H^+, Table 1.4. Materials with 0.70 mmol·g^{-1} of H^+ content were also obtained, but the mesostructure was perturbed. Moreover, the reduction of both surface area and pore diameter was observed with increasing acid content. After nitric acid treatment, the oxidation of the thiol group was observed with formation of the sulfonic acid group. The formed material, Ph-PMO_PrSO_3H, possessed thermal stability up to 300 °C. The oxidation of the thiol group led to a decrease of surface area and pore diameter, and also to a reduction of the organization degree of the pores mesostructure. The final PMO conjugated the

molecular-scale periodicity with the flexibility of the sulfonic arms. Other bissilylated precursors with biphenylene[79] and ethane[80,81] bridges where reacted with MPTMS to give rise to materials with 2D hexagonal arrangement and different degrees of hydrophobicity, thermal stability and flexibility in the framework structure. These materials were tested in water-generating reactions. Moreover, different SDA, as for instance, cationic alkyl surfactant[80] and triblock copolymers,[81] were employed to obtain such acid functionalized ordered materials.

Table 1.4. Structural properties of the selected PMOs with acid properties prepared by co-condensation reaction.

PMO	structure	S_{BET} ($m^2 \cdot g^{-1}$)	dp^a (Å)	a^b (Å)	$[H^+]$ ($mmol \cdot g^{-1}$)
Ph-PMO_$PrSO_3H$[78]	2D *p6mm*	747	28.0	53.6	0.30
Bph-PMO_$PrSO_3H$[79]	2D *p6mm*	775 (443)[c]	19.4 (17.7)[c]	50.2 (50.9) [d]	0.99
Et-PMO_$PrSO_3H$[80]	2D *p6mm*	878 (561)[c]	24.0	52.0	1.35
Et-PMO_$PrSO_3H$[81]	2D *p6mm*	564	81.0	108.5	0.37

[a]Pore width obtained from the BJH method with the corrected Kelvin equation, *i.e.* KJS–BJH method at the maximum of pore size distribution calculated on the basis of adsorption data. [b]Unit cell parameter calculated as ($2d_{100}/\sqrt{3}$). [c]After oxidation of the thiol group.

Recently, Bispo *et al.*[82] described the catalytic efficiency of Ph-PMO_$PrSO_3H$ (prepared with different acid loadings), Bph-PMO_$PrSO_3H$ and SO_3H-Ph-PMO in the dehydration of fructose to HMF (5-hydroxymethylfurfural) in water. The authors found that the catalytic activity of these materials relies on: i) the density of the sulfonic groups; ii) the location of the sulfonic sites and iii) the hydrophobicity of the surface. The material that presented the highest activity had phenylene moieties in the pore walls, propyl sulfonic sites grafted to the silanols of the Ph-PMO and an acid loading of 0.36 $mmol \cdot g^{-1}$.

Materials showing basic functionalities in the framework of the PMOs were also reported in the past few years. In 2006, Wahab *et al.*[83] reported the formation of well-defined 2D hexagonal order PMOs fibers when BTEE was mixed with 1-[3-(trimethoxysilyl)propyl] urea (UREDO) or (3-triethoxysilylpropyl) isocyanate (ICP) in the presence of CTAB/Brij30 surfactant mixture under basic conditions (Table 1.5, Et-PMO_UREDO and Et-PMO_ICP). They showed the influence of the amount of the nitrogen containing precursor in the formation of the PMOs meso-scale order. Disordered materials were formed with molar percentages of nitrogen precursors higher than 25 mol%. The basic nature of UREDO or ICP precursors led to an increase of the pH during the synthesis, which hindered the organization of the micelles in a 2D-hexagonal arrangement. The influence of the reaction temperature on the formation and the internal pore architecture was also observed. The change of the

reaction temperature from 55 to 75 °C originated pore channels aligned parallel to fiber axis with hexagonal arrangement. Li *et al.*[84] synthetized the aminopropyl-functionalized ethane-bridged PMO (Ethane-PMO_APTES) with spherical morphology and cubic *Pm*3*n* meso-order, Table 1.5. The Ethane-PMO_APTES was achieved by co-condensation of 1,2-bis(triethoxysilyl)ethane (BTSE) and aminopropyltriethoxysilane (APTES) in the presence of ODTMA surfactant and methanol as co-solvent in basic medium. The authors observed that methanol was crucial in the formation of spherical morphology and that the particle size could be tuned through variation of the aging temperature and time. This material showed a good mechanical and chemical stability, a specific surface area of 765 $m^2 \cdot g^{-1}$ and a pore diameter of 40.9 Å. This material was tested in liquid chromatographic separation and compared to a commercial APS-2 HYPERSIL NH_2 column. The authors tested the separation of benzene derivatives (toluene, biphenyldimethylesterate and nitrobenzene) at different flow rates, the separation of metronidazole, fluconazole and isonicotinic acid under high pH mobile phase (pH 11.8), and the separation of matrine and oxymatrine, sophocarpine and *N*-oxysophocarpine, under low pH mobile phase (pH 1.6). They found that the Ethane-PMO_APTES has a high chemical stability in a wide pH range and the order of the peaks is the same as in the case of the commercial NH_2 column for all separations.

Table 1.5. Structural properties of the selected PMOs with basic properties prepared by co-condensation reaction.

PMO	structure	S_{BET} ($m^2 \cdot g^{-1}$)	dp[a] (Å)	a[b] (Å)	b[c] (Å)
Et-PMO_UREDO[83]	2D *p6mm*	473	31.7	51.0	19.9
Et-PMO_ICP[83]	2D *p6mm*	556	30.5	56.1	25.6
Ethane-PMO_APTES[84]	Cubic *Pm3n*	765	40.9	56.0[d]	15.1
Ethane-PMO_APTES[85]f	3D *p6mm*	1086	21.5	41.4	19.9
Ethane-PMO_APAETMS[85]f	3D *p6mm*	963	20.5	41.6	21.1
Ethane-PMO_APAEAETMS[85]f	3D *p6mm*	1037	20.0	39.9	19.9
Ph-PMO_APTMS[86]	2D *p6mm*	752	27.2	51.7	24.5
Ph-PMO_EDATMS[86]	2D *p6mm*	870	27.2	51.5	24.3
Ph-PMO_ImTES[86]	2D *p6mm*	754	24.2	51.5	27.7

[a]Pore width obtained from the BJH method with the corrected Kelvin equation, *i.e.* KJS–BJH method at the maximum of pore size distribution calculated on the basis of adsorption data. [b]Unit cell parameter calculated as (a=2d_{100}/√3). [c]Pore wall thickness calculated as (2d_{100}/√3 - dp), where the first term is the unit cell parameter. [d]Unit cell parameter calculated as (a =2d_{210}/31/2). [f]These values are presented for the PMOs prepared using 40 mol% of the amino-organosilane precursor.

Li *et al*.[84] observed that the separating mechanism is similar to that of the NH_2 column, and that the ethane moieties of the Ethane-PMO contributed strongly to the retention. Thus, the

authors concluded that the performance of this material makes it a potential candidate to satisfy more rigorous needs in chromatographic analysis.

Recently, Suriyanon *et al.*[85] prepared three amine-functionalized PMOs *via* co-condensation reaction of BTSE and (3-aminopropyl)trimethoxysilane (APTMS), [3-(2-aminoethylamino)propyl]trimethoxysilane, (APAETMS) and 3-[2-(2-aminoethylamino)ethylamino]propyltrimethoxysilane (APAEAETMS) in the presence of CTAB under basic conditions. Besides the number of amines in the amino-organosilane precursor, the amount of these precursors were also varied between 10 and 40 mol%. All prepared materials presented a hexagonal order of the pores and a high Brunauer–Emmett–Teller (BET) surface area (between 963 and 1230 $m^2 \cdot g^{-1}$). Table 1.5 shows the physical properties of the amine modified-PMOs prepared with 40 mol% of amine-precursor. The authors observed that the amount of nitrogen on the amine-functionalized PMOs augmented with the molecular size and the concentration of the amino-organosilanes used. The increase of the latter parameter also promoted the growth of the wall thickness and the contraction of the unit cell. Suriyanon and co-workers[85] indorsed the latter behavior to the decrease of the pore size diameter and suggested that the changes in the physical and textural properties were related to the hydrogen bonding ability of the amine-functional groups around the micelles of the surfactant.

Coutinho *et al.*[86] reported the synthesis of Ph-PMOs containing propylamine, propylethylenediamine, and propyldihydroimidazole groups in the framework by co-condensation reaction in the presence of ODTMA surfactant (Table 1.5, Ph-PMO_APTMS, Ph-PMO_EDATMS and Ph-PMO_ImTES, respectively). These three amine-PMOs displayed both meso- and molecular-scale up to 10 mol% of functional groups. When the amine functional precursor loading increased above that value, the mesoscopic order was lost, while the molecular periodicity was maintained. This study showed the difficulty to prepare PMOs with both high amine-loadings into the framework pore wall and high mesopores order.

1.4.3 Organic bridge post-synthetic modification

The organic post-synthetic modification involves a transformation of the organic bridge after the PMO synthesis, Figure 1.10.

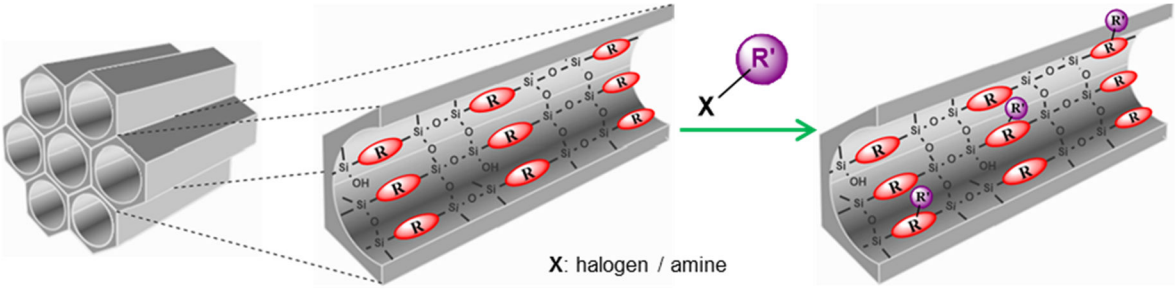

Figure 1.10. Schematic representation of post-synthesis modification of the organic bridges of PMOs. R and R' are different organic functions.

The modification of the organic bridges in the PMO materials was successfully attained immediately after Stein *et al.*,[43] Inagaki *et al.*[42] and Ozin *et al.*[41] reported the preparation of the first PMOs. Stein and Ozin and their co-workers showed the bromination of the ethylene moieties and the opportunity to tune the properties of PMOs for a given application.[41,43] The insertion of a bromine group into the bridge of PMOs enables the incorporation of many other functional groups since bromine is a very good leaving group. Nakai *et al.*[87] reported the bromine addition and successive ethylenediamine (EDA) substitution of the ethylene bridge in the ethylene-PMO, Table 1.6. The authors demonstrated that the bromination reaction had little influence on the 2D hexagonal mesostructure. In contrast, the reaction with EDA leads to an extensive modification of the mesostructure with perturbation of the pores hexagonal arrangement. The authors also reported the synthesis of other PMO materials by direct substitution of EDA with chloro-propyl-ethane resulting in the Cl-Pr-Et-PMO material. The latter presented only a broad low-angle diffraction peak in the PXRD patterns (Table 1.6) and the substitution of chloride by EDA did not affect the structure of this material, which was subsequently tested in the adsorption of arsenate from water. The authors observed that the distance between the amine functional group and the surface of the pore walls had influence in the adsorption of the arsenate. The EDA-Pr-Et-PMO displayed higher capacity in the adsorption of arsenate when compared with EDA-Et-PMO due to the distance between the propyl and the silanol groups, which prevented the interaction of those groups.

De Canck *et al.*[88] reported the bromination of ethylene bridges followed by nucleophilic substitution of the bromide by diaminobutane (DAB), diaminohexane (DAH), diaminododecane (DADD), diethyltriamine (DETA) and tetraethylenepentamine (TEPA).

By varying the reaction conditions, *e.g.* temperature and reaction time, different nitrogen content was achieved for each functionalized PMO.

Table 1.6. Introduction of amine functionalities by organic bridge post-synthetic modification.

PMO	Base PMO	Intermediate reaction	Functional PMO	XRD reflections	Ref.
EDA-Et-PMO	 Ethene-PMO	 trans-bromination	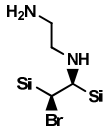	disordered	[87]
EDA-Pr-Et-PMO	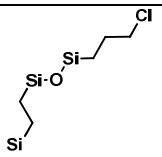 Cl-Pr-Ethane-PMO	-	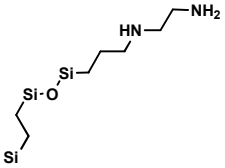		
DAB-Et-PMO	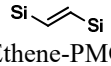 Ethene-PMO	 trans-bromination	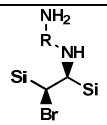 R = $(CH_2)_4$	(100) (110) (200)	[88]
DAH-Et-PMO			R = $(CH_2)_6$		
DADD-Et-PMO			R = $(CH_2)_{12}$		
DETA-Et-PMO			R = $(CH_2)_2NH(CH_2)_2$	(100)	
TEPA-Et-PMO			R = $(CH_2)_2NH(CH_2)_2NH(CH_2)_2NH(CH_2)_2$		
P-Et-PMO		-	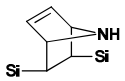	(100) (110) (200)	[89]
DMP-Et-PMO			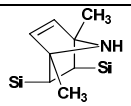	(100) (110) (200)	
MP-Et-PMO			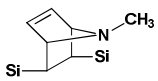	(100) (110) (200)	
PhP-Et-PMO			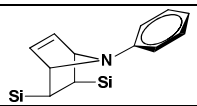	(100) (110) (200)	
TMP-Et-PMO			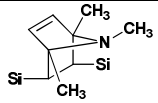	(100) (110) (200)	
ED-Et-PMO		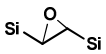	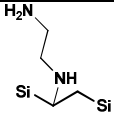	(100)	[90]
NH_2-Ph-PMO	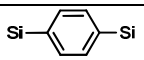 Phenylene-PMO	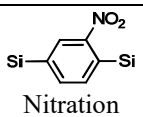 Nitration	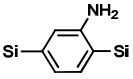	(100)	[44]

The optimal conditions to attain maximum nitrogen content were room temperature and three hours of reaction time. DAB substitution reaction resulted in higher nitrogen content than with DADD. The difficulties obtained in the substitution of bromide by DADD were suggested to be due to poor diffusion of the dodecane chain within the pores of the PMO. Moreover, the nitrogen content of the material is lower for nucleophiles with long alkyl-chain than for the other cases considered. All amine materials presented clear 2D hexagonal mesoporous ordering, with exception of the PMO prepared with the TEPA ligand, which exhibited just a single reflection in the PXRD patterns assigned to the (100) of the 2D hexagonal arrangement, Table 1.6. The materials also revealed type IV N_2 isotherms typically observed for mesoporous materials. The authors observed a decrease on the BET surface area (S_{BET}), pore volume (V_p) and pore diameter (d_p) values upon functionalization, which indicates the anchorage of the functional groups inside the pores. These five PMOs were tested in the CO_2 adsorption with the aim of understanding which of the following properties, *e.g.* nitrogen loading, variation in chain length and the presence of primary and secondary amines, was the most important to obtain a good adsorbent for this gas. When compared with the aminopropyl functionalized SBA-15, De Canck *et al.*[88] found that DADD-Et-PMO presented slightly higher adsorption efficiency with a CO_2/N ratio of 0.42. DADD-Et-PMO, with the lowest nitrogen loading (0.33 $mmol \cdot g^{-1}$), the longest alkyl-chain and the smallest amount of secondary amines, seems to be the most interesting PMO for CO_2 adsorption. The reason for the better performance of the latter material was suggested to be related with the presence of amines, at optimal distances (hence, optimal amount) from each other, so that they could interact simultaneously with the same CO_2 molecule. If very large amounts of amines are present in the material, hydrogen bonding between neighboring amine groups is more probable to occur, which deactivates the amine moieties for CO_2 adsorption. Additionally, hydrophobic interactions between long alkyl-chains were suggested to avoid chain folding, preventing the formation of hydrogen bonding between amines and silanols groups; hence, with long alkyl-chain, amines are free to interact with CO_2.

Recently, Esquivel *et al.*[89] showed the ability of the ethene-PMO to be transformed into pyrrole bridge PMOs through Diels-Alder reaction between the former and a family of pyrrole derivatives (pyrrole, methylpyrrole, dimethylpyrrole, trimethylpyrrole and 1-phenylpyrrole). The obtained pyrrole-PMOs displayed the 2D hexagonal arrangement of the pores, showing the preservation of the meso-order of the parent ethene-PMO. They also

observed reduction in the *d* spacing value after the chemical modification of the double bond of the ethene-PMO, which seems to be associated to the structural contraction as a consequence of the thermal conditions used during the Diels-Alder reaction. This functionalization process also promoted the reduction of the pore size from 71 Å to 53-56 Å, which confirms the formation of surface adducts. Additionally, the pore wall thickness increased in all cases after the chemical modification of the surface as a consequence of the volume occupied by the organic groups introduced. The success of the chemical modification of the Et-PMOs was also confirmed by elemental analysis (EA), ^{13}C NMR and ^{29}Si NMR spectroscopies.

Horiuchi *et al.*[90] also modified the ethene-PMO with ethylenediamine (ED) basic sites by epoxidation of ethylene moieties of the Et-PMO followed by nucleophilic addition, Table 1.6. The resultant ED-Et-PMO, presenting a type IV isotherm and a pore diameter of 62 Å, was tested as a solid base catalyst in the Knövenagel condensation reaction between benzaldehyde and various active methylene compounds. They also produced a material with bifunctional catalytic properties by introducing Au nanoparticles into the ED-Et-PMO. The obtained Au-ED-Et-PMO displayed a reduction of the pore size to 54 Å, which is in agreement with the insertion of gold nanoparticles into the PMO. This material was successfully tested on both alcohol oxidation and Knövenagel condensation in a one-pot tandem reaction. Horiuchi *et al.*[90] also prepared a second bifunctional PMO, using the same procedure, where the Et-PMO was functionalized with *N*,*N*-dimethylethylenediamine followed by introduction of Pd nanoparticles into the pores to catalyze the Tsuji–Trost reaction.

In 2002, Inagaki's research group demonstrated the versatility of the phenylene moieties in the Ph-PMO material, through the introduction of functional groups by electrophilic substitution attack of the phenylene bridge. They showed that chemical modification was possible by post-synthetic sulfonation of the phenylene bridge to offer the SO_3H-Ph-PMO.[42] In 2008, the same group reported the amination of 28% of phenylene moieties of PMO, in a two-step chemical transformation process without destroying both meso- and molecular-scales periodicities.[44] The NH_2-Ph-PMO was successfully applied in the Knövenagel condensation reaction of malononitrile with benzaldehyde. The possibility to reutilize this material for further use was also revealed. Moreover the amination of the

phenylene moieties provides the possibility to transform the amine group into other functional groups.

In order to make the phenylene-PMO even more appellative to catalysis, sorption, scavenging and other applications, Smeulders *et al.*[91] attempted the bromination of the phenylene moieties of the Ph-PMO using different post-modification methodologies. The first method used $AlCl_3$ as a catalyst in combination with Br_2. The second approach relies in the use of *N*-bromosuccinimide (NBS) as bromine source combined with the radical initiator azobisisobutyronitrile (AIBN). The third and last procedure pretended to generate bromine, in situ, by adding sulfuric acid to sodium bromate ($NaBrO_3$). The authors observed that the principles of organic chemistry are not directly transported to nanoporous material science as occurred with the sulfonation and nitration reactions modifications of phenylene bridge PMOs. The bromination reaction using the NBS and AIBN reagents was not effective, while the methods that used Br_2 and $NaBrO_3$ as bromine sources promoted the bromination of the phenylene moieties of PMO. However, these two last procedures gave rise to a huge amount of silicon–carbon bond cleavage and this fact had a destructive effect on the PMO framework.

1.4.4 Grafting

The grafting procedure comprises the chemical modification of the surface free silanols after the PMO synthesis through addition of an organosilicate agent, Figure 1.11.

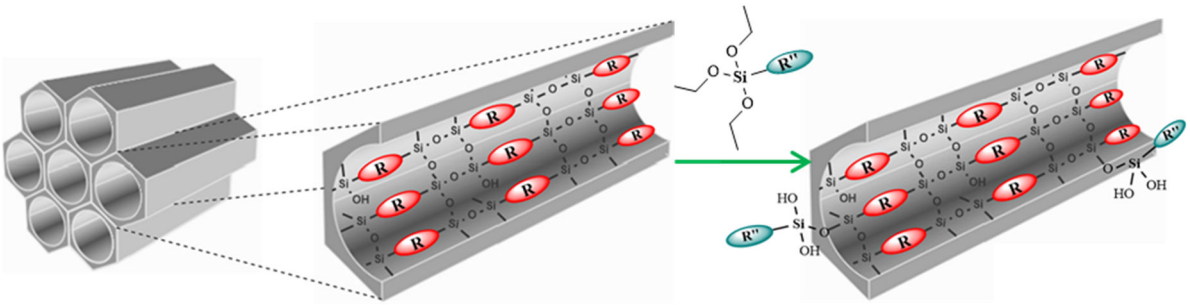

Figure 1.11. Schematic representation of post-synthesis modification of the surface chemistry of PMOs *via* grafting methodology. R and R'' are different organic functions.

In 2005, Zhang *et al.*[92] synthetized a bifunctional material by grafting the MPTMS to free silanols of the methylene-bridge PMO, previously prepared in the presence of structural directing agent P123 under acid conditions. The grafting reaction occurred in the presence of toluene under reflux. The resulting material, SH@Me-PMO, preserved the 2D hexagonal arrangement of the pores observed in the parent material and the S_{BET} and *d*p decreased

providing further evidence that the methylene-PMO was efficiently functionalized *via* grafting. It was possible to introduce into the channels 0.8 mmol·g^{-1} of S content, Table 1.7. Dubé *et al.*[93] prepared the $PFSO_3H$@ethane-PMO, with a loading of 0.8 mmol $H^+ \cdot g^{-1}$, by grafting reaction of the ethane-PMO with the perfluoroalkylsulfonic acid group. This material revealed high catalytic activity in self-condensation of heptanal and heptanal acetalization by 1-butanol, but some problems of lixiviation of the organic functionalities from the PMO were reported by the authors upon the reutilization of the material.

Table 1.7. Structural properties of the selected PMOs with acidic groups prepared by grafting.

PMO	structure	S_{BET} ($m^2 \cdot g^{-1}$)	dp^a (Å)	a^b (Å)	$[H^+]$ (mmol·g^{-1})
SH@Me-PMO[92]	2D *p6mm*	992.1	80	137	0.8
$PFSO_3H$@ethane-PMO[93]	2D *p6mm*	468	68	-	0.8

[a]Pore width obtained from the BJH method with the corrected Kelvin equation, *i.e.* KJS–BJH method at the maximum of pore size distribution calculated based on the adsorption data. [b]Unit cell parameter calculated as ($2d_{100}/\sqrt{3}$).

In 2011, Ph-PMO was functionalized with Mac-Millan catalyst (denoted as Mac@Ph-PMO) through grafting of 3-azidopropyl-trimethoxysilane to the silanols of Ph-PMO followed by "click chemistry" post-modification with the Mac-Millan catalyst, Table 1.8.[94] This material conjugates the hydrophobic surface properties of Ph-PMO to the accessible mesopores between the inner and outer surfaces of the hollow structures, which promotes the acceleration of the mass-transport process. The material was tested in the Diels-Alder cycloaddition of 1,3-cyclopentadiene with *trans*-cinnamaldehyde and reused several times.

Table 1.8. Structural properties of the amine-modified PMOs prepared by grafting.

PMO	structure	S_{BET} ($m^2 \cdot g^{-1}$)	dp^a (Å)	a^b (Å)
Mac@Ph-PMO[94]	Hallow[c]	253	69.0	-
TMS@Ph-PMO[95]	2D *p6mm*	655	37.0	≈47
BzDMS@ Ph-PMO[95]	2D *p6mm*	627	35.0	≈47
DMSFc@ Ph-PMO[95]	2D *p6mm*	738	36.0	≈47
APAETMS@Ph-PMO[96]	2D *p6mm*	180	72.0	116

[a]Pore width obtained from the BJH method with the corrected Kelvin equation, *i.e.* KJS–BJH method at the maximum of pore size distribution calculated on the basis of adsorption data. [b]Unit cell parameter calculated as ($2d_{100}/\sqrt{3}$). [c]This sample displayed the (100) reflection, observed by PXRD.

Gomes *et al.*[95] reported the synthesis of Ph-PMO derivatized with ferrocene to be employed in the catalytic oxidation of styrene. This material was obtained by grafting of trimethylsilyl (TMS), benzyldimethylsilyl (BzDMS) and dimethylsilyl ferrocene (DMSFc) groups to the Ph-PMO, Table 1.8. The insertion of these functional groups along the pore wall channels originated a decrease of the intensity of the (100) reflection, a contraction of the unit cell

parameter and reduction of the BET surface area and pore diameter as expected for this type of grafting reaction. The success of the chemical modifications was followed by Fourier transform infrared (FTIR) and NMR spectroscopies. The DMSFc@Ph-PMOs was tested as solid catalyst in the oxidation of styrene and presented moderate activity and high selectivity. Recently, Sim *et al.*[96] grafted alkyl amine functionalities (APTES, APAETMS and ImTES) onto the silanols of phenylene-bridged PMO and of SBA-15. Ph-PMOs based materials possess a unit cell parameter in the range of 116.0 and 126.7 Å, while the values determined for the amine-modified SBA-15 are in the range of 116.0 and 118.9 Å. All amine-functionalized materials preserved the hexagonal order of the mesopores of the parent-PMOs. The amine-functionalized Ph-PMO and silica were tested in the adsorption of pure CO_2 at 25 °C in a pressure range up to 1.2 atm. The authors observed that the APAETMS@Ph-PMO (see physical properties in Table 1.8) adsorbs a larger amount of CO_2 at a faster adsorption rate when compared with APAETMS@SBA-15, which demonstrates that the functionalization of PMOs with amines is more relevant than a similar degree and nature of functionalization in pure silica for the adsorption of CO_2. Interestingly, the unmodified SBA-15 silica also adsorbs a smaller amount of CO_2 when compared with the unmodified PMO. This behavior was explained by the higher hydrophobicity of the PMO pore wall when compared with that of SBA-15. Hence, water adsorption is expected to be more acute in SBA-15 than in PMO materials, competing more with CO_2 for available adsorption sites on the former class of materials, so, organosilica instead of pure silica supports were proposed for immobilization of amines groups aiming materials for CO_2 adsorption/separation. Despite the fact that PMOs are more expensive than silica, the superior ability of amine modified PMOs to adsorb CO_2 can be transferred and should be explored for such applications.

In summary, the introduction of acidic or basic groups into the PMO frameworks can be made using different methods. The post-functionalization methodologies have been given much attention due to the opportunity to introduce interesting functionalities onto the surface of the pores, and to create different degrees of porosity in the materials, without affecting significantly the arrangement of the pores. Additionally, the possibility to extend typical homogeneous phase reactions to functionalize hybrid materials has been successfully reported in the literature and opens an avenue to tune the materials properties for new applications. The co-condensation of different bissilylated precursors can offer novel PMOs

with better performances that those prepared by post-modified materials, due to the introduction of the functionality as part of the PMO framework, remaining the pores free for the desired application. The development of acid- or amine-PMO materials with optimal features for different applications needs to take into account several different factors, such as, functional group loading, surface area, pore volume and pore size, distances between functional groups and between functional groups and silanols, and the hydrophilic/hydrophobic character of the framework.

As it is understood from Section 1.2, the presence of amines is mostly a requisite in the preparation of adsorbents for biogas upgrading. Thus, besides the factors described above, the tuning of the PMOs properties must also have into account the nature of the amino groups to maximize interactions with CO_2. The ideal PMO adsorbent must be chemically stable and reused in multiple adsorption-desorption cycles. Despite the interest of PMOs for biogas upgrading, no literature was found for the preparation and utilization of PMOs in the separation of CO_2 and CH_4. There are only, two studies where amine modified-PMOs were tested in the CO_2 adsorption.

Table 1.9 summarizes the nitrogen containing PMOs previously described and their possible applications. The presentation of these materials is made through type of synthesis used: condensation, post-synthesis modification of the organic bridge, co-condensation and grafting reaction.

Table 1.9. Potential applications for nitrogen containing PMOs.

PMO	Year	APPLICATION		Ref.
		ADSORPTION	CATALYSIS	
		Condensation		
BTMSPA-PMO	2009	Lysozyme	-	[66]
	2010	Glycine; L-lysine; Isoleucine		[72]
	2011	Nicotine from aqueous solution		[73]
TMSEN-PMO	2012	Metal adsorption from water	-	[67]
BTEVA-PMO	2010	-	Suggested for Knövenagel condensation	[68]
CHTC-PMO	2015	Suggested for multi-step reaction field and biomimetic systems		[69]
		Organic bridge post-synthetic modification		
EDA-Et-PMO	2007	Arsenate	-	[87]
EDA-Pr-Et-PMO				
DAB-Et-PMO	2013	CO_2	-	[88]
DAH-Et-PMO				
DADD-Et-PMO				
DETA-Et-PMO				
TEPA-Et-PMO				
P-Et-PMO	2014	Suggested for both adsorption and catalysis applications		[89]
DMP-Et-PMO				
MP-Et-PMO				
PhP-Et-PMO				
TMP-Et-PMO				
Au-ED-Et-PMO	2015	-	Tested on one pot tandem reaction consisting of alcohol oxidation and Knövenagel condensation to produce ethyl α-cyanocinnamate from benzyl alcohol and ethyl cyanoacetate *via* formation of benzaldehyde	[90]
NH_2-Ph-PMO[a]	2008	-	Knövenagel condensation reaction of malononitrile with benzaldehyde	[44]
Et-PMO_UREDO	2006	Suggested for transport and deliver of chemical or biological species; catalysis; chemosensing and chromogenic discrimination		[83]
Et-PMO_ICP				
		Co-condensation		
Ethane-PMO_APTES	2011	Tested in liquid chromatographic separation and compared to a commercial NH_2 column		[84]
Ethane-PMO_APTES	2015	Suggested for removal of pharmaceutical residues in aqueous phase	-	[85]
Ethane-PMO_APAETMS				
Ethane-PMO_APAEAETMS				
Ph-PMO_APTMS	2008	Interesting for both catalytic and adsorption applications		[86]
Ph-PMO_EDATMS				
Ph-PMO_ImTES				
		Grafting		
MAC@Ph-PMO	2011	-	Asymmetric Diels–Alder reactions	[94]
TMS@Ph-PMO	2013	-	Catalytic oxidation of styrene	[95]
BzDMS@Ph-PMO				
DMSFc@Ph-PMO				
APTES-Ph@PMO	2015	CO_2	-	[96]
APAETMS@Ph-PMO				
ImTES@Ph-PMO				

[a]It is also suggested as a precursor material for the design of highly functionalized PMOs with strong shape-selectivity for catalytic and adsorption processes.

1.5 Computational studies

In the last years, modern computational methodologies were used to support the interpretation of experimental data regarding the structure of PMOs and to advance the understanding of their adsorption and catalytic features. Most studies used approaches based on the density functional theory (DFT) together with small, finite size, molecular models [97–102] but, more recently, studies appeared in the literature relying on classical molecular dynamics (MD) approaches[103] or models repeated periodically in three-dimensions[103–105]. The computational studies also focused on the primer steps of the synthesis of PMO materials, *i.e.*, the interaction between silica monomers or small oligomers and their condensation in order to produce organosilica.

Shirai *et al.*[101] studied the cleavage of Si-C bond in various organosilane precursors (Figure 1.12), with general structure $RSi(OH)_3$, by DFT calculations. Considering the B3LYP/6-311+G(d,p) methodology the authors determined the proton affinities of the carbon atom at the ipso-position and of the carbanion produced after Si-C bond cleavage in the precursors.

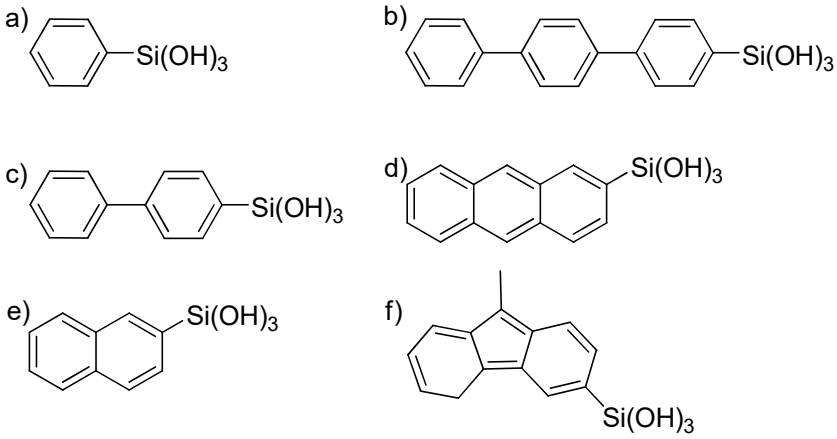

Figure 1.12. Models of organosilane precursors with formula $RSi(OH)_3$, where R is: a) phenyl; b) terphenyl, c) biphenyl, d) anthranyl, e) naphthyl and f) *N*-methylcarbazolyl. Adapted from reference [101].

The selection of the proton affinities at these two sites was taken as they act as indices for the stability of Si-C bond in the presence of acidic and basic conditions, respectively. The obtained computational and experimental results were found to be in qualitative agreement. The authors observed that the terphenyl and *N*-methylcarbaxole R groups are the least stable under acidic conditions, and the terphenyl and anthranyl R groups are the least stable under

basic conditions. Curiously, the cleavage of Si-C bond was observed experimentally for these cases, while the Si-C bond in the other precursors was stronger. Accordingly, the computational study confirmed that the reaction giving rise to the cleavage of Si-C bond, under acid conditions, results *via* formation of σ-complex by introduction of H^+ at the carbon atom at the ipso-position in the organosilane precursors, (Figure 1.13a). The cleavage of Si-C bond, under basic conditions, occurs through generation of the intermediate complex, where the OH^- species links directly the Si atom of the organosilane precursors (Figure 1.13b).

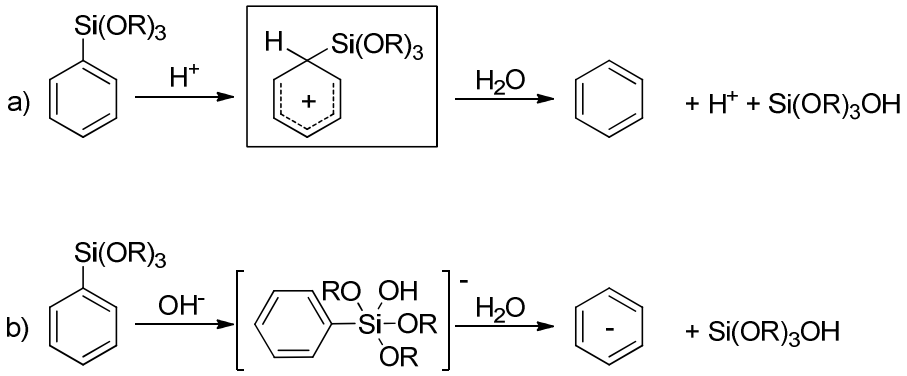

Figure 1.13. General mechanism for Si-C bond cleavage in the reaction of organosilane polycondensation to organosilica under a) acidic and b) basic conditions proposed in reference [101].

Very Recently, Sánchez *et al.*[60] developed a theoretical model to understand the synthesis mechanism of PMS that is believed to be similar to that of the PMOs. This study was made using a multiscale simulation strategy to describe the molecular-level routes behind the construction of silica/cationic surfactant mesophases during the preparation of templated MCM-41 materials. The authors considered a new coarse-grained explicit-solvent model for the synthesis solution with coarse-grained parameters for silicate species tuned with reference to a detailed atomistic model[106,107] that was derived from quantum mechanical calculations.[108,109] The usage of a coarse-grained approach allowed to reach the time and the length scales required for the spontaneous formation of mesophase structures with a realism that enables direct comparison with experimental systems. Sánchez and co-workers[60] observed that at low-concentration surfactant solution, the silica oligomers present an important factor in the formation of hexagonal arrangement of the pores. The silica oligomers present multiple negative charges and are capable to connect to adjacent micelles through the head-group areas, acting as multidentate binding spots. This was found

to be crucial for micelle overcoming their mutual repulsion, due to the positively charged head-groups, to create larger surfactant aggregates. This fact promotes the separation of the system into a dilute solution and a concentrated silica/surfactant ordered mesophase, as observed experimentally. In the case of addition of silica monomers to a low-concentration surfactant solution, these authors observed that the small spherical micelles are fused to form elongated rod-like aggregates, but the presence of monomers only is not enough to form an HLC phase. For occurrence of phase formation it was necessary at least 15-33% of silicate oligomers either in the form of dimers or larger silicate species. Without changing any parameter in the model, they could find different mesophase structures by changing the charge density of the silicate oligomers, either by increasing their degree of condensation or their degree of deprotonation. For instance, with oligomers displaying high silica charge density, the curvature of the mesophase structures is reduced and a lamellar system is obtained. The degree of flexibility of the mesophase could also be modified by changing the composition of the synthesis solution; for instance, by addition/removal of a co-solvent (*e.g.* benzene) to the solution, it was possible to describe the reversibility of the hexagonal phase to lamellar structure as observed experimentally.[110]

Futamura *et al.*[103] studied the effect of the nature of the organic linker in the early stages of the templated synthesis of PMO materials. They considered a classical MD approach to simulate the surfactant–bromide–water solutions with several different organosilicate precursors based on 1,4-bis(triethoxysilyl)benzene, 1,2-bis(triethoxysilyl)ethylene or 1,2-bis(triethoxysilyl)ethane (Figure 1.8). The choice of these three precursors was made having into account different degrees of molecular-scale periodicity found in the materials synthetized experimentally: high degree, low degree, and no molecular-scale periodicity, respectively.[51] Futamura *et al.*[103] observed that the presence or absence of the molecular-scale periodicity in the pore walls of PMOs is defined by tight interaction between the surfactant micelle and the organosilica and by a certain flexibility and orientation of the organic linker. Experimentally, it was found that the PMOs prepared using the 1,1-bis(triethoxysilyl)methane and 1,2-bis(triethoxysilyl)ethane precursors, did not present molecular-scale periodicity, and this fact could be explained by the size of the organic linker and the strength of the interaction between the precursor molecules when compared with the phenylene- and ethylene-PMOs.[51] In addition, the presence of molecular-scale periodicity was endorsed to the surfactant mesostructure. Notice, however, that phenylene- and

biphenyl- PMOs with high degree of molecular scale periodicity were prepared without the presence of surfactants.[111] The classical MD simulations by Futamura *et al*.[103] considered systems composed of water, decyltrimethylammonium surfactants and deprotonated organosilicates obtained from 1,4-bis(triethoxysilyl)benzene, 1,2-bis(triethoxysilyl)ethylene or 1,2-bis(triethoxysilyl)ethane. The results demonstrated that the organic and inorganic fragments of the benzenesilicates and of the ethylenesilicates were evidently introduced between the cationic surfactant head-groups in the micelles, while in the case of ethanesilicates, only the inorganic part interacted with the surface of the micelle. Remarkably, this leads to the construction of micelles taking more surfactants (*i.e.*, larger amount of average micelle size along the simulation) in the former cases comparatively to the latter. These interpretations can be associated to a more efficient screening of the surfactant head-group repulsion, which stimulates the reduction of the curvature of the surface and therefore the formation of bigger micelles.[103] Futamura *et al.*[103] found also that the ordering of the organosilicates in the solutions with benzenesilicates or ethylenesilicates, was much superior when comparing to the organosilicates organization of the solution with ethanesilicates. Such differences were related to the way how the organosilicates are oriented relatively to the micelles. In the cases of the solutions with benzenesilicates or ethylenesilicates, the silicate-organic-silicate axis approximated parallel to the micelle surface, while ethanesilicates prefer to orient their silicate-organic-silicate axis perpendicularly to the surface, which was suggested to be a possible cause for the inferior ordering of the synthetized materials with the ethane linker. In this way, the presence or absence of the periodicity of the molecular order along the channel direction was suggested to be highly dependent of the interactions between surfactant micelles and organosilicates and the relative flexibility and orientation of the organic moieties, *i.e.*, organosilicates with less flexibility interacted strongly with the micelle surface of the surfactant, leading to the preparation of PMOs with higher degrees of molecular-scale periodicity when compared to PMO materials synthetized using more flexible organo-bridged silicates that interacted weakly with the surfactant micelles surface.[103] In summary, the studies above suggest that the hexagonal-order and the periodicity of the molecular-scale in the pore walls of PMOs are defined during the first steps of the templated synthesis process.

The structure of PMOs can be modeled with cluster or periodic model approaches. The first one pretends to study a small portion of the PMO in vacuum and the second one pretends to

model an infinite repetition of a suitable unit cell in the three spatial dimensions. Both approaches present benefits and drawbacks,[112] and the choice of one or another depends on several factors, as for example, computational code and approach, and the property that one wants to calculate.

Density functional theory (DFT) provides a very good compromise between the quality of calculated data and the computational resources requirements. Moreover, modern DFT approaches can take into account dispersion interactions which affect dramatically weakly bonded systems.[112] Since molecular systems like PMO materials are composed of millions of atoms, only small portions of the materials, *e.g.* isolated finite clusters or small unit cells repeated periodically, can be used in computer calculations. The simulation of models based on large clusters or large unit cells requires the reduction of the complexity of the computational approach, either by reducing the quality of the grids used in the calculations or by considering less expensive approaches, *e.g.* semi-empirical or classical methods.[113]

There are few examples of works based on the application of DFT approaches to study PMOs. Onida *et al.*[97] combined Fourier transform infrared spectroscopy (FTIR) spectroscopy and DFT to study the surface properties of the Ph-PMO material, having into account both meso- and molecular-scale periodicities. The FTIR and computational studies were made in the pristine material and also in the material interacting with CO, H_2CO and NH_3 molecules. The authors used the DFT calculations (achieved at the B3LYP/6-31+G* level of theory) to assign the infrared (IR) modes experimentally observed. The calculations employing the molecular models represented in Figure 1.14 were used to compare the vibrational shifts in Ph-PMOs with those obtained for amorphous silica.

The assignment of the most important bands in the Raman and IR spectra of Ph-PMO, Et-PMO, Bph-PMO and thiophene-PMO throughout DFT calculations was conducted by Hoffman *et al.*[98] also using the B3LYP hybrid approach. The authors found that vibrational spectroscopy is unable to provide conclusive observations that can be used to understand the integrity of the Si-C bonds in PMO or similar organosilica materials because wavenumber shifts change from precursors to the corresponding PMO materials. In this way the modes are unpredictable, making each material a single case. Thus, Hoffman and his co-workers proposed the use of solid-state NMR for similar studies.[98]

Theoretical studies are also very useful to understand where functionalization in the organic moieties can occur and which are the preferential sites for adsorption in the functionalized-

or non-functionalized PMOs. This can be done by comparison of the calculated energies for materials having substitutions at different materials or of the calculated energies for adsorbates at different locations in the PMO material, respectively.

Camarota *et al.*[99] studied the low-temperature adsorption of CO on Ph-PMO by FTIR spectroscopy and by theoretical calculations. Again, these authors considered the DFT hybrid B3LYP approach, but incorporating dispersion corrections based on the ideas of Grimme *et al.*[114], and the same cluster model employed by Onida *et al.*[97], which is displayed in Figure 1.14.

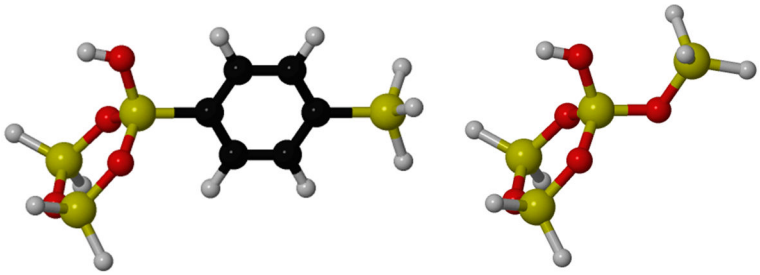

Figure 1.14. Molecular structures of cluster models for Ph-PMO (left) and for amorphous silica (right). Color code for atomic spheres is: H, white; C, black; O, red; and Si, yellow. Adapted from reference [97].

They observed the presence of three kinds of adsorbed CO molecules at low coverage: the first one corresponds to the physisorbed CO, which interacts with the benzene moieties, performing as Lewis bases, and with the H-bonded to the silanol group, acting as week Lewis acidic centers. The second and the third ones correspond to stronger interactions *via* carbon and oxygen atoms. Camarota *et al.*[99] verified that at low CO coverages, both C-bonded and O-bonded species displayed double interaction, promoting an interaction enthalpy higher than that of CO with the isolated silanol of amorphous silica. The enthalpies observed for these interactions are similar, leading to the simultaneously occurrence of the three types of CO adsorption processes mentioned above.

Martinez and Pacchioni[104] studied the interaction of CO, CO_2 and CH_4 molecules with the flat areas of the nanopores of the three-dimensional periodic lattice of *p*-Ph-PMO through the use of a periodic unit cell and DFT calculations (where they applied specific corrections to include dispersion forces). The construction of the models had into account the experimental structural information available in the literature.[51,115] The authors considered two models of *p*-Ph-PMO with different amounts of T^m species of silanols in the surface of the material and different sequences of silica bonded to the aromatic moieties, Figure 1.15.

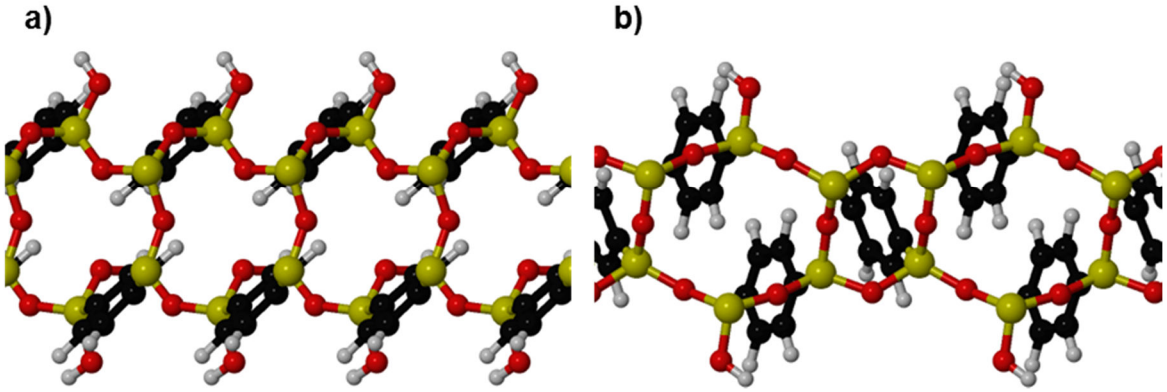

Figure 1.15. Models of the walls of phenylene-PMO formed by six-member rings (a) or formed by a sequence of six- and four-member rings (b). Color code for atomic spheres is: H, white; C, black; O, red; and Si, yellow. Adapted from reference [104].

The three molecules presented preferential interaction with the silanol groups and displayed adsorption energies characteristic of physisorbed states. The authors pretended with this computational study to understand the possibility of the PMO material to store or to separate the molecules previously mentioned. Furthermore, the choice of these three molecules was established on their inherent features, *i.e.*, the CO presents a small permanent dipole moment, the CO_2 manifests a quadrupole moment and the CH_4 displays an apolar nature. The authors observed a similar interaction of the Ph-PMO with the CO and CO_2 molecules, which are considerably stronger than the interaction with the CH_4 molecules. With this study, Martinez and Pacchioni[104] demonstrated that the dispersion part of the interaction is considerable high (about one half of the total value). In order to interpret the influence of dispersion in the adsorption of these molecules, they performed additional calculations where the walls of the PMO were changed either by doping or transforming the inorganic or organic parts of the framework. In the case of the introduction of Ti–OH, Si–O or Al–OH groups they did not observe significant changes in the adsorption energies when compared with the parent material. Martinez and Pacchioni[104] also reported the effect of the organic functionalization of the material in the adsorbate-substrate interaction. In this way, the organic part was modified by the authors through substitution of the C-H in the phenylene bridge by N, giving rise to the pyridine group and by substitution of the phenylene bridge by the biphenylene organic linker. The introduction of the pyridine group as linker instead of the phenylene group originated an increase of the interaction energies with the CO and CO_2 molecules and the opposite effect is verified for the interaction energy with CH_4. In the case of the use of the biphenylene bridge, a reduction of the calculated interaction energies was

found. Despite the change of the organic bridge of the PMOs, the interaction energies of the molecules with the silanols are more than twice bigger than with the organic functions, remaining the silanols groups the preferential adsorption sites as observed for the Ph-PMO.[104]

Kalantzopoulos *et al.*[77] used DFT calculations (PBE functional without dispersion corrections) to elucidate the hydrogen adsorption on phenylene-PMO. They calculated a binding strength of hydrogen with the pore walls of the PMO of -0.55 kcal·mol^{-1}, which is higher than the computed interaction energies for hydrogen interaction with a single benzene molecule or with the aromatic bridge of IRMOF-1. The same authors also performed grand canonical Monte Carlo (GCMC) simulations using a simplistic periodic model derived by Inagaki *et al*. and observed that no hydrogen molecules could be introduced inside the wall structure of the PMO materials.

In summary, computer simulations can be very useful to find locations in the PMO materials where interaction with adsorbates would be enhanced. They can also be employed to predict which chemical groups are able to increase the adsorption capacity and to enhance the selectivity towards a specific adsorbate.

In this PhD Thesis it is expected to find different strategies for the synthesis and modification of aromatic bridged-PMOs in order to tune their properties and to improve their ability for adsorption/separation of CO_2 from CH_4. Thus, the preparation of PMOs with different pore sizes, the inclusion of different amino groups, the introduction of aluminum oxide species and the carbonization of PMOs are investigated for creating materials with high π-π conjugation and different hydrophobic/hydrophilic character.

A PhD Thesis Roadmap for the synthesis, functionalization and characterization of PMO materials is displayed in Figure 1.16, to guide the reader in this journey, and to present the PMOs materials that are reported in each Chapter. In this PhD Thesis Roadmap, it is also possible to known which are the materials that were studied by DFT modelling and tested in the CO_2 and CH_4 adsorption.

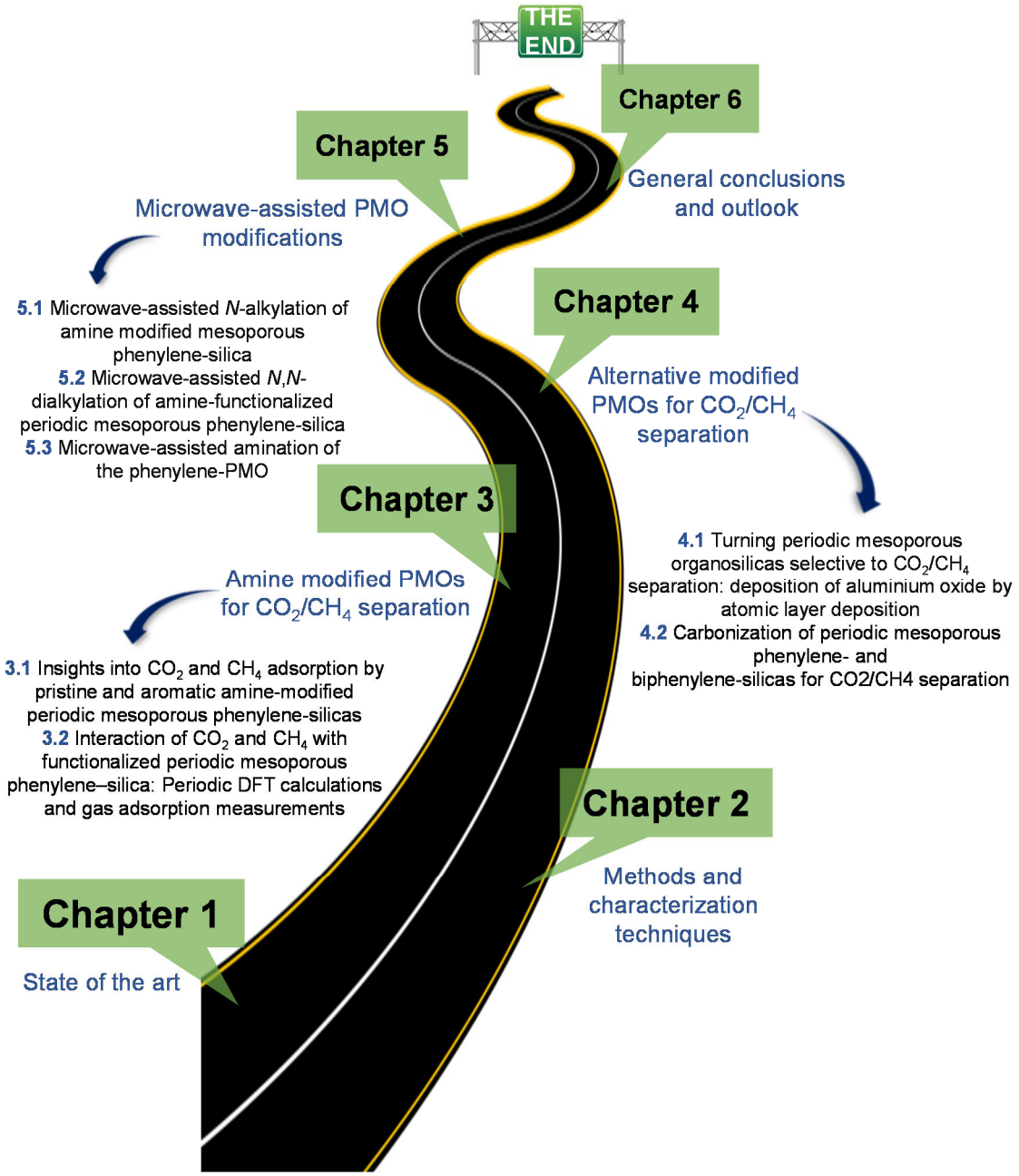

Figure 1.16. PhD Thesis Roadmap: chapters and subchapters.

1.6 Bibliography

1 M. Harasimowicz, P. Orluk, G. Zakrzewska-Trznadel, A.G. Chmielewski, Application of polyimide membranes for biogas purification and enrichment. *J Hazard Mater*. **2007**, 144: 698–702.

2 E. Favre, R. Bounaceur, D. Roizard, Biogas, membranes and carbon dioxide capture. *J Memb Sci*. **2009**, 328: 11–14.

3 S. Heile, S. Rosenberger, A. Parker, B. Jefferson, E.J.J. McAdam, Establishing the suitability of symmetric ultrathin wall polydimethylsiloxane hollow-fibre membrane contactors for enhanced CO_2 separation during biogas upgrading. *J Memb Sci*. **2014**, 452: 37–45.

4 X. Wu, M. Niknam Shahrak, B. Yuan, S. Deng, Synthesis and characterization of zeolitic imidazolate framework ZIF-7 for CO_2 and CH_4 separation. *Micropor Mesopor Mater*. **2014**, 190: 189–196.

5 P.K. Sahoo, M. John, B.L. Newalkar, N.V. Choudhary, K.G. Ayappa, Filling characteristics for an activated carbon based adsorbed natural gas storage system. *Ind Eng Chem Res*. **2011**, 50: 13000–13011.

6 S.J. Bhadra, S. Farooq, Separation of methane–nitrogen mixture by pressure swing adsorption for natural gas upgrading. *Ind Eng Chem Res*. **2011**, 50: 14030–14045.

7 P. Jaramillo, H.S. Matthews, Landfill-gas-to-energy projects: Analysis of net private and social benefits. *Environ Sci Technol*. **2005**, 39: 7365–7373.

8 K.S. Knaebel, H.E. Reinhold, Landfill gas: from rubbish to resource. *Adsorption*. **2003**, 9: 87–94.

9 A. Lohila, T. Laurila, J.P. Tuovinen, M. Aurela, J. Hatakka, T. Thum, M. Pihlatie, J. Rinne, T. Vesala, Micrometeorological measurements of methane and carbon dioxide fluxes at a municipal landfill. *Environ Sci Technol*. **2007**, 41: 2717–2722.

10 S. Cavenati, C.A. Grande, A.E. Rodrigues, Removal of carbon dioxide from natural gas by vacuum swing adsorption. *Energy Fuels*. **2006**, 20: 2648–2659.

11 Y.S. Bae, R.Q. Snurr, Development and evaluation of porous materials for carbon dioxide separation and capture. *Angew Chem*. **2011**, 50: 11586–11596.

12 S. Chaemchuen, N.A. Kabir, K. Zhou, F. Verpoort, Metal-organic frameworks for upgrading biogas *via* CO_2 adsorption to biogas green energy. *Chem Soc Rev*. **2013**, 42: 9304–9332.

13 B.P. Spigarelli, S.K. Kawatra, Opportunities and challenges in carbon dioxide capture. *J CO_2 Util*. **2013**, 1: 69–87.

14 A.E. Rodrigues, C.A. Grande, Biogas to fuel by vacuum pressure swing adsorption i. behavior of equilibrium and kinetic-based adsorbents. *Ind Eng Chem Res*. **2007**, 46: 4595–4605.

15 R. Babarao, Z. Hu, J. Jiang, S. Chempath, S.I. Sandler, Storage and separation of CO_2 and CH_4 in silicalite, C168 schwarzite, and IRMOF-1: A comparative study from Monte Carlo simulation. *Langmuir*. **2007**, 23: 659–666.

16 M.B. Kim, Y.S. Bae, D.K. Choi, C.H. Lee, Kinetic separation of landfill gas by a two-bed pressure swing adsorption process packed with carbon molecular sieve: Nonisothermal operation. *Ind Eng Chem Res*. **2006**, 45: 5050–5058.

17 X. Peng, W. Wang, R. Xue, Z. Shen, Adsorption separation of CH_4/CO_2 on mesocarbon microbeads: Experiment and modeling. *AIChE J*. **2006**, 52: 994–1003.

18 V. Goetz, O. Pupier, A. Guillot, Carbon dioxide-methane mixture adsorption on

activated carbon. *Adsorption*. **2006**, 12: 55–63.
19 H. Yi, F. Li, P. Ning, X. Tang, J. Peng, Y. Li, H. Deng, Adsorption separation of CO_2, CH_4, and N_2 on microwave activated carbon. *Chem Eng J*. **2013**, 215–216: 635–642.
20 D.M. D'Alessandro, B. Smit, J.R. Long, Carbon dioxide capture: Prospects for new materials. *Angew Chem*. **2010**, 49: 6058–6082.
21 G.D. Pirngruber, L. Hamon, S. Bourrelly, P.L. Llewellyn, E. Lenoir, V. Guillerm, C. Serre, T. Devic, A method for screening the potential of MOFs as CO_2 adsorbents in pressure swing adsorption processes. *Chem Sus Chem*. **2012**, 5: 762–776.
22 S. Cavenati, C.A. Grande, A.E. Rodrigues, Adsorption equilibrium of methane, carbon dioxide, and nitrogen on zeolite 13X at high pressures. *J Chem Eng Data*. **2004**, 49: 1095–1101.
23 P. Li, F. Handan Tezel, Adsorption separation of N_2, O_2, CO_2 and CH_4 gases by β-zeolite. *Micropor Mesopor Mater*. **2007**, 98: 94–101.
24 J.-M. Leyssale, G.K. Papadopoulos, D.N. Theodorou, Sorption thermodynamics of CO_2, CH_4, and their mixtures in the ITQ-1 zeolite as revealed by molecular simulations. *J Phys Chem B*. **2006**, 110: 22742–22753.
25 E.L. First, M.M.F. Hasan, C.A. Floudas, Discovery of novel zeolites for natural gas purification through combined material screening and process optimization. *AIChE J*. **2014**, 60: 31–33.
26 M.L. Pinto, J. Pires, J. Rocha, Porous materials prepared from clays for the upgrade of landfill gas. *J Phys Chem C*. **2008**, 112: 14394–14402.
27 J. Pires, V.K. Saini, M.L. Pinto, Studies on selective adsorption of biogas components on pillared clays : Approach for Biogas Improvement. *Environ Sci Technol*. **2008**, 42: 8727–8732.
28 Q. Xue, Y. Liu, Mixed-amine modified SBA-15 as novel adsorbent of CO_2 separation for biogas upgrading. *Sep Sci Technol*. **2011**, 46: 679–686.
29 X. Liu, L. Zhou, X. Fu, Y. Sun, W. Su, Y. Zhou, Adsorption and regeneration study of the mesoporous adsorbent SBA-15 adapted to the capture/separation of CO_2 and CH_4. *Chem Eng Sci*. **2007**, 62: 1101–1110.
30 G.-P. Hao, W.-C. Li, A.-H. Lu, Novel porous solids for carbon dioxide capture. *J Mater Chem*. **2011**, 21: 6447–6451.
31 P.D.C. Dietzel, V. Besikiotis, R. Blom, Application of metal–organic frameworks with coordinatively unsaturated metal sites in storage and separation of methane and carbon dioxide. *J Mater Chem*. **2009**, 19: 7362–7370.
32 J.R. Karra, B.E. Grabicka, Y.-G. Huang, K.S. Walton, Adsorption study of CO_2, CH_4, N_2, and H_2O on an interwoven copper carboxylate metal-organic framework (MOF-14). *J Colloid Interf Sci*. **2013**, 392: 331–336.
33 S.A. Peter, G. V. Baron, J. Gascon, F. Kapteijn, J.F.M. Denayer, Dynamic desorption of CO_2 and CH_4 from amino-MIL-53(Al) adsorbent. *Adsorption*. **2013**, 19: 1235–1244.
34 Y. Park, D.-K. Moon, Y.-H. Kim, H. Ahn, C.-H. Lee, Adsorption isotherms of CO_2, CO, N_2, CH_4, Ar and H_2 on activated carbon and zeolite LiX up to 1.0 MPa. *Adsorption*. **2014**, 20: 631–647.
35 X. Xu, X. Zhao, L. Sun, X. Liu, Adsorption separation of carbon dioxide, methane, and nitrogen on Hβ and Na-exchanged β-zeolite. *J Nat Gas Chem*. **2008**, 17: 391–396.
36 M.D. Rad, S. Fatemi, S.M. Mirfendereski, Development of T type zeolite for separation of CO_2 from CH_4 in adsorption processes. *Chem Eng Res Des*. **2012**, 90:

1687–1695.

37 J. Shang, G. Li, R. Singh, Q. Gu, K.M. Nairn, T.J. Bastow, N. Medhekar, C.M. Doherty, A.J. Hill, J.Z. Liu, P.A. Webley, Discriminative separation of gases by a "molecular trapdoor" mechanism in chabazite zeolites. *J Am Chem Soc*. **2012**, 134: 19246–19253.

38 E. Vilarrasa-García, J.A. Cecilia, M. Bastos-Neto, C.L. Cavalcante, D.C.S. Azevedo, E. Rodriguez-Castellón, CO_2/CH_4 adsorption separation process using pore expanded mesoporous silicas functionalizated by APTES grafting. *Adsorption*. **2015**, 21: 565–575.

39 Y. Belmabkhout, A. Sayari, Adsorption of CO_2 from dry gases on MCM-41 silica at ambient temperature and high pressure. 2: Adsorption of CO_2/N_2, CO_2/CH_4 and CO_2/H_2 binary mixtures. *Chem Eng Sci*. **2009**, 64: 3729–3735.

40 E.J. García, J. Pe, G.D. Pirngruber, C. Jallut, M. Palomino, F. Rey, S. Valencia, Tuning the adsorption properties of zeolites as adsorbents for CO_2 separation: Best compromise between the working capacity and selectivity. *Ind Eng Chem Res*. **2014**, 53: 9860–9874.

41 T. Asefa, M.J. MacLachlan, N. Coombs, G.A. Ozin, Periodic mesoporous organosilicas with organic groups inside the channel walls. *Nature*. **1999**, 402: 867–871.

42 S. Inagaki, S. Guan, Y. Fukushima, T. Ohsuna, O. Terasaki, Novel Mesoporous materials with a uniform distribution of organic groups and inorganic oxide in their frameworks. *J Am Chem Soc*. **1999**, 121: 9611–9614.

43 B. Melde, B. Holland, C. Blanford, A. Stein, Mesoporous sieves with unified hybrid inorganic/organic frameworks. *Chem Mater*. **1999**, 11: 3302–3308.

44 M. Ohashi, M.P. Kapoor, S. Inagaki, Chemical modification of crystal-like mesoporous phenylene-silica with amino group. *Chem Commun*. **2008**, 7: 841–843.

45 N. Hüsing, Porous hybrid materials. In: G. Kickelbick (ed.). Hybrid materials: synthesis, characterization, and applications. Wiley-VCH Verlag GmbH & Co. KGaA, **2007**: 175–223.

46 G. Kickelbick, Introduction to hybrid materials. In: G. Kickelbick (ed.). Hybrid materials: synthesis, characterization, and applications. Wiley-VCH Verlag GmbH & Co. KGaA, **2007**: 1–48.

47 P. Innocenzi, S. Costacurta, T. Kidchob, L. Malfatti, Mesoporous thin films: Properties and applications. In: P. Innocenzi, V.G. Kessler (eds.). Sol-gel methods for materials processing: Focusing on materials for pollution control, water purification and soil remediation. Springer, **2007**: 105–124.

48 A.B. Descalzo, R. Martínez-Máñez, F. Sancenón, K. Hoffmann, K. Rurack, The supramolecular chemistry of organic-inorganic hybrid materials. *Angew Chem*. **2006**, 45: 5924–5948.

49 Y. Wan, D. Zhao, Ordered mesoporous materials. In: K.P. Jong (ed.). Synthesis of solid catalysts. WILEY-VCH Verlag GmbH & Co. KGaA, **2009**: 277–300.

50 P. Van der Voort, D. Esquivel, E. De Canck, F. Goethals, I. Van Driessche, F.J. Romero-Salguero, Periodic mesoporous organosilicas: from simple to complex bridges; a comprehensive overview of functions, morphologies and applications. *Chem Soc Rev*. **2013**, 42: 3913–3955.

51 S. Inagaki, S. Guan, T. Ohsuna, O. Terasaki, An ordered mesoporous organosilica hybrid material with a crystal-like wall structure. *Nature*. **2002**, 416: 304–307.

52 B. Hatton, K.A.I. Landskron, W. Whitnall, D. Perovic, G.A. Ozin, Past, present, and

future of periodic mesoporous organosilicas - The PMOs. *Acc Chem Res*. **2005**, 38: 305–312.

53 W.J. Hunks, G.A. Ozin, Challenges and advances in the chemistry of periodic mesoporous organosilicas (PMOs). *J Mater Chem*. **2005**, 15: 3716–3724.

54 J. García-Martínez, Nanostructured porous materials: Building matter from the bottom up. In: B. Pignataro (ed.). Tomorrow's chemistry today: Concepts in nanoscience, organic materials and environmental chemistry. Wiley-VCH Verlag GmbH & Co. KGaA, **2008**: 47–72.

55 P. Van Der Voort, C. Vercaemst, D. Schaubroeck, F. Verpoort, Ordered mesoporous materials at the beginning of the third millennium: new strategies to create hybrid and non-siliceous variants. *Phys Chem Chem Phys*. **2008**, 10: 347–360.

56 S. Fujita, S. Inagaki, Self-organization of organosilica solids with molecular-scale and mesoscale periodicities. *Chem Mater*. **2008**, 20: 891–908.

57 F. Hoffmann, M. Cornelius, J. Morell, M. Fröba, Silica-based mesoporous organic-inorganic hybrid materials. *Angew Chem*. **2006**, 45: 3216–3251.

58 F. Hoffmann, M. Fröba, Vitalising porous inorganic silica networks with organic functions - PMOs and related hybrid materials. *Chem Soc Rev*. **2011**, 40: 608–620.

59 G.S. Attard, J.C. Glyde, C.G. Göltner, Liquid-crystalline phases as templates for the synthesis of mesoporous silica. *Nature*. **1995**, 378: 366–368.

60 G. Pérez-Sánchez, S.-C. Chien, J.R.B. Gomes, M.N. D. S. Cordeiro, S.M. Auerbach, P.A. Monson, M. Jorge, Multiscale model for the templated synthesis of mesoporous silica: The essential role of silica oligomers. *Chem Mater*. **2016**, 28: 2715–2727.

61 N. Pal, A. Bhaumik, Soft templating strategies for the synthesis of mesoporous materials: inorganic, organic-inorganic hybrid and purely organic solids. *Adv Colloid Interfac Sci*. **2013**, 189–190: 21–41.

62 A. Monnier, F. Schüth, Q. Huo, D. Kumar, D. Margolese, R.S. Maxwell, G. Stucky, M. Krishnamurty, P. Petroff, A. Firouzi, M. Janicke, B. Chmelka, Cooperative formation of inorganic-organic interfaces in the synthesis of silicate mesostructures. *Science*. **1993**, 261: 1299–1303.

63 Q. Yang, J. Liu, L. Zhang, C. Li, Functionalized periodic mesoporous organosilicas for catalysis. *J Mater Chem*. **2009**, 19: 1945–1955.

64 F. Clippel, M. Dusselier, S. Van de Vyver, L. Peng, P.A. Jacobs, B.F. Sels, Tailoring nanohybrids and nanocomposites for catalytic applications. *Green Chem*. **2013**, 15: 1398–1430.

65 M.P. Kapoor, Q. Yang, S. Inagaki, Self-assembly of biphenylene-bridged hybrid mesoporous solid with molecular-scale periodicity in the pore walls. *J Am Chem Soc*. **2002**, 124: 15176–15177.

66 M. Park, S.S. Park, M. Selvaraj, D. Zhao, C.-S. Ha, Hydrophobic mesoporous materials for immobilization of enzymes. *Micropor Mesopor Mater*. **2009**, 124: 76–83.

67 X. Duan, G. Qi, P. Wang, E.P. Giannelis, A highly efficient and selective polysilsesquioxane sorbent for heavy metal removal. *ChemPhysChem*. **2012**, 13: 2536–2539.

68 M. Beretta, J. Morell, P. Sozzani, M. Fröba, Towards peptide formation inside the channels of a new divinylaniline-bridged periodic mesoporous organosilica. *Chem Commun*. **2010**, 46: 2495–2497.

69 N. Mizoshita, S. Inagaki, Periodic mesoporous organosilica with molecular-scale ordering self-assembled by hydrogen bonds. *Angew Chem*. **2015**, 54: 11999–12003.

70 C. Yoshina-Ishii, T. Asefa, N. Coombs, M.J. MacLachlan, G.A. Ozin, Periodic mesoporous organosilicas, PMOs: fusion of organic and inorganic chemistry "inside" the channel walls of hexagonal mesoporous silica. *Chem Commun*. **1999**, 2539–2540.

71 S. Bracco, A. Comotti, P. Valsesia, B.F. Chmelka, P. Sozzani, Molecular rotors in hierarchically ordered mesoporous organosilica frameworks. *Chem Commun*. **2008**, 4798–4800.

72 J.H. Shin, S.S. Park, M. Selvaraj, C.-S. Ha, Adsorption of amino acids on periodic mesoporous organosilicas. *J Porous Mater*. **2012**, 19: 29–35.

73 J.H. Shin, S.S. Park, C. Ha, Adsorption behavior of nicotine on periodic mesoporous organosilicas. *Colloid Surface B* . **2011**, 84: 579–584.

74 A. Kuschel, S. Polarz, Organosilica materials with bridging phenyl derivatives incorporated into the surfaces of mesoporous solids. *Adv Funct Mater*. **2008**, 18: 1272–1280.

75 N. Bion, P. Ferreira, A. Valente, I.S. Gonçalves, J. Rocha, Ordered benzene-silica hybrids with molecular-scale periodicity in the walls and different mesopore sizes. *J Mater Chem*. **2003**, 13: 1910–1913.

76 J. Morell, M. Güngerich, G. Wolter, J. Jiao, M. Hunger, P.J. Klar, M. Fröba, Synthesis and characterization of highly ordered bifunctional aromatic periodic mesoporous organosilicas with different pore sizes. *J Mater Chem*. **2006**, 16: 2809–2818.

77 G.N. Kalantzopoulos, A. Enotiadis, E. Maccallini, M. Antoniou, K. Dimos, A. Policicchio, E. Klontzas, E. Tylianakis, V. Binas, P.N. Trikalitis, R.G. Agostino, D. Gournis, G.E. Froudakis, Hydrogen storage in ordered and disordered phenylene-bridged mesoporous organosilicas. *Int J Hydrogen Energy*. **2014**, 39: 2104–2114.

78 Q. Yang, M.P. Kapoor, S. Inagaki, Sulfuric acid-functionalized mesoporous benzene−silica with a molecular-scale periodicity in the walls. *J Am Chem Soc*. **2002**, 124: 9694–9695.

79 M.P. Kapoor, Q. Yang, Y. Goto, S. Inagaki, Biphenylene bridged bifunctional hybrid mesoporous silsesquioxanes with sulfonic acid functionalities and crystalline pore walls. *Chem Lett*. **2003**, 32: 914–915.

80 Q. Yang, M.P. Kapoor, N. Shirokura, M. Ohashi, S. Inagaki, J.N. Kondo, K. Domen, Ethane-bridged hybrid mesoporous functionalized organosilicas with terminal sulfonic groups and their catalytic applications. *J Mater Chem*. **2005**, 15: 666–673.

81 J. Liu, Q. Yang, M.P. Kapoor, N. Setoyama, S. Inagaki, J. Yang, L. Zhang, Structural relation properties of hydrothermally stable functionalized mesoporous organosilicas and catalysis. *J Phys Chem B*. **2005**, 109: 12250–12256.

82 C. Bispo, P. Ferreira, A. Trouvé, I. Batonneau-Gener, F. Liu, F. Jérôme, N. Bion, Role of acidity and hydrophobicity in the remarkable catalytic activity in water of sulfonic acid-functionalized phenyl-PMO materials. *Catal Today*. **2013**, 218-219: 85–92.

83 M.A. Wahab, I. Imae, Y. Kawakami, I. Kim, C.-S. Ha, Functionalized periodic mesoporous organosilica fibers with longitudinal pore architectures under basic conditions. *Micropor Mesopor Mater*. **2006**, 92: 201–211.

84 C. Li, B. Di, W. Hao, F. Yan, M. Su, Aminopropyl-functionalized ethane-bridged periodic mesoporous organosilica spheres: Preparation and application in liquid chromatography. *J Chromatogr A*. **2011**, 1218: 408–415.

85 N. Suriyanon, P. Punyapalakul, C. Ngamcharussrivichai, Synthesis of periodic mesoporous organosilicas functionalized with different amine-organoalkoxysilanes via direct co-condensation. *Mater Chem Phys*. **2015**, 149: 701–712.

86 D. Coutinho, C. Xiong, K.J. Balkus, Mesoporous benzene silica functionalized with

various amine groups. *Micropor Mesopor Mater*. **2008**, 108: 86–94.

87 K. Nakai, Y. Oumi, H. Horie, T. Sano, H. Yoshitake, Bromine addition and successive amine substitution of mesoporous ethylenesilica: Reaction, characterizations and arsenate adsorption. *Micropor Mesopor Mater*. **2007**, 100: 328–339.

88 E. De Canck, I. Ascoop, A. Sayari, P. Van Der Voort, Periodic mesoporous organosilicas functionalized with a wide variety of amines for CO_2 adsorption. *Phys Chem Chem Phys*. **2013**, 15: 9792–9799.

89 D. Esquivel, E. De Canck, C. Jiménez-Sanchidrián, F.J. Romero-Salguero, P. Van Der Voort, Pyrrole PMOs, incorporating new N-heterocyclic compounds on an ethene-PMO through Diels-Alder reactions. *Mater Chem Phys*. **2014**, 148: 403–410.

90 Y. Horiuchi, D. Do Van, Y. Yonezawa, M. Saito, S. Dohshi, T.-H. Kim, M. Matsuoka, Synthesis and bifunctional catalysis of metal nanoparticle-loaded periodic mesoporous organosilicas modified with amino groups. *RSC Adv*. **2015**, 5: 72653–72658.

91 G. Smeulders, V. Meynen, K. Houthoofd, S. Mullens, J.A. Martens, B.U.W. Maes, P. Cool, Is their potential for post-synthetic brominating reactions on benzene bridged PMOs? *Micropor Mesopor Mater*. **2012**, 164: 49–55.

92 W.-H. Zhang, B. Daly, J. O'Callaghan, L. Zhang, J.-L. Shi, C. Li, M.A. Morris, J.D. Holmes, Large pore methylene-bridged periodic mesoporous organosilicas: Synthesis, bifunctionalization and their use as nanotemplates. *Chem Mater*. **2005**, 17: 6407–6415.

93 D. Dubé, M. Rat, W. Shen, F. Béland, S. Kaliaguine, Perfluoroalkylsulfonic acid-functionalized periodic mesostructured organosilica: a strongly acidic heterogeneous catalyst. *J Mater Sci*. **2009**, 44: 6683–6692.

94 J.Y. Shi, C.A. Wang, Z.J. Li, Q. Wang, Y. Zhang, W. Wang, Heterogeneous organocatalysis at work: functionalization of hollow periodic mesoporous organosilica spheres with MacMillan catalyst. *Chemistry*. **2011**, 17: 6206–6213.

95 A.C. Gomes, M.J. Ferreira, S.M. Bruno, N. Bion, P. Ferreira, A.A. Valente, M. Pillinger, J. Rocha, I.S. Gonçalves, Preparation of crystal-like periodic mesoporous phenylene-silica derivatized with ferrocene and its use as a catalyst for the oxidation of styrene. *Dalt Trans*. **2013**, 42: 14612–14620.

96 K. Sim, N. Lee, J. Kim, E.-B. Cho, C. Gunathilake, M. Jaroniec, CO_2 adsorption on amine-functionalized periodic mesoporous benzenesilicas. *ACS Appl Mater Inter*. **2015**, 7: 6792–6802.

97 B. Onida, L. Borello, C. Busco, P. Ugliengo, Y. Goto, S. Inagaki, E. Garrone, Mesoporous benzene-silica hybrid materials with a different degree of order in the wall structure: an IR comparative study. *J Phys Chem B*. **2005**, 109: 11961–11966.

98 F. Hoffmann, M. Gungerich, P.J. Klar, M. Froba, Vibrational spectroscopy of periodic mesoporous organosilicas (PMOs) and their precursors: A closer look. *J Phys Chem C*. **2007**, 111: 5648–5660.

99 B. Camarota, P. Ugliengo, E. Garrone, C.O. Arean, M.R. Delgado, S. Inagaki, B. Onida, IR and computational characterization of CO adsorption on a model surface, the phenylene periodic mesoporous organosilca with crystalline walls. *J Phys Chem C*. **2008**, 112: 19560–19567.

100 E.A. Prasetyanto, M.B. Ansari, B.-H. Min, S.-E. Park, Melamine tri-silsesquioxane bridged periodic mesoporous organosilica as an efficient metal-free catalyst for CO_2 activation. *Catal Today*. **2010**, 158: 252–257.

101 S. Shirai, Y. Goto, N. Mizoshita, M. Ohashi, T. Tani, T. Shimada, S. Hyodo, S. Inagaki, Theoretical studies on Si-C bond cleavage in organosilane precursors during polycondensation to organosilica hybrids. *J Phys Chem A*. **2010**, 114: 6047–6054.

102 R. Futamura, M. Jorge, J.R.B. Gomes, Structures and energetics of organosilanes in the gaseous phase: A computational study. *Theor Chem Acc*. **2013**, 132: 1–10.

103 R. Futamura, M. Jorge, J.R.B. Gomes, Role of the organic linker in the early stages of the templated synthesis of PMOs. *Phys Chem Chem Phys*. **2013**, 15: 6166.

104 U. Martinez, G. Pacchioni, Interaction of CO, CO_2 and CH_4 with mesoporous organosilica: Periodic DFT calculations with dispersion corrections. *Micropor Mesopor Mater*. **2010**, 129: 62–67.

105 M. Sharifi, C. Köhler, P. Tölle, T. Frauenheim, M. Wark, Proton conductivity of SO_3 H-functionalized benzene-periodic mesoporous organosilica. *Small*. **2011**, 7: 1086–1097.

106 G. Pérez-Sánchez, J.R.B. Gomes, M. Jorge, Modeling self-assembly of silica/surfactant mesostructures in the templated synthesis of nanoporous solids. *Langmuir*. **2013**, 29: 2387–2396.

107 M. Jorge, J.R.B. Gomes, M.N.D.S. Cordeiro, N.A. Seaton, Molecular dynamics simulation of the early stages of the synthesis of periodic mesoporous silica. *J Phys Chem B*. **2009**, 113: 708–718.

108 J.R.B. Gomes, M.N.D.S. Cordeiro, M. Jorge, Gas-phase molecular structure and energetics of anionic silicates. *Geochim Cosmochim Acta*. **2008**, 72: 4421–4439.

109 M. Jorge, J.R.B. Gomes, M.N.D.S. Cordeiro, N.A. Seaton, Molecular simulation of silica/surfactant self-assembly in the synthesis of periodic mesoporous silicas. *J Am Chem Soc*. **2007**, 129: 15414–15415.

110 A. Firouzi, F. Atef, A.G. Oertli, G.D. Stucky, B.F. Chmelka, Alkaline lyotropic silicate-surfactant liquid crystals. *J Am Chem Soc*. **1997**, 119: 3596–3610.

111 K. Okamoto, Y. Goto, S. Inagaki, Self-organization of crystal-like aromatic–silica hybrid materials. *J Mater Chem*. **2005**, 15: 4136–4140.

112 J.P.P. Ramalho, J.R.B. Gomes, F. Illas, Accounting for van der Waals interactions between adsorbates and surfaces in density functional theory based calculations: selected examples. *RSC Adv*. **2013**, 3: 13085–13100.

113 F. Jensen, Introduction to Computational Chemistry. 1st Ed. Chichester, England: John Wiley and Sons, **2004**.

114 S. Grimme, Semiempirical GGA-type density functional constructed with a long-range dispersion correction. *J Comput Chem*. **2006**, 27: 1787–1799.

115 A. Comotti, S. Bracco, P. Valsesia, L. Ferretti, P. Sozzani, 2D multinuclear NMR, hyperpolarized xenon and gas storage in organosilica nanochannels with crystalline order in the walls. *J Am Chem Soc*. **2007**, 129: 8566–8576.

Chapter 2 – Methods and characterization techniques

2. Characterization of PMOs

The PMO materials present high specific surface areas, narrow distribution of pore sizes, tuneable pore size and arrangement, good thermal stability, alternating hydrophobic and hydrophilic bits and the organic moieties are modifiable. In this way, Transmission Electron Microscopy[1] (TEM); Scanning Electron Microscopy[2] (SEM); Powder X-Ray Diffraction[3] (PXRD); -196 °C nitrogen adsorption-desorption isotherms[4,5] (N_2 sorption isotherms); Nuclear Magnetic Resonance[6–8] (NMR) and Fourier Transformed Infrared[9] (FTIR) spectroscopies; Elemental Analysis[10,11] (EA); X-ray photoelectron spectroscopy[12] (XPS) and ThermoGravimetric Analysis[13] (TGA) are the common techniques necessary to evaluate the physical, textural and chemical properties of this kind of materials. PXRD and TEM provide information about the pore arrangement and the molecular-scale periodicity of the material, while TGA affords evidences about the thermal stability of the material and also about the amount of the organic groups incorporated in the PMO. FTIR, NMR spectroscopies and EA give information on the functional groups, local environment of the chemical elements and quantitative chemical elemental data of the material, respectively.

2.1 Synthesis of bissilylated precursors

The 1,4-bis(triethoxysilyl)benzene (BTEB) and 4,4′-bis(triethoxysilyl)-1,1′-biphenyl (BTEBP) were prepared *via* the Grignard reaction which was followed by distillation in vacuum using a procedure described in literature.[14]

Chemicals reagents

Magnesium, (purum, Aldrich), tetraethoxysilane (TEOS, 98%, Aldrich), iodine (99.8%, Fluka), tetrahydrofuran (THF, 99.5%, molecular sieves, Sigma-Aldrich), 1,4-dibromobenzene (98%, Aldrich), hexane (95%, Sigma-Aldrich) and 4,4'-dibromobiphenyl (95%, Aldrich) were used as received.

1,4-bis(triethoxysilyl)benzene synthesis

A typical synthesis starts with the addition of 3 small crystals of iodine to a mixture of dry magnesium turnings (5.14 g), TEOS (60 mL) and dry THF (40 mL) under nitrogen. Then the temperature of the reaction mixture was increased to 50 °C and a solution of 1,4-bromobenzene (16.45 g) in dry THF (31mL) was added dropwise over 2 h. After, the reaction mixture was kept under reflux overnight. The resulting grey-greenish mixture was cooled to room temperature and followed by removal of the THF under vacuum. Then, hexane (80 mL) was added to precipitate any remaining magnesium salts in solution, and the mixture was quickly filtered under nitrogen to afford a clear, light brown solution. Afterwards, the hexane and the remaining TEOS were distilled off under vacuum leading to a brownish oil. The oil was distilled (1.5 torr, 200-205 °C) to give a clear and colorless oil (BTEB, approx. 6.4 g). The characterization of BTEB was in concordance to the one previously described in the literature.[14]

4,4'-bis(triethoxysilyl)biphenyl synthesis

A solution of 4,4'-dibromobiphenyl (15 g) in dry THF (113 mL) and TEOS (75 mL) was added to dry magnesium turnings (4.5 g). The reaction mixture was kept at reflux (75 °C) for 5 days. The resulting turbid, grey-greenish mixture was worked up as with BTEB to afford a viscous brown oil. Distillation (0.3 torr, 205-210 °C) yielded a clear and colorless oil (BTEBP, approx. 1.5 g). The characterization of BTEBP was in concordance with the one previously described in the literature.[14]

2.2 PMO material synthesis and functionalization

The synthesis of the phenylene- and biphenylene- PMOs and their functionalizations are detailed in the following chapters. Figure 2.1 highlights the different families of materials prepared and the chapter where their syntheses, characterizations and applications are reported.

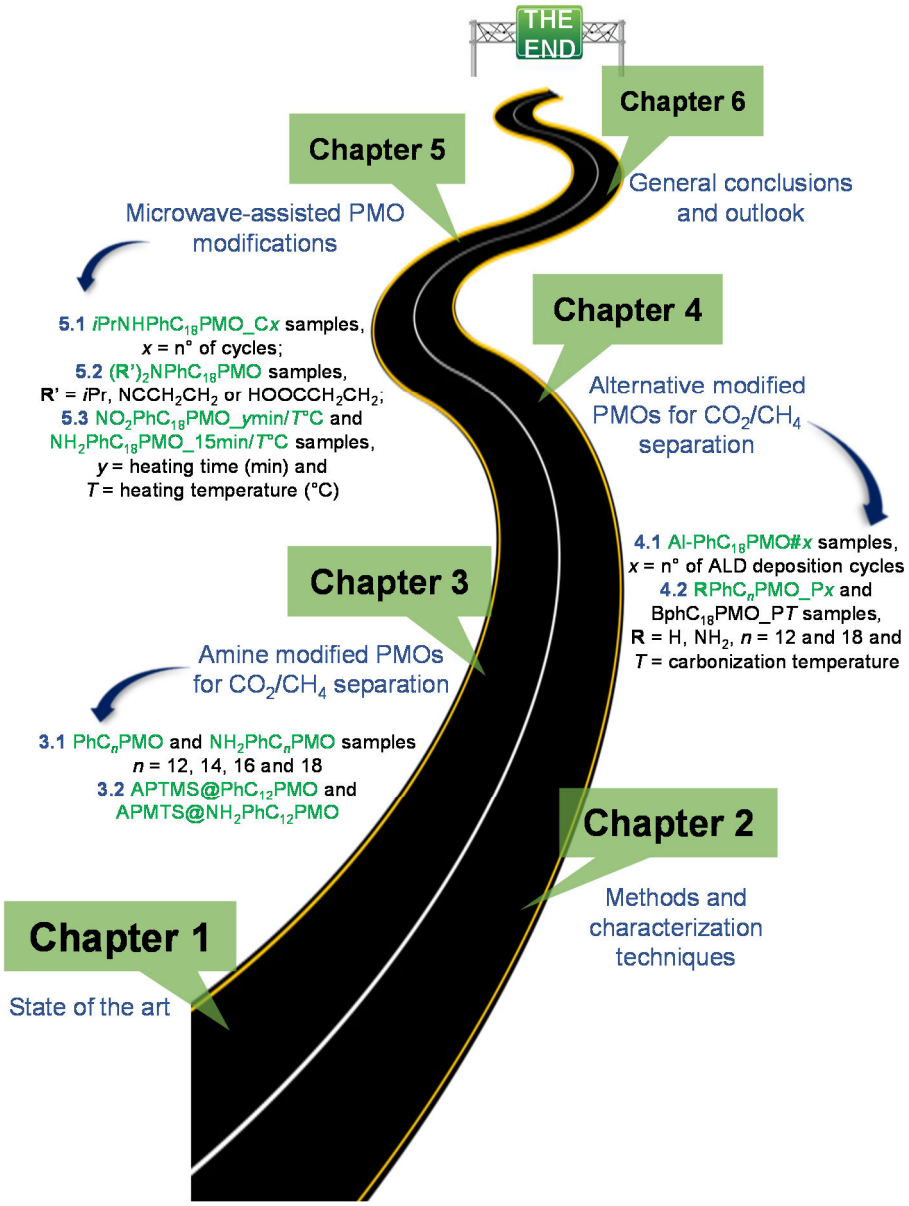

Figure 2.1. PhD Thesis Roadmap: resulting materials from each chapter.

Chemicals reagents

Dodecyltrimethylamonium bromide (C_{12}-TMA, 99%, Aldrich), tetradecyltrimethylammonium bromide (C_{14}-TMA, 99%, Aldrich),

hexadecyltrimethylammonium bromide (C_{16}-TMA, 95%, Aldrich), octadecyltrimethylammonium bromide (C_{18}-TMA, 98%, Aldrich), ethanol (PA, Panreac), hydrochloric acid (HCl, 37% v/v, Carlo Erba), nitric acid (HNO_3, 65% v/v, Panreac), sulfuric acid (H_2SO_4, 95-97% v/v, Panreac), tin chloride ($SnCl_2$, 98%, Aldrich) and isopropylamine ($CH_3CH(NH_2)CH_3$, >99.5%, Aldrich), dry dichloromethane (CH_2Cl_2, extra-dry, ACROS organics), (3-aminopropyl)-trimethoxysilane (APTMS, 98%, Sigma-Aldrich), acetonitrile (99.5%, Sigma), 4,4′-Bis(triethoxysilyl)-1,1′-biphenyl (BTEBP, Aldrich, 95%), 2-bromopropane ($CH_3CH(Br)CH_3$, 99%, Aldrich), potassium iodide (KI, 99.5%, Riedel-de-Haën), dichloromethane (>98%, Fluka), sodium hydrogen carbonate ($NaHCO_3$, 99.5%, Sigma-Aldrich) and 3-chloropropionitrile ($ClCH_2CH_2CN$, 98%, Aldrich) were purchased from commercial sources. All chemicals were used as received.

2.3 Structural and morphological studies

Transmission electron microscopy and scanning electron microscopy

The PMOs prepared in this PhD Thesis have a 2D hexagonal symmetry lattice (so, they have uniform mesopores with a determined diameter arranged in a hexagonal manner), which is expected to be observed using high-resolution TEM with a [001] incident beam, parallel to the channels (Figure 2.2a).[15]

Using high-resolution TEM with [100] incident beam, perpendicular to the channels, we may visualize the molecular-scale order along the channels (Figure 2.2b).[15]

The surface, shape, topography, size and level of aggregation of the powder particles of the PMOs were also studied. The SEM technique was used to obtain this kind of information.[2]

Microscopy techniques can also be used to obtain a chemical characterization of the samples, *i.e.*, it is possible to observe the mapping areas of different elemental composition. This requires the usage of an energy dispersive X-ray spectroscopy (EDS) detector with the TEM or SEM equipments.[1,2]

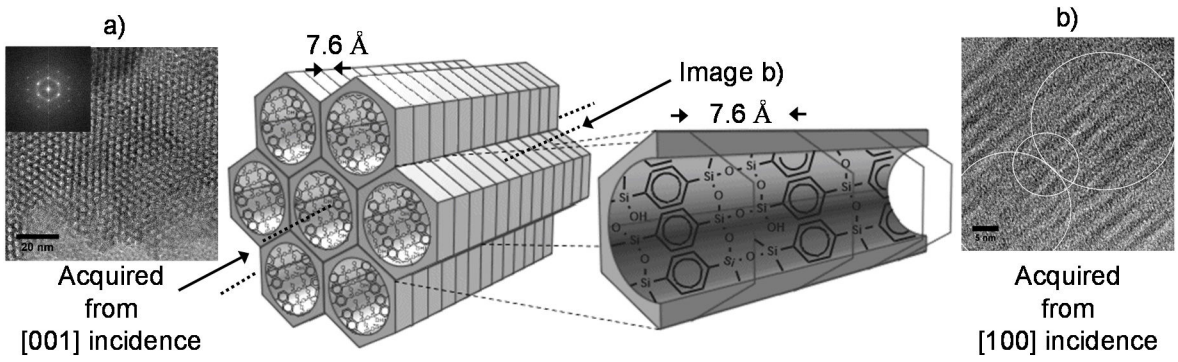

Figure 2.2. Schematic models of mesoporous phenylene-silica resulting from the data collected from TEM images and electron diffraction patterns. The images and the patterns are collected in the correct orientation relation, *i.e.*, the diffraction spots and corresponding lattice planes are normal to each other. a) Image and pattern taken with [001] incidence, parallel to the channels. The pores are organized uniformely and in the hexagonal manner and present a diameter of ≈ 38 Å; b), Image obtained with [100] incident beam, perpendicular to the channels. The circles represent the lattice fringes with a spacing of 7.6 Å that are observed in the pore walls. In this case, the wavy contrast that is perpendicular to the lattice fringes and with a spacing of 45.5 Å ($d = \sqrt{3}a/2$) is not observed as reported previously by Inagaki and co-workers.[15] The contrast of spacings at 7.6 Å and 45.5 Å cannot be observed simultaneously even using the best conditions, once the contrast transfer function of the objective lens on focus condition is different for both.

TEM images were recorded using three different equipments: a 300 kV Hitachi H-9000-NA instrument equipped with CCD camera, a 200 kV High Resolution (HR) and energy filtered (EF) TEM JEOL 2200FS instrument equipped with digital camera, Orius SC1000B, and a TEM JEOL 2100 UHR equipped with analysis EDX Si(Li) and camera CCD Gatan ultrascan (2k x 2k).

The preparation of the samples was done as follows: first, PMO samples shown in Chapter 4.1 were inserted into a polymeric resin and cut by ultramicrotomy with a diamond knife to have a thickness between 50 nm and 70 nm; then, the sections cut were deposited on grids with holey carbon film. The remaining samples considered in this PhD Thesis were deeply crushed using mortar and pestle, dispersed in ethanol and, then, a few drops of the suspensions were placed on holey carbon copper microgrids.

The SEM micrographs were acquired on a SEM-FEG Hitachi SU-70 microscope operated at 25 kV equipped with microanalysis system for energy dispersive spectrometry of X-rays/EDS from Bruker Quantax 400 EDS detector, using the same TEM copper grids.

Powder X-ray diffraction

The structural order of the samples was also studied by PXRD and N_2 sorption-isotherms. From PXRD it can be extracted information about the lattice parameters of the materials and

also about the observed mesoporosity and molecular periodicity of the materials prepared. Despite PMO materials do no present the crystalline arrangement of the atoms, they show organization of the pores and the electron density contrast created by such periodicity (2D hexagonal symmetry in the case of the materials studied in this PhD Thesis) can be detected by the PXRD technique.[15] Thus, we can use the Bragg's law equation:

$$n\lambda_{Cu} = 2d\ sin(\theta) \qquad \text{(Equation 2.1)}$$

to determine the inter-planar distance d, in which n is an integral multiple of the wavelength, λ_{Cu} is the wavelength of the X-ray (in the case a Cu Kα signal) and θ is the incidence angle. The lattice constant (a_0) characteristic of a two-dimensional hexagonal symmetry (*p6mm*) lattice is determined from the d spacing of the 100 reflection using the following equation:

$$a_0 = 2d_{100}/\sqrt{3} \qquad \text{(Equation 2.2)}$$

Furthermore, the samples prepared in this study are expected to possess the molecular-scale periodicity, which is related to the very regular alternation of the hydrophobic and hydrophilic layers. These are expected to be detected using the PXRD technique, by observation of an additional peak at the medium-scale angle range, corresponding to the size of the repeating unit. This periodicity is represented in Figure 2.3 by the interplanar distance d_{001}.

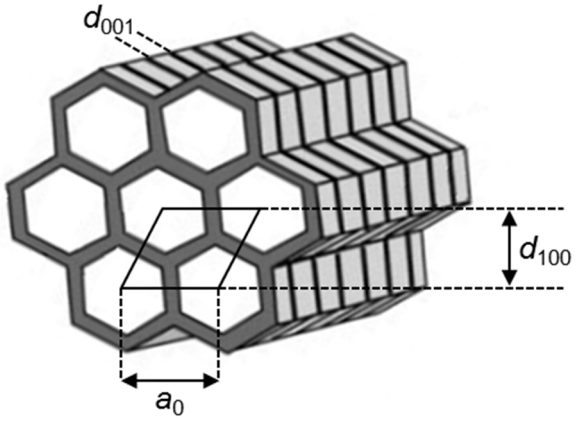

Figure 2.3. Representation of the meso- and molecular- scale orders of a PMO material with 2D hexagonal symmetry. Adapted from reference [15].

Most of the PXRD data were gathered with a Rigaku Geigerflex D Max-C Series diffractometer using Cu-Kα radiation (λ_{Cu} = 1.5406 Å). The diffractograms were acquired

with 2θ from 1-40 °, with a step size of 0.02 ° and acquisition times between 3 and 60 s per step.

As example, a typical diffractogram of $PhC_{18}PMO$ is shown in Figure 2.4.

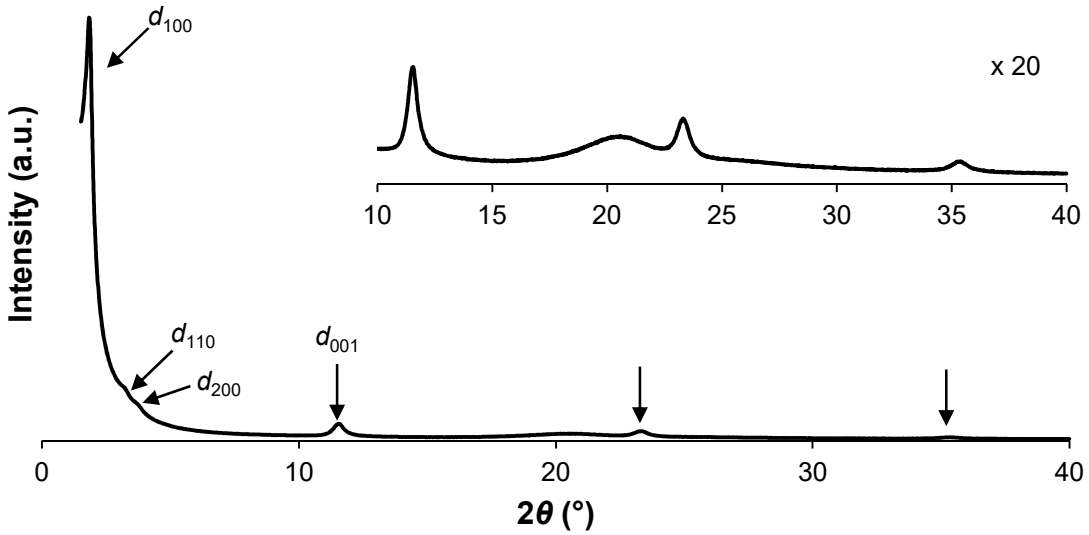

Figure 2.4. PXRD diffraction patterns of $PhC_{18}PMO$, showing the 2D hexagonal arrangement of the pores by observation of *d* spacing of the 100, 110 and 200 reflections and also the molecular-scale periodicity through the presence of the interplanar distance d_{001}.

Low temperature (-196 °C) nitrogen adsorption-desorption isotherms

The N_2 sorption isotherms provide information about the type of isotherm (Figure 2.5) and of the presence or absence of hysteresis loops.[4,5]

A brief description of each type of isotherm is provided below as this technique is important in the characterization of PMO materials.

Reversible type I isotherms are observed for microporous solids with rather small external surface area (*e.g.*, some activated carbons, molecular sieve zeolites and certain porous oxides). As can be observed in Figure 2.5, the type I isotherm presents a concave form and the quantity adsorbed gets close to a limit value. The approximation to this limiting uptake is ruled by the accessible micropore volume and not by the internal surface area. The uptake steep observed at very low relative pressure is related to the improved adsorbent-adsorptive interactions in narrow micropores (micropores of molecular dimensions). The type I isotherms can be divided in type Ia and Ib isotherms for -196 °C nitrogen and -186 °C argon adsorption. Type Ia isotherms is usually detected for microporous materials having mainly narrow micropores (of width < ~ 1 nm) while the type Ib isotherms are observed in materials

with wide-range pore size distributions from broader micropores and perhaps narrow mesopores (< ~ 2.5 nm).

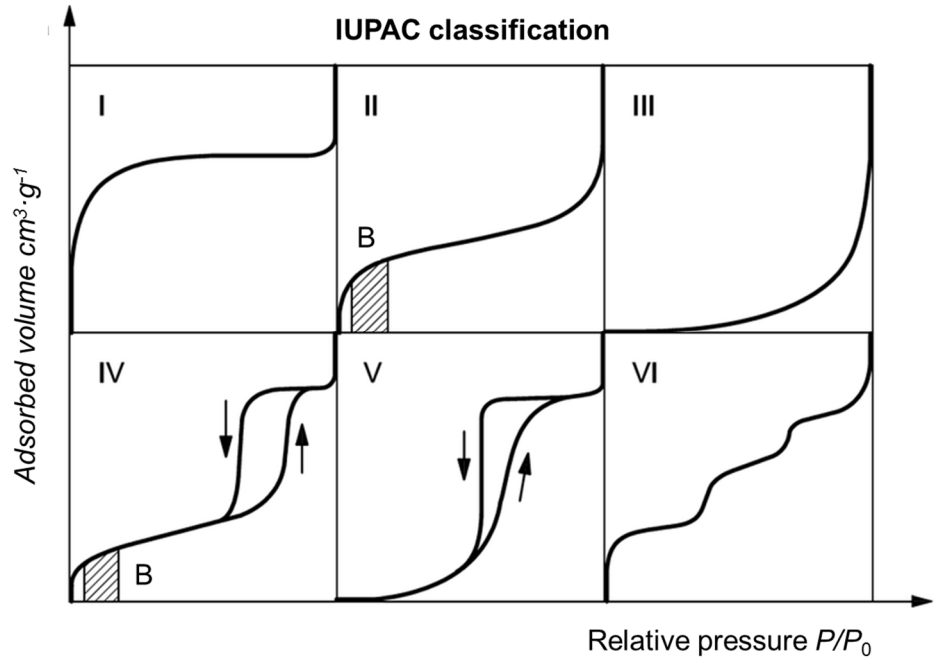

Figure 2.5. Types of physisorption isotherms. Adapted from reference [5].

The reversible type II isotherms are observed in nonporous or macroporous materials that adsorb most gases by the physisorption mechanism. The shape is the result of unrestricted monolayer-multilayer adsorption up to high relative pressure. This type of curve shows a point B, and if the lap is loud, point B generally agrees to the achievement of monolayer coverage.

Type III isotherm does not present monolayer formation because point B is absent. Materials presenting this kind of isotherm curve show relatively weak adsorbent-adsorbate interactions and the adsorbed molecules are gathered around the most promising locations on the surface of the materials. This type of isotherm curve is typically observed in nonporous or macroporous solids.

Mesopores adsorbents show type IV isotherms. The adsorption performance in mesoporous materials results from the adsorbent-adsorptive interactions and also from the interactions among the molecules in the condensed state. In this kind of isotherm, the initial monolayer-multilayer adsorption on the mesoporous walls is followed by pore condensation. A distinctive characteristic of this kind of isotherms is a final saturation plateau, of variable length. As type I isotherms, type IV isotherms can be divided in type IVa and type IVb

isotherms. The type IVa isotherm presents capillary condensation due to hysteresis. This happens when the pore width exceeds a determined critical size, depending on the adsorption system and temperature. For adsorbents presenting small mesopores, fully reversible type IVb isotherms are observed. Type IVb isotherms are also observed in materials showing conical and cylindrical mesopores that are closed at the tapered end.

Type V isotherm form is similar to type III isotherm and this can be endorsed to quite weak adsorbent–adsorbate interactions. These isotherms are archetypal for water adsorption on hydrophobic microporous and mesoporous adsorbents.

The reversible stepwise type VI isotherm is typically observed in highly uniform nonporous surface materials due to layer-by-layer adsorption. The height of step denotes the capacity of each layer to adsorb, but the step sharpness is dependent on the system and the temperature. This isotherm type is typically observed in the adsorption of argon or krypton in graphitized carbon blacks at low temperature.

The -196 °C N_2 adsorption-desorption isotherms technique allows also to determine specific surface area (S_{BET}), size distribution of the pores and pore volume of the PMO materials.[16] PMO materials usually display type IV isotherms (IUPAC classification) because of the narrow distribution of pore sizes as typically observed for conventional mesoporous materials such as MCM-41. To calculate the specific surface area, the most used method is the Brunauer, Emmett and Teller (BET),[17,18] and to determine the pore size distribution the Kelvin equation is usually utilized.[16] For the specific case of mesoporous materials, the pore size distribution is determined employing also the mathematic correction method KJS (Kruk, Jaroniec, and Sayari).[19,20]

Additionally, type I isotherms can be also observed in some of the PMO materials presented in the following chapters. The adsorption data of PMO materials displaying both mesopores and micropores can be treated with quenched solid classical density functional theory (QSDFT)[21] that is another method used to determine the pore size distribution. This method is better suited than the KJS one once it takes into account the effects of surface heterogeneity, which significantly improve the reliability of the pore size analysis of heterogeneous micro- and meso- porous materials.[18,22]

N_2 sorption isotherms were recorded at -196 ºC using a Gemini V 2.00 instrument model 2380. Functionalized PMO materials were dehydrated overnight at 120 or 150 ºC to an ultimate pressure of 1024 mbar and then cooled to room temperature prior to adsorption.

2.4 Chemical studies

Nuclear magnetic resonance spectroscopy

Solution and solid state NMR studies were made in order to obtain information of the chemical structure of the prepared bissilylated precursors and materials, respectively. Different chemical reactions were performed in this PhD Thesis in order to tune the properties of the materials. The solid state NMR spectroscopy allows to observe the chemical environments of the different nuclei in the materials.[6–8] The appearance of peaks at different chemical shifts is expected when a chemical modification is introduced in the PMOs. NMR spectroscopy typical resonances of the pristine and functionalized aromatic PMO materials prepared in this PhD Thesis are displayed in Table 2.1.

Table 2.1. Typical NMR chemical shifts resonances that can be observed in the PMO materials prepared in this PhD Thesis.

Chemical shift (ppm)	**Possible assignment**
	^{13}C NMR
58.0, 39.6 and 15.9	Residues of surfactants; ethoxyl groups formed during the surfactants extraction
8-35	$\underline{C}H_3$ bonded to a primary carbon (R-$\underline{C}H_3$)
15-50	$\underline{C}H_2$ bonded to a primary carbon (R-$\underline{C}H_2$-R)
20-60	$\underline{C}H$ bonded to a primary carbon (R-$\underline{C}H$-$(R)_2$)
40-60	$\underline{C}H$ or $\underline{C}H_2$ directed bonded to nitrogen atom ($\underline{C}$-N)
50-80	$\underline{C}H$ or $\underline{C}H_2$ directed bonded to oxygen atom ($\underline{C}$-O)
115-125	Nitrile groups (-$\underline{C}$N)
110-170	Aromatic carbons
160-185	Carboxylic acid (R($\underline{C}$O)X) derivatives
	^{29}Si NMR
-48	$T^{1'}$ $[(HO)_2SiR'(OSi)]$[a] silicon species of grafted alkyl silane agents
-58	$T^{2'}$ $[(HO)SiR'(OSi)_2]$ [a] silicon species of grafted alkyl silane agents
-68	$T^{3'}$ $[SiR'(OSi)_3]$ [a] silicon species of grafted alkyl silane agents
-61	T^1 $[(HO)_2SiR(OSi)]$ [a] silicon species of aromatic PMOs
-71	T^2 $[(HO)SiR(OSi)_2]$ [a] silicon species of aromatic PMOs
-81	T^3 $[SiR(OSi)_3]$ [a] silicon species of aromatic PMOs
-90 to -140	Q^n silicon species[b] of aromatic PMOs
	^{15}N NMR
≈ -320	Aromatic primary aromatic amines (NH_2 species for NH_2PhC_nPMO)
-292	Secondary aromatic amines (iPr$\underline{N}$HPhC_{18}PMO)
-270	Secondary aromatic amines ($NCCH_2CH_2\underline{N}HPhC_{18}PMO$)
-244	Tertiary aromatic amines ((iPr)$_2\underline{N}PhC_{18}$PMO and ($NCCH_2CH_2)_2\underline{N}PhC_{18}PMO$)
	^{27}Al NMR
5	Al^{VI} octahedral coordinated aluminium
38	Al^{V} bipyramidal coordinated aluminium
62	Al^{IV} tetrahedral coordinated aluminium

[a]T^m species calculated from $[T^m = RSi(OSi)_m(OH)_{3-m}]$. [b]$Q^n$ species calculated from $[Q^n = Si(OSi)_n(OH)_{4-n}]$. The presence of Q^n species provide information about the presence of carbon–silicon bond cleavage.

Most of ^{13}C, ^{29}Si, ^{15}N and ^{27}Al NMR spectra were recorded on a Bruker Avance III 400 spectrometer operating at 9.4 T at 100.62, 79.49, 40.54 and 100.62 MHz, respectively.

^{13}C cross-polarization (CP) magic-angle spinning (MAS) NMR spectra were obtained with 4 μs ^{1}H 90° pulse, contact time (CT) of 1 ms, a spinning rate (ν_R) of from 7 to 15 kHz and a recycle delay (RD) of 4 s.

^{29}Si MAS NMR spectra were collected employing a 40º flip angle pulse; ν_R of 5 kHz and RD of 60 s. Despite being a quantitative technique, the acquisition of spectra with acceptable signal to noise ratio, requires long time once the natural abundance of ^{29}Si is of ≈ 4.7 %, which is quite low. ^{29}Si CP-MAS NMR spectra were acquired with a 4 μs ^{1}H 90° pulse, a CT of 8 ms, a ν_R of 5 kHz and 5 s of RD. The ^{29}Si CP-MAS NMR is just a qualitative technique because it involves the transference of polarization between ^{1}H and ^{29}Si nuclei. The spectra are obtained in a short period of time with improved signal to noise ratio, being very useful to clearly identify the chemical environments that can be quantified in the ^{29}Si MAS NMR spectra.

The ^{13}C and ^{29}Si NMR spectra were quoted in ppm from trimethylsilane.

^{15}N CP-MAS NMR spectra were recorded with 4 μs ^{1}H 90° pulse, CT of 8 ms, a ν_R of 5 kHz and a RD of 5 s. These spectra took long time to be acquired due to the really low natural abundance of ^{15}N (≈0.37%), resulting in a sensitive penalty. ^{15}N NMR spectra were referenced against a solid sample of natural abundance L-glycine, a secondary reference standard with respect to nitromethane.

^{27}Al MAS NMR spectra were done employing a 10º flip angle pulse, a ν_R of 14 kHz and RD of 1 s. In this case, a MAS quantitative technique was used due to the high natural abundance of ^{27}Al, which is 100%, being the acquisition of the spectra much faster than in the cases above.

Fourier transform infrared spectroscopy

The FTIR spectroscopy is a versatile tool and was used here as a complementary technique to NMR for confirming the introduction of new functional groups into the PMO materials. The FTIR generated spectra can be acquired through three different ways: transmission/absorption, reflection and emission modes.[9] In the transmission/absorption mode, radiation goes through the sample, and some part of the radiation can be absorbed while another part can be transmitted. In reflection mode, the incident beam penetrates the surface of the sample and interacts with the matrix and, after partial absorption of the radiation, returns to the surface. The emission mode, which is rarely used, consists in sample

heating in such a way that the functional groups of the sample can emit at characteristic wavelength.[9] The FTIR spectroscopy in reflectance mode was used throughout the different studies in this PhD Thesis. Also, the transmission/absorption mode with attenuated total reflectance (ATR) technique was used. The ATR technique is usually associated with the acquisition of spectra of unwieldy samples, but its use has been spreading, because the spectra generated by this technique are obtained quickly in a wide range of samples without minimal preparation.

The typical FTIR spectroscopy absorption bands of the parent and of the functionalized aromatic-PMO materials prepared in this PhD Thesis are presented in Table 2.2.

Table 2.2. Typical FTIR absorption bands that can be observed in the PMO materials prepared in this PhD Thesis.

Frequency (cm^{-1})	**Possible assignment**
1180-1360	C–N stretching mode
1300–2000	Overtones of benzene ring vibrations
1345-1385 and 1515-1560	N–O symmetrical and asymmetrical stretching modes
1400-1600	C=C stretching modes of aromatic groups
1500-1680	N–H bending vibration (“scissoring” mode)
1650-1780	C=O stretching band
2500-3300	O–H stretching band of carboxylic acid
2750-3050	Alkyl C–H stretching bands
3000-3100	Aromatic C–H stretching bands
3300-3500	H–O–H bending vibrations and N–H stretching modes (doublet for NH_2)
3200–3800	Stretching modes of silanol

Most of the FTIR spectra were collected in absorbance mode and were performed in a FTIR Bruker Tensor 27 instrument with a Golden Gate ATR in the range of 4000 to 350 cm^{-1} with 256 scans and 4 cm^{-1} resolution. The samples were dehydrated overnight at 100 °C before analyses.

Elemental analysis

EA enables the determination of the percentage of each atom in the PMO.[10,11] In this work, this technique was extremely important i) for quantifying the amount of nitrogen species introduced in the materials during the amination reactions *via* distinct synthesis conditions and ii) for attaining the amine densities.

Elemental analysis CHN were carried out with a TruSpec 630-200-200 CNHS Analyser. Analysis Parameters: sample amount was between 1 and 2 mg; combustion furnace temperature was 1075 ºC; afterburner temperature was 850 ºC. Detection method: carbon –

infrared absorption; hydrogen – infrared absorption, nitrogen – thermal conductivity. The samples were dried at 100 °C for 24 h before the analyses.

X-ray photoelectron spectroscopy

XPS is a semi-quantitative spectroscopic technique that allows the determination of the elemental composition, empirical formula, chemical state and electronic state of the existing elements into the material.[12] This spectroscopy technique can be useful to observe the chemical modifications at the surface of the material, as it can identify the introduction of new elements into the surface and to elucidate changes in the chemical bonds established by certain elements.

The XPS spectra were acquired by Carlos P. M. Sá at Centro de Materiais da Universidade do Porto (CEMUP), using a Kratos Axis Ultra HAS spectrometer, with monochromatized Al Eo radiation (15 eV). All the materials were compressed into pellets prior to the XPS studies. In order to correct possible deviations, produced by electric charge of the materials, the C 1s line at 285.0 eV was taken as internal standard. The percentage of each element into the materials was determined from the areas of the relevant bands in the survey XPS spectra.

2.5 Thermal stability studies

The thermal stability studies are important to extract information of the degradation temperature of the materials.[13] This information is important to understand if the expected chemical functionalities were inserted in the material and to define the conditions to be used under the different techniques to avoid material degradation. The desorption temperature used during the adsorption measurements took always into account the thermal stability of each material. To study the thermal stability of the materials, TGA analyses were performed on a Shimadzu TGA-50 instrument with a program rate of 5 $^{o}C \cdot min^{-1}$ in air.

2.6 CO_2/CH_4 adsorption studies

The adsorption isotherms of carbon dioxide and methane were measured using two different apparatuses, namely, the manometric and the volumetric one, as described below.

Manometric experimental setup

Adsorption isotherms of carbon dioxide and methane were measured on PMO materials, at 308 K and pressures up to 2 bar, using an in-house built manometric apparatus, Figure A1 (*c.f.* Appendix A). The samples were activated, according to the heating program shown in Figure A2 (first at 80 °C during 5 hours and then at 160 °C during 10 hours), under vacuum of *ca*. 14 mbar. The CO_2 and CH_4 gases were used as provided by Air Liquide (France), with a purity of 99.998% and 99.95% respectively.

The experimental adsorption measurement technique adopted was previously described in detail[23] and, therefore, is shortly summarized here. Before performing each adsorption measurement, the void volume was determined by helium picnometry. To perform an adsorption experiment, the gas to be adsorbed is fed into the gas tank until an initial pressure P is reached while the sample is kept isolated, in another tank, by a closed valve. After the gas feed, the pressure in the gas tank is allowed to stabilize over a given period of time. The adsorption process starts when the valve isolating the sample is opened, and a pressure decrease is observed until a plateau is reached. Pressure and temperature readings are constantly recorded over time, so that the adsorption uptake can be computed as a function of time. This procedure is repeated sequentially for different values of pressure, starting from the previously equilibrated pressure point.

Each experimental pure component adsorption isotherm was fitted to a Langmuir model. The fitting parameters were then used to calculate the Henry's constant of adsorption (K_H, in $mmol \cdot g^{-1} \cdot bar^{-1}$) for each gas and each adsorbent by taking the slope of the isotherm in the limit of zero coverage. The Henry constant thus measures the affinity of each gas toward the solid surface. The Langmuir equation is expressed in Equation 2.3:

$$q = \frac{qs \times b \times P}{1 + b \times P} \qquad \text{(Equation 2.3)}$$

where q is the amount adsorbed, q_S is the Langmuir saturation capacity, b is the Langmuir surface affinity parameter and P is the pressure.

We then estimated the low-coverage CO_2 selectivity (S) of each material by taking the ratio of the Henry's constants for the two gases (Equation 2.4):

$$S^{CO_2/CH_4} = \frac{K_H^{CO_2}}{K_H^{CH_4}} = \frac{q_s^{CO_2} \times b^{CO_2}}{q_s^{CH_4} \times b^{CH_4}} \quad \text{(Equation 2.4)}$$

The measurements made using this equipment were performed by our collaborators at the Laboratório Associado LSRE-LCM, Faculty of Engineering, University of Porto, Christophe Siquet, João Santos and Miguel Jorge.

Volumetric experimental setup

Adsorption isotherms of CO_2 and CH_4 on prepared samples were measured up to 1000 kPa at 25 °C, using the volumetric method. These experiments were done on a custom-made stainless steel volumetric apparatus, with a pressure transducer (Pfeiffer Vacuum, APR 266), and equipped with a vacuum system that allows a vacuum better than 10^{-2} Pa. The temperature was controlled with a stirred thermostatic water bath (Grant Instrument, GD-120) and before every experiment the samples were degassed for 2.5 h at 150 °C. Each experimental pure component adsorption isotherm was fitted using the virial model, where the non-ideality of the gas phase was taken into account by using the second and third virial coefficients, and the experimental excess adsorbed amounts were converted to the absolute adsorbed amounts by taking into account the porous volume of the material and the density of the gas phase using the virial coefficients. Selectivity values were estimated using a method proposed by Myers[24] and the implementation is described in detail in previous works.[25] The virial equation of state fitted to the adsorption data is in the form:

$$p = \frac{n^{ads}}{K_H} \exp\left(C_1 n^{ads} + C_2 n^{ads^2} + C_3 n^{ads^3}\right) \quad \text{(Equation 2.5)}$$

where, K_H is the Henry constant, and C_1, C_2, and C_3 are the constants of the virial-series expansion.

The CO_2 and CH_4 adsorption measurements made using this technique were performed under supervision of Moisés Pinto and João Pires at CCB – Center of Chemistry and Biochemistry, Faculty of Sciences, University of Lisbon.

2.7 Computational studies

Density functional theory (DFT) is currently one of the most effective and also most common quantum mechanical methodologies to matter. Its applications go from atoms to molecules and solids. Currently, DFT is regularly used for calculating a wide range of properties in chemistry (*e.g.* molecular structures, reaction paths, etc.) and in physics (*e.g.* band structures of solids).

The final aim of most approaches in solid state physics and quantum chemistry is the resolution of the time-independent, non-relativistic Schrödinger equation,[26] toward obtaining relevant information about a system. However, for non hydrogenoid species, a precise solution of Schrödinger equation is not possible and several approximations need to be made. The Born-Oppenheimer approximation,[27] is the approximation most accepted, being centered on the fact that nuclei are several thousand times heavier than electrons, therefore the system wave function is allowed to be fragmented into its electronic and nuclear components. Then, for a system with many-electrons and assumed nuclear potential, the variational principle describes a procedure to obtain its estimated ground-state energy and wave function, besides other important properties.

Two large classes of conventional electronic structure methods were developed to tackle many-body problems and can be divided into wave function-based methods and DFT methods. The former class comprise the often called *ab initio* approaches like the Hartree-Fock (HF), Møller-Plesset perturbation theory (MP), configuration interaction (CI), and coupled cluster (CC) methods.[28] For these methods, the system wave function with N electrons depends on $3N$ spatial variables (and the spin in case of the unrestricted formalisms), and so their complexities grow with the increase of number of electrons. Differently in the other class, DFT methods,[29] use functionals of the electron density, which is a function of only 3 spatial variables.

The DFT theory relies on the Hohenberg and Kohn (H-K) theorems. The first H-K theorem validates that the electron density exclusively controls the Hamiltonian operator and consequently all the properties of the system, while the second theorem states that the functional relating to the ground-state energy of the system brings the lowest energy if and only if the input density is the true ground state density (*i.e.* nothing but the variational principle). Currently, the precision and efficacy of DFT-based approaches depend not only

on the basis-set for the expansion of the Kohn-Sham orbitals, but also on the quality of the applied exchange-correlation (XC) functionals.[30]

The first DFT approach proposed was the local density approximation (LDA)[31], which was followed by the local-spin density approximation (LSDA) proposed by Slater[32]. Both, found vast application in physics but the consideration of an homogeneous electron density was demonstrated to be inadequate (and inaccurate) for most applications in chemistry.

Then, the generalized gradient approximation (GGA) appeared, which has into account the non-homogeneity of the true electron density, *i.e*, it incorporate also the gradient of the electron density with the distance from the nucleus. Between the most frequently used combinations of XC functionals of the GGA family are the BP86 (exchange from Becke's B88 functional with correlation from Perdew's P86 functional), PW91 (exchange-correlation from Perdew-Wang 91), PBE (exchange-correlation from Perdew, Burke, and Ernzerhof), RPBE (revised version of the Perdew-Burke-Ernzerhof functional due to Hammer and Norskov), and BLYP (B88 exchange with correlation from Lee, Yang and Parr).[33–46] For example, the most applied functional to model metallic surfaces is the PW91, followed closely by PBE and RPBE.[47] GGA functionals usually provide better atomization energies, and structural properties, when compared to LSDA functionals. Nevertheless, GGA functionals give too small barrier heights and fail in describing van der Waals interactions.

More flexible XC functionals, labelled meta-GGAs (*e.g.* TPSS)[48,49] and hybrid (or meta-hybrid) functionals with nonlocal HF exchange[41] (*e.g.* hybrid B3LYP and meta hybrid M06) appeared to offer better accuracy, although they may present convergence problems. They are also more computationally costly than approaches based on the GGA.

In order to solve the GGA limitations to describe systems where van der Waals interactions (vdW) assume an important role, *i.e.* weakly bonded systems, several different strategies have been introduced in the last decade. In the case of DFT-D2, that is the approach used in the PMO modeling studies performed in this PhD Thesis, it is considered a simple empirical dispersion correction, which was suggested by Grimme *et al*.,[50] where the dispersion contributions are considered by pairwise interactions from the London formula.[51] Other approaches with different degrees of empiricism have been proposed to introduce the effects of dispersion in DFT calculations and were the focus of a recent review.[52]

Based on the description above, the choice of the most suitable DFT method for a specific application is based on a compromise between accuracy and computational cost. Figure 2.6 illustrates the variation of the XC functional simplicity and expected accuracy on going from the earth of Hartree (null exchange, null correlation) to the heaven of chemical accuracy, with errors in energy differences lower than 1 kcal·mol^{-1}; the green steps illustrate that the inclusion of dispersion corrections to any of the DFT classes in principle leads them closer to the heaven of accuracy in case of weakly bonded systems.

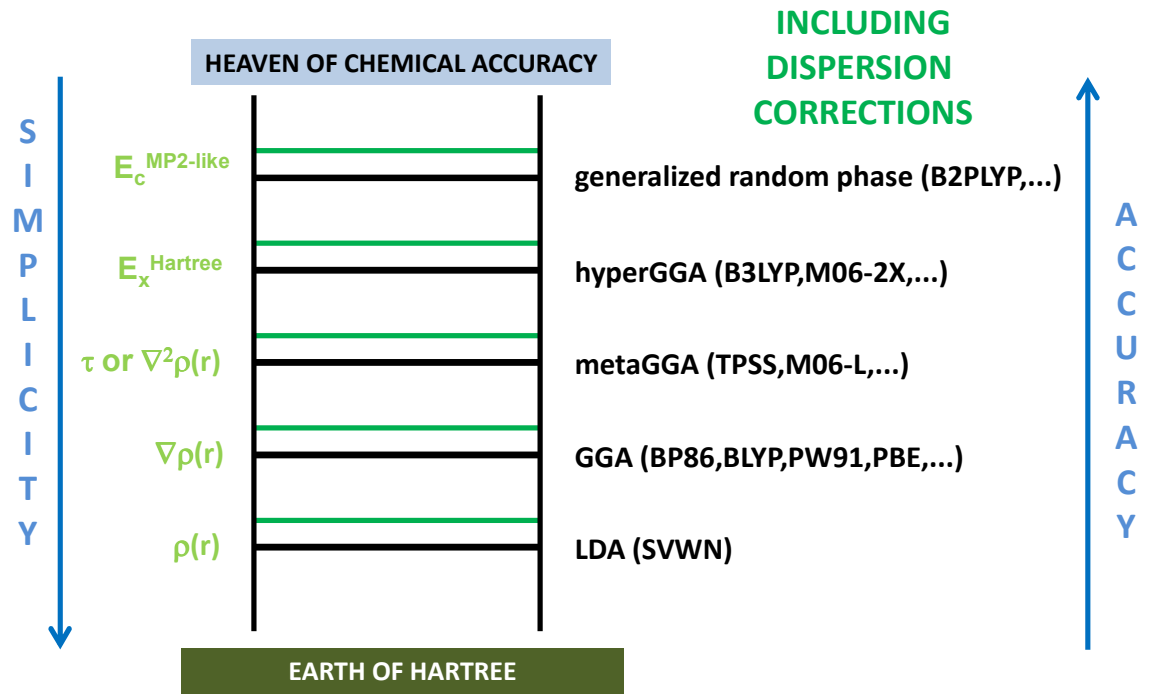

Figure 2.6. Jacob's ladder methodology for the systematic improvement of DFT functionals in agreement to the metaphor of Perdew and Schmidt,[53] showing some of the most common functionals within each step. Adapted from reference [54].

Therefore, if a DFT user climbs the ladder will get better accuracy at the expenses of a larges computational resources. Thus, for very accurate calculations, the DFT studies are limited to structural models of up to a few tens of atoms while standard DFT calculations (*c.f.* those using approaches at the bottom of the ladder) can tackle much larger systems that can reach up to hundreds or a few thousands of atoms, when using standard computational systems.

Two approaches can be considered to model extended surfaces (which is the case in this PhD Thesis): the so-called i) cluster model and ii) periodic slab model (*c.f.* sub-chapter 1.5).[55] The results for a cluster model are critically dependent on the choice of the cluster size, stoichiometry and shape. Thus, the choice of the cluster model to offer useful information

has to be explored *a priori* by checking the convergence of the results with the cluster. In the case of the periodic model approach, a small number of atoms (unit cell) is extended periodically, and more frequently, in the three spatial dimensions (XYZ) to simulate the characteristics of infinite systems (periodic boundary conditions). The infinite repetition eliminates the limitations affecting the cluster models, *i.e.*, the so-called border effects. In the periodic model approach, the computational cost is directly dependent on the number (size) and the symmetry of the elements in the unit cell. Bulk crystalline systems can be studied with the periodical repetition of just a few atomic positions, *e.g.* by using their primitive cells. The study of alloys, contaminants, or vacancies can be made by increasing the model and substituting or removing one or more atoms in the periodic system. In the methodologies repeating periodically in the three spatial dimensions a specific unit cell, the surfaces of the materials can be generated by using a unit cell consisting of several layers of the material (slab) and a vacuum region in the direction normal to the surface (Figure 2.7). This strategy has been considered to model an infinite wall of the PMO materials and to obtain atomic level information of their surface chemistry. Note, that for studying adsorption, the sizes of the slabs in the X and Y directions, assuming that the vacuum section is in the Z direction, are dependent on the volumes of the adsorbates and on the surface coverage, *i.e.*, larger unit cells have to be employed in the case of large adsorbates in order to avoid spurious adsorbate-adsorbate interactions with their images in the neighboring repeated cells. By playing with the sizes of the slabs in the X and Y directions it is possible to simulate easily the effects of surface coverage. Also, the vacuum region in the Z direction must be the smallest as possible to make the DFT computations feasible when plane-waves basis sets are employed since these will be filling the entire unit cell space. Vacuum regions of ≈ 10 Å were found to sufficient to study small adsorbates but larger regions are required to study larger adsorbates.

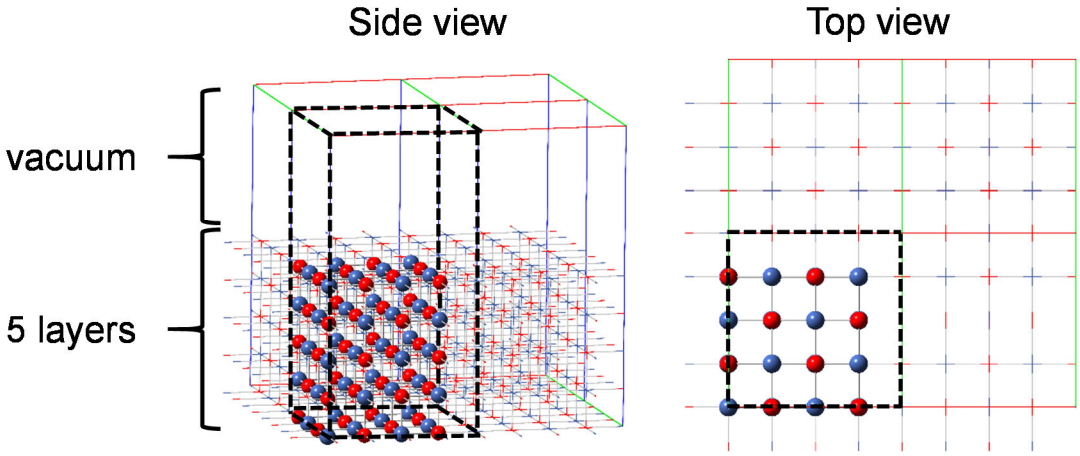

Figure 2.7. Example of a periodic unit cell (dashed line) that is appropriate to model a surface of a solid with NaCl structure. Adapted from reference [52].

Further details about the computational modelling of the bare surface of distinct PMO materials and of the interactions of CO_2 and CH_4 molecules with such PMO are provided in Sub-chapter 3.2.

2.8 Bibliography

1 D.B. Williams, C.B. Carter, Transmission electron microscopy, a textbook for materials science. 2nd Ed. New York: Springer, **2009**.

2 J. Goldstein, D.E. Newbury, D.C. Joy, C.E. Lyman, P. Echlin, E. Lifshin, L. Sawyer, J.R. Michael, Scanning electron microscopy and X-ray microanalysis. 3rd Ed. New York: K.A.P. Publishers, **2003**.

3 M.F. Toney, X-ray Diffraction. In: C.R. Brundle, C.A. Evans, S. Wilson (eds.). Encyclopedia of materials characterization. Butterworth-Heinemann: Boston, **1992**.

4 K.S.W. Sing, D.H. Everett, R.A.W. Haul, L. Moscou, R.A. Pierotti, J. Rouquerol, T. Siemieniewaska, Reporting physisorption data for gas/solid systems with special reference to the determination of surface area and porosity. *Pure Appl Chem*. **1985**, 57: 603–619.

5 M. Thommes, K. Kaneko, A. V. Neimark, J.P. Olivier, F. Rodriguez-Reinoso, J. Rouquerol, K.S.W. Sing, Physisorption of gases, with special reference to the evaluation of surface area and pore size distribution (IUPAC Technical Report). *Pure Appl Chem*. **2015**, 89: 1051–1069.

6 M.J. Duer, Introduction to solid-state NMR spectroscopy. Wiley-Blackwell, **2005**.

7 D.D. Laws, H.-M.L. Bitter, A. Jerschow, Solid-state NMR spectroscopic methods in chemistry. *Angew Chem*. **2002**, 41: 3096–3129.

8 C.P. Slichter, Principles of magnetic resonance in springer series in solid-state sciences, Vol. 1. 3rd Ed. Springer-Verlag Berlin Heidelberg, **1990**.

9 B. Stuart, Infrared spectroscopy: fundamentals and applications. John Wiley and Sons, Ltd, **2004**.

10 W. Kirmse, Organic elemental analysis: ultramicro, micro, and trace methods. Elsevier Inc., **1983**.

11 V.P. Fadeeva, V.D. Tikhova, O.N. Nikulicheva, Elemental analysis of organic compounds with the use of automated CHNS analyzers. *J Anal Chem*. **2008**, 63: 1094–1106.

12 C.R. Brundle, X-ray photoelectron spectroscopy. In: C.R. Brundle, C.A. Evans, S. Wilson (ed.). Encyclopedia of materials characterization. Boston: Butterworth-Heinemann, **1992**.

13 P.K. Gallacher, Handbook of thermal analysis and calorimetry. **1998**.

14 R.J.P. Corriu, J.J.E. Morea, P. Thepot, M.W. Chi Man, New mixed organic-inorganic polymers: hydrolysis and polycondensation of bis(trimethoxysilyl) organometallic precursors. *Chem Mater*. **1992**, 4: 1217–1224.

15 S. Inagaki, S. Guan, T. Ohsuna, O. Terasaki, An ordered mesoporous organosilica hybrid material with a crystal-like wall structure. *Nature*. **2002**, 416: 304–307.

16 S.J. Gregg, K.S.W. Sing, Adsorption, surface area and porosity. 2nd Ed. London and New York: Academic Press, **1982**.

17 S. Brunauer, P.H. Emmett, E. Teller, Adsorption of gases in multimolecular layers. *J Am Chem Soc*. **1938**, 60: 309–319.

18 E. R. Cohen, T. Cvitas, J.G. Frey, B. Holmström, K. Kuchitsu, R. Marquardt, I. Mills, F. Pavese, M. Quack, J. Stohner, A.J.T. Strauss, M. Takami, Quantities, units and symbols in physical chemistry. 3rd Ed. Cambridge, UK: RSC Publishing, **2007**.

19 M. Kruk, M. Jaroniec, A. Sayari, Application of large pore MCM-41 molecular sieves to improve pore size analysis using nitrogen adsorption measurements. *Langmuir*. **1997**, 13: 6267–6273.

20 M. Jaroniec, L.A. Solovyov, Improvement of the Kruk-Jaroniec-Sayari method for pore size analysis of ordered silicas with cylindrical mesopores. *Langmuir*. **2006**, 22: 6757–6760.

21 A. V. Neimark, Y. Lin, P.I. Ravikovitch, M. Thommes, Quenched solid density functional theory and pore size analysis of micro-mesoporous carbons. *Carbon*. **2009**, 47: 1617–1628.

22 M. Thommes, J. Morell, K.A. Cychosz, M. Fröba, Combining nitrogen, argon, and water adsorption for advanced characterization of ordered mesoporous carbons (CMKs) and periodic mesoporous organosilicas (PMOs). *Langmuir*. **2013**, 29: 14893–14902.

23 M. Jorge, M. Fischer, J.R.B. Gomes, C. Siquet, J.C. Santos, A.E. Rodrigues, Accurate model for predicting adsorption of olefins and paraffins on MOFs with open metal sites. *Ind Eng Chem Res*. **2014**, 53: 15475–15487.

24 A.L. Myers, Equation of state for adsorption of gases and their mixtures in porous materials. *Adsorption*. **2003**, 9: 9–16.

25 J. Pires, V.K. Saini, M.L. Pinto, Studies on selective adsorption of biogas components on pillared clays : approach for biogas improvement. *Environ Sci Technol*. **2008**, 42: 8727–8732.

26 E. Schrödinger, An undulatory theory of the mechanics of atoms and molecules. *Phys Rev*. **1926**, 28: 1049–1070.

27 M. Born, R. Oppenheimer, quantum theory of molecules. *Ann Phys*. **1927**, 84: 0457–0484.

28 W.J. Hehre, L. Radom, P.V.R. Schleyer, J.A. Pople, Ab initio molecular orbital theory. New York: John Wiley, **1986**.

29 F. Jensen, Introduction to computational chemistry. 1st Ed. Chichester, England: John Wiley and Sons, **2004**.

30 Kohn, W.; Sham, L.J. Self-consistent equations including exchange and correlation effects. *Phys Rev*. **1965**, 140: A1133–A1138.

31 P.A.M. Dirac, Note on exchange phenomena in the thomas atom. *P Camb Philos Soc*. **1930**, 26: 376–385.

32 J.C. Slater, A simplification of the Hartree-Fock method. *Phys Rev*. **1951**, 81: 385–390.

33 A.D. Becke, Density functional calculations of molecular-bond energies. *J Chem Phys*. **1986**, 84: 4524–4529.

34 A.D. Becke, Density-functional exchange-energy approximation with correct asymptotic-behavior. *Phys Rev A*. **1988**, 38: 3098–3100.

35 J.P. Perdew, Y. Wang, Accurate and simple Density functional for the electronic exchange energy – generalized gradient approximation. *Phys Rev B*. **1986**, 33: 8800–8802.

36 J.P. Perdew, Density-functional approximation for the correlation-energy of the inhomogeneous electron-gas. *Phys Rev B*. **1986**, 33: 8822–8824.

37 J.P. Perdew, Correction. *Phys Rev B*. **1986**, 34: 7406–7406.

38 C.T. Lee, W.T. Yang, R.G. Parr, Development of colle-salvetti correlation-energy formula into a functional of the electron-density. *Phys Rev B*. **1988**, 37: 785–789.

39 J.P. Perdew, K. Burke, M. Ernzerhof, Generalized gradient approximation made simple. *Phys Rev Lett*. **1996**, 77: 3865–3868.

40 B. Hammer, L.B. Hansen, J.K. Nørskov, Improved adsorption energetics within density-functional theory using revised Perdew-Burke-Ernzerhof functionals. *Phys Rev B*. **1999**, 59: 7413–7421.

41 A.D. Becke, Density-functional thermochemistry. III. The role of exact exchange. *J Chem Phys*. **1993**, 98: 5648–5652.

42 J. Sauer, Molecular-models in ab initio studies of solids and surfaces - from ionic-crystals and semiconductors to catalysts. *Chem Rev*. **1989**, 89: 199–255.

43 N.W. Ashcroft, N.D. Mermin, Solid state physics. Philadelphia, Holt-Saunders, **1976**.

44 D.R. Hamann, M. Schluter, C. Chiang, Norm-conserving pseudopotentials. *Phys Rev Lett*. **1979**, 43: 1494–1797.

45 J.P. Perdew, J.A. Chevary, S.H. Vosko, K.A. Jackson, M.R. Pederson, D.J. Singh, C. Fiolhais, Atoms, molecules, solids, and surfaces - applications of the generalized gradient approximation for exchange and correlation. *Phys Rev B*. **1992**, 46: 6671–6687.

46 R. Armiento, A.E. Mattsson, Functional designed to include surface effects in self-consistent density functional theory. *Phys Rev B*. **2005**, 72: 085108–1:13.

47 J.B. Krieger, J. Chen, G.J. Iafrate, A. Savin, In electron correlations and materials properties. New York: Plenum, **1999**.

48 G.Y. Sun, J. Kurti, P. Rajczy, M. Kertesz, J. Hafner, G. Kresse, Performance of the Vienna ab initio simulation package (VASP) in chemical applications. *J Mol Struct*. **2003**, 624: 37–45.

49 J.M. Tao, J.P. Perdew, V.N. Staroverov, G.E. Scuseria, Climbing the density functional ladder: nonempirical meta-generalized gradient approximation designed for molecules and solids. *Phys Rev Lett*. **2003**, 91: 146401–1:4.

50 S. Grimme, J. Antony, S. Ehrlich, H. Krieg, A consistent and accurate ab initio parametrization of density functional dispersion correction (DFT-D) for the 94 elements H-Pu. *J Chem Phys*. **2010**, 132: 154104–1:19.

51 F. London, The general Theory of Molecular Forces. *Trans Faraday Soc*. **1937**, 33: 8–26.

52 J.P.P. Ramalho, J.R.B. Gomes, F. Illas, Accounting for van der Waals interactions between adsorbates and surfaces in density functional theory based calculations: selected examples. *RSC Adv*. **2013**, 3: 13085–13100.

53 J.P. Perdew, K. Schmidt, Jacob's ladder of density functional approximations for the exchange-correlation energy. In: AIP Conf. Proc. **2001**: 1–20

54 J.R.B. Gomes, J.L.C. Fajín, M.N.D.S. Cordeiro, C. Teixeira, P. Gomes, R.S. Pillai, G. Novell-Leruth, J. Toda, M. Jorge, Density functional treatment of interactions and chemical reactions at interfaces. In: J. Maurin, J.M. Pelletier (eds.). Density functional theory: principles, applications and analysis. New York: Nova Science Publishers, Inc., **2013**: 1–58.

55 H. Hellmann, A New Approximation method in the problem of many electrons. *J Chem Phys*. **1935**, 3: 61–61.

Chapter 3– Amine modified PMOs for CO_2/CH_4 separation

This Chapter describes the preparation of PMOs with different pore sizes; their modification with different kinds of amines (aromatic and alkyl amines); and the evaluation of the synthetized materials in the adsorption of pure CO_2 and CH_4. Additionally, DFT calculations were used to assess the preferential locations of the CO_2 and CH_4 molecules into the materials; to interpret some of the experimental results; and to understand which functionalization brings improvements in the CO_2/CH_4 separation.

3.1 Insights into CO_2 and CH_4 adsorption by pristine and aromatic amine-modified periodic mesoporous phenylene-silicas

Adapted from:

Mirtha A. O. Lourenço, Christophe Siquet, João Santos, Miguel Jorge, José R. B. Gomes and Paula Ferreira

Insights into CO_2 and CH_4 adsorption by pristine and aromatic amine-modified periodic mesoporous phenylene-silicas

J. Phys. Chem. C, **2016**, 120: 14236−14245

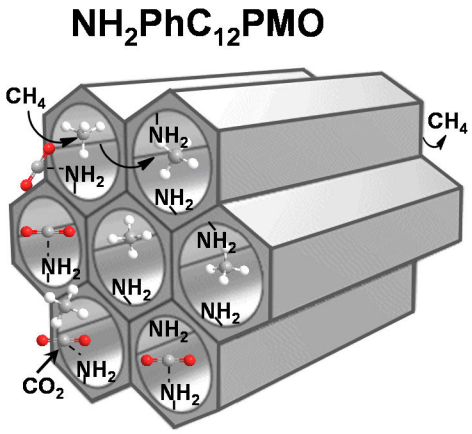

My direct contribution:

I declare that I have prepared, functionalized and characterized all the PMO described in this Sub-chapter. I have also performed all the density functional theory calculations. The experimental adsorption studies using a manometric apparatus were performed by Christophe Siquet, João Santos and Miguel Jorge at the University of Porto.

3.1.1 Motivation

As it was seen in Sub-chapter 1.2 the biogas is a renewable energy source that is composed mainly by methane but presents also a large amount of carbon dioxide as the main contaminant. It was also demonstrated the needs of removal CO_2 from CH_4 and the drawbacks associated to the systems that are being employed to separate these gases. Therefore, an energy efficient process to uptake the CO_2 contaminant from CH_4 is required for the wide application of biogas with the purpose of increasing the purity of the gaseous stream. It is well known that the adsorption process is a very attractive technique for small to medium-scale operations, but it relies on the availability of highly effective adsorbent materials.

The development of adsorbents to uptake the CO_2 gas from biogas *via* adsorptive separation involves the preparation of materials with different nature and structure.[1] Various mesoporous and microporous adsorbents (carbons[2–6], MOFs[2,7,8], zeolites[2,9–13], clays[14,15], and silica-based mesoporous materials[16,17]) have been proposed for CO_2 adsorption/separation from biogas as it was demonstrated in Sub-chapter 1.2. Although, these adsorbents are still not ideal for CO_2 uptake from biogas mainly due to their unsatisfactory performances. Thus, the ideal adsorbent is still undiscovered and, in an attempt to achieve a material with better ability to uptake CO_2 from biogas, it is explored the possibility of applying periodic mesoporous phenylene-silicas (PMOs)[18–20] as adsorbents for CO_2/CH_4 gas separation. The interest to use PMOs as adsorbents in this field relies in the assumption that these materials possess high specific surface areas, high pore volumes and are easy to be modified as it was possible to observe in Sub-chapter 1.4.[18–24] Additionally, PMOs also have the advantages of exhibiting meso- and molecular-scale periodicities that can promote a good diffusion of the molecules (adsorbates but also the reagents required to modify the PMOs) within the channels of the PMO because of the increased organization of the pores and of the presence of the organic functions (such as ethylene, phenylene, biphenylene, etc.) that are well integrated in the walls of this class of materials. Moreover, the molecular-scale periodicity resulting from the alternating organic-inorganic groups along the pore wall, assigns alternating hydrophobic-hydrophilic character. Furthermore, it is possible to control the porosity of the PMOs using the template-assisted self-assembly method.[18–24] All of the features above increase the attractiveness of PMOs as potential adsorbents for CO_2/CH_4 adsorption/separation. Recently, alkyl amine functionalities (more

specifically the *N*-[3-(trimethoxysilyl)propyl]-ethylenediamine) grafted on the silanols of phenylene-bridged PMO and of SBA-15 were tested in the adsorption of pure CO_2 at 25 °C in a pressure range up to 1.2 atm.[25] It was observed that the alkyl amine-PMO adsorbs a larger amount of CO_2 at a faster adsorption rate when compared with SBA-15, which demonstrates that the functionalization of PMOs with amines is more relevant than a similar degree and nature of functionalization in silica for the adsorption of CO_2. Interestingly, the unmodified SBA-15 silica also adsorbs a smaller amount of CO_2 when compared with the unmodified PMO. This behavior was explained by the higher hydrophobicity of the PMO pore wall when compared with that of SBA-15. Hence, water adsorption is expected to be more acute in SBA-15 than in PMO materials, competing more with CO_2 for available adsorption sites on the former class of materials, so, organosilica instead of pure silica supports were proposed for immobilization of amines groups aiming materials for CO_2 adsorption/separation.[25] Despite the fact that PMOs are more expensive than silica, the superior ability of amine modified PMOs to adsorb CO_2 can be transferred and should be explored for these applications.

Here, it is considered the phenylene-bridged PMOs as potential candidates for the CO_2/CH_4 separation. In this way, phenylene-bridged PMO with different pore sizes were prepared by changing the alkyl chain length of the cationic surfactant[26] since the pore size and pore curvature may play an important role on the diffusion of the reagents or gas molecules inside the pores. Additionally, the amount of amine functionalities into the materials, their locations and the type of silanols are certainly important variables on the adsorptive properties of these materials. So, after the synthesis of the PMOs, the mono-nitration of the phenylene bridges was performed with nitric acid in the presence of sulfuric acid. Then, the nitro group was reduced to the amine in the presence of tin chloride and hydrochloric acid.[27] To the best of our knowledge, the amination of the phenylene bridge in the PhC_nPMOs with $n < 18$, was not attempted before. Hence it is described for the first time the synthesis and characterization of aromatic amine-funtionalized PMOs with pore sizes ranging from 2.4 and 3.7 nm. All materials are tested on the CO_2 and CH_4 adsorption. The physicochemical characterization is performed to fully understand the potential of these materials for CO_2/CH_4 separation.

3.1.2 Experimental section

Materials synthesis

PhC$_n$PMO adsorbents preparation: phenylene-bridged PMOs with different pore sizes (hereafter denoted PhC$_n$PMOs, n = 12, 14, 16 or 18) were prepared following procedures previously described in literature,[27,28] with slight modification in the amount of NaOH and surfactant used (*c.f.* Table 3.1.1). The home-made 1,4-bis(triethoxysilyl)benzene (BTEB, *c.f.* Chapter 2.1) precursor[29] is hydrolyzed and condensed around a surfactant, the C$_n$-trimethylammonium bromide template (C$_n$-TMA, n =12, 14, 16 or 18), Figure 3.1.1.

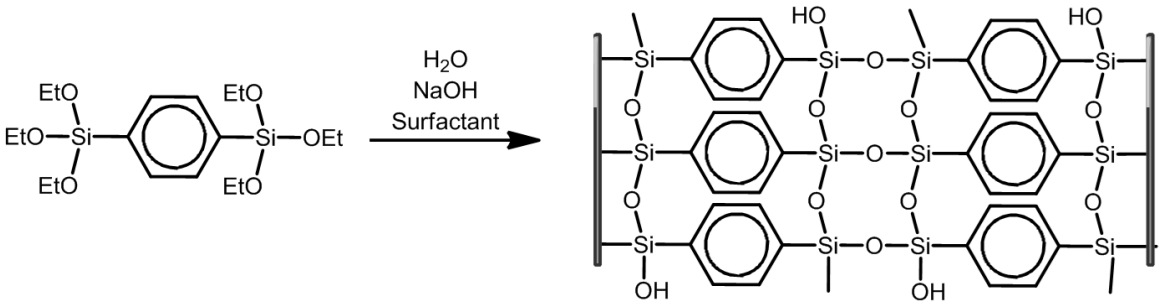

Figure 3.1.1. Synthesis route for PhC$_n$PMOs, n = 12, 14, 16 and 18, prepared with C$_{12}$-TMA, C$_{14}$-TMA, C$_{16}$-TMA and C$_{18}$-TMA surfactants, respectively.

In a typical synthesis of the PhC$_n$PMO materials, the surfactant is dissolved in a mixture of distilled water and 6 M aqueous sodium hydroxide at 20 – 60 °C. BTEB was subsequently added dropwise under vigorous stirring, at room temperature. The molar ratio BTEB: water is always constant and equal to 1 : 531 (molar ratio corresponding only to the distilled water), with the quantities of surfactant and NaOH adjusted according to the surfactant used (*c.f.* Table 3.1.1).

Table 3.1.1. Molar ratio of the surfactant and NaOH for each PhC$_n$PMO in relation to the BTEB precursor.

	PhC$_{18}$PMO	**PhC$_{16}$PMO**	**PhC$_{14}$PMO**	**PhC$_{12}$PMO**
Surfactant	0.96	1	1.05	1.4
NaOH	4.05	3.85	3.65	3.04

The mixture was kept for 20 minutes in an ultrasonic bath (Bransonic ultrasonic cleaner 1510E-DTH). The reaction mixture was stirred for 24 hours at room temperature, and was then transferred into a Teflon lined autoclave for additional 24 hours at 100 °C. The final precipitate was recovered by filtration, washed with warm distilled water and dried at 60 °C.

To obtain porous PMO materials, the surfactants were removed through solvent extraction.[18–20,26,28] An aliquot of 0.5 g of the as-synthesized powder was stirred in a solution of 4.5 g of 37% HCl and 125 mL ethanol, for 8 hours at 80 °C. The powder was filtered off, washed with ethanol and water and dried overnight at 60 °C. The confirmation of the template removal was made through ^{13}C NMR spectroscopy and TGA analysis.

NH_2PhC_nPMO adsorbents preparation: the amine phenylene-modifications (to prepare NH_2PhC_nPMO, n =12, 14, 16 or 18) were made using the same two-step procedure reported by Inagaki *et al*.[27] First a strong acid treatment with HNO_3/H_2SO_4 was used to incorporate the nitro groups into the phenylene moieties of PMO followed by treatment with $SnCl_2$/HCl to reduce the nitro groups to the desired amine functionalities (Figure 3.1.2).

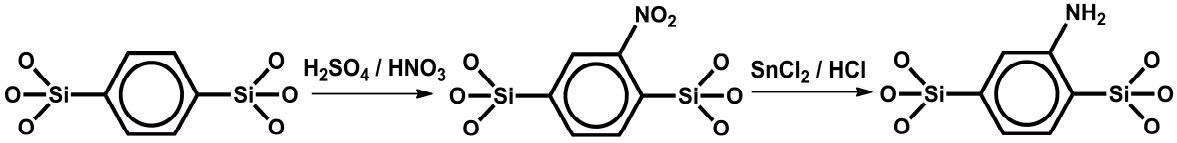

Figure 3.1.2. Synthesis route for the amine functionalization of the PhC_nPMOs, n=12, 14, 16 and 18.

Materials characterization

All PMO materials were evaluated by PXRD, -196 °C N_2-sorption isotherms and TEM. The chemical properties of the materials were evaluated by elemental analysis, ^{13}C, ^{15}N and ^{29}Si NMR and FTIR spectroscopies. The thermal stability was evaluated by TGA. The N_2-sorption isotherms, TEM, ^{13}C CP-MAS NMR, FTIR, TGA, EA and CO_2 and CH_4 adsorption data are available in the Appendix A.

Adsorption measurement procedure

Adsorption isotherms of carbon dioxide and methane were measured on as-synthesized and amine-modified PMO materials, at 308 K and pressures up to 2 bar, using an in-house built manometric apparatus, using the procedure described in Sub-chapter 2.6.

Each experimental pure component adsorption isotherm was fitted to a Langmuir model. The fitting parameters were then used to calculate the Henry's constant of adsorption (K_H, in $mmol \cdot g^{-1} \cdot bar^{-1}$) for each gas and each adsorbent by taking the slope of the isotherm in the limit of zero coverage. The Henry constant thus measures the affinity of each gas toward the solid surface. The Langmuir equation is expressed in Equation 3.1.1:

$$q = \frac{qs \times b \times P}{1 + b \times P} \qquad \text{(Equation 3.1.1)}$$

where q is the amount adsorbed, q_S is the Langmuir saturation capacity, b is the Langmuir surface affinity parameter and P is the pressure.

We then estimated the low-coverage CO_2 selectivity (S) of each material by taking the ratio of the Henry's constants for the two gases (Equation 3.1.2):

$$S^{CO_2/CH_4} = \frac{K_H^{CO_2}}{K_H^{CH_4}} = \frac{q_s^{CO_2} \times b^{CO_2}}{q_s^{CH_4} \times b^{CH_4}} \qquad \text{(Equation 3.1.2)}$$

3.1.3 Results and discussion

Characterization of materials

The structural order of the non-modified samples was studied by PXRD. Figure 3.1.3a shows the PXRD patterns of surfactant-free $PhC_{12}PMO$, $PhC_{14}PMO$, $PhC_{16}PMO$ and $PhC_{18}PMO$ samples. The patterns are in agreement with those reported in previous studies,[26,28] being compatible with a two-dimensional hexagonal symmetry (*p6mm*) lattice. The *d* spacing of the strong low-angle (100) reflection changes slightly from sample to sample. The lattice parameters, *a,* calculated from the 2θ values of the (100) peaks for the surfactant-free $PhC_{12}PMO$, $PhC_{14}PMO$, $PhC_{16}PMO$ and $PhC_{18}PMO$ materials are 4.14; 4.32; 4.76; and 5.36 nm, respectively (Table 3.1.2). The increase of the lattice parameters results in larger pore sizes (Figure 3.1.3d) as a function of the alkyl-tail lengths. The evidence for the hexagonal arrangement of the pores is obtained from the presence of the tiny (110) and (200) low-angle reflections observed in Figure 3.1.3a.[26,28] In addition to the low-angle peaks, the PXRD patterns display medium-range reflection at $d \sim 0.76$ nm, due to molecular-scale periodicity in the PMO pore walls along the channel direction.[28]

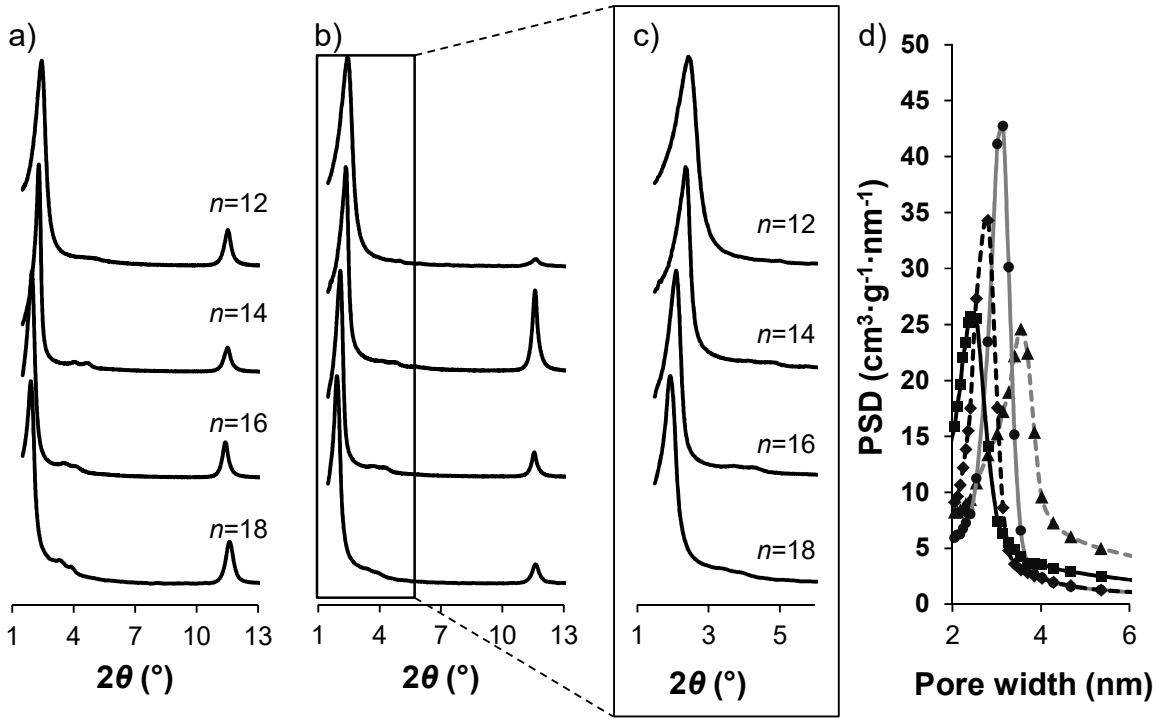

Figure 3.1.3. PXRD patterns of the: a) PhC_nPMOs; b) and c) NH_2PhC_nPMOs. Pore size distribution profiles (d) calculated from the N_2 adsorption isotherm for $NH_2PhC_{12}PMO$ (squares, black line); $NH_2PhC_{14}PMO$ (rhombus, black dashed line); $NH_2PhC_{16}PMO$ (circles, grey line); and $NH_2PhC_{18}PMO$ (triangles, grey dashed line).

The four different samples display these peaks at exactly the same *d* spacing, which is in agreement with Bion *et al.*[26] Thus, the non-modified PMOs materials exhibit molecular-scale periodicity in the walls and, in addition, have different pore sizes. The structural order of the aminated samples was studied by PXRD and N_2 adsorption–desorption isotherms. Figure 3.1.3b and c shows the PXRD patterns of NH_2PhC_nPMO materials. As in the simple PMOs, the first strong low-angle (100) reflection peak associated to the (110) and (200) small reflections are characteristic of a two-dimensional hexagonal symmetry (*p6mm*) lattice, Figures 3.1.3b and c. Thus, the hexagonal arrangement is maintained upon amination. The *d* spacings in the aminated samples are similar to the *d* spacings of the pristine PMOs. The lattice parameters, *a*, of the hexagonal array of mesopores obtained for the $NH_2PhC_{12}PMO$, $NH_2PhC_{14}PMO$, $NH_2PhC_{16}PMO$ and $NH_2PhC_{18}PMO$ materials are 4.19, 4.37, 4.88 and 5.34 nm, respectively, which means that the presence of the amino group does not significantly change those values relatively to the pristine materials (Table 3.1.2). In addition to the low-angle peaks, the PXRD patterns of all aminated samples display medium-range reflections at $d \sim 0.760 \pm 0.002$ nm, which are identical to those of the initial PMO

materials, implying that amination also did not significantly change the molecular-scale periodicity of the pore walls.

Table 3.1.2. Structural properties of PhC_nPMOs and NH_2PhC_nPMOs materials. Pore parameters obtained from X-ray diffraction patterns and nitrogen sorption data.

Sample	d_{100} (nm)	a^a (nm)	S_{BET} ($m^2 \cdot g^{-1}$)	V_P ($cm^3 \cdot g^{-1}$)	$d_P{}^b$ (nm)	b^c (nm)
$PhC_{12}PMO$	3.59	4.14	1004	0.14	2.54	1.60
$NH_2PhC_{12}PMO$	3.63	4.19	924	0.23	2.41	1.78
$PhC_{14}PMO$	3.74	4.32	843	0.24	2.80	1.52
$NH_2PhC_{14}PMO$	3.79	4.37	778	0.16	2.80	1.57
$PhC_{16}PMO$	4.12	4.76	832	0.45	3.14	1.62
$NH_2PhC_{16}PMO$	4.22	4.88	623	0.33	3.14	1.74
$PhC_{18}PMO$	4.65	5.36	782	0.68	3.70	1.66
$NH_2PhC_{18}PMO$	4.62	5.34	719	0.55	3.54	1.80

[a]Unit cell parameter calculated as($2d_{100}/\sqrt{3}$). [b]Pore width obtained from the BJH method with the corrected Kelvin equation, *i.e.* KJS–BJH method at the maximum of pore size distribution calculated on the basis of adsorption data. [c]Pore wall thickness calculated as ($2d_{100}/\sqrt{3}$ - d_P), where the first term is the unit cell parameter.

The presence of different mesopore sizes was confirmed by low temperature (-196 °C) N_2 adsorption–desorption experiments. In Figure A1.3 (Appendix A), the samples display a type IV isotherm (IUPAC classification), usually observed for conventional mesoporous materials such as MCM-41, indicating mesopores of uniform size. The introduction of the amine into the mesochannels is confirmed by the reduction of the BET specific surface area (S_{BET}). The $NH_2PhC_{12}PMO$, $NH_2PhC_{14}PMO$, $NH_2PhC_{16}PMO$ and $NH_2PhC_{18}PMO$ materials present S_{BET} of 924, 778, 623 and 719 $m^2 \cdot g^{-1}$, respectively (Table 3.1.2). A comparison of the pore size distribution (PSD) curves of $NH_2PhC_{12}PMO$, $NH_2PhC_{14}PMO$, $NH_2PhC_{16}PMO$ and $NH_2PhC_{18}PMO$ materials reveals a maximum shifting from 2.4 to 3.5 nm (Figure 3.1.3d and Table 3.1.2), respectively.

TEM images (Figure A1.4a, Appendix A) reveal the high order along the channels for the $NH_2PhC_{18}PMO$, $NH_2PhC_{16}PMO$, $NH_2PhC_{14}PMO$ and $NH_2PhC_{12}PMO$. Figure A1.4b (Appendix A) shows the TEM image in the direction parallel to the channels of the $NH_2PhC_{16}PMO$, supporting the hexagonal arrangement of the pores observed by PXRD and confirming the high order of these materials.

Solid-state ^{13}C CP-MAS NMR and ^{29}Si CP-MAS NMR spectra of PhC_nPMO and NH_2PhC_nPMO materials are shown in Figures A1.5 (Appendix A) and Figure 3.1.4, respectively. Solid-state ^{13}C CP-MAS NMR spectra support the amination of PhC_nPMOs materials. The pristine materials present a typical resonance at 133 ppm of the aromatic carbons as reported in the literature.[28] Tiny peaks can be detected in the region 0 to 50 ppm

in the spectra of $PhC_{18}PMO$ sample, which are associated to the residual presence of non-extracted template molecules. These resonances are not observed in the spectra of the other PhC_nPMOs. The ^{13}C CP-MAS NMR spectra of NH_2PhC_nPMO materials exhibit resonances at *ca*. 122, 133 and 150 ppm assigned to the sp^2 carbons of the phenylene ring. These values are in agreement with the results previously reported for the $NH_2PhC_{18}PMO$.[27] The ^{29}Si CP-MAS NMR spectra of the PhC_nPMO and NH_2PhC_nPMO exhibit peaks at *ca.* -81, -70 and -61 ppm attributed to T^3, T^2 and T^1 organosiliceous species [$T^m = RSi(OSi)_m(OH)_{3-m}$], respectively, which are illustrated in Figure 3.1.4.

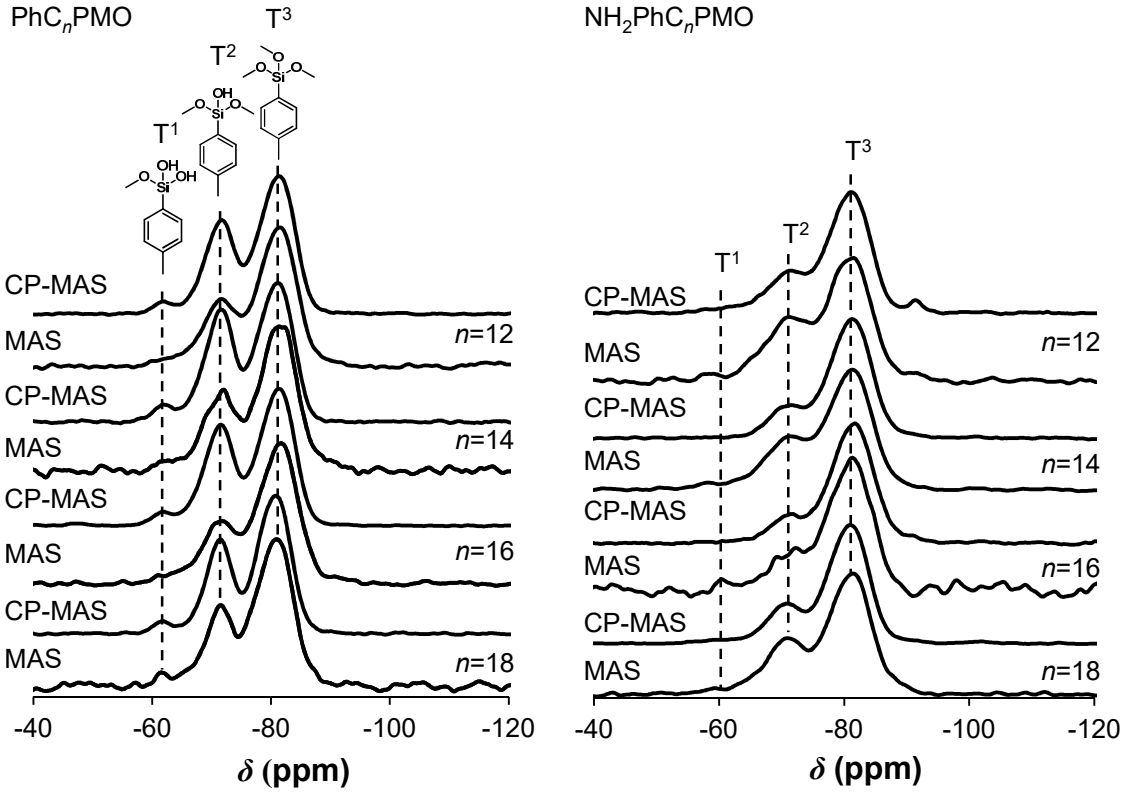

Figure 3.1.4. ^{29}Si CP-MAS and MAS NMR spectra of PhC_nPMOs and NH_2PhC_nPMO. The observed resonances are assigned to the corresponding T^m silanols species in the PMO materials.

The percentages of T^m species in each material are calculated from the deconvolution of the ^{29}Si MAS NMR spectra, using the typical assumption of Gaussian distributions of isotropic chemical shifts for each type of T^m species and are presented in Table A1.1. Generally, the overlapping of T^m resonances is observed, giving rise to small variations between best-fit intensity parameters and, hence, to uncertainties related with the relative populations of the T^m sites. The degree of condensation varies between 66 and 71 % for the PhC_nPMOs and between 66 and 74 % for the NH_2PhC_nPMO materials. No peaks assigned to

Q^n [Q^n = $Si(OSi)_n(OH)_{4-n}$] species were observed, proving that no carbon–silicon bond cleavage occurred during the amination of the PMO materials.

The ^{15}N NMR spectra of the NH_2PhC_nPMO materials (not shown) display in all cases only a single peak corresponding to the aromatic amine at -325 ppm as observed before for $NH_2PhC_{18}PMO$ (Sub-chapter 5.1) and $NH_2PhC_{12}PMO$ (Sub-chapter 3.2). The success of the amination of the phenylene moieties in the PMOs was also verified by Fourier infrared transform (FTIR) spectroscopy, Figure A1.6 (Appendix A).

Figure A1.7 (Appendix A) presents the TGA analysis of the pristine and amine modified PhC_nPMOs. The first weight loss observed below 100 °C is related to desorption of physisorbed water. No weight loss from 100 to 300 °C, which is due to the small quantity of remained surfactant, was detected for pure PMOs with exception of $PhC_{18}PMO$ (2% weight loss), confirming the ^{13}C CP-MAS NMR results. The decomposition and release of the organic moieties from the framework takes place above 600 °C in the parent PhC_nPMOs. The introduction of the amino groups in the PMOs leads to a reduction of thermal stability from 600 to 400 °C for all NH_2PhC_nPMOs as observed by TGA, Figure A1.7 (Appendix A). Table A1.2 (Appendix A) displays the density of the amino group linked to the phenylene moieties into the PMOs materials. The PMO with the smallest pore size presents the lowest density of NH_2 groups. This probably occurs as a consequence of steric hindrance during the functionalization.

Experimental pure-component adsorption isotherms

Pure-component adsorption isotherms of CO_2 and CH_4 at 35 °C on the $PhC_{12}PMOs$, shown in terms of absolute amount adsorbed per unit mass of adsorbent (q), are displayed in Figure 3.1.5. The introduction of the amino group into the channels of the $PhC_{12}PMO$ leads to an increase in the adsorption of CO_2 (uppermost curves in Figure 3.1.5). Additionally, the adsorption of methane in the $NH_2PhC_{12}PMO$ is slightly lower than in the as-synthesized material (lowermost curves in Figure 3.1.5).

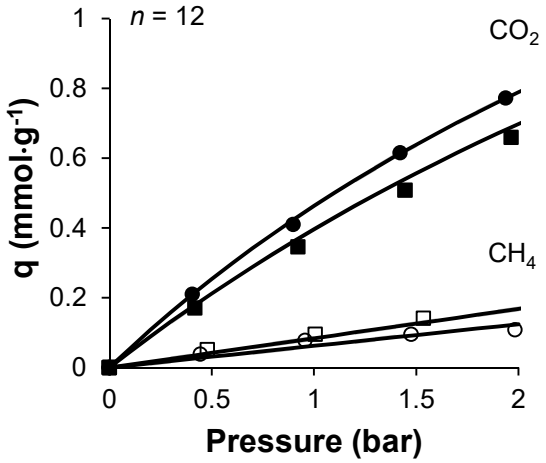

Figure 3.1.5. Adsorption equilibrium isotherms of pure CO_2 (closed symbols) and CH_4 (open symbols) molecules in the as-synthesized (squares) and amine functionalized (spheres) $PhC_{12}PMOs$. Solid lines represent the fits to Langmuir model.

Table 3.1.3 depicted the calculated Henry's constants of adsorption for pure CO_2 and CH_4 molecules in the pristine and amine functionalized PhC_nPMOs adsorbents. Considering the low CH_4 adsorption values obtained for all prepared PMOs, it is possible to generalize that these materials are weak CH_4 adsorbents. Additionally, the amination in the $PhC_{12}PMO$ provides an improvement in the adsorption of the material. It should be emphasized that this evidence is not observed for all PhC_nPMOs. The amination of the PhC_nPMOs is favoring the adsorption of CO_2 in the case of the materials with the smallest pores such as $NH_2PhC_{12}PMO$ and $NH_2PhC_{14}PMO$ (Figure 3.1.5, Figure A1.8 and Table 3.1.3), while an opposite effect is observed in the materials with the largest pore sizes (*c.f.* $NH_2PhC_{16}PMO$ and $NH_2PhC_{18}PMO$). A systematic analysis of the features of these materials is necessary to understand other reasons besides pore size and BET surface area factors that may be influencing the adsorption profiles recorded in this work.

The Henry's constants of $PhC_{18}PMO$, $PhC_{16}PMO$, Ph $C_{14}PMO$ and $PhC_{12}PMO$ for CO_2 are 0.40, 0.48, 0.41 and 0.46 $mmol \cdot g^{-1} \cdot bar^{-1}$ respectively (Table 3.1.3). As it can be seen, these values seem to be fairly independent of the pore size. Although the size of the pores can influence the distance between functional groups and, consequently, the Henry's constants, it is often observed that in materials with large pores, low-coverage adsorption is dominated by surface chemistry. As such, the variation of K_H may be related with the concentration of silanols (T^1 and T^2 species, Figure 3.1.4), phenylene density and nitrogen density (in the case of the amine functionalized PhC_nPMOs) of each material. The quantification of these

characteristics for each material considered in this work is displayed in Table 3.1.3. The percentages of nitrogen and carbon were taken directly from elemental analyses. The percentage of silanol species was calculated from ^{29}Si MAS NMR by deconvolution of the T^1 and T^2 species in the NMR spectrum of each material (denoted as T^1_{NMR} and T^2_{NMR}, Table A1.1, Appendix A). As the percentages of siliceous and of oxygen species vary from sample to sample, the T^m siliceous species percentages were converted to the percentages of T^m siliceous species present in the sample (denoted here as T^1_{SMP} and T^2_{SMP}) by combining the NMR results with the elemental analysis data. It is hypothesized that the CO_2 molecules interact more favorably with the T^1 and T^2 siliceous species in each sample. Therefore, the total percentage of siliceous species (denoted here as %Si-O) of each material (Table A1.2, Appendix A) was calculated using the following Equation 3.1.3:

$$\%\text{Si-O} = \%\text{Si} + \%\text{O} = 100\% - (\%\text{N} + \%\text{C} + \%\text{H}) \qquad \text{(Equation 3.1.3)}$$

Table 3.1.3. Comparison of structural and chemical properties of the as-synthesized and amine functionalized PhC_nPMOs adsorbents with experimental Henry's constants of pure CO_2 and CH_4 adsorption, and the equilibrium selectivity.

PMO	d_P[a] (nm)	%N[b]	%C[b]	$\%T^1_{SMP}$[c]	$\%T^2_{SMP}$[c]	$K_H^{CO2,d}$ (mmol·g^{-1}·bar^{-1})	$K_H^{CH4,d}$ (mmol·g^{-1}·bar^{-1})	S[e]
$PhC_{18}PMO$	3.70	-	38.39	1.17	15.99	0.400	0.074	5.40
$NH_2PhC_{18}PMO$	3.54	3.03	35.81	1.32	15.51	0.341	0.070	4.89
$PhC_{16}PMO$	3.14	-	36.38	0.96	19.26	0.478	0.076	6.26
$NH_2PhC_{16}PMO$	3.14	3.16	32.12	1.14	14.86	0.416	0.078	5.31
$PhC_{14}PMO$	2.80	-	38.56	1.41	18.43	0.414	0.083	4.98
$NH_2PhC_{14}PMO$	2.80	2.89	31.29	1.28	17.20	0.470	0.086	5.49
$PhC_{12}PMO$	2.54	-	37.21	1.22	18.92	0.457	0.084	5.43
$NH_2PhC_{12}PMO$	2.41	2.58	31.57	0.77	20.61	0.560	0.062	8.97

[a]Pore width obtained from the BJH method with the corrected Kelvin equation, *i.e.* KJS–BJH method at the maximum of pore size distribution calculated on the basis of adsorption data. [b]Obtained directly from elemental analyses. Note that the percentage of carbon can be also calculated for clean non-functionalized phenylene-PMO as exemplified in the footnote of Table A1.2. [c]Calculated from the ^{29}Si MAS NMR by deconvolution of the T^1 and T^2 species in the spectrum of each material. This percentage was converted to the percentage in the sample through the use of elemental analysis. [d]Henry's constants of adsorption, determined from fitting the experimental adsorption data to the Langmuir isotherm model; [e]Low-coverage adsorption selectivity for CO_2, estimated from the ratio of the pure component Henry's constants shown in the previous two columns.

The %Si-O, %N, %C and %H represent the sum of the percentages of silicon and oxygen, nitrogen, carbon and hydrogen, respectively, of each material, and are obtained from elemental analyses. Then, the percentage of T^m_{NMR} species was multiplied by the percentage of Si-O to obtain $\%T^m_{SMP}$. The evident correlation between the percentage of T^m species in each sample and the corresponding K_H^{CO2} values supports the hypothesis raised above.

The analysis of the data in Table 3.1.3 shows that the presence of T^2 silanol species in the PMO is correlated with the amount of adsorbed CO_2, *i.e.*, in general the K_H^{CO2} augments with the increase of $\%T^2_{SMP}$.

This observation is consistent with a picture that the presence of ^{29}Si T^2 silanol species in the PMO brings a positive effect on the adsorption of CO_2 by creating hydrogen bonds with the acidic CO_2. Curiously, K_H^{CO2} reduces with the increase of the percentage of the silanediol species, *i.e.*, with the amount of silanols with T^1 environments (*c.f.* Figure 3.1.4). This suggests that when two hydroxyl groups are linked to the same silicon atom, they are very probably establishing intramolecular bonds of the type O–H···O,[31] hence, less Si–O–H moieties are available to interact with CO_2. As the T^1 species content in the different PMO is inversely proportional to the T^2 species content (*c.f.* Table A1.1, 1st and 2nd column), the amount of adsorbed CO_2 by each PMO is influenced mainly by the number of basic T^2 silanol species. The correlation between the percentage of T^2_{SMP} silanol on each sample and the Henry constants is presented in Figure A1.9a.

The CO_2 molecules can also interact with the organic moieties but such interaction is expected to be much weaker than that with the silanol species. In fact, Martinez *et al.*[32] found through density functional theory (DFT) calculations that the adsorption energy between CO_2 and silanols with the T^2 environment was twice that occurring between CO_2 and the organic bridges. Preliminary DFT calculations (PBE-D2 level of theory) employing a computational recipe and a PMO model similar to those used by Martinez *et al*.[32] show that CO_2 is positioned close to a T^2 silanol species in the pristine PMO material, as can be observed in Figure 3.1.6a. Although at low pressure it is not expected interaction between the organic bridges and CO_2 molecules, the presence of the organic moieties may contribute to enhance the interaction of CO_2 with the T^2 silanols by interrupting long range hydrogen bond interaction within silanols.

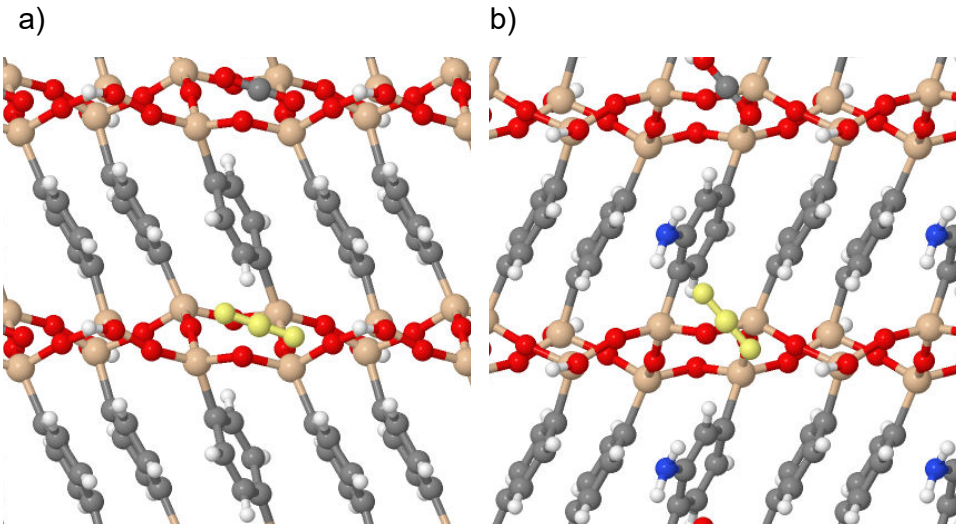

Figure 3.1.6. CO_2 preferential location on a) PhC_nPMOs and b) NH_2PhC_nPMOs. The CO_2 is highlighted in yellow.

Therefore, at low pressure, the CO_2 molecules interact only with available silanols on the surface of the materials while regions close to the organic moieties will be populated only at high pressure. Based on these premises, it is tentatively defined a correlation equation (Equation 3.1.4) that may represent the number of CO_2 preferential adsorption sites in the non-aminated PMO materials, f_{OH}, as:

$$f_{OH} \cong \%T^2_{SMP} / \%C \qquad \text{(Equation 3.1.4)}$$

where $\%T^2_{SMP}$ and %C correspond to the percentages of T^2 silanols and carbon atoms on the PMO material. The %C appears as uniformed weight factor of the materials. The f_{OH} values for the non-aminated PMOs are compared in Table 3.1.4 with the Henry constants for the corresponding materials. Interestingly, the ordering of the calculated f_{OH} values is identical to that of the Henry's constants of pure CO_2.

Table 3.1.4. Number of CO_2 preferential adsorption sites calculated with Equation 3.1.4 and Henry's constants of adsorption for pure CO_2 on the PhC_nPMOs adsorbents.

PMO	f_{OH} ($\%T^2_{SMP}$ / %C)	$K_H^{CO_2}$ (mmol·g^{-1}·bar^{-1})
$PhC_{18}PMO$	0.42	0.40
$PhC_{16}PMO$	0.53	0.48
$PhC_{14}PMO$	0.48	0.41
$PhC_{12}PMO$	0.51	0.46

This suggests that the properties used to establish the relationship in Equation 3.1.4 are the most important in defining the CO_2 adsorption affinities of the PhC$_n$PMO, n = 12, 14, 16, and 18, materials considered in this work.

In the case of the aminated materials, *i.e.*, NH_2PhC$_n$PMOs, the calculation of the f_{OH} values is more complicated, due to the existence of nearly 50% of phenylene moieties that could not be functionalized during the experimental syntheses. Moreover, the aminated phenylene motifs interact much more strongly with CO_2 molecules than the bare phenylene moieties. Thus, the aminated PhC$_n$PMOs present different degrees of hydrophobicity and different degrees of acidity in the same material when compared with the pristine materials. Additionally, different interactions between amino groups, silanol species and phenylene moieties can occur due to the distribution of the amino groups on the walls of the materials. These factors increase the degree of complexity in the determination of f_{OH}. Still, DFT calculations (Sub-chapter 3.2) for the adsorption of CO_2 on a periodic model of the walls of the aminated phenylene PMO, derived from the model developed by Martínez *et al.*[32] by substitution of a phenyl hydrogen atom with an amino group, show that the CO_2 adsorbate interacts preferentially with the isolated T^2 silanol species, in a bridging configuration where it also interacts with a neighboring amino group (*c.f.* Figure 3.1.6b). So, the main difference to the corresponding non-aminated PMOs is the strength of the interaction, which is slightly higher in the aminated materials than in the pristine PMOs. In principle, this simultaneous interaction of the CO_2 with silanols and amino groups will have a greater probability of occurrence in materials having smaller pore sizes, because the pore curvature is expected to allow these two functional groups to be closer to each other than in the materials with larger pore sizes. Positively, our assumptions seem to be supported by the b affinity parameters (Table A1.3, Appendix A), which are found to only increase upon amination in the case of the C_{12} materials, to be similar in the case of C_{14} PMOs, and to decrease in the cases of the C_{16} and C_{18} materials. So, in the case of the materials with the largest pore sizes, the coefficient related to the affinity between the sorbent and the sorbate decreases upon the amination reaction. Thus, it can be approximated that, at low pressure, the number of sites for CO_2 adsorption in the aminated samples is identical to the number of T^2 type silanols. In fact, as it can be seen in Figure A1.8b, the percentage of T^2_{SMP} silanol types on the aminated samples is correlated with the values of the Henry constants. In this way, Equation 3.1.4 can also be used to calculate the number of CO_2 preferential adsorption sites

in the aminated PMO materials. The calculated f_{OH} values for the NH_2PhC_nPMOs materials are compared in Table 3.1.5 with the Henry's constants of pure CO_2.

Table 3.1.5. Correlation of chemical properties with the calculated low-coverage adsorption capacities of pure CO_2 for the NH_2PhC_nPMOs adsorbents.

PMO	f_{OH} (%T^2 / %C)	$K_H^{CO_2}$ (mmol·g^{-1}·bar^{-1})
$NH_2PhC_{18}PMO$	0.43	0.34
$NH_2PhC_{16}PMO$	0.46	0.42
$NH_2PhC_{14}PMO$	0.55	0.47
$NH_2PhC_{12}PMO$	0.65	0.56

Encouragingly, as found for the as-synthesized materials, the latter quantities are in excellent qualitative agreement, again suggesting that the amounts of adsorbed CO_2 in these materials are correlated with the percentages of T^2 silanols divided by the % of carbon determined by EA, which is a normalizing factor. As expected, the discrepancies between the two quantities are larger in the aminated materials than in the as-synthesized ones because of the heterogeneous distribution of the amino groups and of possible formation of structural defects upon the amination reaction. Once again, the adsorption of carbon dioxide at low pressure in materials displaying a large variety of organic and inorganic adsorption sites can be described by a very simple correlation (Equation 3.1.4). This observation is a convincing sign of the local nature of the adsorption mechanism, which involves a quite limited number of surface atoms, and it is in agreement with recent theoretical studies on these materials.[32]

Comparison to other materials

The capacity of $NH_2PhC_{12}PMO$ to capture carbon dioxide and methane is compared in Table 3.1.6 with the capacities reported in the literature for other classes of adsorbents, namely, metal organic frameworks (MOFs), zeolites, zeolitic imidazolate framework (ZIFs), silicas, carbons and clays. Notice that data were determined at different temperatures with concomitant effects on the values of the capacities. For instance, in the case of the MAC (microwave activated carbon) material, a 20% reduction in the CO_2 capacity is found on increasing temperature from 25 °C to 35 °C. A similar reduction (of 27%) was also found for the $PhC_{18}PMO$ when enhancing the temperature from 25 °C to 35 °C. Although, the ratio of adsorption capacity of CO_2/CH_4 is improved with this increase of temperature. The results obtained for the PMO materials in this work were obtained at the 35 °C and a pressure of 1 bar.

Table 3.1.6. Capacities of different adsorbents in the CO_2/CH_4 separation at 1 bar.

Type	Materials	CO_2 capacity ($mmol \cdot g^{-1}$)	CH_4 capacity ($mmol \cdot g^{-1}$)	Temperature	$\frac{CO_2 \text{ capacity}}{CH_4 \text{ capacity}}$
Carbons	MAC[6]	2.13	0.98	25 °C	2.2
		1.69	0.81	35 °C	2.1
	Activated Carbon[33]	≈2.1	≈0.9		2.3
Clays	PILC Al_w[15]	≈0.40	≈0.07	25 °	5.7
MOFs	MOF-14(Cu)[34]	≈2.50	≈1.00		2.5
	CPO-27-Ni[35]	≈7.50	≈4.38		1.7
	CPO-27-Mg[35]	≈8.75	≈4.29		2.0
	amino-MIL-53(Al)[36]	1.96	≈0.30	30 °C	6.5
Silicas	a-MCMBs[4]	1.97	1.23	25 °C	1.6
Zeolites and ZIFs	Hβ-zeolite[37]	1.76	0.38	30 °C	4.6
	Naβ-zeolite[37]	≈2.80	≈0.70		4.0
	ZIF-7[38]	2.34	0.13	25 °C	18.0
	T-type zeolite[39]	≈1.90	≈0.30	35 °C	6.3
	LiX zeolite[33]	≈3.90	≈0.69		5.7
	13X zeolite[10]	≈4.08	≈0.50		8.2
	Chabazite zeolite (**r_2**KCHA)[40]	≈3.70	≈1.10		3.4
PMOs	$PhC_{18}PMO$	0.49	0.11	25 °C	4.5
		0.36	0.07	35 °C	5.1
	$NH_2PhC_{12}PMO$	0.46	0.08		5.8

The data in Table 3.1.6 show that the capacity of the $NH_2PhC_{12}PMO$ material to adsorb either CO_2 or CH_4 is quite low when compared to the other materials, but the ratio between the capacities for CO_2 and CH_4 is among the best. Importantly, the capacity to adsorb methane is very low which may be seen as very convenient for separation processes. If one compares the ratios of the capacities for capturing the two gases by different materials reported in literature with our best material ($NH_2PhC_{12}PMO$), measured at the same temperature and pressure (35 °C, 1 bar), it is possible to verify that the $NH_2PhC_{12}PMO$ material presents a relatively high capacity ratio, being superior than both MAC and activated carbon, 5.8 versus 2.1 and 2.3, respectively. Additionally, the capacity ratio of $NH_2PhC_{12}PMO$ is similar to those obtained in most of zeolites presented in Table 3.1.6 at the same working conditions, showing that PMO materials incorporating different functionalities can be good candidates for CO_2/CH_4 separation processes.

3.1.4 Conclusions

To summarize, amine-modified phenylene PMOs with different pore sizes were successfully synthetized and characterized. All pristine and amine-modified phenylene PMO materials showed two-dimensional hexagonal symmetry (*p6mm*) lattice and molecular-scale periodicities observed by PXRD and TEM. It was evaluated the performance of the materials on adsorption of pure carbon dioxide and methane at 35 °C at low pressure. The adsorption of CO_2 was much higher than that of CH_4, anticipating high CO_2 selectivity. Direct correlations between the amounts of CO_2 adsorbed and material pore sizes or specific surface areas were not found. In order to understand the differences obtained for the CO_2 adsorption within all materials, the Henry's constants of adsorption were determined, as well as their chemical features. A simple expression considering the % of T^2_{SMP} silanol species was found to provide a good prediction of the experimental Henry's law constants for pure CO_2 adsorption on each material. The adsorbent with the best chemical features to adsorb CO_2 was the $NH_2PhC_{12}PMO$, presenting a Henry constant of 0.56 $mmol \cdot g^{-1} \cdot bar^{-1}$ at 35 °C. However, the corresponding Henry constant for CH_4 is extremely low (0.06 $mmol \cdot g^{-1} \cdot bar^{-1}$ at 35 °C), turning it potentially interesting for the separation of this gas from CO_2.

PMOs can be used as adsorbents with improved characteristics for CO_2 adsorption/separation from CH_4 at low pressure. For that, they should present high degree of silica condensation (high amounts of T^2 silanols and small quantities of T^1 silanols). In addition, the pore sizes and BET surfaces seem not to play a direct role on the adsorption capacities, our results may indicate the existence of an indirect relation. Thus, the pore size should affect the curvature of the pore, the degree of condensation and thus the silanol type content. This information may be used in the future to design more effective functionalized PMO materials for biogas upgrading.

3.2 Interaction of CO_2 and CH_4 with functionalized periodic mesoporous phenylene–silica: Periodic DFT calculations and gas adsorption measurements

Adapted from:

Mirtha A. O. Lourenço, Christophe Siquet, Mariana Sardo, Luís Mafra, João Pires, Miguel Jorge, Moisés L. Pinto, Paula Ferreira and José R. B. Gomes

Interaction of CO_2 and CH_4 with functionalized periodic mesoporous phenylene–silica: Periodic DFT calculations and gas adsorption measurements

J. Phys. Chem. C, **2016**, 120: 3863–3875

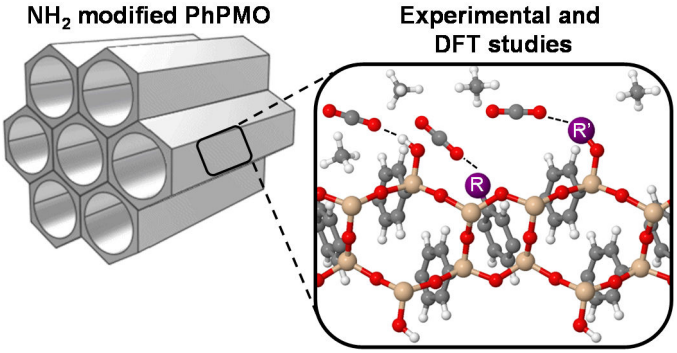

My direct contribution:

I declare that I have prepared, functionalized and characterized the PMO materials and performed all the DFT calculations. I also carried out the experimental CO_2 and CH_4 pure adsorption using a volumetric apparatus under guidance of Moisés L. Pinto and João Pires (University of Lisbon). The experimental adsorption studies using a manometric apparatus were performed at the University of Porto by Christophe Siquet, João Santos and Miguel Jorge. The NMR studies were performed at the University of Aveiro by Mariana Sardo and Luís Mafra.

3.2.1 Motivation

Having into account the strong need for a major breakthrough in finding an optimal adsorbent for the CO_2/CH_4 separation, the chemical modification of the benzene moieties in the PMO framework with, for instance, basic amino groups, can be accomplished to optimize their features for the separation of these gases, *i.e.*, by enhancing interactions with one of the gases.[25] These functional groups can additionally display interesting synergistic effects in materials that already exhibit high π-π conjugation and mixed hydrophobic/hydrophilic character.

Our main aim in this work is to introduce amine modifications in PhPMO in order to increment the interactions with CO_2 without improving those with CH_4 gases. This strategy will improve the potential of these materials to separate CO_2/CH_4 mixtures, *i.e.*, making these materials candidates for biogas upgrading. As it was described and understood in Sub-chapter 3.1, the amination of the PhPMO (NH_2PhPMO) is only effective on materials with small pore size, improving the affinity to the CO_2 gas. In the present work, non-functionalized (PhC_{12}PMO) and amine functionalized PhC_{12}PMOs (NH_2PhC_{12}PMO), having pore sizes of approximately 2.5 nm, were synthesized following the strategy reported in Sub-chapter 3.1. Two additional materials, *i.e.*, APTMS@PhC_{12}PMO and APTMS@NH_2PhC_{12}PMO, were obtained by post-grafting 3-aminopropyltriethoxysilane (APTMS) into the PhC_{12}PMO and NH_2PhC_{12}PMO materials. Thus, different kinds of amines were incorporated into the PhC_{12}PMO through two different methodologies. Theoretical and experimental gas adsorption studies were carried out to evaluate the affinities of these materials towards CO_2 and CH_4, and to understand the interactions between the materials' functional groups and these two gases. To the best of our knowledge only a single previous experimental study describes the grafting of the APTMS to the free silanols of the PhC_{12}PMO, but the resulting material (APTMS@PhC_{12}PMO) presented large pore sizes and was only tested in the adsorption of CO_2.[25] Similarly, few theoretical studies of PMOs were published in the literature,[22] and none of them evaluate phenylene bridge or silanol functionalized PMO materials for gas adsorption/separation. After validation of the computational approach, additional calculations were performed to predict if other functional groups, *e.g.* $–NO_2$, $–SO_3H$, $–NH(^iPr)$ and $–CH_2NH_2$, were also effective in promoting selective interactions with CO_2. The results of our study highlight the potential of

a synergistic approach involving theory and experiment to guide the rational design of materials for gas separation applications.

3.2.2 Experimental and computational details

Synthesis of PMOs.

The syntheses of $PhC_{12}PMO$ and the $NH_2PhC_{12}PMO$ are described in Sub-chapter 3.1.2. The materials APTMS@$PhC_{12}PMO$ and APTMS@$NH_2PhC_{12}PMO$ were obtained from $PhC_{12}PMO$ and $NH_2PhC_{12}PMO$, respectively, as can be observed in Figure 3.2.1. To prepare the APTMS@$PhC_{12}PMO$ and APTMS@$NH_2PhC_{12}PMO$ materials, 1 g of $PhC_{12}PMO$ and $NH_2PhC_{12}PMO$ were dried at 80 °C under vacuum atmosphere during 3 h. After the activation of the pores, dry dichloromethane (10 mL) was added and (3-aminopropyl)trimethoxysilane (0.439 g) was added drop wise to the suspension. The mixtures were vigorously stirred for 48 h. The obtained materials were filtered off and further washed with a large amount of distilled water and dried in an oven at 60 °C overnight. The APTMS post-grafting reaction was repeated for two additional cycles.

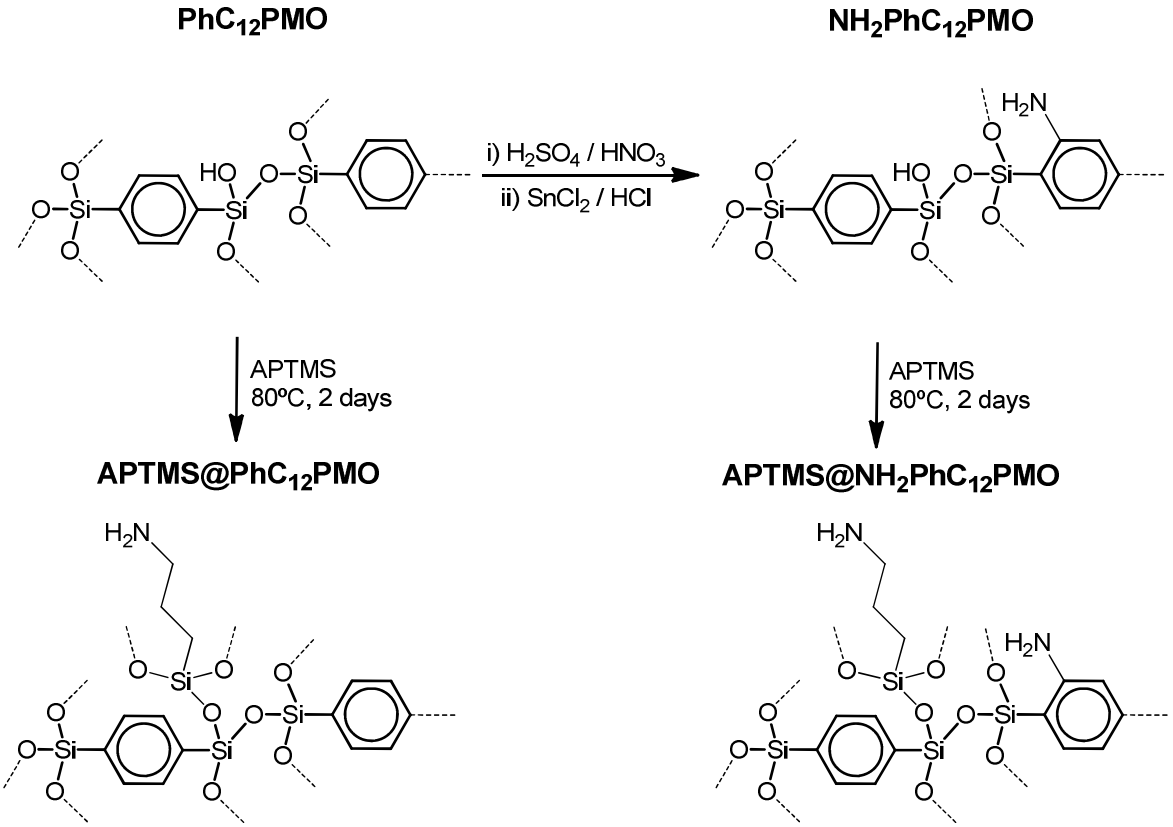

Figure 3.2.1. Functionalization of $PhC_{12}PMO$ material with amino groups.

Characterization of PMOs.

The structural order and the textural physical properties of all PMO materials were evaluated by PXRD, -196 °C N_2-sorption isotherms and TEM. ^{29}Si MAS NMR and ^{13}C and ^{29}Si CP-MAS NMR spectra were collected to check the stability of the Si-C bonds in the PMOs and to verify the chemical structure of the organic bridge, respectively. FTIR spectroscopy was also used to verify the chemical bonds of all prepared PMOs. The nitrogen density was determined by EA. PXRD, N_2–sorption isotherms, ^{29}Si NMR, FTIR, TGA and EA and some other data is presented in Appendix A.

Gas adsorption details.

Adsorption isotherms of CO_2 and CH_4 on prepared samples were measured up to 1000 kPa at 25 °C, using the volumetric method, using the procedure described in Sub-chapter 2.6. Each experimental pure component adsorption isotherm was fitted using the Virial model, where the non-ideality of the gas phase was taken into account by using the second and third virial coefficients, and the experimental excess adsorbed amounts were converted to the absolute adsorbed amounts by taking into account the porous volume of the material and the density of the gas phase using the virial coefficients. Selectivity values were estimated using a method proposed by Myers[41] and the implementation is described in detail in previous works.[15] The virial equation of state fitted to the adsorption data is in the form:

$$p = \frac{n^{ads}}{K_H} \exp\left(C_1 n^{ads} + C_2 n^{ads^2} + C_3 n^{ads^3}\right) \qquad \text{(Equation 3.2.1)}$$

where K_H is the Henry constant, and C_1, C_2, and C_3 are the constants of the virial-series expansion.

Adsorption isotherms of pure CO_2 and CH_4 were also measured on as-synthesized and amine-modified PMO materials at 35 °C and pressures up to 200 kPa using an in-house built manometric apparatus. The samples were activated first at 80 °C during 5 h and then at 160 °C during 10 h, under vacuum of *ca*. 1.4 kPa. The CO_2 and CH_4 gases were used as provided by Air Liquide (France), with a purity of 99.998% and 99.95%, respectively. The experimental adsorption measurements technique adopted was also previously described.[30]

DFT calculations.

Periodic slab calculations were performed with the VASP computer code.[42–44] DFT calculations considered the PBE exchange-correlation functional,[45] based on the GGA. The non-spin polarized DFT calculations include a correction for the van der Waals interactions according to the D2 method proposed by Grimme using the default parameters.[46–48] The suitability of the PBE-D2 approach is supported by results in a previous study where the calculated adsorption energy for CO with PhPMO (-14.3 $kJ \cdot mol^{-1}$)[32] was found to be in close agreement with the experimental adsorption enthalpy (-13.2 $kJ \cdot mol^{-1}$)[24] obtained from variable temperature infrared (VTIR) spectroscopy and with the range of binding energies calculated with the B3LYP-D approach for CO interacting with cluster models.[22,24] Valence electrons were described by plane-wave basis sets and core electrons with projector-augmented wave (PAW) potentials.[49] A kinetic energy cutoff of 415 eV was used. The atomic positions in the supercells used to model the walls of the different PMO materials were fully relaxed with the quasi-Newton algorithm, and the stopping-criteria for electronic and ionic updates were 10^{-7} eV and -0.05 eV/Å, respectively. Dipole corrections in the direction perpendicular to the PMO wall were applied.

The cell dimensions and the atomic coordinates for the structural model of the walls in the PhPMO material were kindly provided by Martínez and Pacchioni.[32] The structure is shown in Figure 3.2.2 and corresponds to a sequence of six and four member rings of organosilica tetrahedra with T^3 to T^2 [T^m=$RSi(OH)_{(3-m)}(OSi)_m$, in which R represents an organic group] silicon environments in a ratio of 2:1, grounded on information from solid state NMR obtained by Comotti *et al*.[50] Notice that Martínez and Pacchioni[32] considered also a structural model of the walls of the nanopores based on a sequence of six member rings only, with T^3 to T^2 in a ratio of 1:1, derived from the three-dimensional periodic lattice having the planes of the aromatic rings parallel to each other reported by Inagaki *et al*.[28], but found the former structure, with non-planar benzene moieties, to be more stable (~ 30 $kJ \cdot mol^{-1}$ per formula unit) than the latter. Important for the discussion below is the fact that the adsorption energy of CO_2 – either in the model with six and four member rings or with six rings only – is about 50% larger than that corresponding to CH_4. Thus, the information obtained with one or the other model is expected to be qualitatively similar.

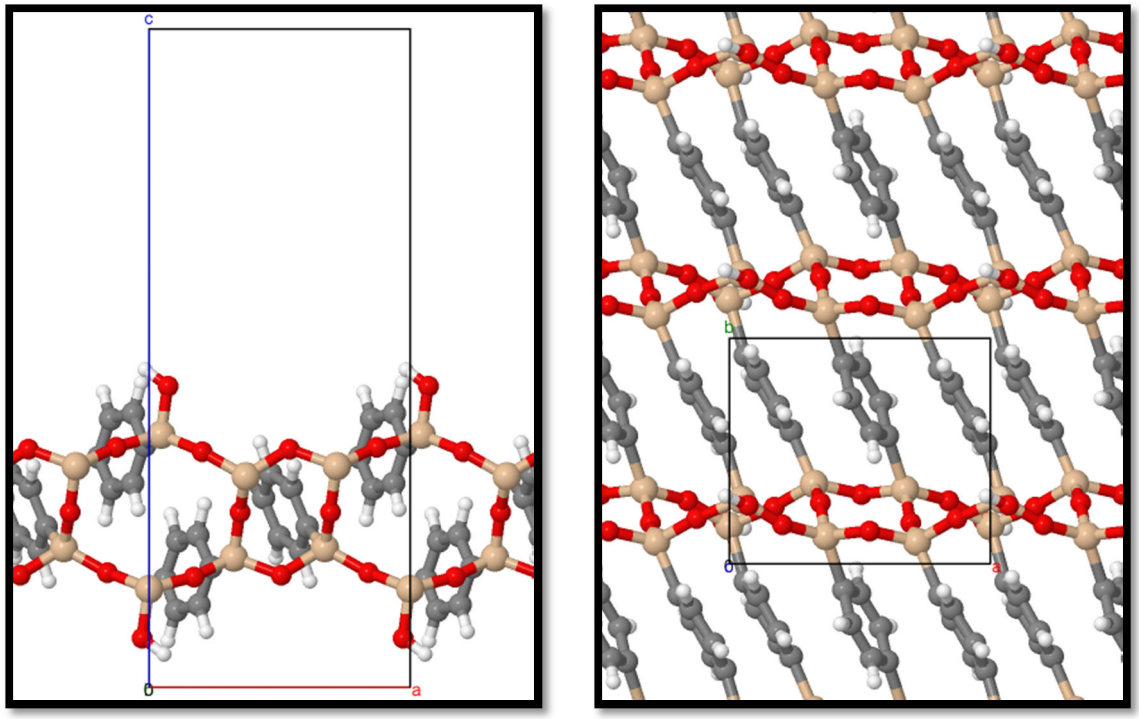

Figure 3.2.2. Side (left) and top (right) views of the unit cell (inline) used to model the PhPMO material with fully-optimized atomic positions. Color code for atomic spheres is: H, white; C, grey; O, red; and Si, pink.

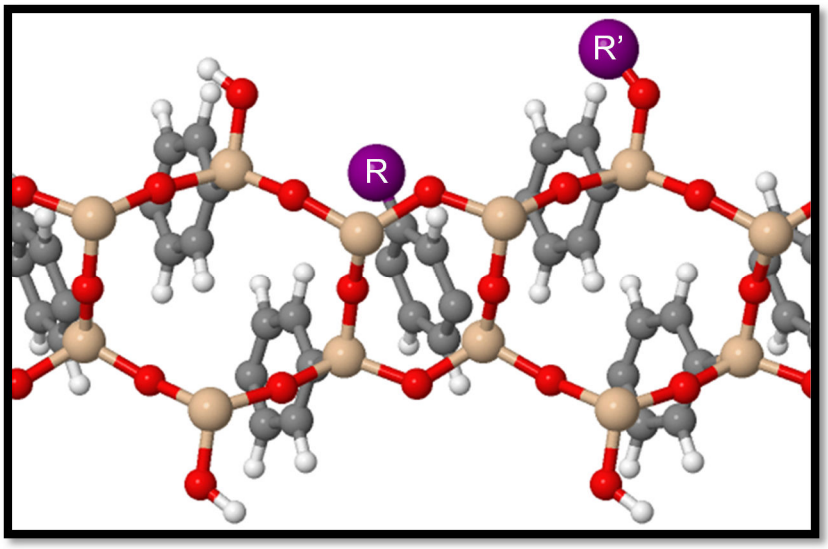

Figure 3.2.3. Functionalization of the PhPMO by post-modification, *i.e.*, by replacement of a single H atom in the aromatic rings with an **R** group (R = NH_2, NO_2, NH-*i*-Pr, CH_2NH_2 and SO_3H) and by grafting, *i.e.*, by substitution of a silanol H atom by an **R'** group (R' = APTMS). Purple is used for the substituent groups and color code for remaining spheres as in Figure 3.2.2.

The structures of the functionalized materials were obtained by single substitution of protons in the aromatic rings of the unit cell of PhPMO shown in Figure 3.2.2 by different functional **R** groups, *e.g.* $–NH_2$, $–NO_2$, –NH-*i*-Pr, $–CH_2NH_2$ and $–SO_3H$ (*c.f.* Figure 3.2.3). The

selection of the functional groups considered above was primarily based on their different polarities and on the presence of amine moieties, which in principle will be beneficial for improving the interactions with CO_2 without changing significantly those with CH_4. The substitution was made at several different positions and the structures of the models obtained were fully relaxed. Since the unit cell in Figure 3.2.2 contains three phenyl groups, this strategy led to the functionalization of 33% of the aromatic rings, which is similar to the maximum functionalization obtained experimentally (see below). The model corresponding to the functionalization with the APTMS group (**R'**) was obtained by introduction of this group at the free silanol (substitution of the proton by APTMS) available in the structure of the PhPMO model (*c.f.* Figure 3.2.3). The percentage of APTMS groups grafted to the PMO was 50%.

The models described above were used to study separately the adsorption of CO_2 and CH_4 by fully optimizing the atomic positions of the adsorbate/adsorbent complex. The adsorption energies were calculated as standard practice by subtracting the energies of the individual adsorbate and adsorbent fragments from the energy of the complex. Thus, negative values of the energy correspond to favorable gas/PMO interactions.

3.2.3 Results and discussion

Characterization of materials.

The structural integrity of the prepared adsorbents was determined from the combination of PXRD and N_2 sorption isotherms. Figure A2.1 (Appendix A) shows the PXRD diffraction patterns of $PhC_{12}PMO$, $NH_2PhC_{12}PMO$, APTMS@$PhC_{12}PMO$ and APTMS@$NH_2PhC_{12}PMO$ materials. The pristine $PhC_{12}PMO$ possesses a two-dimensional hexagonal symmetry (*p6mm*) lattice with a *d* spacing of 3.59 nm for the strong (100) reflection at low-angle (Table A2.1, Appendix A). In the case of the aminated samples, slight changes are observed in the PXRD (Figure A2.1, Appendix A) corresponding to the loss of definition of the 2D hexagonal arrangement, which is in agreement with the introduction of the amine functional groups inside the pores since some loss of regularity in the structure is expected during the amination reactions.[51] The lattice parameters of the hexagonal array of mesopores (calculated from the 2θ values of the (100) peaks) obtained for the $NH_2PhC_{12}PMO$, APTMS@$PhC_{12}PMO$ and APTMS@$NH_2PhC_{12}PMO$ samples are 3.63, 3.34 and 3.50 nm, respectively (Table A2.1, Appendix A). The molecular-scale periodicity

in the $PhC_{12}PMO$ pore walls along the channel direction is observed by the presence of a medium-range reflection at $d \sim 0.76$ nm.[28] The pristine material and all amine functionalized materials present these peaks at the same *d* spacing. Thus, the preparation of different amine functionalized phenylene PMOs is made with the preservation of both meso- and molecular-order.

The presence of different amine functional groups inside the pore was confirmed by N_2 adsorption–desorption experiments, with isotherms depicted in Figure A2.2 (Appendix A). The parent $PhC_{12}PMO$ exhibits a type IV isotherm[52], typically detected for conventional mesoporous materials such as MCM-41[53], indicating narrow distribution of mesopores of uniform size. The introduction of the amine functional groups (NH_2 group in the aromatic moieties or/and APTMS covalently bonded to the free silanols) into the mesochannels is supported by the reduction of the BET surface area and pore volume (Table A2.1 and Figure A2.2, Appendix A). The $PhC_{12}PMO$, $NH_2PhC_{12}PMO$, APTMS@$PhC_{12}PMO$ and APTMS@$NH_2PhC_{12}PMO$ materials present BET surface areas of 1004, 924, 634 and 305 $m^2 \cdot g^{-1}$, respectively (Table A2.1, Appendix A). The reduction in surface area and pore volume is much more pronounced for the APTMS-containing materials, due to the bulky nature of this group, which protrudes within the pore space. A comparison of the pore size distribution (PSD) curves of pristine PMO and amine functionalized $PhC_{12}PMO$ materials is presented in Figure A2.3 (Appendix A) and in Table A2.1, and reveals a maximum shifting from 2.54 to 2.23 nm, respectively.

Solid-state ^{13}C CP-MAS NMR, ^{29}Si MAS and CP-MAS NMR spectra of $PhC_{12}PMO$, $NH_2PhC_{12}PMO$, APTMS@$C_{12}PMO$ and APTMS@$NH_2PhC_{12}PMO$ materials are displayed in Figures 3.2.4 and A2.4 (Appendix A), respectively. ^{13}C CP-MAS NMR spectra support the different amine functionalizations of $PhC_{12}PMO$ materials. The parent PMO (Figure 3.2.4a) shows a characteristic resonance at 133 ppm that corresponds to the C of the phenylene bridge as reported in the literature.[28]

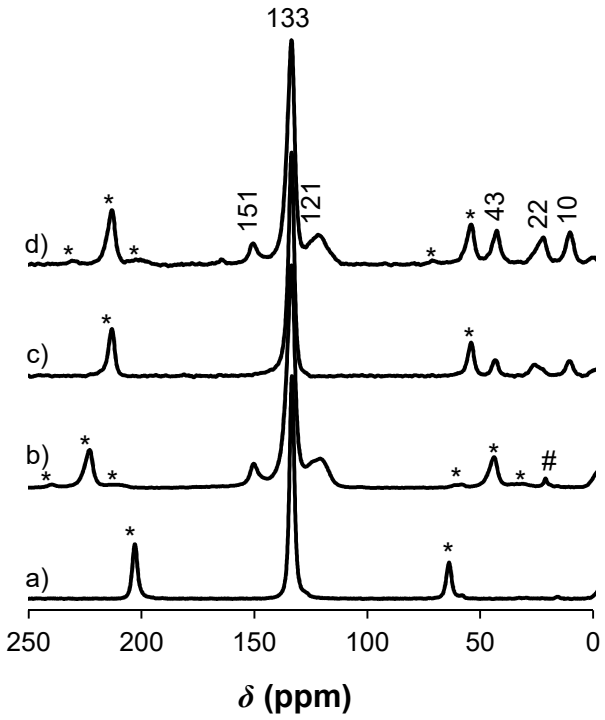

Figure 3.2.4. ^{13}C CP-MAS NMR spectra of a) $PhC_{12}PMO$, b) $NH_2PhC_{12}PMO$, c) APTMS@$PhC_{12}PMO$ and d) APTMS@$NH_2PhC_{12}PMO$. The asterisks correspond to the spinning side bands. The number symbol denotes traces of surfactant.

On the other hand, the spectra for the $NH_2PhC_{12}PMO$ material presents resonances at *ca*. 121, 133 and 151 ppm assigned to the distinct sp^2 carbons associated to the amine functionalized phenylene group. These results are in agreement with previous reports for $NH_2PhC_{12}PMO$.[27] As expected, the spectrum for APTMS@$NH_2PhC_{12}PMO$ also displays the three characteristic peaks corresponding to aminated phenyl groups, while that of APTMS@$PhC_{12}PMO$ displays the single resonance at 133 ppm. The grafting of the APTMS to the free silanols in both $PhC_{12}PMO$ and $NH_2PhC_{12}PMO$ is verified by ^{29}Si NMR measurements (Figure A2.4, Appendix A). The three resonances appearing at *ca.* 10, 22 and 43 ppm in the ^{13}C CP-MAS NMR spectra correspond to the carbons of the propyl chain of the APTMS@$PhC_{12}PMO$ and APTMS@$NH_2PhC_{12}PMO$ materials (Figure 3.2.4c-d). Figure 3.2.4d shows a tiny peak at around 164 ppm that is assigned to amines binding CO_2 from the atmosphere.

The ^{29}Si MAS and CP-MAS NMR spectra (Figure A2.4, Appendix A) of the pristine $PhC_{12}PMO$ display resonances at *ca.* -82, -71 and -61 ppm assigned to T^3, T^2 and T^1 (T^m = $SiR(OSi)_m(OH)_{3-m}$) organosiliceous species, respectively. The strong acid treatment used in the amination reaction of the pristine $PhC_{12}PMO$ material induces, in very slight

amounts, the carbon–silicon bond cleavage of the BTEB precursor; this is observed by the presence of a faint resonance at *ca.* -91 ppm (Figure A2.4, Appendix A) corresponding to Q^2 [Q^n = $Si(OSi)_n(OH)_{4-n}$] species. The grafting of the APTMS to the T^1 and T^2 silanols of both $PhC_{12}PMO$ and $NH_2PhC_{12}PMO$ leads to the reduction in intensity of the resonances corresponding to these species (see Figure A2.4 and Table A2.2, Appendix A) with respect to T^3 environments. In addition, a new resonance appears at *ca.* -58 ppm, labeled as $T^{2'}$ in this work (Figure A2.4, Appendix A), corresponding to the silanol species of the APTMS silicon atom. It is worth mentioning that the difference between T^2 and $T^{2'}$ species is due, respectively, to the presence of an aromatic and an alkylamine carbon residue bonded to the Si center.

The functionalization of the $PhC_{12}PMO$ material was also followed by FTIR (Figure A2.5, Appendix A). The presence of aromatic primary amines in the $NH_2PhC_{12}PMO$ is confirmed by the C–N stretching band at 1265 cm^{-1} and the in plane N–H bending vibration close to 1620 cm^{-1}. This latter band overlaps with the band of H–O–H bending vibrations and the N–H stretching modes appearing at 3400 and 3352 cm^{-1}. The amino group of the APTMS in APTMS@$PhC_{12}PMO$ and in APTMS@$NH_2PhC_{12}PMO$ materials presents N–H stretching modes appearing at 3356 $cm^{-1}$and at 3354 and 3402 cm^{-1}, respectively. The aromatic C–H stretching bands appear in the parent PMO at 3065 cm^{-1}, while in the $NH_2PhC_{12}PMO$ they appear at 3066 cm^{-1} and in the APTMS grafted amine functionalized and non-functionalized $PhC_{12}PMOs$ they appear at 3064 cm^{-1}. The APTMS@$PhC_{12}PMO$ and the APTMS@$NH_2PhC_{12}PMO$ materials present the C–H stretching vibrations for saturated aliphatic species at 2862 and 2928 cm^{-1} and at 2867 and 2939 cm^{-1}, respectively.

The introduction of the amino group in the phenylene moieties of $PhC_{12}PMOs$ and the grafting of APTMS to the free silanols of $PhC_{12}PMO$ lead to a reduction of thermal stability from 600 °C to 400 °C and to 300 °C, respectively, as observed by TGA (Figure A2.6, Appendix A). The $PhC_{12}PMO$ material presenting both types of amines (NH_2 and APTMS) is thermally stable only up to 250 °C.

Table A2.3 (Appendix A) presents the density of amino groups in the $PhC_{12}PMO$ materials determined by EA. The $NH_2PhC_{12}PMO$ has a nitrogen percentage of 2.58% that corresponds to amine density of 1.85 $mmol \cdot g^{-1}$. The grafting of APTMS into the $PhC_{12}PMO$ leads to a density of amino groups of 1.39 $mmol \cdot g^{-1}$. The APTMS@$NH_2PhC_{12}PMO$ has a total amine

density of 2.60 mmol·g^{-1}, which results from the sum of the aromatic amine density of 1.85 mmol·g^{-1} and of the APTMS amine density of 0.75 mmol·g^{-1}.

Experimental pure-component adsorption isotherms.

Pure-component adsorption isotherms of CO_2 and CH_4 at 25 °C are shown in Figure 3.2.5. The Henry's constant (K_H) was determined for each pure gas adsorbed in each material using the Virial model in order to evaluate the interaction of the chemical surface of our materials with pure CO_2 and pure CH_4 at low coverage. The fitting parameters for the Virial model are provided in Table 3.2.1.

The adsorption isotherms in Figure 3.2.5 suggest that the introduction of the amines into the $PhC_{12}PMO$ material leads to an increase in the amount of adsorbed CO_2 and in the Henry's constants, increasing in the order $PhC_{12}PMO$ < $NH_2PhC_{12}PMO$ < APTMS@$NH_2PhC_{12}PMO$ < APTMS@$PhC_{12}PMO$, *i.e.*, the non-functionalized material presents less affinity for CO_2 than the aminated samples. In the case of methane adsorption, the $PhC_{12}PMO$ material has the highest adsorption affinity, manifested in the highest Henry's constant (Table 3.2.1), although the differences observed for the different materials suggest that in all cases the adsorption is significantly lower than that observed for CO_2.

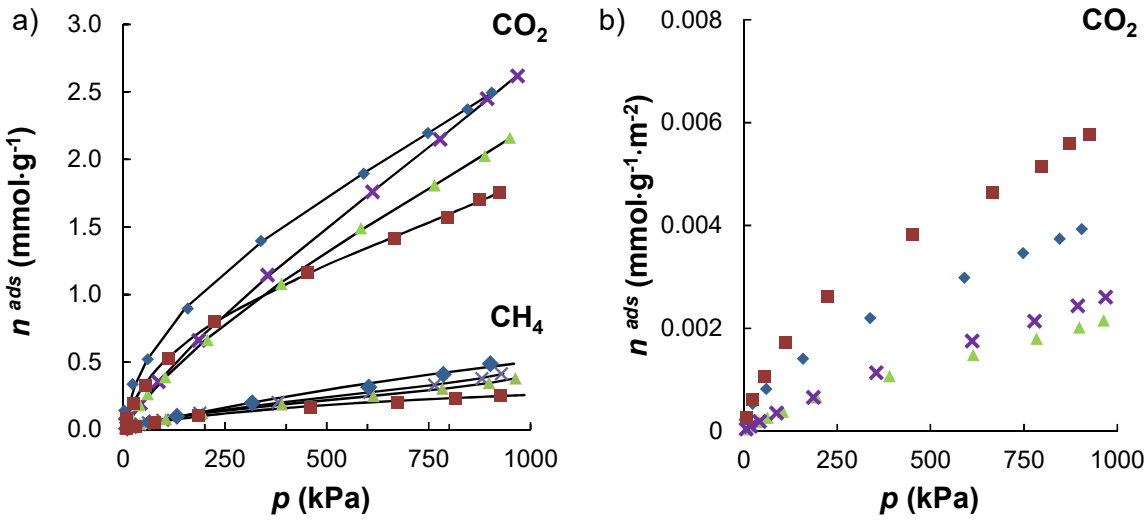

Figure 3.2.5. Adsorption equilibrium isotherms of CO_2 and CH_4 at 25 °C on the prepared materials expressed as a) mmol·g^{-1} and b) mmol·m^{-2}. Solid lines were obtained by fitting the experimental points to the Virial model. ▲ labels correspond to $PhC_{12}PMO$, × labels correspond to $NH_2PhC_{12}PMO$, ♦ labels correspond to APTMS@$PhC_{12}PMO$, and ■ labels correspond to APTMS@$NH_2PhC_{12}PMO$.

The amine functionalization of the aromatic moieties of the $PhC_{12}PMO$ leads to, as expected, a reduction of the BET surface area and pore volume (Table A2.1, Appendix A) but the CO_2 adsorption affinity is slightly increased (Table 3.2.1). This is a consequence of the introduction of amino groups covalently bonded to the phenylene bridges of the $PhC_{12}PMO$ material, corresponding to a nitrogen content of 2.58% (Table A2.3, Appendix A). This is better noticed when the adsorption isotherms are normalized by the BET surface area (Figure 3.2.5b). Therefore, the introduction of an aromatic amine into the PMO channels reveals that the chemical functionalization of the PMO material is more important for CO_2 capture than the amplitude of textural properties such as the surface area and pore diameter. This is a consequence of the energetically more important interactions between the CO_2 molecules and the amino groups than with other sites available in the parent $PhC_{12}PMO$ material.

Table 3.2.1 demonstrates that the $NH_2PhC_{12}PMO$ material has slightly lower affinity for CH_4 than $PhC_{12}PMO$, suggesting that the introduction of the amine moiety at the aromatic rings weakens the interaction of PMO with CH_4. This tiny reduction in the CH_4 adsorption is also in accordance with the decrease in the BET surface area and pore volume. Still, the adsorption of CH_4 is small in both cases. The grafting of the APTMS onto the silanols of the pristine $PhC_{12}PMO$ to obtain the APTMS@$PhC_{12}PMO$ material is accompanied by a very pronounced decrease of its surface area and pore volume.

Table 3.2.1. Virial coefficients (C_1, C_2 and C_3) and Henry's constants (K_H) for the adsorption of methane and carbon dioxide at 25 °C on the prepared materials.[a]

Gas	Material	K_H (mmol·g^{-1}·kPa^{-1}) x 10^{-2}	C_1 g·mmol^{-1}	C_2 (g·mmol^{-1})^2	C_3 (g·mmol^{-1})^3	*Selectivity*
CH_4	$PhC_{12}PMO$	0.13	7.458	-11.487		
	$NH_2PhC_{12}PMO$	0.11	5.200	-7.296		
	APTMS@$PhC_{12}PMO$	0.07	0.797			
	APTMS@$NH_2C_{12}PMO$	0.08	4.504			
CO_2	$PhC_{12}PMO$	0.45	0.562	-0.112		3.2 (3.5[b])
	$NH_2PhC_{12}PMO$	0.48	0.507	-0.151	0.015	3.6 (4.4[b])
	APTMS@$PhC_{12}PMO$	1.83	1.647	-0.476	0.048	6.7 (26.1[b])
	APTMS@$NH_2PhC_{12}PMO$	1.08	1.750	-0.434		6.2 (13.5[b])

[a]Obtained by nonlinear least-squares fitting of the virial equation to the adsorption data. [b]Ratio of the Henry's constant for CO_2 to that for CH_4.

The nitrogen content (Table A2.3, Appendix A) of APTMS@$PhC_{12}PMO$ is 1.93%, which can be compared with that determined for $NH_2PhC_{12}PMO$ (2.58%). Interestingly, the former displays higher adsorption capacity and Henry's constant for CO_2 than the latter material, thus revealing that the type of amine has a stronger influence on the sorption capacity for

CO_2 than the amount of nitrogen introduced in the PMO channels, suggesting that alkyl amines interact more favorably with CO_2 than the aromatic amines, because the former amines present higher basicity than the latter.[54]

The APTMS@NH_2PhC_{12}PMO material shows lower adsorption capacity for CO_2 (*c.f.* Figure 3.2.5a) than APTMS@PhC_{12}PMO, but when the adsorption isotherm is expressed taking into account the BET surface area (Figure 3.2.5b) a substantial increase in the adsorption of CO_2 can be perceived. This is likely to be due to the larger degree of amination resulting from the simultaneous presence of aromatic and alkyl amines in the same PMO material, despite the concomitant lower BET surface area (305 $m^2 \cdot g^{-1}$) and pore size (2.23 nm) when compared with the other materials described above, *c.f.* Table A2.1 (Appendix A). Note that this material only presents 0.75 $mmol \cdot g^{-1}$ of APTMS amine density, much lower than in APTMS@PhC_{12}PMO (1.39 $mmol \cdot g^{-1}$), and this type of amine interacts more strongly with the CO_2 molecule than the aromatic amine.

The Ideal Adsorbed Solution Theory (IAST)[55] was applied to the analysis of the adsorption data by fitting the Virial equation to the pure-component isotherms and calculating the selectivity of the separation and the equilibrium phase diagrams using a method proposed by Myers[41] with the implementation described in detail in previous works.[14,15] As can be seen in Figure 3.2.6, the differences in the predicted selectivities exhibited by the different materials for the CO_2/CH_4 separation can be quite large. In fact, the materials with APTMS groups grafted to the silanols of the PMO present much higher selectivity values than PhC_{12}PMO and NH_2PhC_{12}PMO. These two latter materials present similar selectivity, but it can be noticed that there are a slight increase in the selectivity at low pressures for NH_2PhC_{12}PMO (3.6 at 100 kPa) when compared with PhC_{12}PMO (3.2 at 100 kPa).

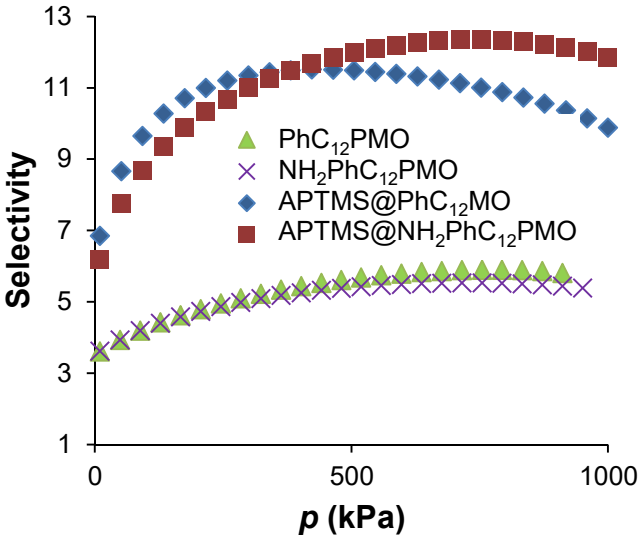

Figure 3.2.6. Average selectivity for the CO_2/CH_4 separation on the different materials at 25 °C. ▲ labels correspond to $PhC_{12}PMO$, × labels correspond to $NH_2PhC_{12}PMO$, ♦ labels correspond to APTMS@$PhC_{12}PMO$, and ■ labels correspond to APTMS@$NH_2PhC_{12}PMO$.

This indicates that the aromatic amine is not bringing the desired effect in the selectivity over the entire range of pressures (Table 3.2.1). Variation of selectivity with pressure is also seen in the case of the APTMS materials. At low pressures, APTMS@$PhC_{12}PMO$ presents higher selectivity than APTMS@$NH_2PhC_{12}PMO$ but this ordering is reversed at higher pressures. This is most probably related with the kind of amines and their amount present on the materials. The APTMS@$PhC_{12}PMO$ material presents only alkyl amines that seem to interact more strongly with CO_2 than aromatic amines. Alkyl amines are also available in APTMS@$NH_2PhC_{12}PMO$ material but their amount, determined by EA, is one half of the amount of aminopropyl groups presented in APTMS@$PhC_{12}PMO$ (Table A2.3, Appendix A). Thus, at low pressure, APTMS@$PhC_{12}PMO$ shows better selectivity than APTMS@$NH_2PhC_{12}PMO$ because of the more important role of the type of amine than of its quantity. Still, the nitrogen content in the latter PMO is larger than that in the former (2.60 versus 1.39 $mmol \cdot g^{-1}$). The interaction of CO_2 with the aromatic amines is less favorable than with the alkylamines of grafted APTMS moieties but is more stable than any other site available in these PMOs. Hence, at high pressure, the larger amount of amines in APTMS@$NH_2PhC_{12}PMO$ dictates a better selectivity for CO_2. These effects are even clearer in the ratio of the values of the Henry constants determined for CO_2 and CH_4 adsorption on each of the materials studied experimentally in this work (Table 3.2.1), which can be also used as an estimate of the ability of the materials for separating these gases. As can be seen

in Table 3.2.1, the largest ratio was calculated for APTMS@PhC$_{12}$PMO, which appears to be the most interesting adsorbent for CO_2/CH_4 separation.

The impact of all of the variables on the separation is illustrated in Figure 3.2.7, where it can be observed that APTMS@NH$_2$PhC$_{12}$PMO shows slightly better performance than APTMS@PhC$_{12}$PMO.

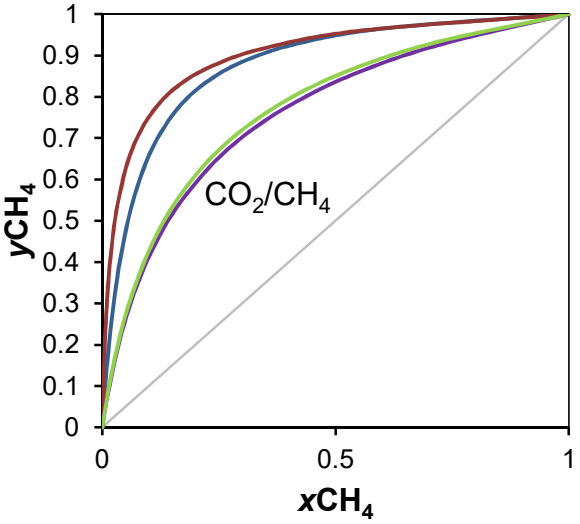

Figure 3.2.7. Isothermal (25 °C), isobaric (500 kPa) *xy* phase diagrams of the CO_2/CH_4 mixtures on, from top to bottom, APTMS@NH$_2$PhC$_{12}$PMO (brown line), APTMS@Ph-C$_{12}$PMO (blue line), PhC$_{12}$PMO (green line) and NH$_2$PhC$_{12}$PMO (purple line). y_{CH_4} is the molar fraction of methane in the gas phase; x_{CH_4} is the molar fraction of methane in the adsorbed phase.

Moreover, these two materials are much better than PhC$_{12}$PMO and NH$_2$PhC$_{12}$PMO. Considering a 0.5 molar composition of methane (y_{CH_4}), a reasonable value for biogas composition and some natural gas sources, the composition in the adsorbed phase (x_{CH_4}) is 0.02 on APTMS@NH$_2$PhC$_{12}$PMO and 0.06 on APTMS@PhC$_{12}$PMO, at 500 kPa and 25 °C. Thus, the adsorbed phase is much richer in carbon dioxide than in methane for both materials with an adsorption of almost pure carbon dioxide (about 0.94 – 0.98 molar composition at 500 kPa and 25 °C) at 0.5 composition in the gas phase. Complete phase diagrams were also obtained (Figure A2.7, Appendix A), which confirm a similar performance of these two materials.

Important for establishing the adequacy of these materials for typical adsorptive applications is the understanding of any structural changes upon degasification. After adsorption experiments, the aminated materials were reactivated using vacuum during 4 h at 100 °C.

The ^{15}N CP-MAS NMR spectrum of reactivated $NH_2PhC_{12}PMO$ (Figure 3.2.8a) presents a peak corresponding to an aromatic amine at *ca.* -321 ppm, which is in agreement with the literature.[27] The absence of additional peaks in $NH_2PhC_{12}PMO$ confirms that no CO_2 molecules are left covalently bonded to the aromatic amines of the material. Upon grafting with APTMS (APTMS@$NH_2PhC_{12}PMO$), four peaks were observed at *ca.* -262, -295, -320, and -348 ppm (Figure 3.2.8b). The latter two resonances are assigned to the aromatic amine and to the propylamine groups, respectively. The remaining resonances at *ca*. -262 and -295 ppm are assigned to species containing a carbonyl group resulting from the chemisorption of the CO_2 molecules. The presence of such species is also evident in the ^{13}C CP-MAS NMR showing resonances at *ca.* 178 and 164 ppm (Figure A2.8, Appendix A), confirming the observations in the ^{15}N CP-MAS spectra, *i.e.*, a minor quantity of CO_2 remains bonded to the amines after activation at 100 °C. The ^{13}C resonance appearing at 164 ppm has been assigned to carbamate species by solid-state NMR and FTIR,[56] and is associated to the presence of the peak at -265 ppm in the ^{15}N CP-MAS NMR. The peak at 178 ppm appears only when CO_2 is adsorbed into the APTMS@$NH_2PhC_{12}PMO$ material, which coincides with the presence of a distinct resonance at -262 ppm in the ^{15}N CP-MAS NMR for this same material. Thus, it is assumed that this resonance, in a chemical shift region typical of carbonyl groups, is due to a chemisorbed CO_2 species involving the simultaneous participation of the aromatic and aliphatic amines. The nature of such species cannot be unambiguously assigned from the data in the present study as this would require further experiments under well controlled conditions (pressure, temperature, moisture levels). The spectrum of APTMS@$PhC_{12}PMO$ after material activation shows the presence of two peaks at *ca.* -293 and -352 ppm (Figure 3.2.8c). The latter peak is assigned to APTMS attached to the surface of the material, while the former peak corresponds to carbamate species as observed for analogous materials also functionalized with the aminopropyl group.[56] The persistence of CO_2 species after the degassing procedure above-mentioned is not surprising. Indeed, it was previously shown that higher temperature was needed (about 150 °C) to completely remove the CO_2 from amine functionalized materials, and at 100 °C only about 91% of bonded CO_2 could be removed.[56]

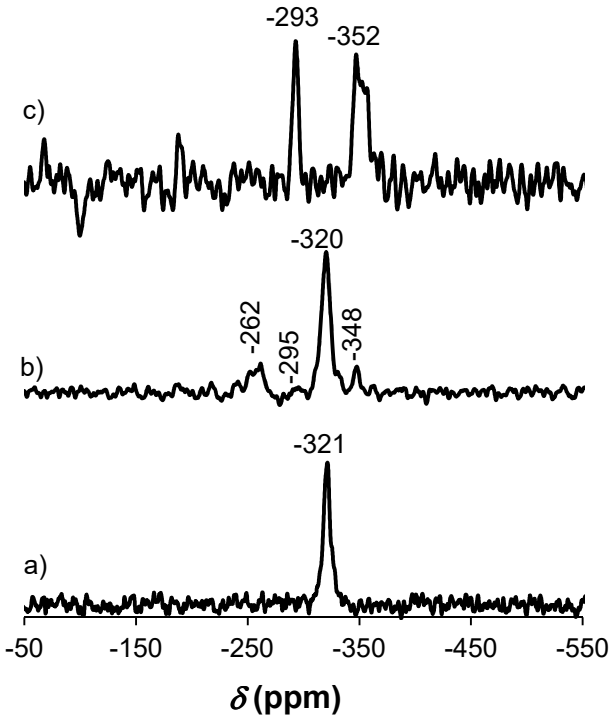

Figure 3.2.8. ^{15}N CP-MAS NMR spectra of the reactivated materials: a) $NH_2PhC_{12}PMO$; b) APTMS@$NH_2PhC_{12}PMO$; and c) APTMS@$PhC_{12}PMO$ after a first cycle of CO_2 adsorption.

All prepared materials were also tested for adsorption of pure CH_4 and CO_2, but measured in a pressure range between 0 and 200 kPa at 35 °C. Figure A2.9 and Table A2.4 (Appendix A) show the results obtained for the most promising material, APTMS@$PhC_{12}PMO$. As expected, APTMS@$PhC_{12}PMO$ adsorbs more CO_2 amount at 25 °C than at 35 °C, given that adsorption is an exothermic process. The CH_4 pure adsorption capacities and the related Henry's constant are similar for both temperatures (25 °C and 35 °C), but this is most likely because of the low adsorbed amounts of this gas together with the relatively small temperature difference between isotherms (10 °C), which makes it difficult observe the effect of temperature.

Computer simulations of all prepared functionalized PMO materials.

Computational tools were used to understand the interaction between CO_2 and CH_4 molecules and the different functionalities in the prepared PMOs. As referred above, the structure used to model the PhPMO material was functionalized in 33% of the phenylene moieties. In the case of the functionalization with the amino functional group, it was studied

carefully the substitution of –H by –NH_2 in several different positions of the aromatic rings but only the two most favorable positions are shown in Figure 3.2.9.

-R group	A	B
-NH_2	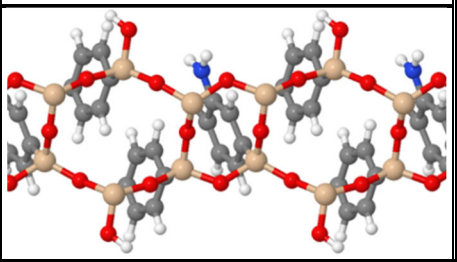	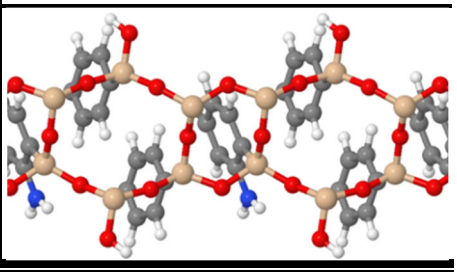

Figure 3.2.9. Side views of the two most favorable configurations for NH_2PhPMOs. Color code for atomic spheres: N, blue and remaining atoms as in Figure 3.2.2.

The APTMS (–$Si(OH)_2C_3H_5NH_2$) group was grafted onto the free silanols (Si-OH) of the most favorable structures optimized for PhPMO and NH_2PhPMO to obtain models of the walls of the APTMS@PhPMO and APTMS@NH_2PhPMO materials, respectively. Several different starting configurations of the APTMS moiety were considered because of the high number of degrees of freedom of this group. The two most favorable positions for each APTMS functionalized PhPMO are presented in Figure 3.2.10. The adsorption energies for the CO_2 and CH_4 molecules interacting with each of the PMO models described above are reported in Table 3.2.2, and views of the most favorable locations are given in Figure 3.2.11. The PBE-D2 energies for CO_2 adsorption vary between -19.8 $kJ \cdot mol^{-1}$ in the case of the parent PhPMO and -29.0 $kJ \cdot mol^{-1}$ for the APTMS@PhPMO material, while for CH_4 the adsorption energies are in the interval between -9.5 and -13.7 $kJ \cdot mol^{-1}$ for APTMS@NH_2PhPMO and APTMS@PhPMO, respectively. Thus, the adsorption energies of CO_2 with the different materials are much higher than the adsorption energies obtained for CH_4 and, despite the limitations associated to the structural models used and the non-consideration of kinetic data, the calculated results are in line with the strength of the Henry's constants calculated from experimental adsorption isotherms (Table 3.2.1).

In particular, the adsorption energies for CO_2 increase in the order PhPMO < NH_2PhPMO < APTMS@NH_2PhPMO < APTMS@PhPMO, which is the same order obtained for the Henry's constants for the CO_2 gas. The ratio between the adsorption energies calculated for CO_2 and CH_4 molecules on the same material shows the highest value for

APTMS@NH_2-PhPMO and a decrease in the order APTMS@NH_2PhPMO > NH_2PhPMO > APTMS@PhPMO > PhPMO.

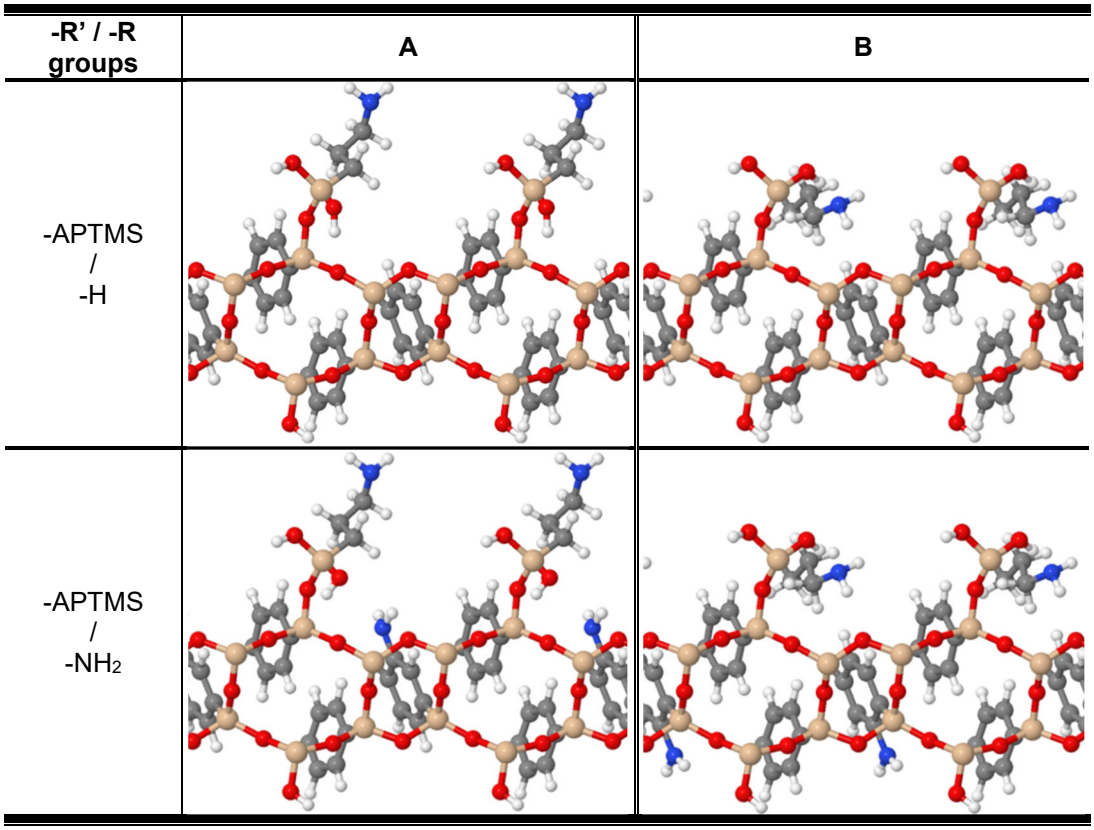

Figure 3.2.10. Side views of the two most favorable configurations optimized for APTMS@PhPMO (top) and APTMS@NH_2PhPMO (bottom). Color code for atomic spheres as in Figure 3.2.9.

From the views of the optimized configurations shown in Figure 3.2.11 and from the values of selected atomic distances reported in Table A2.5 (Appendix A) it can be concluded that CO_2 interacts preferentially with the silanol group in the case of PhPMO, with a SiOH···OCO nearest-neighbor distance of 2.28 Å. In the case of NH_2PhPMO, the CO_2 interaction occurs with both the silanol and amino groups at nearest-neighbor distances of 2.45 and 2.60 Å, respectively. For APTMS@PhPMO, CO_2 interacts with both the amino group and an acidic hydrogen **(H20)** of the alkyl chain of the APTMS group at nearest-neighbor distances of 2.58 and 2.75 Å, respectively. The CO_2 in APTMS@NH_2PhPMO interacts with the silanol group and an acidic hydrogen **(H20)** of the alkyl chain of the APTMS group, at nearest-neighbor distances of 2.45 and 2.62 Å, respectively. A direct relationship between geometric parameters and calculated adsorption energies is unclear, with the exception that in the case of the parent compound the CO_2 molecule is interacting

with a single site on the PMO wall while in the aminated materials the most favorable interactions involve two sites. This is likely to be the main cause for the significantly more favorable adsorption energies observed in all the aminated materials with respect to the pristine PhPMO (Table 3.2.2).

Table 3.2.2. Calculated low-coverage adsorption energies of CO_2 and CH_4 species in the four different aminated PhPMOs.

-R'/ -R groups	**CO_2 adsorption energy** ($kJ \cdot mol^{-1}$)	**CH_4 adsorption energy** ($kJ \cdot mol^{-1}$)	**Ratio CO_2/CH_4**
-H / -H	-19.8	-12.9	1.53
-H / -NH_2 (A)[a]	-26.2	-11.7	2.24
-APTMS / -H (A)[b]	-29.0	-13.7	2.12
-APTMS / -NH_2 (A)[b]	-25.9	-9.5	2.73

[a]**A** corresponds to the structure of the leftmost panel in Figure 3.2.9. [b]**A** corresponds to the structure of the leftmost panel in Figure 3.2.10.

In the case of methane, the interactions seem to be predominantly with a hydrogen atom from the aromatic ring in the case of the PhPMO material; with the amino group in the case of NH_2PhPMO; in the cavity defined by the hydrogen atoms from the silanol (**H29**) and amino (**H28**) groups and from the alkyl chain of the APTMS (**H20**) group in the case of APTMS@PhPMO; and with the hydrogen atom (**H29**) of one free silanol of the aminopropil group (APTMS) in the case of APTMS@NH_2PhPMO. The nearest-neighbor distances (Table A2.5, Appendix A) are 3.07, 2.36, 2.58 and 2.14 Å, respectively.

As in the case of CO_2, a direct relationship between the calculated energies and the selected geometrical parameters is not evident. Nevertheless, it arises that the interaction of methane with the models having an amino group in the aromatic ring is weaker than those calculated for the corresponding materials without such groups (*c.f.* compare adsorption energies reported in Table 3.2.2 for PhPMO and APTMS@PhPMO with those for NH_2PhPMO and APTMS@NH_2PhPMO).

From the pure CO_2 and CH_4 experimental adsorption in the prepared PMO, it is possible to conclude that all these materials adsorb similar amounts of methane, in very small quantities, while the CO_2 adsorption is much higher. Therefore, it is more relevant to examine the CO_2 adsorption energies calculated for the prepared materials than the adsorption energies obtained for CH_4.

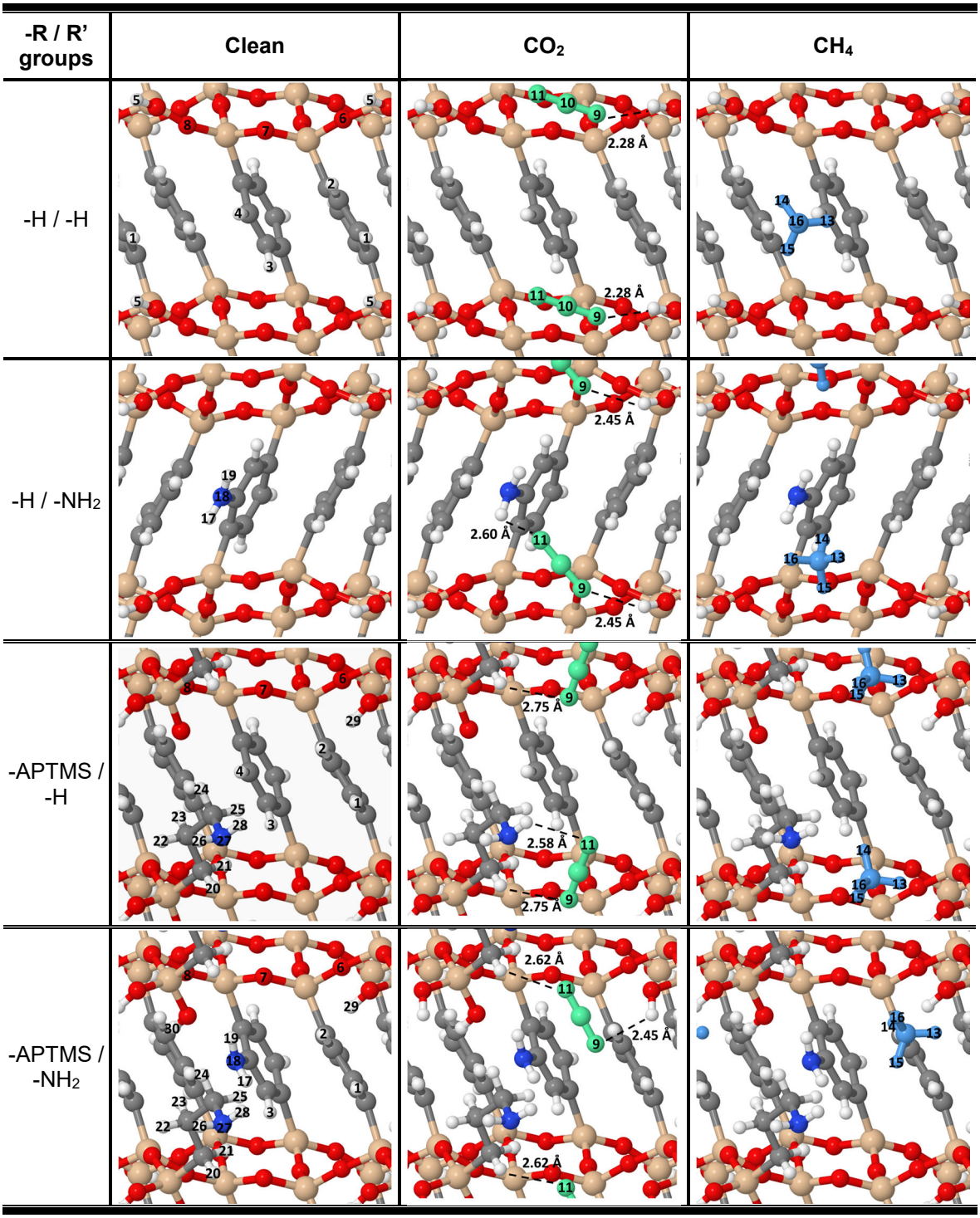

Figure 3.2.11. Top views of the optimized clean, and CO_2 or CH_4 covered aminated PhPMO materials. Color code for adsorbent atoms as in Figure 3.2.9, and light green and light blue are used for atoms in CO_2 and CH_4 adsorbates, respectively. The numbering is the same as used in Table A2.5 containing selected geometrical parameters.

The correlation between the adsorption energies obtained for the CO_2 molecules and the Henry's constants for the CO_2 adsorption in each material are in good agreement, showing

that despite the inherent limitations of the computational model (for example, consideration of a single lowest energy adsorption site, thus neglecting entropic factors), it can be used to predict the potential of other functionalized phenylene-PMOs for the adsorption of CO_2 or for the separation of CO_2 from CH_4.

Molecular simulation of other R functionalized PhPMO materials.

Since the adsorption energies calculated with DFT for CO_2 and CH_4 in the parent and aminated PhPMOs compared well with the experimentally determined gas adsorption capacities of such materials, further DFT calculations were performed to understand how other functional groups (*e.g.* $–NO_2$, –NH-*i*-Pr, $–CH_2NH_2$ and $–SO_3H$) interact with CO_2 and CH_4, with the purpose of optimizing resources and avoiding the synthesis of ineffective materials. These functional groups were chosen on the basis of their different polarities and of the ease of preparation of PMO-functionalized materials.[27,28] To enable direct comparison with the results presented in the previous section, only one third of the aromatic phenylene moieties were functionalized with such groups. The two most favorable configurations for each new PMO derived from PhPMO obtained after full optimization are presented in Figure 3.2.12. The interaction of CO_2 and CH_4 molecules with the two configurations in Figure 3.2.12 for each **R**PhPMO was analyzed by DFT. The calculated adsorption energies are reported in Table 3.2.3 and the final configurations for the two adsorbates interacting with each material are depicted in Figure 3.2.13. Selected geometrical parameters are supplied in Table A2.6 (Appendix A).

The comparison of the energetic data in Tables 3.2.2 and 3.2.3 shows that the introduction of the nitro group ($–NO_2$) in the phenylene moieties of the PhPMOs increases slightly the interaction of both CO_2 (-2.1 $kJ{\cdot}mol^{-1}$) and CH_4 (-0.4 $kJ{\cdot}mol^{-1}$). These tiny differences seem to be associated to the interaction of the carbon atom of CO_2 and one of the hydrogen atoms of CH_4 with an oxygen atom of the nitro group (Table A2.6, Appendix A). The DFT results suggest that nitrated materials are less promising than the aminated PMOs for this separation.

Table 3.2.3. Calculated low-coverage adsorption energies of CO_2 and CH_4 molecules in different **R** functionalized PhPMOs.

-R group	CO_2 adsorption energy $kJ.mol^{-1}$	CH_4 adsorption energy $kJ.mol^{-1}$	Ratio CO_2/CH_4
$–NO_2$	-21.9	-13.3	1.64
–NH-*i*-Pr	-27.6	-17.6	1.35
$–CH_2NH_2$	-31.1	-15.2	2.05
$–SO_3H$	-26.9	-10.6	2.54

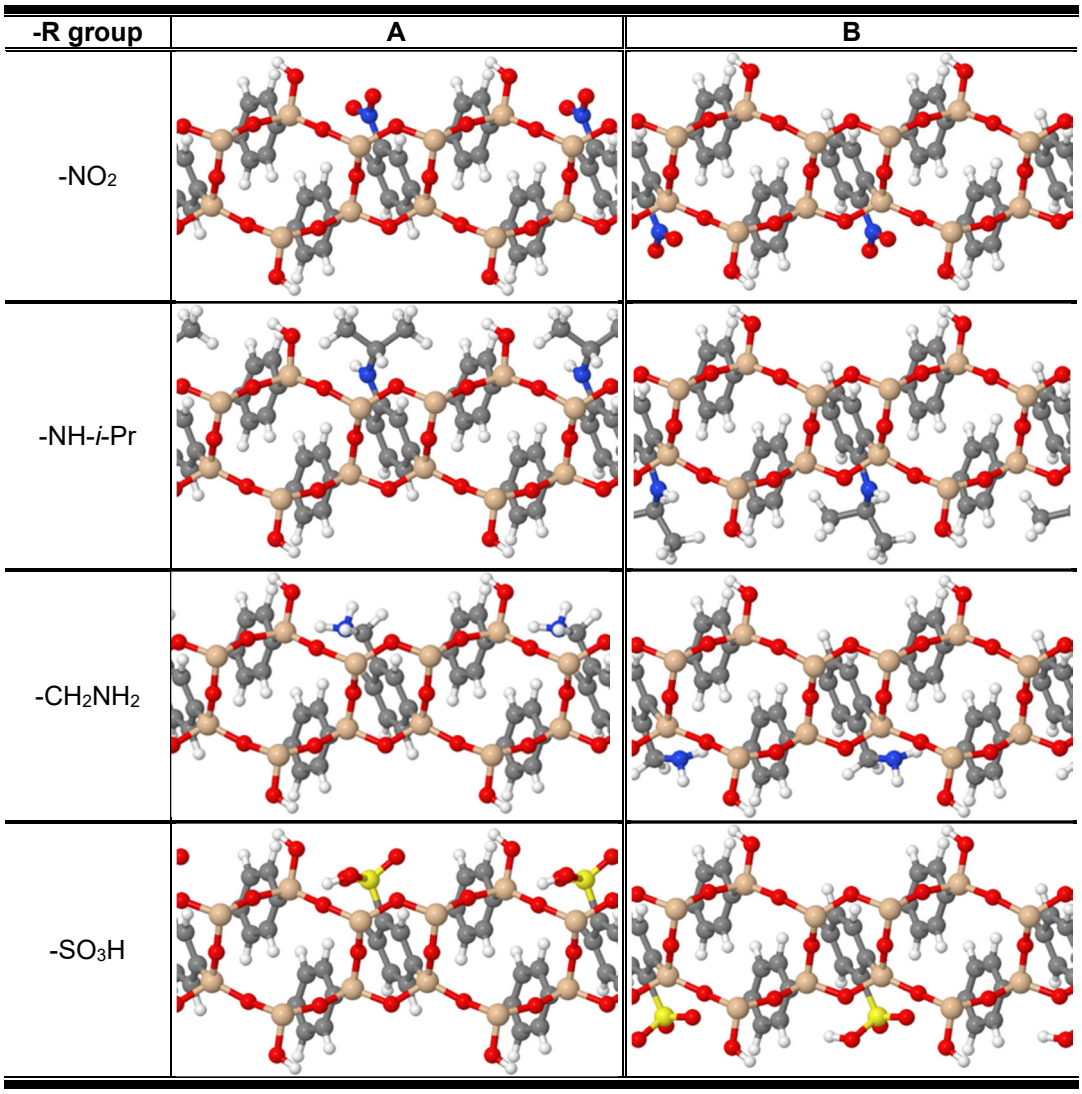

Figure 3.2.12. Side views of the two most favorable configurations for **R** functionalized PhPMOs.

The introduction of an *iso*-propylamine group in the phenylene bridge of PhPMO leads to significant increases in the adsorption energies calculated for both CO_2 (-7.8 kJ·mol^{-1}) and CH_4 (-4.7 kJ·mol^{-1}) when compared with the parent PhPMO value. However, relative to NH_2PhPMO, the CO_2 energy is only slightly increased, while that of methane increases more significantly. These changes are most likely a consequence of improved interactions of CO_2 with the amine moiety and of methane with the propyl groups. Indeed, some authors,[16,57] reported that propyl amines can improve the interaction with CO_2. Nevertheless, based on the DFT adsorption energies calculated in this work, the *i*-PrNHPhPMO material is anticipated to present similar CO_2 adsorption capacity but poorer selectivity for CO_2/CH_4 separations than those observed for NH_2PhPMO. Since an additional

synthetic step is required to obtain *i*-PrNHPhPMO, the latter becomes less interesting than NH_2PhPMO for this adsorption application.

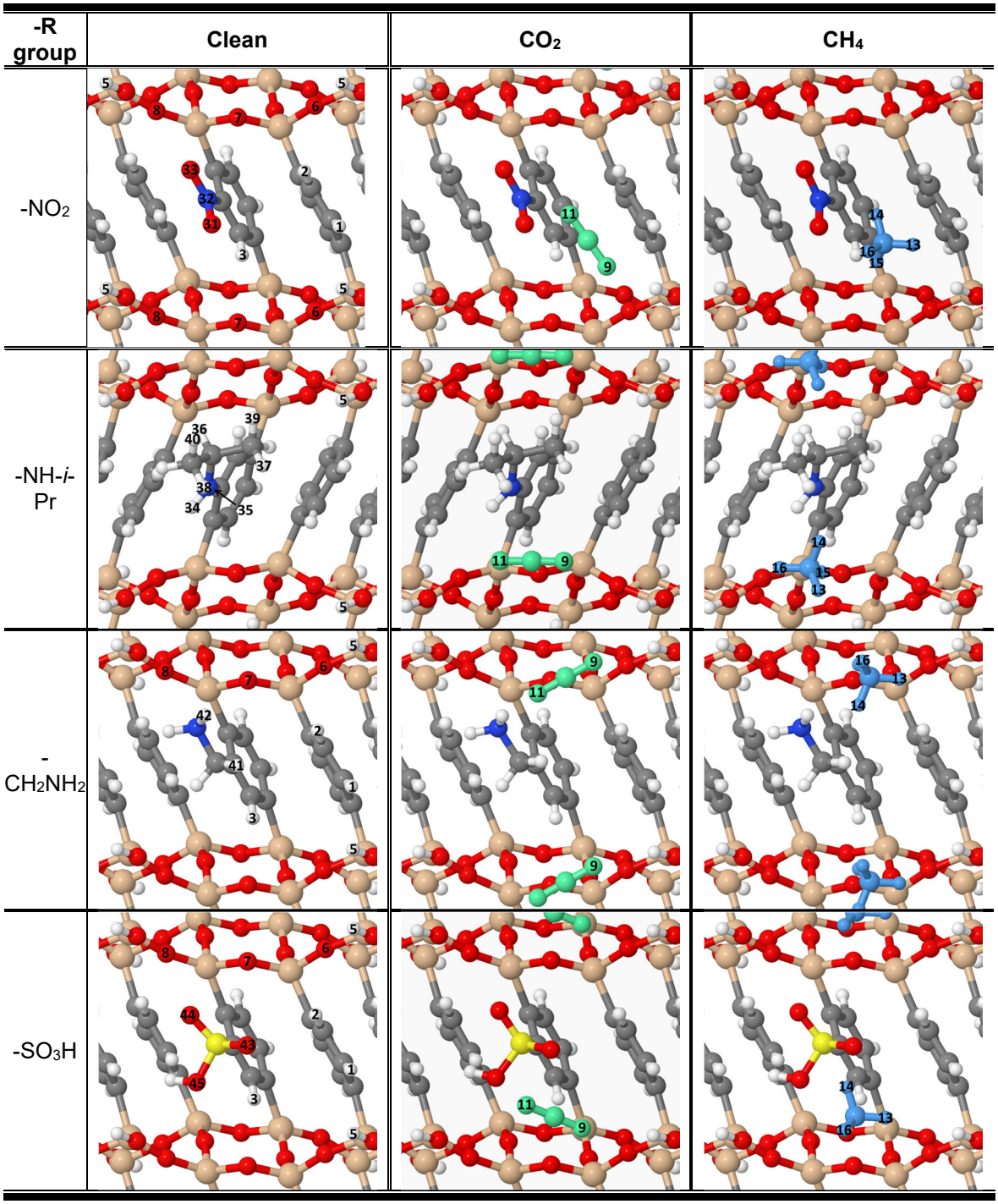

Figure 3.2.13. Top views of the most stable configurations for clean and CO_2 or CH_4 covered **R**PhPMOs optimized at the PBE-D2 level of theory. The numbering is the same as used in Table A2.6 containing selected geometrical parameters.

The material with the $–CH_2NH_2$ functional group shows the strongest adsorption energy with the CO_2 molecule of all PhPMOs studied in this work. The adsorption energy is -31.1 $kJ·mol^{-1}$, *i.e.*, an increase of -2.1 $kJ·mol^{-1}$ when compared with APTMS@PhPMO, suggesting that the former material may show more interesting CO_2 adsorption affinity than the latter without significantly changing the selectivity of the CO_2/CH_4 separation.

Finally, the calculated energies for the substitution of a hydrogen atom in the phenylene ring by a sulfonic acid group ($–SO_3H$) suggest that the resulting material will have adsorption profiles for CO_2 and CH_4 similar to those displayed by NH_2PhPMO and APTMS@NH_2PhPMO. Interestingly, the CO_2 molecule interacts with the hydrogen atom from the -SiOH group but not with that from the $–SO_3H$ group. This suggests that the interaction with the former is more important and that the quite short distance between the –SiOH and the $-SO_3H$ groups hinders the formation of simultaneous contacts with these two groups.

3.2.4 Conclusions

PhC_{12}PMOs functionalized with different types of amines were successfully prepared and characterized. The pristine and amine-functionalized PhC_{12}PMO materials exhibit both meso- and molecular-scale orders observed by PXRD. These materials were tested for adsorption of pure CO_2 and CH_4 at 25 and 35 °C. All prepared materials presented much higher CO_2 adsorption than that of CH_4. The introduction of amines into the PhC_{12}PMO material generally gave rise to an increase in the quantity of adsorbed CO_2 over the studied pressure range. More importantly, it significantly increased the Henry's constants of CO_2, growing in the order PhC_{12}PMO < NH_2PhC_{12}PMO < APTMS@NH_2PhC_{12}PMO < APTMS@PhC_{12}PMO, *i.e.*, the APTMS@PhC_{12}PMO material has more affinity for CO_2 than any other PMO material. Thus, it was observed that the type of amine presents a dominant effect on the CO_2 sorption affinity, more so than the nitrogen content in the PMO channels, demonstrating that alkyl amines interact more favorably with CO_2 than aromatic amines. Furthermore, the observed reduction in surface area and pore volume upon functionalization is more than compensated by the increased affinity under the conditions studied here. After the adsorption study, the chemical integrity of the amine modified PMOs was evaluated by ^{13}C CP-MAS and ^{15}N CP-MAS NMR, indicating that PMO materials release the CO_2 after activation and can be reused.

Periodic DFT calculations were successfully used for the first time to evaluate the behavior of different kinds of amine-functionalized PhPMO on the CO_2 and CH_4 adsorption and correlated with the Henry's constants. The same trend was found in both DFT calculations and gas adsorption measurements, showing that this type of theoretical studies can be used to predict if a chemical modification of the PMO promotes an increase in the selectivity of CO_2 relative to CH_4. Furthermore, DFT calculation were also used to studied the preferential adsorption sites and adsorption energies of CO_2 and CH_4 molecules on PMOs functionalized in the phenylene moieties with different groups (–NO_2, –NH-*i*-Pr,–CH_2NH_2, and –SO_3H), in order to guide the synthesis of new promising materials. It was found that the PhPMO functionalized with CH_2NH_2 is most likely to enhance CO_2 adsorption without changing significantly the adsorption of CH_4, and is thus a promising candidate for future experimental studies.

3.3 Bibliography

1 A.E. Rodrigues, C.A. Grande, Biogas to fuel by vacuum pressure swing adsorption I. Behavior of equilibrium and kinetic-based adsorbents. *Ind Eng Chem Res*. **2007**, 46: 4595–4605.

2 R. Babarao, Z. Hu, J. Jiang, S. Chempath, S.I. Sandler, Storage and separation of CO_2 and CH_4 in silicalite, C168 schwarzite, and IRMOF-1: A comparative study from Monte Carlo simulation. *Langmuir*. **2007**, 23: 659–666.

3 M.B. Kim, Y.S. Bae, D.K. Choi, C.H. Lee, Kinetic separation of landfill gas by a two-bed pressure swing adsorption process packed with carbon molecular sieve: Nonisothermal operation. *Ind Eng Chem Res*. **2006**, 45: 5050–5058.

4 X. Peng, W. Wang, R. Xue, Z. Shen, Adsorption separation of CH_4/CO_2 on mesocarbon microbeads: Experiment and modeling. *AIChE J*. **2006**, 52: 994–1003.

5 V. Goetz, O. Pupier, A. Guillot, Carbon dioxide-methane mixture adsorption on activated carbon. *Adsorption*. **2006**, 12: 55–63.

6 H. Yi, F. Li, P. Ning, X. Tang, J. Peng, Y. Li, H. Deng, Adsorption separation of CO_2, CH_4, and N_2 on microwave activated carbon. *Chem Eng J*. **2013**, 215–216: 635–642.

7 D.M. D'Alessandro, B. Smit, J.R. Long, Carbon dioxide capture: Prospects for new materials. *Angew Chem*. **2010**, 49: 6058–6082.

8 G.D. Pirngruber, L. Hamon, S. Bourrelly, P.L. Llewellyn, E. Lenoir, V. Guillerm, C. Serre, T. Devic, A method for screening the potential of MOFs as CO_2 adsorbents in pressure swing adsorption processes. *ChemSusChem*. **2012**, 5: 762–776.

9 S. Cavenati, C.A. Grande, A.E. Rodrigues, Removal of carbon dioxide from natural gas by vacuum swing adsorption. *Energy Fuels*. **2006**, 20: 2648–2659.

10 S. Cavenati, C.A. Grande, A.E. Rodrigues, Adsorption equilibrium of methane, carbon dioxide, and nitrogen on zeolite 13X at high pressures. *J Chem Eng Data*. **2004**, 49: 1095–1101.

11 P. Li, F. Handan Tezel, Adsorption separation of N_2, O_2, CO_2 and CH_4 gases by β-zeolite. *Micropor Mesopor Mater*. **2007**, 98: 94–101.

12 J.-M. Leyssale, G.K. Papadopoulos, D.N. Theodorou, Sorption thermodynamics of CO_2, CH_4 , and their mixtures in the ITQ-1 zeolite as revealed by molecular simulations. *J Phys Chem B*. **2006**, 110: 22742–22753.

13 E.L. First, M.M.F. Hasan, C.A. Floudas, Discovery of novel zeolites for natural gas purification through combined material screening and process optimization. *AIChE J*. **2014**, 60: 31–33.

14 M.L. Pinto, J. Pires, J. Rocha, Porous materials prepared from clays for the upgrade of landfill gas. *J Phys Chem C*. **2008**, 112: 14394–14402.

15 J. Pires, V.K. Saini, M.L. Pinto, Studies on selective adsorption of biogas components on pillared clays : Approach for biogas improvement. *Environ Sci Technol*. **2008**, 42: 8727–8732.

16 Q. Xue, Y. Liu, Mixed-amine modified SBA-15 as novel adsorbent of CO_2 separation for biogas upgrading. *Sep Sci Technol*. **2011**, 46: 679–686.

17 X. Liu, L. Zhou, X. Fu, Y. Sun, W. Su, Y. Zhou, Adsorption and regeneration study of the mesoporous adsorbent SBA-15 adapted to the capture/separation of CO_2 and CH_4. *Chem Eng Sci*. **2007**, 62: 1101–1110.

18 T. Asefa, M.J. MacLachlan, N. Coombs, G.A. Ozin, Periodic mesoporous organosilicas with organic groups inside the channel walls. *Nature*. **1999**, 402: 867–871.

19 S. Inagaki, S. Guan, Y. Fukushima, T. Ohsuna, O. Terasaki, Novel mesoporous materials with a uniform distribution of organic groups and inorganic oxide in their frameworks. *J Am Chem Soc*. **1999**, 121: 9611–9614.

20 B. Melde, B. Holland, C. Blanford, A. Stein, Mesoporous sieves with unified hybrid inorganic/organic frameworks. *Chem Mater*. **1999**, 11: 3302–3308.

21 P. Van der Voort, D. Esquivel, E. De Canck, F. Goethals, I. Van Driessche, F.J. Romero-Salguero, Periodic mesoporous organosilicas: from simple to complex bridges; a comprehensive overview of functions, morphologies and applications. *Chem Soc Rev*. **2013**, 42: 3913–3955.

22 P. Ferreira, C. Bispo, M.A.O. Lourenço, J.R.B. Gomes, N. Bion, K.D.O. Vigier, F. Jérôme, Making periodic mesoporous organosilicas functional materials. In: M. Aliofkhazraei (ed.). Comprehensive guide for mesoporous materials, Vol. 4: application and commercialization. Nova Science Publishers, Inc., **2015**: 261–295.

23 F. Hoffmann, M. Fröba, Vitalising porous inorganic silica networks with organic functions-PMOs and related hybrid materials. **2011**, 40: 608–620.

24 B. Camarota, P. Ugliengo, E. Garrone, C.O. Arean, M.R. Delgado, S. Inagaki, B. Onida, IR and computational characterization of CO adsorption on a model surface, the phenylene periodic mesoporous organosilca with crystalline walls. *J Phys Chem C*. **2008**, 112: 19560–19567.

25 K. Sim, N. Lee, J. Kim, E.-B. Cho, C. Gunathilake, M. Jaroniec, CO_2 adsorption on amine-functionalized periodic mesoporous benzenesilicas. *ACS Appl Mater Inter*. **2015**, 7: 6792–6802.

26 N. Bion, P. Ferreira, A. Valente, I.S. Gonçalves, J. Rocha, Ordered benzene-silica hybrids with molecular-scale periodicity in the walls and different mesopore sizes. *J Mater Chem*. **2003**, 13: 1910–1913.

27 M. Ohashi, M.P. Kapoor, S. Inagaki, Chemical modification of crystal-like mesoporous phenylene-silica with amino group. *Chem Commun*. **2008**, 7: 841–843.

28 S. Inagaki, S. Guan, T. Ohsuna, O. Terasaki, An ordered mesoporous organosilica hybrid material with a crystal-like wall structure. *Nature*. **2002**, 416: 304–307.

29 R.J.P. Corriu, J.J.E. Morea, P. Thepot, M.W. Chi Man, New mixed organic-inorganic polymers: hydrolysis and polycondensation of bis(trimethoxysilyl) organometallic precursors. *Chem Mater*. **1992**, 4: 1217–1224.

30 M. Jorge, M. Fischer, J.R.B. Gomes, C. Siquet, J.C. Santos, A.E. Rodrigues, Accurate model for predicting adsorption of olefins and paraffins on MOFs with open metal sites. *Ind Eng Chem Res*. **2014**, 53: 15475–15487.

31 P.K. Jal, S. Patel, B.K. Mishra, Chemical modification of silica surface by immobilization of functional groups for extractive concentration of metal ions. *Talanta*. **2004**, 62: 1005–1028.

32 U. Martinez, G. Pacchioni, Interaction of CO, CO_2 and CH_4 with mesoporous organosilica: Periodic DFT calculations with dispersion corrections. *Micropor Mesopor Mater*. **2010**, 129: 62–67.

33 Y. Park, D.-K. Moon, Y.-H. Kim, H. Ahn, C.-H. Lee, Adsorption isotherms of CO_2, CO, N_2, CH_4, Ar and H_2 on activated carbon and zeolite LiX up to 1.0 MPa. *Adsorption*. **2014**, 20: 631–647.

34 J.R. Karra, B.E. Grabicka, Y.-G. Huang, K.S. Walton, Adsorption study of CO_2, CH_4, N_2, and H_2O on an interwoven copper carboxylate metal-organic framework (MOF-14). *J Colloid Interf Sci*. **2013**, 392: 331–336.

35 P.D.C. Dietzel, V. Besikiotis, R. Blom, Application of metal–organic frameworks

with coordinatively unsaturated metal sites in storage and separation of methane and carbon dioxide. *J Mater Chem*. **2009**, 19: 7362–7370.

36 S.A. Peter, G. V. Baron, J. Gascon, F. Kapteijn, J.F.M. Denayer, Dynamic desorption of CO_2 and CH_4 from amino-MIL-53(Al) adsorbent. *Adsorption*. **2013**, 19: 1235–1244.

37 X. Xu, X. Zhao, L. Sun, X. Liu, Adsorption separation of carbon dioxide, methane, and nitrogen on Hβ and Na-exchanged β-zeolite. *J Nat Gas Chem*. **2008**, 17: 391–396.

38 X. Wu, M. Niknam Shahrak, B. Yuan, S. Deng, Synthesis and characterization of zeolitic imidazolate framework ZIF-7 for CO_2 and CH_4 separation. *Micropor Mesopor Mater*. **2014**, 190: 189–196.

39 M.D. Rad, S. Fatemi, S.M. Mirfendereski, Development of T type zeolite for separation of CO_2 from CH_4 in adsorption processes. *Chem Eng Res Des*. **2012**, 90: 1687–1695.

40 J. Shang, G. Li, R. Singh, Q. Gu, K.M. Nairn, T.J. Bastow, N. Medhekar, C.M. Doherty, A.J. Hill, J.Z. Liu, P.A. Webley, Discriminative separation of gases by a "molecular trapdoor" mechanism in chabazite zeolites. *J Am Chem Soc*. **2012**, 134: 19246–19253.

41 A.L. Myers, Equation of state for adsorption of gases and their mixtures in porous materials. *Adsorption*. **2003**, 9: 9–16.

42 G. Kresse, J. Hafner, Ab initio molecular dynamics for liquid metals. *Phys Rev B*. **1993**, 47: 558–561.

43 G. Kresse, J. Furthmüller, Efficiency of ab-initio total energy calculations for metals and semiconductors using a plane-wave basis set. *Comput Mater Sci*. **1996**, 6: 15–50.

44 G. Kresse, Efficient iterative schemes for ab initio total-energy calculations using a plane-wave basis set. *Phys Rev B*. **1996**, 54: 11169–11186.

45 J.P. Perdew, K. Burke, M. Ernzerhof, Generalized gradient approximation made simple. *Phys Rev Lett*. **1996**, 77: 3865–3868.

46 S. Grimme, Semiempirical GGA-type density functional constructed with a long-range dispersion correction. *J Comput Chem*. **2006**, 27: 1787–1799.

47 J.P.P. Ramalho, J.R.B. Gomes, F. Illas, Accounting for van der Waals interactions between adsorbates and surfaces in density functional theory based calculations: selected examples. *RSC Adv*. **2013**, 3: 13085–13100.

48 J.L.C. Fajín, M.N.D.S. Cordeiro, J.R.B. Gomes, F. Illas, On the need for spin polarization in heterogeneously catalyzed reactions on nonmagnetic metallic surfaces. *J Chem Theory Comput*. **2012**, 8: 1737–1743.

49 G. Kresse, D. Joubert, From ultrasoft pseudopotentials to the projector augmented-wave method. *Phys Rev B*. **1999**, 59: 1758–1775.

50 A. Comotti, S. Bracco, P. Valsesia, L. Ferretti, P. Sozzani, 2D multinuclear NMR, hyperpolarized xenon and gas storage in organosilica nanochannels with crystalline order in the walls. *J Am Chem Soc*. **2007**, 129: 8566–8576.

51 B.B.J. Melde, B.B.T. Holland, C.C.F.C.F.C. Blanford, A. Stein, Mesoporous sieves with unified hybrid inorganic/organic frameworks. *Chem Mater*. **1999**, 11: 3302–3308.

52 K.S.W. Sing, D.H. Everett, R.A.W. Haul, L. Moscou, R.A. Pierotti, J. Rouquerol, T. Siemieniewaska, Reporting physisorption data for gas/solid systems with special reference to the determination of surface area and porosity. *Pure Appl Chem*. **1985**, 57: 603–619.

53 J.S. Beck, J.C. Vartuli, W.J. Roth, M.E. Leonowicz, C.T. Kresge, K.D. Schmitt, C.T.W. Chu, D.H. Olson, E.W. Sheppard, A new family of mesoporous molecular sieves prepared with liquid crystal templates. *J Am Chem Soc*. **1992**, 114: 10834–10843.

54 R.W. Zwanzig, Influence of molecular electric quadrupole moments on dielectric constants. *J Chem Phys*. **1956**, 25: 211–216.

55 A.L. Myers, J.M. Prausnitz, Thermodynamics of mixed-gas adsorption. *AIChE J*. **1965**, 11: 121–127.

56 M.L. Pinto, L. Mafra, J.M. Guil, J. Pires, J. Rocha, Adsorption and activation of CO_2 by amine-modified nanoporous materials studied by solid-state NMR and $^{13}CO_2$ adsorption. *Chem Mater*. **2011**, 23: 1387–1395.

57 E. De Canck, I. Ascoop, A. Sayari, P. Van Der Voort, Periodic mesoporous organosilicas functionalized with a wide variety of amines for CO_2 adsorption. *Phys Chem Chem Phys*. **2013**, 15: 9792–9799.

Chapter 4 – Alternative PMOs for CO_2/CH_4 separation

In this Chapter, it will be described the tuning of the chemical, textural and physical properties of PMOs through the use of atomic layer deposition (ALD) and pyrolysis methodologies for creating novel adsorbent materials. The ALD technology was used to add active aluminium species to the walls of different phenylene-silica materials. Phenylene- and biphenylene-PMOs were thermally treated in nitrogen atmosphere to create graphitized materials with different porosities. These two kinds of methodologies were used to generate different surface interfaces into the PMOs, allowing the study of their effect on the CO_2 and CH_4 pure adsorption.

4.1 Turning periodic mesoporous organosilicas selective to CO_2/CH_4 separation: deposition of aluminium oxide by atomic layer deposition

Adapted from:

Mirtha A. O. Lourenço, Ricardo M. Silva, Rui F. Silva, Nicola Pinna, Stephane Pronier, João Pires, José R. B. Gomes, Moisés L. Pinto, Paula Ferreira

Turning periodic mesoporous organosilicas selective to CO_2/CH_4 separation: deposition of aluminium oxide by atomic layer deposition

J. Mater. Chem. A, **2015**, 3: 22860-22867

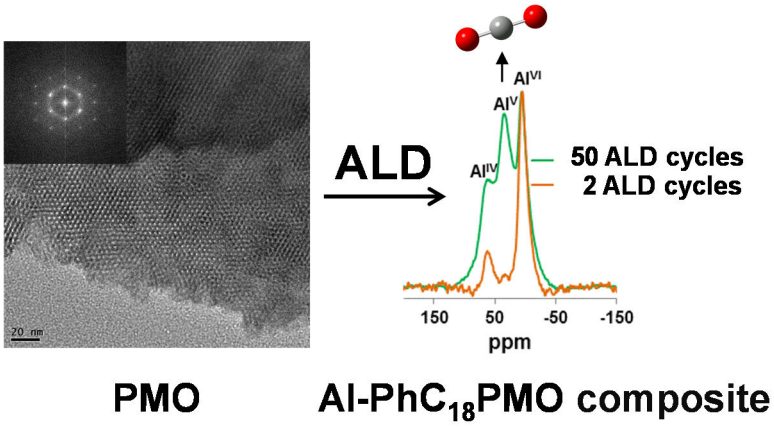

My direct contribution:

I declare that I have prepared the BTEB precursor and the starting PMO material. The ALD depositions were performed by Ricardo Silva under supervision of Nicola Pinna and Rui F. Silva. Stephane Pronier collected the TEM images. I have characterized all the materials prior and after the deposition of the aluminium oxide. Using a volumetric apparatus, I also carried out at the University of Lisbon the CO_2 and CH_4 pure adsorption experiments under the guidance of Moisés L. Pinto and João Pires.

4.1.1 Motivation

As it was seen in Chapter 3, PMOs with phenylene-bridge ($PhC_{18}PMO$) can be easily modified[1–3] to turn its surface prompt to adsorb selectively CO_2. To date, enhancement of the selectivity of porous materials towards CO_2 has mainly been attempted by organic modifications.[4–11] Zeolites and MOFs with aluminium (Al) open centres incorporated into their matrix structure have been shown to improve the adsorption of CO_2.[12–18] Herein, it is described for the first time the use of atomic layer deposition (ALD) to modify the $PhC_{18}PMO$ surface with Al_2O_3 in order to design a novel CO_2 adsorbent. ALD comprises a sequence of self-limiting chemical reactions between gas-phase precursor molecules and the solid surface. The self-limiting nature of ALD gives rise to a conformal growth and an additional control over the total stack thickness. The film thickness in a planar substrate can be determined precisely by the number of coating cycles.[19] In this work, by varying the number of ALD deposition cycles, the quantity of aluminium oxide deposited as well as the type of aluminium species on the $PhC_{18}PMO$ were studied.

4.1.2 Experimental details

PMO synthesis

The mesoporous phenylene bridged PMO was synthesized according to the literature procedures with slight modifications.[20–22] The synthesis of $PhC_{18}PMO$ started with the hydrolysis and condensation of home-made 1,4-bis(triethoxysilyl)benzene (BTEB, *c.f.* Sub-chapter 2.1, 4.78 g) precursor[23] in the presence of octadecyltrimethylammonium bromide surfactant template (C_{18}-TMA, 4.8 g) in 124 mL of distilled water with 8 mL of 6 M NaOH solution. This solution was kept for 20 minutes in an ultrasonic vessel and stirred for 24 hours at room temperature. After 24 hours of ageing, the solution was transferred to Teflon-lined stain-steel autoclave for hydrothermal treatment. The hydrothermal treatment begins with a pre-heating of the autoclave in an oven at 200 °C during 40 minutes, and then it was transferred to another oven at 100 °C. After 24 hours, the solid was filter and washed. The template was extracted by an ethanol/HCl solution to obtain a free-pore $PhC_{18}PMO$.

Al_2O_3-PMO preparation

ALD was performed with a cross flow home-made reactor working in continuous mode, using water and trimethylaluminium (Sigma Aldrich, 97%) as precursors. The precursors were alternately introduced through ALD pneumatic valves from their reservoirs, which were kept at room temperature. Alumina (Al_2O_3) was deposited onto the $PhC_{18}PMO$ at 200 °C, under 100 sccm of N_2 flow, using reactant pulse times of 0.05 s and 0.10 s for water and trimethylaluminium, respectively, and 30 s between pulse times. The typical operating pressures varied from 1.6 to 2.0 Pa during the precursor pulses. The quantity of Al_2O_3 deposited by ALD onto the $PhC_{18}PMO$ was determined by direct measurements performed before and after the ALD coating using an analytical balance with a precision of 0.1 mg. The resultant composite materials are denoted from now on as Al-$PhC_{18}PMO$#*x*, where *x* corresponds to the number of deposition cycles.

An additional sample, $PhC_{18}PMO$+Al_2O_3_a was prepared by physical mixture of $PhC_{18}PMO$ and amorphous Al_2O_3. The amorphous alumina was synthetized according to the literature[24] with some experimental modifications. The aluminium isopropoxide (Al(O*i*Pr)$_3$, Aldrich, 1 g) was solubilized in ethanol (EtOH, PA, Carlo Erba, 9.75 mL). Then, 0.46 g of nitric acid (HNO_3, 65 %, Panreac) was added to the solution, and the solution was vigorous stirred overnight at room temperature (RT). Then, the solution was transferred to an oven for 2 days at 60 °C to induce the controlled evaporation of the solvent and to obtain the dry material. The obtained material was calcined at 400 °C during 4 h with a heating ramp of 5 °C·min^{-1}.

Materials characterization

The physical, textural and chemical properties of the pristine $PhC_{18}PMO$ and Al-$PhC_{18}PMO$ composites were evaluated by SEM, scanning transmission electron microscopy (STEM), PXRD, N_2 sorption isotherms, TEM, FTIR, ^{29}Si MAS and CP-MAS NMR, ^{13}C CP-MAS and ^{27}Al MAS NMR spectroscopies. The thermal stability of materials was evaluated by TGA. Description of the experimental conditions is presented at Chapter 2 and some of the characterization data is presented in Appendix B.

High pressure adsorption of CO_2 and CH_4

Adsorption experiments of CO_2 and CH_4 on selected samples were conducted up to 1000 kPa at 25 °C, using the volumetric method using the procedure described in Sub-chapter 2.6. The non-ideality of the gas phase was taken into account by using the second and third virial

coefficients, and the experimental excess adsorbed amounts were converted to the absolute adsorbed amounts by taking into account the porous volume of the material and the density of the gas phase using the virial coefficients. Selectivity values were estimated using a method proposed by Myers[25] and the implementation is described in detail in previous works[26].

4.1.3 Results and discussion

The influence of ALD deposition cycles on the morphological changes of $PhC_{18}PMO$ was investigated with a particular focus on the decrease of the surface area and pore volume. A series of Al_2O_3 depositions onto the $PhC_{18}PMO$ were performed using different number of cycles (2, 10, 20, 50 and 100 cycles). Weight gain measurements were performed on 25 mg $PhC_{18}PMO$ samples after the ALD coating to establish a relation with the number of cycles and the quantity of Al_2O_3 (here denoted as Al) deposited as shown in Table 4.1.1. This Table shows that the weight gain increases with the number of coating cycles.

Table 4.1.1. Weight gain measurements between 0 and 100 Al_2O_3 ALD cycles and Si/Al ratios determined by EDS.

Sample	**Weight** (mg)	***Δ* weight** (mg)	$[Si/Al]_{EDS}$
$PhC_{18}PMO$	25.0	-	0
Al-$PhC_{18}PMO$#2	n.m.[a]	n.m.[a]	n.m.[a]
Al-$PhC_{18}PMO$#10	28.7	+ 3.7	10.47
Al-$PhC_{18}PMO$#20	31.8	+ 6.8	2.54
Al-$PhC_{18}PMO$#50	32.6	+ 7.6	1.87
Al-$PhC_{18}PMO$#100	35.3	+ 10.3	0.94

[a]not measured.

The Si/Al ratios determined by EDS (Table 4.1.1) reveal that the Al contents in the $PhC_{18}PMO$ increase with the number of applied ALD cycles. The difference between these values proves that the ALD precursors modified the pristine $PhC_{18}PMO$ material. It is interesting to note that Si/Al ratio does not decrease linearly with the weight gain.

The top surface morphology of the $PhC_{18}PMO$ coated with Al_2O_3 after 50 ALD cycles, *i.e.*, Al-$PhC_{18}PMO$#50 sample, was analysed from SEM and STEM bright field images (Figure 4.1.1a and b) and corresponding EDS elemental mapping, which show the homogeneous distribution at µm-scale of both aluminium and silicon on the composite (Figure 4.1.1c and d).

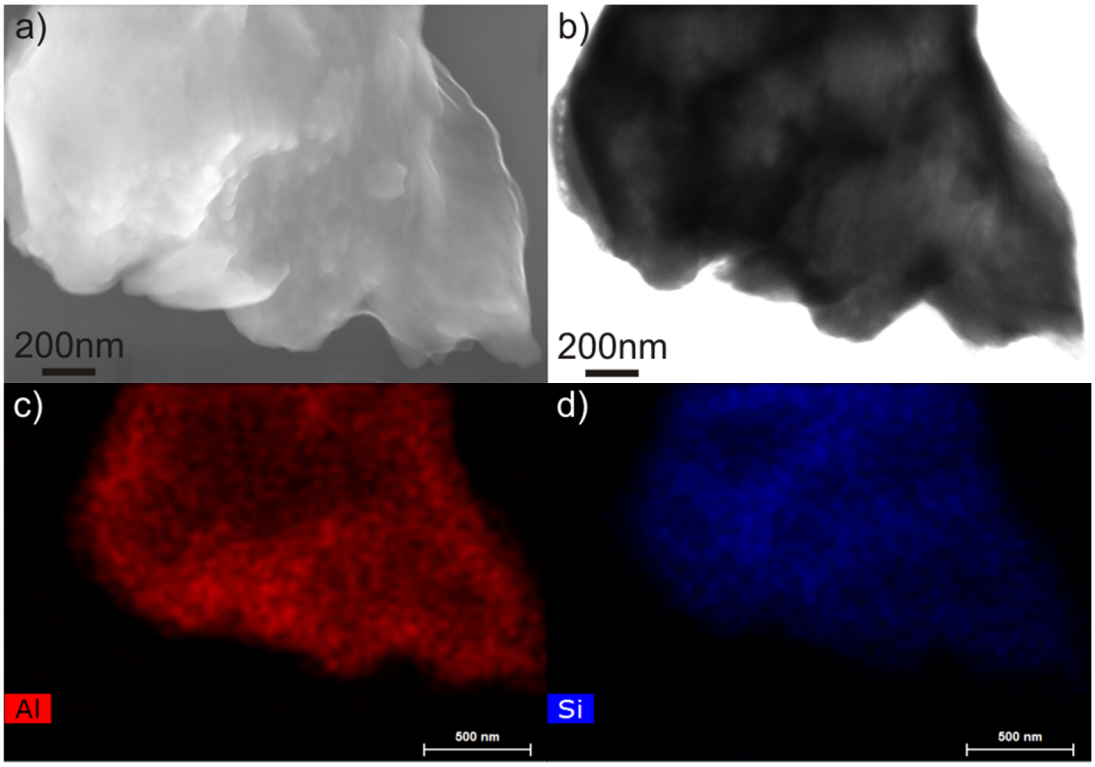

Figure 4.1.1. a) SEM and b) STEM bright field micrograph images of Al-PhC$_{18}$PMO#50. The elemental map reveals the homogeneous distribution of aluminium (c) and of silicon (d).

PXRD patterns of PhC$_{18}$PMO, Al-PhC$_{18}$PMO#2, Al-PhC$_{18}$PMO#10, Al-PhC$_{18}$PMO#20, Al-PhC$_{18}$PMO#50 and Al-PhC$_{18}$PMO#100, *c.f.* Figure 4.1.2, show the two-dimensional hexagonal symmetry (*p6mm*) lattice for all materials due to the presence of the first strong low-angle (100) reflection with d_{100} = 4.82 nm and the two much less intense (110) and (200) peaks. It is possible to observe in Figure 4.1.2 the decrease of intensity of the peaks with the increase of the number of Al_2O_3 deposition cycles. In addition, Figure 4.1.2 and numerical values in Table 4.1.2 display a slight shift to higher angles in the d_{100} diffraction peak as the number of deposition cycles increase. The peak at d = 0.762 nm corresponds to the molecular-scale crystal-like structure. The reduction in the intensity of this peak is also observed upon modification by Al_2O_3. A slight shift to higher angles is again observed. Peaks associated to both meso- and molecular- scale periodicities are preserved after modification suggesting that the PhC$_{18}$PMO structure is not affected by the ALD conditions.

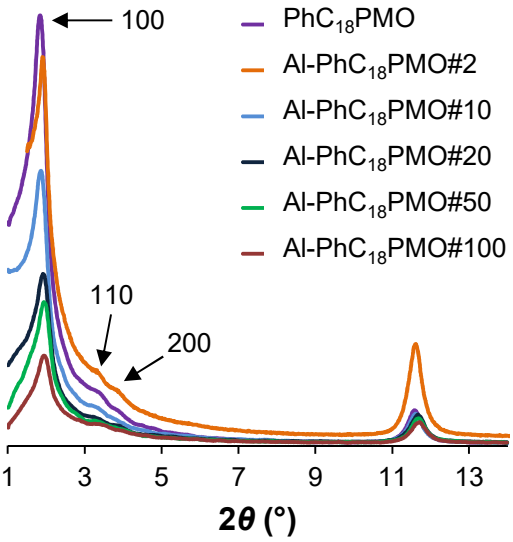

Figure 4.1.2. X-ray diffraction patterns of $PhC_{18}PMO$, Al-$PhC_{18}PMO$#2, Al-$PhC_{18}PMO$#10, Al-$PhC_{18}PMO$#20, Al-$PhC_{18}PMO$#50 and Al-$PhC_{18}PMO$#100.

For CO_2 adsorption application, it is of crucial importance that the pores are still accessible after ALD modification. The low temperature (-196 °C) nitrogen adsorption–desorption isotherms and pore size distribution (PSD) curves (Table 4.1.2 and Figure B1.2, Appendix B) confirm the type IV isotherms (IUPAC classification) for $PhC_{18}PMO$ and ALD modified $PhC_{18}PMO$ with narrow distribution of pore sizes, typically observed for conventional mesoporous materials such as MCM-41, with a hexagonal structure. After 100 cycles of Al_2O_3 deposition, a significant decrease in the N_2 adsorbed amounts is observed. This may indicate that some of the pores are clogged.

Table 4.1.2. Physical properties of $PhC_{18}PMO$, Al-$PhC_{18}PMO$#2, Al-$PhC_{18}PMO$#10, Al-$PhC_{18}PMO$#20, Al-$PhC_{18}PMO$#50 and Al-$PhC_{18}PMO$#100.

Sample	d_{100} (nm)	a^a (nm)	S_{BET} ($m^2 \cdot g^{-1}$)	V_P ($cm^3 \cdot g^{-1}$)	$d_P{}^b$ (nm)
$PhC_{18}PMO$	4.82	5.57	971	1.25	3.85
Al-$PhC_{18}PMO$#2	4.65	5.36	645	0.79	3.81
Al-$PhC_{18}PMO$#10	4.72	5.45	648	0.52	3.82
Al-$PhC_{18}PMO$#20	4.62	5.34	513	0.39	3.74
Al-$PhC_{18}PMO$#50	4.57	5.28	445	0.34	3.73
Al-$PhC_{18}PMO$#100	4.53	5.23	204	0.18	3.74

[a]Unit cell parameter calculated as ($a = 2d_{100}/\sqrt{3}$). [b]Pore width obtained from the maximum on the BJH pore size distribution calculated on the basis of adsorption data.

Table 4.1.2 reveals a sharp decrease of the surface area and pore volumes with the growth of the amount of ALD Al (approximately linear). The slight decrease in the pore diameter may indicate that just a little amount of Al_2O_3 is deposited inside the pores. From our results,

the Al_2O_3 is mostly deposited on the top surface area of the particles leading to partial clogging of the pores. This effect was most pronounced for the sample Al-PhC_{18}PMO#100. The TEM cross-section image and corresponding EDS analyses of the pristine PhC_{18}PMO and the composites Al-PhC_{18}PMO#2, Al-PhC_{18}PMO#50 and Al-PhC_{18}PMO#100 are shown in Figures 4.1.3 and B1.3. The collected images show the hexagonal arrangement of the pores for all materials suggesting that the Al modification using ALD technology is not contributing to disrupt of the pore structure of the parent PhC_{18}PMO (*c.f.* Figure 4.1.3), which is in agreement with the PXRD diffractograms (*c.f.* Figure 4.1.2). Additionally, it is also possible to observe the mass contrast in the images of the Al-PhC_{18}PMO composites. The darker zones correspond to the Al content inserted into the pores or present at the surface of the materials, Figures 4.1.3 (Al-PhC_{18}PMO#100) and B1.3 (Appendix B). TEM EDS analyses seem to indicate a low degree of aluminium impregnation inside the pores of the PhC_{18}PMO. The aluminium oxide is mostly deposited at the external surface of the particle for all composite materials, Figure B1.3 (Appendix B). This behaviour is more evident for the composite materials obtained with larger number of deposition cycles, *e.g.* Al-PhC_{18}PMO#50 and Al-PhC_{18}PMO#100. The insets illustrate the FFT of hexagonal arrangement of the pores of the composites.

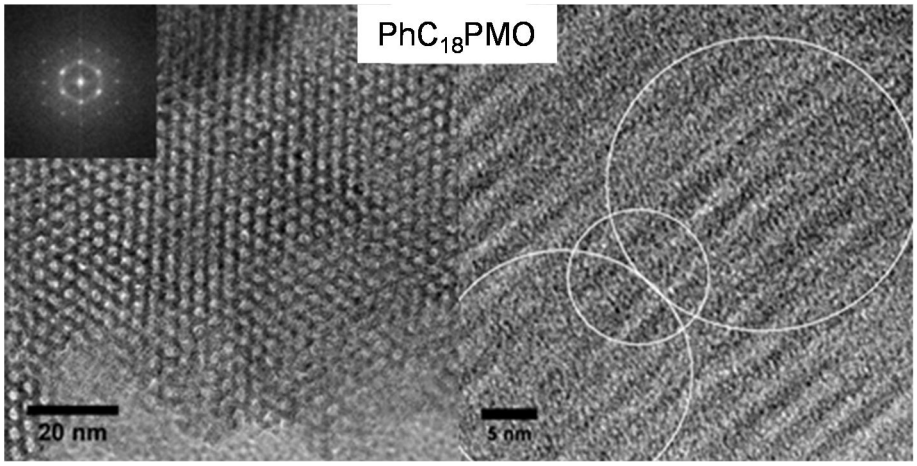

Figure 4.1.3. TEM cross-section images of PhC_{18}PMO, Al-PhC_{18}PMO#2, Al-PhC_{18}PMO#50 and Al-PhC_{18}PMO#100. In the left side is presented typically the view parallel to the porous channels, while the right side shows the view perpendicular to the channels. The circles in the top-right panel are used to better illustrate the molecular-scale periodicity. The insets show the FFT of the hexagonal arrangement of the pores. (Continues next page)

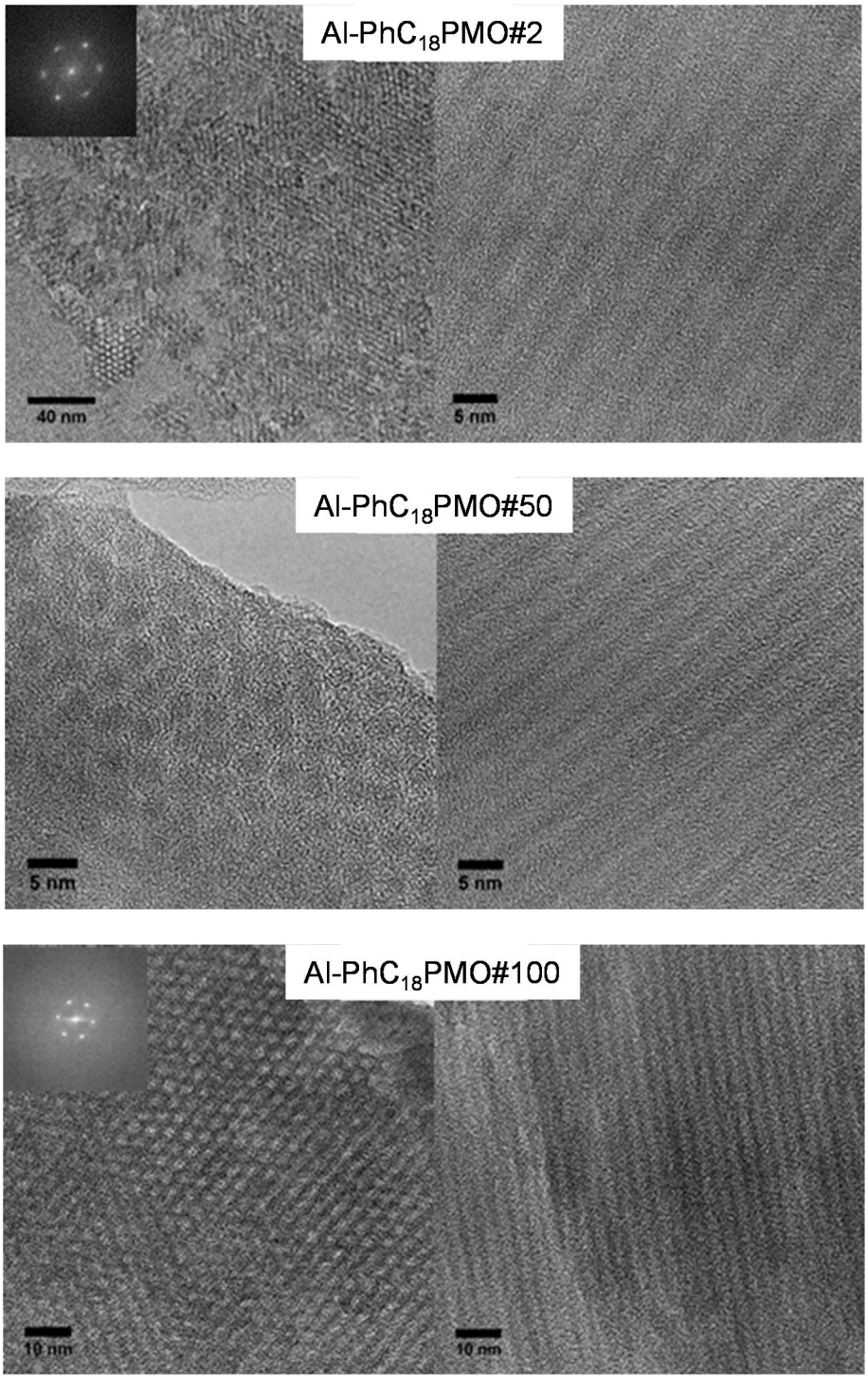

Figure 4.1.3. TEM cross-section images of $PhC_{18}PMO$, Al-$PhC_{18}PMO$#2, Al-$PhC_{18}PMO$#50 and Al-$PhC_{18}PMO$#100. In the left side is presented typically the view parallel to the porous channels, while the right side shows the view perpendicular to the channels. The circles in the top-right panel are used to better illustrate the molecular-scale periodicity. The insets show the FFT of the hexagonal arrangement of the pores.

Different techniques were employed for evaluating if any change in the chemistry of the material occurs upon the modification of the $PhC_{18}PMO$ material with different amounts of Al_2O_3. The spectra (Figure B1.4a) obtained with Fourier transform infrared spectroscopy (FTIR) show that the $PhC_{18}PMO$ parent material displays adsorption bands assignable to the phenylene ring vibrations (1300–2000 cm^{-1}) and strong adsorption bands (900-650 cm^{-1}), C–H species (2980-3060 cm^{-1}, Figure B1.4b), and stretching modes of silanol (3632 cm^{-1}, Figure B1.4b). The increase of the amount of Al_2O_3 deposited in the pristine $PhC_{18}PMO$ is observed in the FTIR spectra by the reduction of the intensity of the bands between 350 and 1200 cm^{-1}. The ^{29}Si and ^{13}C CP-MAS NMR spectra of Al-$PhC_{18}PMO$#50 (Figure B1.5 and Figure B1.6) were also collected for comparison with the already described pristine PMO.[20] ^{29}Si CP-MAS NMR spectrum of Al-$PhC_{18}PMO$#50 exhibits the typical peaks at *ca.* -81, -72 and -61 ppm attributed to T^3, T^2 and T^1 [T^m = $RSi(OSi)_m(OH)_{3-m}$] organosiliceous species, respectively, without any alteration comparing with the parent material.[2,20] The material obtained from deposition of Al_2O_3 by ALD at 200 °C does not present resonances in the region of the Q^n species [Q^n = $Si(OSi)_n(OH)_{4-n}$] proving that the C-Si bonds are intact. Table B1.1 shows the percentages of T^m species in $PhC_{18}PMO$ and Al-$PhC_{18}PMO$#50. These percentages are calculated from the deconvolution of the ^{29}Si MAS NMR spectra, using the common assumption of Gaussian distributions of isotropic chemical shifts for each type of T^m species. Usually, the overlapping of T^m resonances is noticed, leading to small variations between best-fit intensity parameters and, consequently, to uncertainties associated with the relative populations of the T^m sites. The degree of condensation is 59% for the $PhC_{18}PMO$ and 64% for the Al-$PhC_{18}PMO$#50 composite. The increase of approximately 5% in the T^3 silicon species and the reduction of T^2 site in the Al-$PhC_{18}PMO$#50 composite are probably due to some condensation of alumina to the free hydroxyl group of the T^2 silicon environment of the $PhC_{18}PMO$. Furthermore, ^{13}C CP-MAS NMR spectrum supports the preservation of the material chemistry displaying only one peak at *ca.* 133 ppm that is assigned to the carbons of the phenylene bridge. ^{27}Al MAS NMR spectrum (Figure 4.1.4) shows the presence of three peaks at 5, 38 and 62 ppm assigned to the Al^{VI} octahedral, Al^{V} bipyramidal and Al^{IV} tetrahedral coordinated aluminium, respectively. Note that the Al_2O_3 deposited by ALD is amorphous. However, the tetrahedral and the bipyramidal Al-sites can promote acidity in the material. This property can allow the use of Al-$PhC_{18}PMO$ composites

in CO_2/CH_4 separation once promotes the interaction between composite and the CO_2 quadrupole and consequently improves the selectivity.

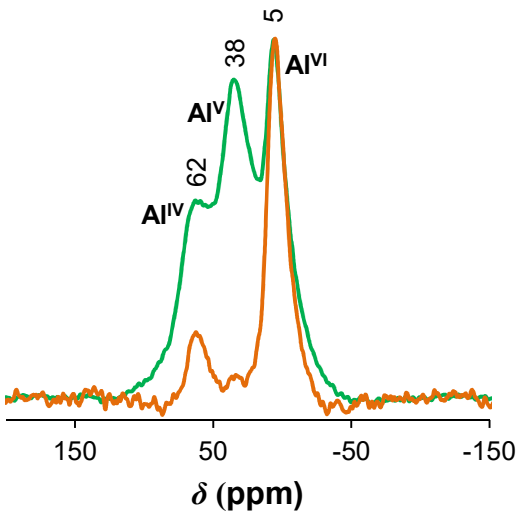

Figure 4.1.4. ^{27}Al MAS NMR spectra of Al-PhC_{18}PMO#2 (green line) and Al-PhC_{18}PMO#50 (orange line).

Figure 4.1.4 also shows the ^{27}Al MAS NMR spectrum of the Al-PhC_{18}PMO#2 composite. This material presents two main distinct peaks, which are assigned to the Al^{VI} octahedral and Al^{IV} tetrahedral coordinated aluminium species. A third peak attributed to pentacoordinated aluminium species (Al^{V}) grows in importance with the increase of the number of cycles, which is a sign of the formation of defects.

The TGA curve of Al-PhC_{18}PMO#50 (Figure B1.7) exhibits a first weight loss below 100 °C due to desorption of physisorbed water. It is possible to observe a 3 % weight loss from 100 to 250 °C due to the presence of a small quantity of non-extracted template. At 400 and 630 °C, it is possible to observe two weight losses of 23 % due to the decomposition and release of the organic moieties from the bridges of the PhC_{18}PMO material. Note that the pristine PhC_{18}PMO material presents a thermal stability up to 550 °C and above that temperature only one weight loss is observed.[2,20] Thus, the introduction of the Al content decreases the thermal stability of the material. This means that the degradation of the organic content is aided by the deposited Al_2O_3 in two steps due to the presence of different types of Al coordination. The first step of degradation of the phenylene bridges occurs probably due to the contact of infiltrated pentacoordinated alumina (Al^{V}) with the organic moieties of the PhC_{18}PMO. The other weight loss at 630 °C corresponds to the degradation and release of the remaining phenylene moieties. These organic moieties probably are in contact with the

octahedral alumina (Al^{VI}). Note that this temperature of degradation is superior to the temperature needed to promote the degradation of phenylene bridges of the pristine $PhC_{18}PMO$ (550 °C). This picture is supported by the larger stability of the Al^{VI} species which presumably protect the organic bridges in their vicinity with a concomitant increase in their thermal stability.

High pressure adsorption of methane and carbon dioxide was performed on samples Al-$PhC_{18}PMO$#50, Al-$PhC_{18}PMO$#2 and parent $PhC_{18}PMO$. These PMOs modified with ALD were chosen because they presented different properties as above discussed, but they still maintained a significant surface area and pore volume (Table 4.1.2). The adsorbed amounts on the samples modified with ALD (Al-$PhC_{18}PMO$#50, Al-$PhC_{18}PMO$#2) decreased for both carbon dioxide and methane (Figure 4.1.5). It can be noted that the decreasing is more pronounced on the sample treated with more ALD cycles (Al-$PhC_{18}PMO$#50). This is expected taking into account the significant decrease in pore volume comparing with that determined for the parent $PhC_{18}PMO$ (about 60 %, Table 4.1.2). However, the decrease in the adsorbed amounts is different for carbon dioxide and methane. Comparing the isotherms for $PhC_{18}PMO$ and Al-$PhC_{18}PMO$#50, it becomes clear that the decrease is less pronounced with carbon dioxide, probably because of the specific interaction of this molecule with the surface of the materials. In fact, the isotherm data was fitted with a virial equation (lines in Figure 4.1.5; parameters in Table 4.1.3) and observed that the Henry constant (K_H), which is sensitive to the interaction of the molecules with the surface of the materials, increases with the number of ALD cycles for the carbon dioxide case and conversely decreases for the methane case. This indicates that the surface of the $PhC_{18}PMO$ is increasing the affinity for carbon dioxide with the number of ALD cycles, while the contrary is observed for methane. Another way to ascertain this increase is to represent the adsorbed amounts per surface area of the materials (S_{BET}) instead of mass, in order to take into account the decrease of the surface observed due to ALD treatment and to normalize the results by surface affinity. These results (Figure B1.8) clearly show a significant increase of about two times from $PhC_{18}PMO$ to Al-$PhC_{18}PMO$#50 in the adsorbed amount of carbon dioxide per surface area when more Al_2O_3 is introduced in the pores of $PhC_{18}PMO$. This change has a dramatic impact on the separation properties of the materials as it will be discussed below.

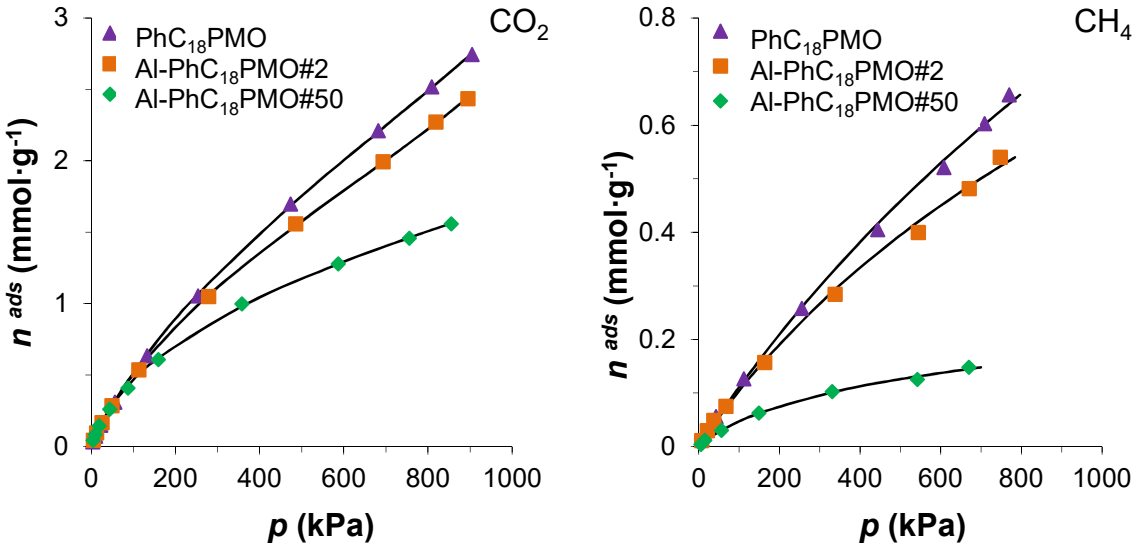

Figure 4.1.5. Carbon dioxide and methane adsorption isotherms at 25 °C on the $PhC_{18}PMO$, Al-$PhC_{18}PMO$#2 and Al-$PhC_{18}PMO$#50. The lines represent the fitting of the virial equation.

Table 4.1.3. Virial coefficients (C_1 and C_2) and Henry constants (K_H) for the adsorption of methane and carbon dioxide on the pristine and modified $PhC_{18}PMO$s.[a]

Gas	Material	K_H	C_1	C_2
		mmol·g^{-1}·kPa^{-1}	g·mmol^{-1}	(g·mmol^{-1})^2
CH_4	PMO	1.17×10^{-3}	0.536	
	Al-$PhC_{18}PMO$#2	1.14×10^{-3}	0.935	
	Al-$PhC_{18}PMO$#50	0.674×10^{-3}	7.853	
	$PhC_{18}PMO$+Al_2O_3_a	0.467×10^{-3}	-0.319	
CO_2	PMO	6.41×10^{-3}	0.474	-0.074
	Al-$PhC_{18}PMO$#2	7.03×10^{-3}	0.730	-0.141
	Al-$PhC_{18}PMO$#50	8.47×10^{-3}	1.429	-0.286
	$PhC_{18}PMO$+Al_2O_3_a	0.86×10^{-3}	-0.613	0.111

[a]Obtained by the nonlinear least-squares the virial equation to the adsorption data.

Using the virial equation fitted to the adsorption data and the Ideal Adsorbed Solution Theory (IAST),[27] the selectivity of the separation and the equilibrium phase diagrams for the adsorbed phase can be obtained using a method proposed by Myers[25] with the implementation described in detail in previous works[26,28] As can be seen from Figure 4.1.6, the inclusion of Al_2O_3 on the $PhC_{18}PMO$ induces a very significant increase in the selectivity of the CO_2/CH_4 separation, *i.e.*, the Al-$PhC_{18}PMO$#50 case is much more pronounced than the Al-$PhC_{18}PMO$#2. This is most probably related with the aluminium pentacoordinated species (Al^V) that are present in large amount in the Al-$PhC_{18}PMO$#50 and almost absent in Al-$PhC_{18}PMO$#2. This type of aluminium oxide species is very acidic[29,30] and can interact strongly with the carbon dioxide quadrupolar moment (3.3×10^{-16} cm^2).[31] It is worth

mentioning that the selectivity values found for the CO_2/CH_4 separation on Al-PhC_{18}PMO#50 sample are similar to those found on some pillared clays with aluminium oxide pillars.[26,28]

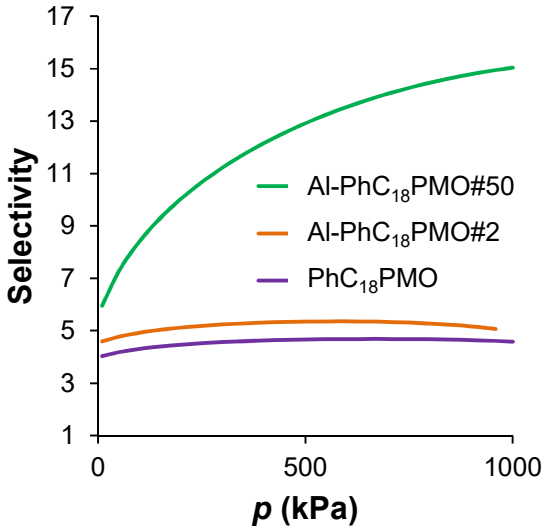

Figure 4.1.6. Average selectivity for the CO_2/CH_4 separation on the pristine and modified PhC_{18}PMOs.

The influence on the separation can be best illustrated in Figure 4.1.7 where it can be seen that the sample Al-PhC_{18}PMO#50 has an improved performance over the other samples.

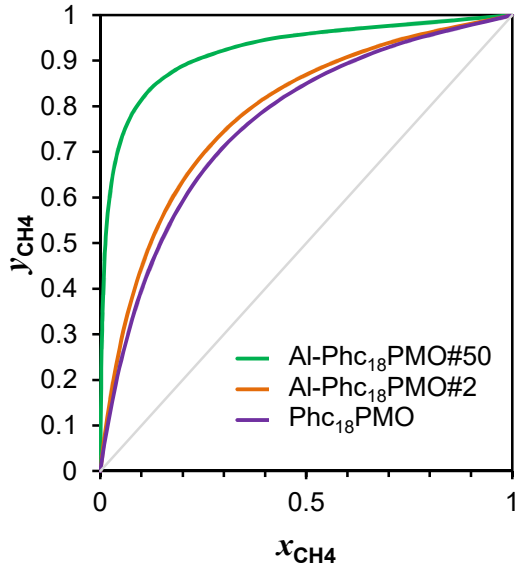

Figure 4.1.7. Isothermal (25 °C), isobaric (500 kPa) *xy* phase diagrams of the CO_2/CH_4 mixtures on the pristine and modified PhC_{18}PMOs. y_{CH4} is the molar faction of methane in the gas phase; x_{CH4} is the molar faction of methane in the adsorbed phase.

If we consider a sample with 0.5 molar composition (y_{CH4}), typical of biogas composition and some natural gas sources, the composition in the adsorbed phase (x_{CH4}) is 0.15 on

$PhC_{18}PMO$, 0.13 on Al-$PhC_{18}PMO$#2 and 0.02 at Al-$PhC_{18}PMO$#50, at 500 kPa and 25 °C. This means that the adsorbed phase is richer in carbon dioxide than in methane and that Al-$PhC_{18}PMO$#50 adsorbs almost pure carbon dioxide (0.98 molar composition) under these conditions. Complete phase diagrams can also be obtained (Figure B1.9), which confirm the best performance of the Al-$PhC_{18}PMO$#50 sample. Thus, the small decrease in adsorption capacity due to the ALD treatment is largely compensated by the increase in the selectivity. The application of adsorbent materials on the separation of gases is only industrially viable if the material can be easily regenerated with minimum loss of capacity after each regeneration cycle. Here, it was tested the regeneration possibility on the Al-$PhC_{18}PMO$#2 and Al-$PhC_{18}PMO$#50 composites using just vacuum during a half hour at ambient temperature. This corresponds to what happens industrially during the regeneration step of a vacuum swing adsorption process (VSA).[32] From the presented results (Figure 4.1.8), only a slight decrease in the high pressure region can be noted in both composites, although more significant in Al-$PhC_{18}PMO$#50. This is a first good indication that these materials can be easily regenerated and that they are stable to be used under cyclic separation processes. Additional confirmation using a higher number of cycles would be needed to confirm the stability required for application in industry.

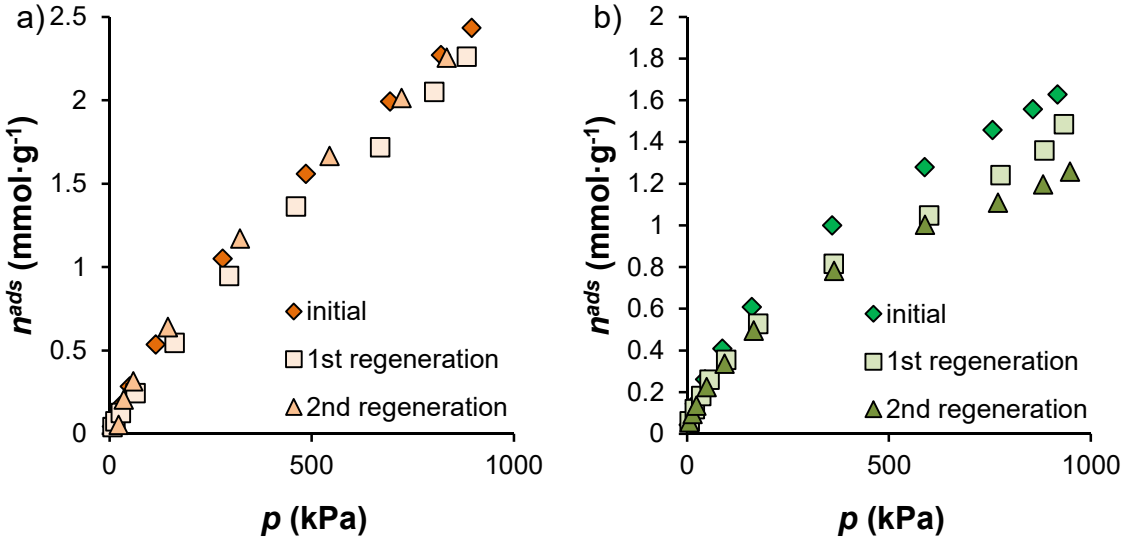

Figure 4.1.8. Adsorbed amounts of the CO_2 in a) Al-$PhC_{18}PMO$#2 and b) Al-$PhC_{18}PMO$#50 after first and second regeneration steps of the composites with vacuum at 25 °C during a half hour.

The advantage of impregnating Al_2O_3 on the $PhC_{18}PMO$ using ALD is also evaluated through the comparison of Al-$PhC_{18}PMO$#50 composite and the physical mixture of

$PhC_{18}PMO$ with amorphous alumina powder regarding the CO_2 and CH_4 adsorption. For a more realistic comparison, the amorphous alumina used presents a similar chemical composition to that of Al-$PhC_{18}PMO$#50 (see Figure B1.10). In addition, the physical mixture of $PhC_{18}PMO$ and amorphous alumina is made in the same ratio obtained for the Al-$PhC_{18}PMO$#50 composite. This is possible having into account the weight gain presented in Table 4.1.1. The mixture of $PhC_{18}PMO$ with amorphous alumina is here denoted as $PhC_{18}PMO$+Al_2O_3_a and was tested for the CH_4 and CO_2 adsorption at 25 °C. It is possible to observe that $PhC_{18}PMO$+Al_2O_3_a adsorbs a smaller amount of CO_2 and a larger quantity of CH_4 when compared with Al-$PhC_{18}PMO$#50 (Figure B1.11a). The presence of nearly 25 % of amorphous alumina induces a negative effect in the CO_2 adsorption in the $PhC_{18}PMO$. In addition the selectivity for $PhC_{18}PMO$+Al_2O_3_a, presented in Figure B1.11b, is about 1.86 at 500 kPa, while the $PhC_{18}PMO$ presents a selectivity of approximately 4 and the Al-$PhC_{18}PMO$#50 presents a selectivity of 13 at the same range of pressure. Furthermore the $PhC_{18}PMO$+Al_2O_3_a showed the worst separation performance among all materials (Figure B1.12a) and the equimolar composition in the adsorbed phase is achieved at about 0.70 molar composition of methane in the gas phase, at 500 kPa and 25 °C (Figure B1.12b), which is significantly lower than those observed for the other materials tested. Having into account the performance of $PhC_{18}PMO$+Al_2O_3_a material on the CO_2 adsorption, the presence of the same alumina/$PhC_{18}PMO$ ratio and same chemical composition achieved for the Al-$PhC_{18}PMO$#50, it is possible to conclude that the use of ALD to deposit alumina in the $PhC_{18}PMO$ powder brings benefits for the CO_2/CH_4 separation. This can be due to a good dispersion of nanoparticles of amorphous alumina that is achieved with the ALD method not only in the surface, but also inside the pores of Al-$PhC_{18}PMO$#50, probably promoting some roughness and microporosity. The interactions of the alumina and the gas molecules are then increased, since the alumina particles are very small. Another consequence of this type of deposition is the eventual chemical reaction of some alumina with some of the T^2 free silanols of $PhC_{18}PMO$ giving rise to some Si-O-Al chemical bonds. In this way, the ALD allows the deposition of amorphous alumina on the $PhC_{18}PMO$, in order to produce composites with interesting physical and chemical characteristics to be selective in the CO_2/CH_4 separation.

4.1.4 Comparison to other materials

The capacity of Al-PhC$_{18}$PMO#50 to capture carbon dioxide and methane is compared in Table 4.1.4 with the capacities reported for other types of adsorbents. Notice that data were determined at different temperatures, thus, some differences on the values of the capacities can be due to the temperature.

Table 4.1.4. Capacities of different adsorbents in the CO_2/CH_4 separation at 100 kPa.

Type	Materials	CO_2 capacity (mmol·g^{-1})	CH_4 capacity (mmol·g^{-1})	Temperature (°C)	Selectivity[a]
Clays	PILC Al$_w$[26]	≈0.4	≈0.07	25	≈12.0
	PILC Al$_B$[26]	≈0.4	≈0.08		≈10.0
	PCH[33]	≈0.7	≈0.08		≈7.0
Carbons	SC700P[34]	≈3.0	≈1.40		≈4.2
MOFs	amino-MIL-53(Al)[35]	1.96	≈0.30	30	6.5[b]
	MIL-53(Al) tablets (Basolite® A100)[36]	≈2.0	≈0.70		≈3.0
Silicas	a-MCMBs[37]	12.4	6.10	25	≈1.9
ZIF	ZIF-7[38]	2.34	0.13		≈18.0
PMOs	Al-PhC$_{18}$PMO#50	≈0.5	≈0.04		≈9.0

[a]Selectivity at 100 kPa. [b]This value correspond to the CO_2/CH_4 capacity ratio.

The Al-PhC$_{18}$PMO#50 presents slightly better results in the CO_2 and CH_4 adsorption capacities than PILC-Al$_B$ and PILC$_w$. The Al-PhC$_{18}$PMO#50 presents at 100 kPa a selectivity of 9 which is lightly smaller than the selectivity reported for the PILCs at the same range of pressure. Although, the selectivity of the Al-PhC$_{18}$PMO#50 increases with the pressure and at near of 1000 kPa these materials has a selectivity of 15 while the selectivity of these PILCs remains constant in the all range of pressure (100-1000 kPa). The Al-PhC$_{18}$PMO#50 adsorbs less CO_2 than PCH clay, SC700P activated carbon, amino-MIL-53(Al) and MIL-53(Al) pellets (Basolite® A100) MOFs and a-MCMBs Silicas, but it is much superior in selectivity. The ZIF-7 is the only material that presents better CO_2 adsorption and selectivity at the same temperature and pressure. Although, information of the behaviour of these materials at higher pressures than 100 kPa is missing.

4.1.5 Conclusions

The phenylene-C_{18}PMO surface was successfully modified for the first time by ALD deposition of amorphous Al_2O_3 with different content. The meso-structure order and molecular-scale periodicity of the pore walls of PhC_{18}PMO are preserved after modification of high Al content (Al-PhC_{18}PMO#100 with [Si/Al] = 0.94). The ALD method allows increasing the amount of the Al_2O_3 on the composite varying the number of cycles, proving to be a robust method for tailoring the content of Al_2O_3 amount on the PhC_{18}PMO. The reduction of the surface area and pore volume is observed with the increase of Al content. In the case of a large number of ALD cycles (*i.e.*, 50), the formation of Al^V aluminium oxide species is observed. The acidity of these species is most probably responsible for the observed increase in the CO_2/CH_4 separation selectivity. The Al-PhC_{18}PMO#50 sample has interesting properties for application into methane purification (upgrading and sweetening) that is essential before bio and natural gas commercialization. The regeneration of the modified materials was easy under vacuum and showed good stability.

4.2 Carbonization of periodic mesoporous phenylene- and biphenylene-silicas for CO_2/CH_4 separation

Adapted from:

Mirtha A. O. Lourenço, Moisés L. Pinto, João Pires, José R. B. Gomes and Paula Ferreira

Carbonization of periodic mesoporous phenylene- and biphenylene-silicas for CO_2/CH_4 separation

Submitted for publication, **2016**

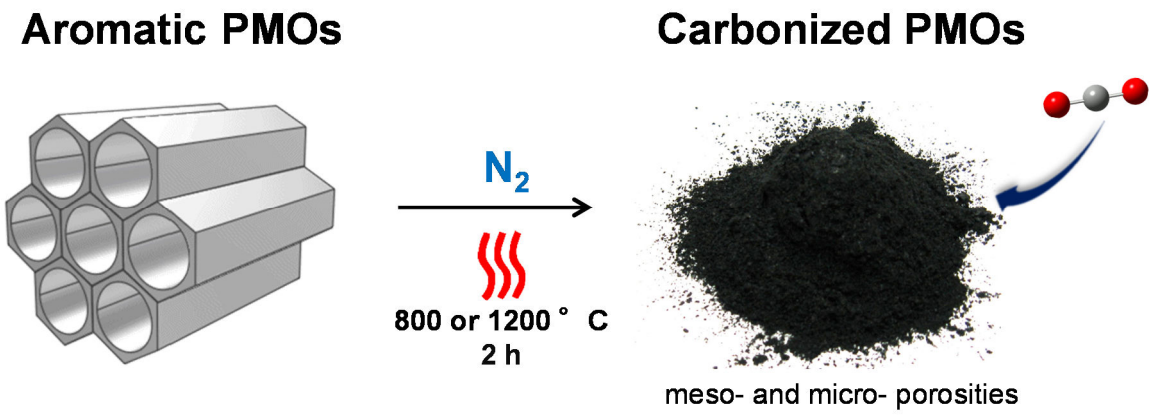

My direct contribution:

I declare that I have prepared, functionalized, pyrolysed and characterized the resulting PMO materials. I also carried out the experimental CO_2 and CH_4 pure adsorption measurements at the University of Lisbon using a volumetric apparatus, under guidance of Moisés L. Pinto and João Pires.

4.2.1 Motivation

Periodic mesoporous organosilica (PMO) materials have been proposed as potential adsorbents due to their high specific surface areas, high pore volumes and good thermal stability.[22,39,40] These materials also allow good diffusion of the molecules through the channels, since the organic functions are integrated within the walls. Moreover, PMO characteristics can be tuned by changing the bissilylated organic bridge and the template molecule, which define the type of porous structure and the pore size[20] as it was seen in Sub-chapter 3.1. The introduction of amino groups into the organic bridge has been one of the ways to improve selectivity of PMOs towards CO_2 adsorption[1] as we could observe in Sub-chapters 3.1 and 3.2. Additionally, alkyl amine groups have been grafted to the free silanols at the PMO hydrophilic part[41] as demonstrated in Sub-chapter 3.2. The addition of aluminium oxide to the PMO surface using atomic layer deposition makes the phenylene-PMO ($PhC_{18}PMO$) was effective for the CO_2/CH_4 separation as could be observed in the previous Sub-chapter 4.1. Despite all the attempts to improve efficiency of PMOs for CO_2 adsorption, thus improving its separation from CH_4, significant additional work is required in order to make them competitive with zeolites and activated carbons in terms of capacity and cost efficiency. Therefore, in the present work the surface and structural properties of PMOs are modified through pyrolysis with the aim of improving their capabilities for gas adsorption and gas separation applications. PMOs with two different aromatic bridges, phenylene and biphenylene moieties were prepared. The carbonized PMOs were prepared using two different structure-directing agents (C_{12}-TMA and C_{18}-TMA) in order to obtain different pore sizes. As the alkyl chain length of the surfactant and the nature of the bridge of PMOs were varied, it was studied their influence on the morphology, on the surface properties (surface area, pore volume, pore size distribution and particle type) and on the thermal stability of the prepared PMOs. The pyrolysis process was made on the as-synthetized PMOs (with surfactant within the channels) and on the surfactant-extracted PMOs, at two different temperatures (800 °C and 1200 °C) under inert conditions. Additionally, PMOs were chemically modified before pyrolysis, aiming to improve the capacity and selectivity for CO_2/CH_4 separation.

This study is focused on the understanding of the physical and chemical modifications promoted in the aromatic bridged PMO materials as a consequence of the carbonization process and the concomitant effects in the CO_2 capacity and CO_2/CH_4 selectivity. To the

best of our knowledge, only the pyrolysis of non-aromatic PMOs was reported in the literature[42–48] and none of such pyrolysed materials was tested for the CO_2/CH_4 separation.

4.2.2 Experimental details

PMO synthesis

The phenylene[20,22] (*c.f.* Sub-chapter 3.1) and biphenylene[49] bridged PMOs were synthesized according to the literature procedures, starting by with the hydrolysis and condensation of bissilylated precursors in the presence of supramolecular structure agent, the C_{18}-TMA or C_{12}-TMA. After 24 hours of stirring at room temperature, the solution was transferred to Teflon-lined stain-steel autoclave for hydrothermal treatment at 100 °C. After 24 hours, the solid was filtered and washed. The as-prepared materials are denoted as PhC_nPMO_AS or BphC_nPMO_AS, where *n* is the number of carbons of the alkyl chain of the selected surfactant. The templates were removed using an ethanol/HCl solution, giving rise to PhC_nPMO and BphC_nPMO materials. The introduction of the amino group into the phenylene moieties (to obtain NH_2PhC_{12}PMO) was made upon two-step treatment with very strong acid solutions of HNO_3 and H_2SO_4 and also of $SnCl_2$ and HCl using the procedure reported by Ohashi *et al*.[1]

Carbonization of PMOs

The prepared PMOs materials were carbonized in an alumina crucible at 800 °C or 1200 °C under nitrogen atmosphere. The pyrolysis was performed in two steps. Initially the temperature was raised up to 200 °C using a heating rate of 5 °C·min^{-1}. The materials were kept at this temperature over 2 hours. Then, the temperature was increased at 5 °C·min^{-1} till it reaches the final temperature (800 or 1200 °C), at which the material was maintained for 2 h. Natural cooling to the room temperature was made under nitrogen flow. The pyrolysed PMOs are denoted by the suffix P*T*, where P means pyrolysed material and *T* indicates the temperature of the carbonization process (*T* = 800 or 1200 °C).

In the case of the PMO submitted to acid chemical treatment, the materials were previously heated with the H_2SO_4 at 160 °C during 6 h and then carbonized at 800 °C.

Materials characterization

The properties of the carbonized PMOs were assessed by PXRD, -196 °C N_2 sorption, TEM, FTIR, ^{29}Si MAS and CP-MAS NMR and ^{13}C CP-MAS NMR spectroscopies and TGA

analysis. TEM, N_2-sorption isotherms, ^{13}C CP-MAS NMR, TGA, EA and some CO_2 and CH_4 adsorption data can be assessed in the Appendix B.

High pressure CO_2 and CH_4 adsorption

Adsorption experiments of CO_2 and CH_4 were performed at 25 °C up to 1000 kPa, using the volumetric method presented in the previous Chapter (Sub-chapter 2.6). The non-ideality of the gas phase was taken into account through the use of the second and third virial coefficients. Additionally, the experimental excess adsorbed amounts were converted to the absolute adsorbed amounts having into account the pore volume of the each sample and the density of the gas phase using the virial coefficients. Each experimental pure component adsorption isotherm was fitted using the Virial model. Selectivity values were estimated using a method proposed by Myers[34] and the implementation is described in detail in previous works[35].

4.2.3 Results and discussion

The surfactant-extracted PMOs, $PhC_{18}PMO$ (*c.f.* Sub-chapter 3.1), $PhC_{12}PMO$ (*c.f.* Chapter 3) and $BphC_{18}PMO$[50] possess 2D hexagonal symmetry (*p6mm*) lattice with *d* spacings associated to the (100) reflection (*c.f.* Figure 4.2.1) of 4.65, 3.59 and 4.96 nm, respectively (Table B2.1 in the Appendix B). These materials also present molecular-scale periodicity observed by the presence of a medium range reflection at $d \sim 0.76$ nm for the PhC_nPMOs (*c.f.* Sub-chapter 3.1) and at 1.19 nm for the $BphC_{18}PMO$[50]. The as-prepared and surfactant-extracted PMO materials were pyrolysed at 800 °C. The two most promising materials were further pyrolysed at 1200 °C. The structural order of the carbonized samples were studied by PXRD, TEM and N_2 adsorption–desorption isotherms. Figure 4.2.1 also shows the PXRD patterns of the pyrolysed samples. It is possible to observe that all materials preserved the (100) reflection, indicating that the meso-scale periodicity is preserved after the pyrolysis conditions. The materials $PhC_{18}PMO\_P800$, $PhC_{12}PMO\_P800$ and $BphC_{18}PMO\_P800$ have *d* spacings of 4.09, 3.27 and 4.20 nm, respectively (Table B2.1). The slightly reduction of the *d* spacing values on the pyrolysed samples is compatible with the reduction of the pore diameter during the pyrolysis process at 800 °C. The use of the surfactant, the increase of temperature to 1200 °C or even the use of H_2SO_4 chemical treatment before carbonization leads to a reduction of intensity of the (100) reflection in the

PRXD. This reduction is more pronounced for the materials pyrolysed at 1200 °C and may indicate a partial collapse of the porous structure. The medium-range reflections at $d \sim 0.76$ and 1.19 nm can be observed in the PXRD pattern of phenylene- and biphenylene- PMOs, respectively, after pyrolysis at 800 °C. The phenylene-PMO treated at higher temperature ($PhC_{12}PMO\_P1200$) does not present this reflection, pointing to the loss of the molecular-scale periodicity after such hard conditions. However, in the case of the biphenylene-PMO the molecular-scale periodicity peak is always present in the diffraction patterns even after treatment at 1200 °C.

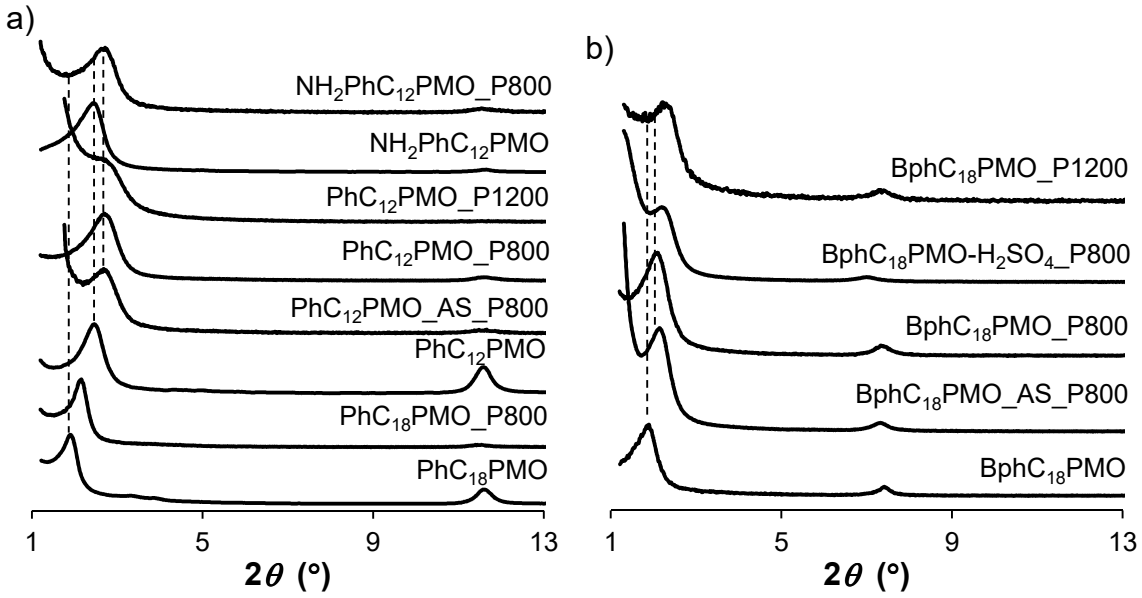

Figure 4.2.1. X-ray diffraction patterns of pyrolysed PMO materials: a) phenylene-PMOs; and b) biphenylene-PMOs.

TEM images of pyrolysed PMOs are showed in Figure B2.1 in the Appendix B. TEM images of $PhC_{18}PMO\_P800$ and the $PhC_{12}PMO\_P800$ show high order of the pores along the channel direction. Additionally, both materials show the hexagonal arrangement of the pores and present particles with elongated form such as the parent PMOs. Interesting, the use of surfactant during the pyrolysis process and the use of amine linked to the phenylene moieties of the $PhC_{12}PMO$ gives rise to carbonized materials with lower mesoporous organization than the $PhC_{12}PMO\_P800$, corroborating the PXRD results. Moreover, the $PhC_{12}PMO\_AS\_P800$ and $NH_2PhC_{12}PMO\_P800$ present particles with both elongated and spherical shapes. The increase of the pyrolysed temperature from 800 to 1200 °C ($PhC_{12}PMO\_P1200$) leads to the appearance of smaller particles. TEM images of carbonized biphenylene-PMOs at different conditions are also presented in Figure B2.1 and it is possible

to notice that all biphenylene-PMOs present high order along the channels. Furthermore, the TEM image in the direction parallel to the channels of the $BphC_{18}PMO\_P1200$ supports the maintenance of the 2D hexagonal arrangement of the pores. Curiously, the shape of the particles of these materials change with the temperature. The parent biphenylene-PMO presents particles with helical form,[50] but during the heating process at 800 °C under inert atmosphere, the $BphC_{18}PMO\_P800$ starts showing particles with spherical shape. The spherical particles are more evident on biphenylene-PMOs carbonized under extreme conditions (pyrolysis at 1200 °C or at 800 °C in the presence of the surfactant).

The N_2 adsorption–desorption experiments of carbonized PMOs are presented in Figure B2.2 in the Appendix B, and the pore size distribution (PSD) curves are showed in Figure 4.2.2. The free surfactant parent PMOs, $PhC_{18}PMO$ (*c.f.* Sub-chapter 3.1), $PhC_{12}PMO$ (*c.f.* Chapter3) and $BphC_{18}PMO$[50] samples display type IV isotherms (IUPAC classification),[51] as shown previously, typically detected on conventional mesoporous materials. In Figure B2.2, it is possible to observe that the $PhC_{18}PMO\_P800$ presents a type IV isotherm similar to what happens with the parent material. A slightly reduction of the Brunauer, Emmett and Teller (BET)[52,53] specific surface area (S_{BET}) and pore volume (V_p) can be observed after pyrolysis, but a significant decrease of the pore diameter (d_p) from 3.70 to 3.02 nm is evident (Table B2.1). The presence of microporosity was also studied by applying the *t*-plot method to the N_2 adsorption curve of the material. In the case of $PhC_{18}PMO\_P800$ signs of microporosity were not observed. Since difficulties in applying the *t*-plot method to type IV isotherms are common,[51] the quenched solid density functional theory (QSDFT)[54,55] was then applied to the N_2 adsorption isotherm of the pyrolysed PMOs to evaluate both micro- and meso-pores size distribution, as represented in Figure 4.2.2.

Figure 4.2.2a shows that the pyrolysis of $PhC_{18}PMO$ at 800 °C originates a material with different types of porosities. Two mesopore sizes are obtained at *ca*. 3.4 nm (in small amount) and at *ca*. 2.1 nm (in major quantity). The pore diameter around 1.1 nm is assigned to the presence of micropores. In the case of $PhC_{12}PMO$ the carbonization at 800 °C leads to a material with an isotherm that resembles a type Ib isotherm, typical of microporous materials with wide micropores and possibly narrow mesopores (Figure B2.2), which agrees with the pore size distribution that displays mainly pores around 1.1 nm (Figure 4.2.2a). Interestingly, the $PhC_{12}PMO\_P800$ presents a reduction of S_{BET}, but an increase of V_p when compared to the parent $PhC_{12}PMO$ (Table B2.1) that could eventually be ascribed to the

decrease in the particle size. The effect of the surfactant presence within the channels of the $PhC_{12}PMO$ during the pyrolysis at 800 °C is minimal. Both $PhC_{12}PMO\_P800$ and $PhC_{12}PMO\_AS\_P800$ display similar PSD curves (Figure 4.2.2a). Nevertheless, $PhC_{12}PMO\_AS\_P800$ presents higher S_{BET} and V_p and lower V_{micro} than the $PhC_{12}PMO\_P800$ material (Table B2.1).

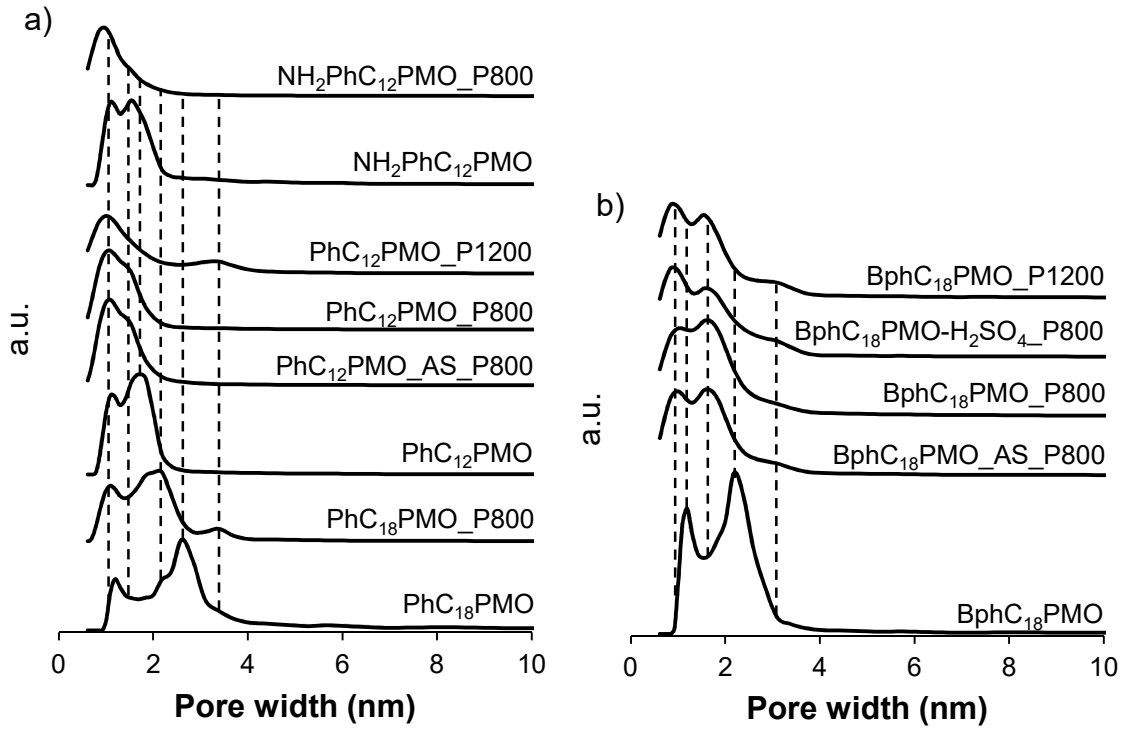

Figure 4.2.2. Pore size distribution profiles calculated from the N_2 adsorption isotherm of carbonized: a) phenylene-PMOs and b) biphenylene-PMOs. The PSD curves were calculated using the QSDFT method for carbon surfaces.

The presence of amines in the phenylene moieties of $PhC_{12}PMO$ also produces a material with an isotherm similar to a type Ib isotherm[51] after pyrolysis, but with a more pronounced reduction of S_{BET}, V_p and V_{micro} than the sample without amine groups (please compare $NH_2PhC_{12}PMO\_P800$ and $PhC_{12}PMO\_P800$ samples in Figure 4.2.2a and Table B2.1). The reduction of the specific surface area and of the pore volumes may result from the collapse of some pores during the pyrolysis[42] and/or may occur by the presence of amines, which increase the reactivity of the material upon carbonization of the phenylene moieties to form carbon[56] giving rise to silica/carbon framework. When the carbonization of the organic moieties is fast, the free carbon can be deposited on the pores leading to their blockage. Note, that the presence of amines during the pyrolysis process originated smaller micropores, Figure 4.2.2a. When the temperature is increased from 800 °C to 1200 °C

($PhC_{12}PMO\_P1200$), it is possible to observe an isotherm that has features of type Ib + IVa isotherms with a small hysteresis but without the presence of a defined final plateau, usually observed in adsorbents with a wide distribution of pore sizes (from micro to wide mesopores).[51] The $PhC_{12}PMO\_P1200$ shows mainly micropores (Figure 4.2.2a) when compared to $PhC_{12}PMO\_P800$, but also possesses some mesopores evidenced by the broad peak centered at 3.3 nm. A reduction of the S_{BET} and V_{micro} is also observed when the temperature is increased (Table B2.1).

The textural properties of pyrolysed phenylene-PMOs were also studied and are represented in Figure 4.2.2b. Similarly to the results obtained for the pyrolysed phenylene-PMOs, it is verified a contraction of the pore structure upon pyrolysis of biphenylene-PMOs (Figure 4.2.2b and Table B2.1). The pyrolysis of $BphC_{18}PMO$ at 800 °C gives rise to a material with a isotherm resembling a type Ib isotherm although with some type II character (Figure B2.2), and presenting higher S_{BET}, but lower V_p and d_p than the parent material (*c.f.* Table B2.1). The shrinkage of the pores is observed in Figure 4.2.2b, where the $BphC_{18}PMO\_P800$ shows mainly micropores. The observed micropores in this material varies between 1 and 2 nm, with maxima of pore size distributions centered at 1.0 nm and 1.7 nm. The presence of the surfactant ($BphC_{18}PMO\_P800\_AS$) only promotes a reduction of the S_{BET} and V_p of the sample when compared to the $BphC_{18}PMO\_P800$ materials (Table B2.1). This can be related to the carbonization of the surfactant species at 800 °C remaining inside the pores, which eventually leads to their obstruction. Interestingly, and opposite to the observed for the pyrolysed phenylene-PMO samples, it is possible to perceive a slightly increase in the V_{micro}. The increase in the microporosity when the surfactant is present in the $BphC_{18}PMO\_P800$ material (*c.f.* compare V_{micro} of $BphC_{18}PMO\_P800\_AS$ and $BphC_{18}PMO\_P800$ in the Table B2.1) during the pyrolysis process can be associated to the formation of smaller micropores during the surfactant carbonization (*c.f.* Figure 4.2.2b, $BphC_{18}PMO\_P800$ material presents micropores with 1.0 nm while the $BphC_{18}PMO\_P800\_AS$ sample has micropores with 0.9 nm). Curiously, the chemical attack of $BphC_{18}PMO$ with H_2SO_4 before pyrolysis also stimulates a reduction of S_{BET} and V_p and an increase of the V_{micro}. Thus, the $BphC_{18}PMO\text{-}H_2SO_4\_P800$ has more micropores (Table B2.1) and they are faintly smaller than those observed in the $BphC_{18}PMO\_P800$, (Figure 4.2.2b). The increase of the temperature from 800 °C to 1200 °C has higher impact in the formation of a material with more micropores than the use of surfactant or the

consideration of chemical attack by sulfuric acid before pyrolysis. In this way, $BphC_{18}PMO\_P1200$ is the carbonized biphenylene-PMO material with the highest V_{micro} prepared in this study (Table B2.1). The reduction verified on the micropore size (Figure 4.2.2b) is in agreement with the progressive contraction of structure upon increasing temperature treatment. These results are in line with the deviation of the d_{100} reflection for higher 2θ values in the PXRD shown in Figure 4.2.1.

Solid-state ^{29}Si CP-MAS NMR and ^{13}C CP-MAS NMR spectra of pyrolysed PMOs materials are shown in Figures 4.2.3 and Figure B2.3 in the Appendix B, respectively. The ^{29}Si CP-MAS NMR spectra of the PhC_nPMO (Chapter 3 and Appendix A) and $BphC_{18}PMO$[50] display resonances at *ca*. -81, -70 and -61 ppm which are attributed to T^3, T^2 and T^1 organosiliceous species of the type $T^m = RSi(OSi)_m(OH)_{3-m}$, respectively. In both parent PMO materials no peaks endorsed to Q^n [$Q^n = Si(OSi)_n(OH)_{4-n}$] chemical environments were detected. After pyrolysis of the materials, the patterns of the ^{29}Si NMR spectra became considerably noisy, displaying in general broader peaks. This observation may be related with the partial formation of graphitic carbon species known to be paramagnetic. Moreover, the pyrolysis treatment promotes Si-C cleavages observed by the appearance of Q^n chemical environments. Although, different degrees of Si-C cleavage are observed when the pyrolysis conditions are varied. The phenylene-PMOs with different pore sizes originate similar ratios of T^m: Q^n species after pyrolysis at 800 °C. The presence of amines and/or surfactant molecules, and the increase of the temperature from 800 to 1200 °C give rise, in the phenylene-PMO, to an increase of the Q^n species, which indicates an enhancement of the cleavage of the Si-C bonds within these conditions. The presence of surfactant inside the channels of the biphenylene-PMO samples does not intensify the Si-C bond cleavage. Contrarily, the use of sulfuric acid to promote dehydration or the increase of temperature from 800 to 1200 °C promote the formation of larger amount of Q^n species, which means that these extreme conditions stimulate the cleavage of the Si-C bonds.

Solid-state ^{13}C CP-MAS NMR spectra of the pristine PhC_nPMO materials present a typical resonance at 133 ppm of the aromatic carbons as reported in Chapter 3. In the case of the parent $BphC_{18}PMO$ the ^{13}C CP-MAS NMR spectra exhibit resonances at *ca*. 126, 130, 135 and 141 ppm assigned to the sp^2 carbons, which are related with the biphenylene group.[50] Tiny peaks can be detected in the region 0 to 50 ppm. Figure B2.3 in the Appendix B shows that the phenylene- and biphenylene-PMOs samples carbonized at 800 °C only display one

broad resonance at *ca.* 132 ppm (Figure B2.3b, d and f) and at *ca*. 129 ppm (Figure B2.3h), respectively.

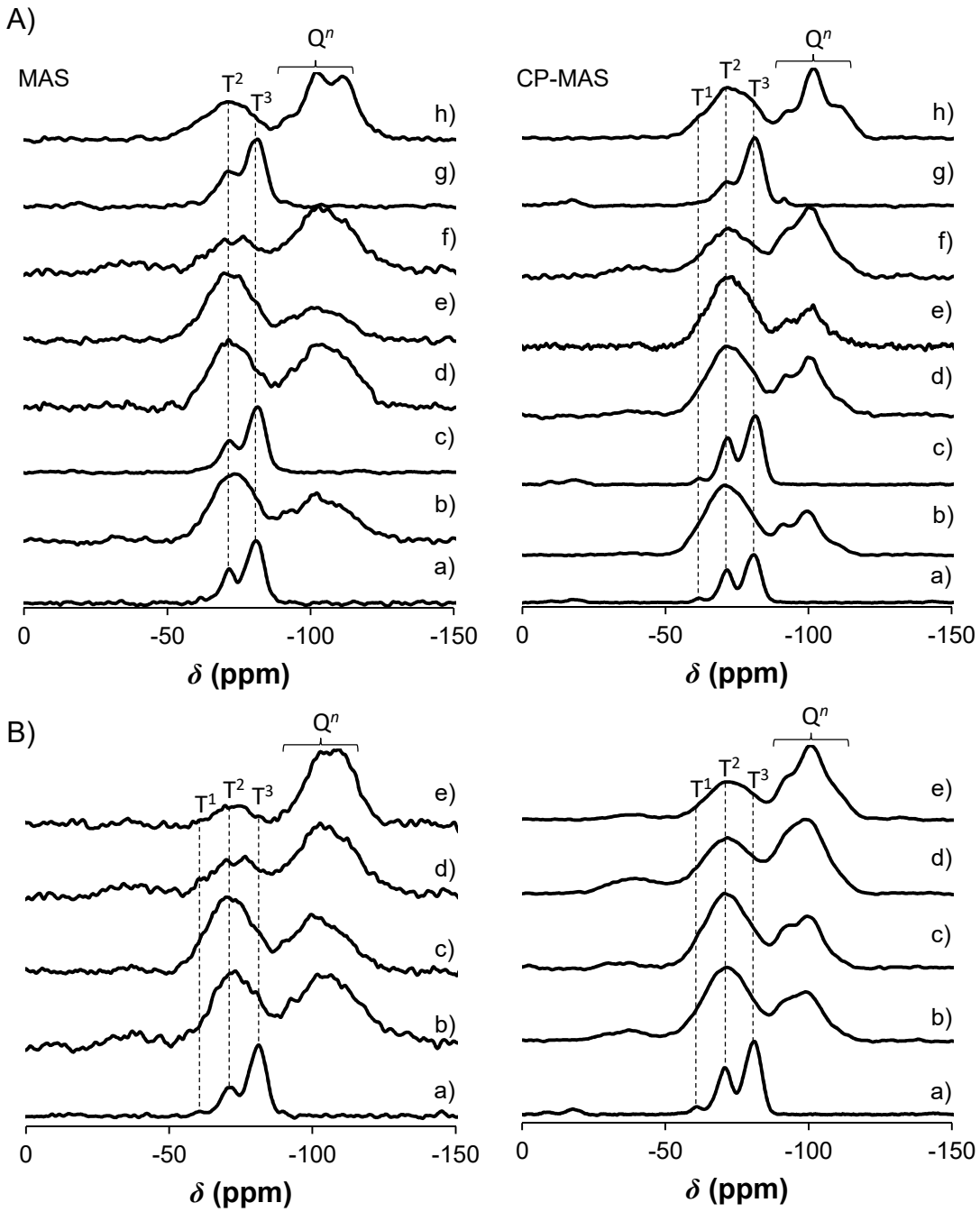

Figure 4.2.3. ^{29}Si MAS (left) and CP-MAS (right) NMR spectra of A) phenylene-pyrolysed PMOs: a) $PhC_{18}PMO$; b) $PhC_{18}PMO\_P800$; c) $PhC_{12}PMO$; d) $PhC_{12}PMO\_AS\_P800$; e) $PhC_{12}PMO\_P800$; f) $PhC_{12}PMO\_P1200$; g) $NH_2PhC_{12}PMO$; and h) $NH_2PhC_{12}PMO\_P800$, and B) biphenylene-pyrolysed PMOs materials: a) $BphC_{18}PMO$; b) $BphC_{18}PMO\_AS\_P800$; c) $BphC_{18}PMO\_P800$; d) $BphC_{18}PMO\text{-}H_2SO_4\_P800$; and e) $BphC_{18}PMO\_P1200$.

The thermal stability of the pyrolysed PMOs was evaluated by TGA and the results are presented in Figure B2.4 in the Appendix B. The parent PhC_nPMOs (*c.f.* Chapter 3) and $BphC_{18}PMO$[50] materials are stable up to 550 °C. After pyrolysis, all PMOs are found to be thermally stable up to *ca*. 300 °C as observed by TGA (Figure B2.4). The first weight loss, occurring below 100 °C in all materials, is associated to desorption of physisorbed water. Then, at 300 °C most of the phenylene- and biphenylene-PMOs present an increase of weight that is related to the oxidation of carbon in oxygen atmosphere. This effect is more pronounced in phenylene- and biphenylene-PMOs treated at 1200 °C. Above 300°C, the decomposition and release of the organic moieties from the framework take place, which happens at lower temperatures than in the parent PMOs. This lowering in the temperature for the release of organic moieties is compatible with the breakage of Si-C bonds as suggested above.

Table B2.2 in the Appendix B presents the elemental analysis results of the pyrolysed PMO materials, demonstrating the significant reduction on C and H content comparatively to the parent PhC_nPMOs (*c.f.* Chapter 3) and parent $BphC_{18}PMO$[50]. This loss probably occurs due to some carbonization of the organic bridges and consequently volatilization of the burnt products. Furthermore, both NH_2PhC_{12}PMO_P800 and $BphC_{18}PMO\text{-}H_2SO_4$_P800 have the major loss of C amount on the phenylene- and biphenylene-PMOs carbonized materials, meaning that the chemical attack of the bridges before carbonization facilitated the burnt of the chemical species. Comparatively to the parent $NH_2PhC_{12}PMO$ (*c.f.* Chapter 3), the amount of N in the case of the NH_2PhC_{12}PMO_P800 material is decreased, which suggests occurrence of C-N bond cleavage during the carbonization. Additionally, the pyrolysis of both as-synthetized PMOs (PhC_{12}PMO_AS_P800 and $BphC_{18}$PMO_AS_P800) do not lead to materials with representative nitrogen content, meaning that the surfactant is somehow lost during the process.

Figure 4.2.4 presents the X-ray photoelectron spectroscopy (XPS) spectra of both $NH_2PhC_{12}PMO$ and NH_2PhC_{12}PMO_P800, in order to observe which kind of amines are into the PMO material after the pyrolysis. Signals of Si 2p, Si 2s, C 1s, N 1s, and O 1s were observed in the XPS spectrum of both samples (*c.f.* Figure 4.2.4). It can be seen in Figure 4.2.4a that the N 1s signal appears at 400.36 eV, which corresponds to the N atom in the amino groups (NH_2) linked to the phenylene moieties of the $NH_2PhC_{12}PMO$ material. This material also shows σ* features in the range above of ~ 405 eV, that can be related to

its highly conjugated character (π-π*). Note, that this signal at higher binding energies is frequently observed in the C 1s, O 1s and S 2p regions of materials with poor electrical conductivity (which is the case) and can be associated to the existence of zones of different conductivity resulting from X-ray irradiation and differential charge accumulation in the surface of the material. In the case of the $NH_2PhC_{12}PMO\_P800$ material (*c.f.* Figure 4.2.4b), the N 1s signal appears at 400.58 eV (which is similar to the value obtained for the $NH_2PhC_{12}PMO$), indicating that the N atom remains mainly in the form of amino group.

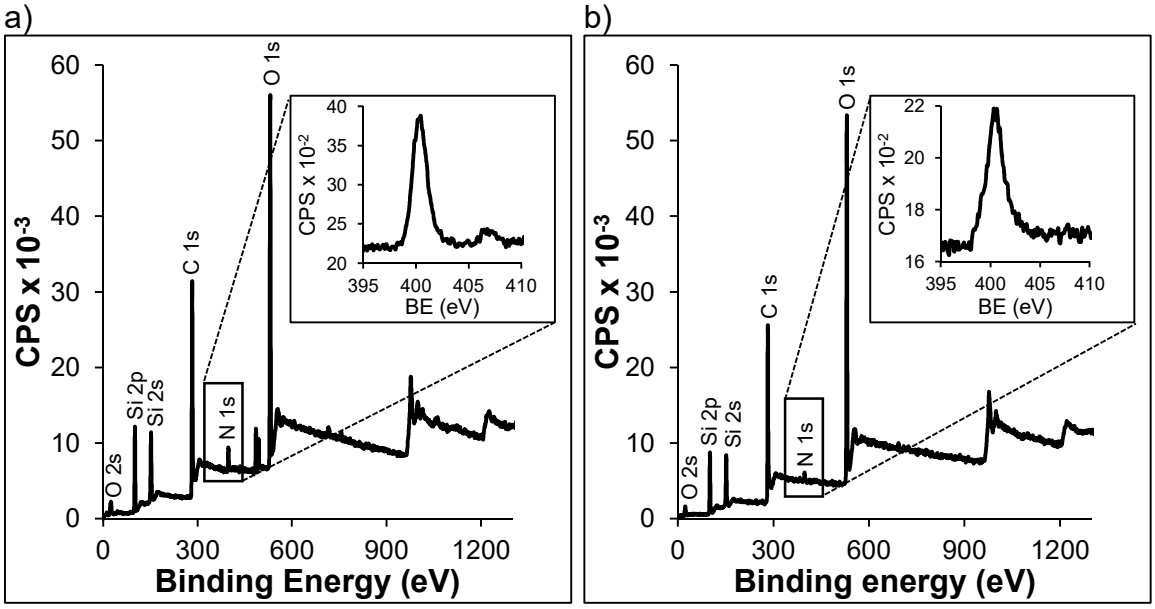

Figure 4.2.4. Wide-scan XPS spectra of the a) $NH_2PhC_{12}PMO$ and b) $NH_2PhC_{12}PMO\_P800$ (right) materials. The inset correspond to the XPS N 1s high resolution spectrum.

Experimental Pure-Component Adsorption Isotherms

The pyrolysed phenylene- and biphenylene-PMOs were tested as adsorbents on the CO_2 and CH_4 adsorption at 25 °C and the obtained results are shown in Figure 4.2.5. The evaluation of the surface interaction of each materials with pure CO_2 and pure CH_4 at low coverage was made through the determination of the Henry's constant (K_H) using the Virial model. The fitting parameters for the Virial model are presented in Table 4.2.1.

Figure 4.2.5a shows the CO_2 and CH_4 adsorption isotherms of each pyrolysed phenylene-PMO. The $PhC_{12}PMO\_P800$ adsorbs more CO_2 than the parent $PhC_{12}PMO$ (*c.f.* Chapter 3) and any other treated PMO with phenylene moieties in the framework (Figure 4.2.5a), presenting the highest K_H (1.11 x 10^{-2} mmol·g^{-1}·kPa^{-1}) of this family of materials (Table 4.2.1). Interestingly, $PhC_{12}PMO\_P800$ is also the material of the pyrolysed

phenylene-PMOs with the highest V_{micro}, suggesting the importance of these physical parameters on the adsorption of CO_2 (Table B2.1). Thus, any modification on the pyrolysis conditions (increase of the pore size, use of template, incorporation of amines in the phenylene moieties or increase of temperature) gives rise to materials with less CO_2 adsorption capacity (Figure 4.2.5a and Table B2.2). The PhC_{18}PMO_P800 and PhC_{12}PMO_P1200 are the materials demonstrating lower CO_2 adsorption in the range of pressure considered and present the smallest K_H values ((0.36×10^{-2} and 0.34×10^{-2} mmol·g^{-1}·kPa^{-1}, respectively, Table 4.2.1) for the materials considered in this work. Curiously, the PhC_{18}PMO_P800 does not present V_{micro} and the PhC_{12}PMO_P1200 is the pyrolysed phenylene material with the lowest amount of micropores from the C_{12} family (Table B2.1). Additionally, these materials have a significant amount of mesopores, indicating that this type of pores is not beneficial for CO_2 adsorption.

As observed for the adsorption of CO_2, the PhC_{12}PMO_P800 is also the material which adsorbs more CH_4 at high pressures, but presents one of the lowest K_H (0.21×10^{-2} mmol·g^{-1}·kPa^{-1}) found in this study. The use of the surfactant, the introduction of amines in the phenylene bridge, and the increase of pyrolysis temperature promote an increase of K_H. Thus, PhC_{12}PMO_P1200 is the pyrolysed phenylene-PMO presenting the highest K_H (0.30×10^{-2} mmol·g^{-1}·kPa^{-1}). Interestingly, a relation between the microporosity of the pyrolysed phenylene-PMOs and the CH_4 adsorption was found: materials with the lowest V_{micro} tend to present improved properties to adsorb more CH_4 than materials with highest V_{micro}.

Figure 4.2.5b shows the CO_2 and CH_4 adsorption isotherms for carbonized biphenylene-PMOs. The $BphC_{18}$PMO_P800 presents similar CO_2 adsorptive properties and the same K_H relatively to its phenylene counterpart (Table 4.2.1). Remarkably, the $BphC_{18}$PMO_P1200 is the pyrolysed biphenylene-PMO with the best CO_2 adsorptive properties and the highest K_H (2.34×10^{-2} mmol·g^{-1}·kPa^{-1}) of this family of materials and also of all PMOs materials prepared in this study.

The enhancement of the pyrolysis temperature of biphenylene-PMOs improves the CO_2 adsorption. This result is in the opposite direction to what was observed in the case of material PhC_{12}PMO_P1200, *c.f.* Table 4.2.1.

The increase of temperature from 800 to 1200 °C may intensify the formation of micropores on the structure of $BphC_{18}$PMO_P1200, favouring the CO_2 adsorption (Figure 4.2.1 and

Table B2.1). In the case of CH_4 adsorption, the pyrolysed biphenylene-PMO shows a different behaviour. $BphC_{18}PMO\_P800$ is the material which adsorbs more CH_4 in all pressure range, with a K_H of 0.59 x 10^{-2} mmol·g^{-1}·kPa^{-1}. The pyrolysis of the $BphC_{18}PMO$ containing surfactant within the pores results in a material presenting inferior CH_4 adsorption performance (Figure 4.2.5b and Table 4.2.1).

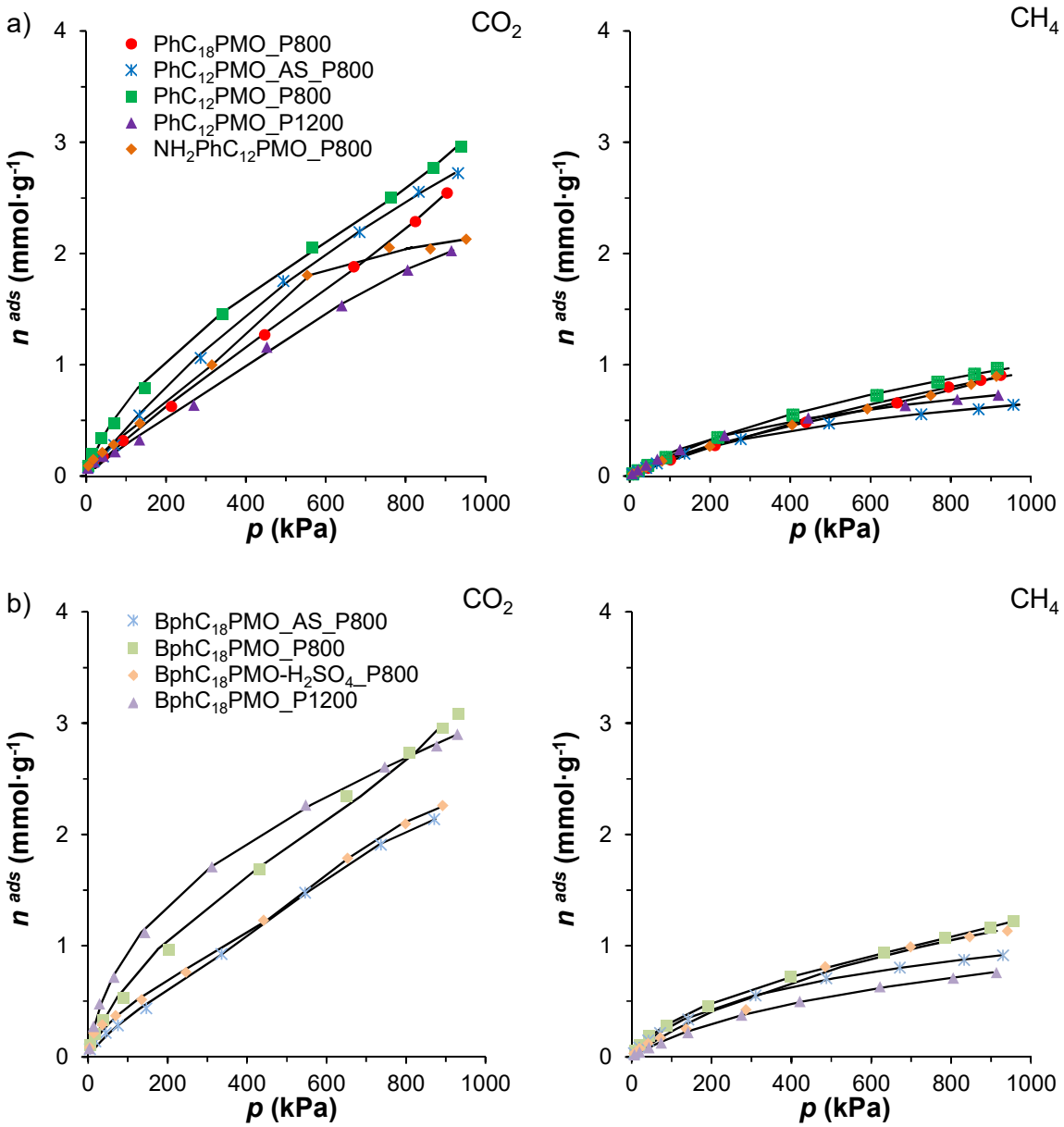

Figure 4.2.5. Adsorption equilibrium isotherms of CO_2 and CH_4 at 25 °C on pyrolysed a) phenylene- and b) biphenylene-PMOs.

The chemical attack with H_2SO_4 previously to the pyrolysis leads also to a material with low CH_4 adsorption capacity especially at low pressure values. The increase of the pyrolysis

temperature to 1200 °C gives rise to the $BphC_{18}PMO\_P1200$ which presents the worst result regarding the adsorption of this gas (K_H of 2.22 x 10^{-2} mmol·g^{-1}·kPa^{-1}, Figure 4.2.5b and Table 4.2.1).

Table 4.2.1. Henry's constants (K_H) and Virial coefficients (C_1 and C_2) for the adsorption of methane and carbon dioxide at 25 °C on the pyrolysed PMOs.[a]

Gas	Material	K_H[a] (mmol g^{-1} kPa^{-1}) x 10^{-2}	C_1[a] g mmol^{-1}	C_2[a] (g mmol^{-1})^2	C_3[a] (g mmol^{-1})^3	*Selectivity*
CH_4	$PhC_{18}PMO\_P800$	0.14	0.453			
	$PhC_{12}PMO\_AS\_P800$	0.22	1.859			
	$PhC_{12}PMO\_P800$	0.21	0.720			
	$PhC_{12}PMO\_P1200$	0.30	1.834			
	$NH_2PhC_{12}PMO\_P800$	0.22	2.100	-1.323		
	$BphC_{18}PMO\_AS\_P800$	0.45	1.670			
	$BphC_{18}PMO\_P800$	0.59	2.218	-0.790		
	$BphC_{18}PMO\text{-}H_2SO_4\_P800$	0.27	0.679			
	$BphC_{18}PMO\_P1200$	0.22	1.266	-0.648	0.178	
CO_2	$PhC_{18}PMO\_P800$	0.36	0.250	-0.062		2.36 (2.48[b])
	$PhC_{12}PMO\_AS\_P800$	0.46	0.163			3.30 (2.12[b])
	$PhC_{12}PMO\_P800$	1.11	0.865	-0.149		4.60 (5.40[b])
	$PhC_{12}PMO\_P1200$	0.34	0.800			1.78 (1.13[b])
	$NH_2PhC_{12}PMO\_P800$	0.81	2.777	-2.565	0.725	2.87 (3.65[b])
	$BphC_{18}PMO\_AS\_P800$	0.53	1.461	-1.044	0.247	1.59 (1.16[b])
	$BphC_{18}PMO\_P800$	1.11	0.876	-0.159		2.95 (1.88[b])
	$BphC_{18}PMO\text{-}H_2SO_4\_P800$	1.14	2.758	-1.745	0.363	2.33 (4.24[b])
	$BphC_{18}PMO\_P1200$	2.34	1.060	-0.126		9.50 (10.70[b])

[a]Determined by nonlinear least-squares fitting of the virial equation to the adsorption data at 500 kPa. [b]Ratio between the Henry's constant for CO_2 and for CH_4.

These results are remarkable, once they can be correlated to the pores structure obtained using different pyrolysis conditions. Thus, the increase of V_{micro} on the pyrolysed biphenylene-PMOs reduces the CH_4 adsorption performance (Table 4.2.1 and Table B2.1). In general, the increase of microporosity on the pyrolysed PMOs improves the CO_2 adsorption properties and diminishes the CH_4 adsorption behaviour. This is in agreement with results found on carbon-based adsorbents where it was found that narrow micropores favours CO_2 adsorption while large micropores are more suitable for CH_4 adsorption.[34,57–59]

The selectivity of the separation and the equilibrium phase diagrams are also determined in this study from the analysis of the adsorption data using the Ideal Adsorbed Solution Theory[27], by fitting the Virial equation to the pure-component isotherms and also by using the method proposed by Myers[25,26,60]. Figure 4.2.6 shows the differences in the selectivities

displayed for the CO_2/CH_4 separation by pyrolysed PMO adsorbents. The differences between the values of selectivity can be quite large. In fact, the $BphC_{18}PMO\_P1200$ adsorbent has superior selectivity (9.5 at 500 kPa) to all other pyrolysed phenylene- or biphenylene-PMOs.

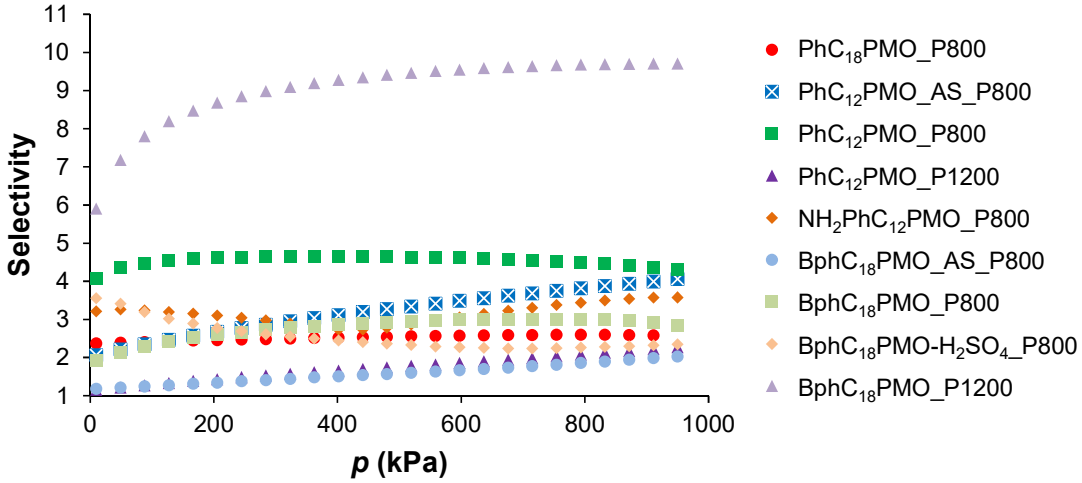

Figure 4.2.6. Average selectivity for the CO_2/CH_4 separation on the different pyrolysed PMOs at 25 °C.

$PhC_{12}PMO\_P800$ displays a selectivity of 4.6 at 500 kPa. It is noteworthy that the materials with the highest selectivity on the CO_2/CH_4 separation are the materials with highest microporosity of each PMO family. Curiously, the amount of micropores (V_{micro}) on the material is not directly proportional to the CO_2 and CH_4 adsorption ability and also to the selectivity to separate these gases. This means that behind the microporosity factor there are other potential features influencing the CO_2 and CH_4 adsorption namely the pore diameter and the chemical nature of the moieties.

The ability of the materials to separate CO_2 and CH_4 can be also estimated by the ratio of the K_H values, determined for CO_2 and CH_4 adsorption on each adsorbent experimentally considered in this work (*c.f.* Table 4.2.1). The results obtained present the same trend as observed before. The biggest ratio was determined for $BphC_{18}PMO\_P1200$, which seems to be the most remarkable adsorbent for CO_2/CH_4 separation.

Figure 4.2.7 demonstrates the influence of all variables on the separation, where the $BphC_{18}PMO\_P1200$ presents slightly improved behaviour than $PhC_{12}PMO\_P800$. Furthermore, these two adsorbents present better results than any other PMO prepared in this study.

Having into account a 0.5 molar composition of methane (y_{CH_4}), which is a realistic value for biogas composition and for some natural gas sources, the composition in the adsorbed phase (x_{CH_4}) is 0.08 on $BphC_{18}PMO\_P1200$ and 0.15 on $PhC_{12}PMO\_P800$, at 500 kPa and 25 °C.

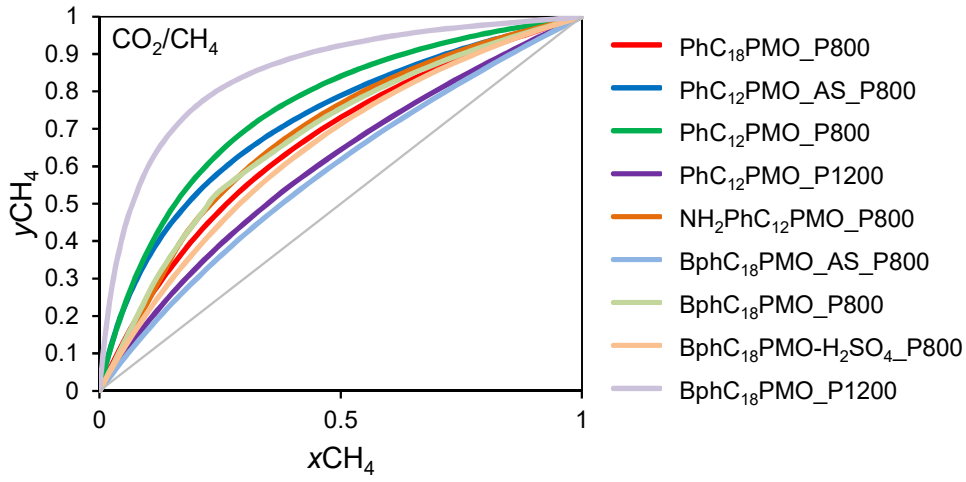

Figure 4.2.7. Isothermal (25 °C), isobaric (500 kPa) *xy* phase diagams of the CO_2/CH_4 mixtures on pyrolysed phenylene and biphenylene PMOs. y_{CH_4} is the molar fraction of methane in the gas phase; x_{CH_4} is the molar fraction of methane in the adsorbed phase.

Therefore, the most interesting material to separate CO_2 from CH_4 is the $BphC_{18}PMO\_P1200$, where the adsorbed phase is much richer in CO_2 than in CH_4, adsorbing carbon dioxide with a purity of around 0.92 molar composition at 500 kPa and 25 °C, for a 0.5 composition in the gas phase. Comprehensive phase diagrams were also calculated (Figure B2.4 in the Appendix B), which support these results.

4.2.4 Conclusions

Phenylene- and biphenylene- PMO families were heated at two different carbonization temperatures under inert conditions, resulting in carbonized PMO materials with differences in both the chemistry and the textural properties of the materials. The reduction of pore size to micro-pores is the most significant difference observed when compared with the unpyrolysed materials, but the surface areas and the particles size are also smaller. Interesting, the highest carbonization temperature; the presence of the surfactant and amine groups; and the use of H_2SO_4 during the carbonization process lead to the production of materials with small pore size and high amount of micropores. The hexagonal arrangement

of the pores remains after the carbonization process even when the materials were pyrolysed at 1200 °C (observed by PXRD and TEM techniques). Furthermore, the molecular-scale periodicity of the carbonized materials with the exception of biphenylene-PMO was strongly affected by the pyrolysis treatment probably as result of Si-C bond cleavage.

All materials were tested in the pure CO_2 and pure CH_4 adsorption at 25 °C. The CO_2 adsorption capacity and the selectivity for CO_2/CH_4 separation were enhanced for all pyrolysed materials. The highest selectivity on the CO_2/CH_4 separation was observed for materials with the highest microporosity. The most interesting material for CO_2/CH_4 separation is the biphenylene-PMO pyrolysed at 1200 °C, presenting the highest K_H for the CO_2 (2.34×10^{-2} mmol·g^{-1}·kPa^{-1}) observed in this PhD study (Chapters 3 and 4), which is remarkable for a material without further amine functionalization.

4.3. Bibliography

1 M. Ohashi, M.P. Kapoor, S. Inagaki, Chemical modification of crystal-like mesoporous phenylene-silica with amino group. *Chem Commun*. **2008**, 7: 841–843.

2 S. Inagaki, S. Guan, T. Ohsuna, O. Terasaki, An ordered mesoporous organosilica hybrid material with a crystal-like wall structure. *Nature*. **2002**, 416: 304–307.

3 P. Ferreira, C. Bispo, M.A.O. Lourenço, J.R.B. Gomes, N. Bion, K.D.O. Vigier, F. Jérôme, Making periodic mesoporous organosilicas functional materials. In: M. Aliofkhazraei (ed.). Comprehensive guide for mesoporous materials, Vol. 4: application and commercialization. Nova Science Publishers, Inc., **2015**: 261–295.

4 A. Zukal, I. Dominguez, J. MayerovĂ, J. Čejka, Functionalization of delaminated zeolite ITQ-6 for the adsorption of carbon dioxide. *Langmuir*. **2009**, 25: 10314–10321.

5 V. Zeleňak, M. Badaničova, D. Halamova, J. Čejka, A. Zukal, N. Murafa, G. Goerigk, Amine-modified ordered mesoporous silica: Effect of pore size on carbon dioxide capture. *Chem Eng J*. **2008**, 144: 336–342.

6 C. Chen, W.S. Ahn, CO_2 capture using mesoporous alumina prepared by a sol–gel process. *Chem Eng J*. **2011**, 166: 646–651.

7 O.G. Nik, B. Nohair, S. Kaliaguine, Aminosilanes grafting on FAU/EMT zeolite: Effect on CO_2 adsorptive properties. *Micropor Mesopor Mater*. **2011**, 143: 221–229.

8 T.W. Pechar, S. Kim, B. Vaughan, E. Marand, M. Tsapatsis, H.K. Jeong, C.J. Cornelius, Fabrication and characterization of polyimide–zeolite L mixed matrix membranes for gas separations. *J Membr Sci*. **2006**, 277: 195–202.

9 W.Z. F. Su, C. Lu, S. C. Kuo, Adsorption of CO_2 on Amine-functionalized Y-type zeolites. *Energ Fuel*. **2010**, 24: 1441–1448.

10 U. Martinez, G. Pacchioni, Interaction of CO, CO_2 and CH_4 with mesoporous organosilica: Periodic DFT calculations with dispersion corrections. *Micropor Mesopor Mater*. **2010**, 129: 62–67.

11 A. Torrisi, R.G. Bell, C. Mellot-Draznieks, Functionalized MOFs for enhanced CO_2 capture. *Cryst Growth Des*. **2010**, 10: 2839–2841.

12 Z. Zhou, Y. Qi, M. Xie, Z. Cheng, W. Yuan, Synthesis of CaO-based sorbents through incorporation of alumina/aluminate and their CO_2 capture performance. *Chem Eng Sci*. **2012**, 74: 172–180.

13 S. Biswas, T. Rémy, S. Couck, D. Denysenko, G. Rampelberg, J.F.M. Denayer, D. Volkmer, C. Detavernier, P. Van Der Voort, Partially fluorinated MIL-47 and Al-MIL-53 frameworks: influence of functionalization on sorption and breathing properties. *Phys Chem Chem Phys*. **2013**, 15: 3552–3561.

14 S.-H. Lo, C.-H. Chien, Y.-L. Lai, C.-C. Yang, J.J. Lee, D.S. Rajaa, C.-H. Lin, A mesoporous aluminium metal–organic framework with 3 nm open pores. *J Mater Chem A*. **2013**, 1: 324–329.

15 Q. Yang, S. Vaesen, M. Vishnuvarthan, F. Ragon, C. Serre, A. Vimont, M. Daturi, G. De Weireld, G. Maurin, Probing the adsorption performance of the hybrid porous MIL-68(Al): a synergic combination of experimental and modelling tools. *J Mater Chem*. **2012**, 22: 10210–10220.

16 X. Si, J. Zhang, F. Li, C. Jiao, S. Wang, S. Liu, Z. Li, H. Zhou, L. Sun, F. Xu, Z. Zhou, Y. Qi, M. Xie, Z. Cheng, W. Yuan, Synthesis of CaO-based sorbents through incorporation of alumina/aluminate and their CO_2 capture performance. *Chem Eng Sci*. **2012**, 74: 172–180.

17 P. Rallapalli, K.P. Prasanth, D. Patil, R.S. Somani, R. V. Jasra, H.C. Bajaj, Sorption studies of CO_2, CH_4, N_2, CO, O_2 and Ar on nanoporous aluminum terephthalate [MIL-53(Al)]. *Porous Mater*. **2011**, 18: 205–210.

18 X. Shang, X. Wang, W. Nie, X. Guo, X. Zou, W. Ding, X. Lua, Facile strategy for synthesis of mesoporous crystalline γ-alumina by partially hydrolyzing aluminum nitrate solution. *J Mater Chem*. **2012**, 22: 23806–23814.

19 M. Knez, K. Nielsch, L. Niinistö, Synthesis and surface engineering of complex nanostructures by atomic layer deposition. *Adv Mater*. **2007**, 19: 3425–3438.

20 N. Bion, P. Ferreira, A. Valente, I.S. Gonçalves, J. Rocha, Ordered benzene-silica hybrids with molecular-scale periodicity in the walls and different mesopore sizes. *J Mater Chem*. **2003**, 13: 1910–1913.

21 G. Smeulders, C.J. Van Oers, K. Van Havenbergh, K. Houthoofd, M. Mertens, J.A. Martens, S. Bals, B.U.W. Maes, V. Meynen, P. Cool, Smart heating profiles for the synthesis of benzene bridged periodic mesoporous organosilicas. *Chem Eng J*. **2011**, 175: 585–591.

22 T. Asefa, M.J. MacLachlan, N. Coombs, G.A. Ozin, Periodic mesoporous organosilicas with organic groups inside the channel walls. *Nature*. **1999**, 402: 867–871.

23 R.J.P. Corriu, J.J.E. Morea, P. Thepot, M.W. Chi Man, New mixed organic-inorganic polymers: hydrolysis and polycondensation of bis(trimethoxysilyl) organometallic precursors. *Chem Mater*. **1992**, 4: 1217–1224.

24 S. Hartmann, A. Sachse, A. Galarneau, Challenges and strategies in the synthesis of mesoporous alumina powders and hierarchical alumina monoliths. *Materials*. **2012**, 5: 336–349.

25 A.L. Myers, Equation of state for adsorption of gases and their mixtures in porous materials. *Adsorption*. **2003**, 9: 9–16.

26 J. Pires, V.K. Saini, M.L. Pinto, Studies on selective adsorption of biogas components on pillared clays : approach for biogas improvement. *Environ Sci Technol*. **2008**, 42: 8727–8732.

27 A.L. Myers, J.M. Prausnitz, Thermodynamics of mixed-gas adsorption. *AIChE J*. **1965**, 11: 121–127.

28 M.L. Pinto, J. Pires, J. Rocha, Porous materials prepared from clays for the upgrade of landfill gas. *J Phys Chem C*. **2008**, 112: 14394–14402.

29 G. Cre, V. Montouillout, A. Vimont, L. Mariey, T. Cseri, F. Mauge, Nature, structure and strength of the acidic sites of amorphous silica alumina: an IR and NMR study. *J Phys Chem B*. **2006**, 110: 15172–15185.

30 L. Heeribout, R. Vincent, P. Batamack, C. Dor, J. Fraissard, Brønsted acidity of amorphous silica – aluminas studied by ^{1}H NMR. *Catal Lett*. **1998**, 53: 23–31.

31 R.W. Zwanzig, Influence of molecular electric quadrupole moments on dielectric constants. *J Chem Phys*. **1956**, 25: 211–216.

32 R.T. Yang, Gas separation by adsorption processes. Butterworths Publishers: Boston, **1987**.

33 V.K. Saini, M. Pinto, J. Pires, Natural clay binder based extrudates of mesoporous materials: improved materials for selective adsorption of natural and biogas components. *Green Chem*. **2011**, 13: 1251–1259.

34 A.S. Mestre, C. Freire, J. Pires, A.P. Carvalho, M.L. Pinto, High performance microspherical activated carbons for methane storage and landfill gas or biogas upgrade. *J Mater Chem A*. **2014**, 2: 15337–15344.

35 S.A. Peter, G. V. Baron, J. Gascon, F. Kapteijn, J.F.M. Denayer, Dynamic desorption of CO_2 and CH_4 from amino-MIL-53(Al) adsorbent. *Adsorption*. **2013**, 19: 1235–1244.

36 A.F.P. Ferreira, A.M. Ribeiro, S. Kulaç, A.E. Rodrigues, Methane purification by adsorptive processes on MIL-53(Al). *Chem Eng Sci*. **2015**, 124: 79–95.

37 X. Peng, W. Wang, R. Xue, Z. Shen, Adsorption separation of CH_4/CO_2 on mesocarbon microbeads: Experiment and modeling. *AIChE J*. **2006**, 52: 994–1003.

38 X. Wu, M. Niknam Shahrak, B. Yuan, S. Deng, Synthesis and characterization of zeolitic imidazolate framework ZIF-7 for CO_2 and CH_4 separation. *Micropor Mesopor Mater*. **2014**, 190: 189–196.

39 S. Inagaki, S. Guan, Y. Fukushima, T. Ohsuna, O. Terasaki, Novel mesoporous materials with a uniform distribution of organic groups and inorganic oxide in their frameworks. *J Am Chem Soc*. **1999**, 121: 9611–9614.

40 B. Melde, B. Holland, C. Blanford, A. Stein, Mesoporous sieves with unified hybrid inorganic/organic frameworks. *Chem Mater*. **1999**, 11: 3302–3308.

41 K. Sim, N. Lee, J. Kim, E.-B. Cho, C. Gunathilake, M. Jaroniec, CO_2 adsorption on amine-functionalized periodic mesoporous benzenesilicas. *ACS Appl Mater Interf*. **2015**, 7: 6792–6802.

42 S. Masse, G. Laurent, F. Babonneau, High temperature behavior of periodic mesoporous ethanesilica glasses prepared from a bridged silsesquioxane and a non-ionic triblock copolymer. *J Non Cryst Solids*. **2007**, 353: 1109–1119.

43 B. Toury, F. Babonneau, Synthesis of periodic mesoporous organosilica from bis(triethoxysilyl)methane and their pyrolytic conversion into porous SiCO glasses. *J Eur Ceram Soc*. **2005**, 25: 265–270.

44 A. Pauletti, S. Handjani, C. Fernandez-Martin, C. Gervais, F. Babonneau, A new example of periodic mesoporous SiCO glasses with cubic symmetry stable at 1000°C. *J Ceram Soc Japan*. **2008**, 116: 449–453.

45 B. Toury, R. Blum, V. Goletto, F. Babonneau, Thermal stability of periodic mesoporous SiCO glasses. *J Sol-Gel Sci Technol*. **2005**, 33: 99–102.

46 S.S. Park, Y. Jung, C. Xue, R. Che, D. Zhao, C.S. Ha, Free-standing mesoporous silica/carbon composite films with crystalline silica wall from ethylene-bridged organosilane. *Chem Mater*. **2010**, 22: 18–26.

47 M. Weinberger, S. Puchegger, T. Fröschl, F. Babonneau, H. Peterlik, N. Hüsing, Sol-gel processing of a glycolated cyclic organosilane and its pyrolysis to silicon oxycarbide monoliths with multiscale porosity and large surface areas. *Chem Mater*. **2010**, 22: 1509–1520.

48 Z. Yang, Y. Xia, R. Mokaya, Periodic mesoporous organosilica mesophases are versatile precursors for the direct preparation of mesoporous silica/carbon composites, carbon and silicon carbide materials. *J Mater Chem*. **2006**, 16: 3417–3425.

49 M.P. Kapoor, Q. Yang, S. Inagaki, Self-assembly of biphenylene-bridged hybrid mesoporous solid with molecular-scale periodicity in the pore walls. *J Am Chem Soc*. **2002**, 124: 15176–15177.

50 M.A.O. Lourenço, A. Mayoral, I. Díaz, A.R. Silva, P. Ferreira, Amino-modified periodic mesoporous biphenylene-silica. *Micropor Mesopor Mater*. **2015**, 217: 167–172.

51 M. Thommes, K. Kaneko, A.V. Neimark, J.P. Olivier, F. Rodriguez-Reinoso, J. Rouquerol, K.S.W. Sing, Physisorption of gases, with special reference to the

evaluation of surface area and pore size distribution (IUPAC Technical Report). *Pure Appl Chem*. **2015**, 89: 1051–1069.

52 S. Brunauer, P.H. Emmett, E. Teller, Adsorption of gases in multimolecular layers. *J Am Chem Soc*. **1938**, 60: 309–319.

53 K. Sing, The use of nitrogen adsorption for the characterisation of porous materials. *Colloid Surface A*. **2001**, 187–188: 3–9.

54 A.V. Neimark, Y. Lin, P.I. Ravikovitch, M. Thommes, Quenched solid density functional theory and pore size analysis of micro-mesoporous carbons. *Carbon*. **2009**, 47: 1617–1628.

55 M. Thommes, J. Morell, K.A. Cychosz, M. Fröba, Combining nitrogen, argon, and water adsorption for advanced characterization of ordered mesoporous carbons (CMKs) and periodic mesoporous organosilicas (PMOs). *Langmuir*. **2013**, 29: 14893–14902.

56 R. Gadiou, A. Didion, R.I. Gearba, D.A. Ivanov, I. Czekaj, R. Kötz, C. Vix-Guterl, Synthesis and properties of new nitrogen-doped nanostructured carbon materials obtained by templating of mesoporous silicas with aminosugars. *J Phys Chem Solids*. **2008**, 69: 1808–1814.

57 D. Lozano-Castelló, D. Cazorla-Amorós, A. Linares-Solano, D.F. Quinn, Influence of pore size distribution on methane storage at relatively low pressure: preparation of activated carbon with optimum pore size. *Carbon*. **2002**, 40: 989–1002.

58 K.R. Matranga, A.L. Myers, E.D. Glandt, Storage of natural-gas by adsorption on activated carbon. *Chem Eng Sci*. **1992**, 47: 1569–1579.

59 X.S. Chen, B. Mcenaney, T.J. Mays, J. Alcaniz-Monge, D. Cazorla-Amoros, A. Linares-Solano, Theoretical and experimental studies of methane adsorption on microporous carbons. *Carbon*. **1997**, 35: 1251–1258.

60 M.L. Pinto, J. Pires, J. Rocha, Porous materials prepared from clays for the upgrade of landfill gas. *J Phys Chem C*. **2008**, 112: 14394–14402.

Chapter 5 – Microwave-assisted PMO modifications

In this Chapter, it is described the application of the microwave-assisted irradiation to tune the surface properties of the phenylene-PMO through the modification of the phenylene moieties with primary amino groups, followed by their mono- and di-alkylation.

5.1 Microwave-assisted *N*-alkylation of amine modified mesoporous phenylene-silica

Adapted from:

Mirtha A. O. Lourenço, Renée Siegel, Luís Mafra and Paula Ferreira

Microwave-assisted N-alkylation of amine functionalized crystal-like mesoporous phenylene-silica

Dalton Trans., **2013**, 42: 5631–5634

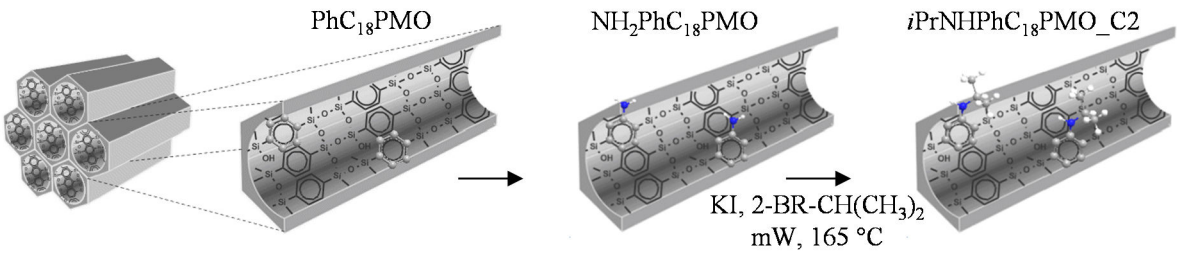

My direct contribution:

I declare that I have prepared, functionalized and characterized the PMOs materials.

Luís Mafra and Renée Siegel performed and helped with the analysis of the ^{15}N solid-state spectra.

5.1.1 Motivation

As it was seen in Sub-chapter 1.4, the PMO materials were initially modified by changing the organic-bridge of bissilylated precursors used on their synthesis.[1] The chemical modification of the organic moieties integrating this material allows also to tune their applicability, which seems to be very promising but so far not many examples were reported.[2] Some examples of post-synthesis functionalization in phenylene PMO deal with the sulfonation of the aromatic ring,[3] the incorporation of arenetricarbonyl complexes of Mo and Cr,[4–6] and the amination of phenylene moieties of the PMO.[7]

In this work, it is showed that is possible in a simple way to modify homogenously the chemistry of periodic mesoporous phenylene-silica by inclusion of interesting functional groups. Herein, it is reported the first example of the *N*-alkylation of the periodic mesoporous phenylene silica with an amino group at the aromatic ring. It is also a novelty the use of microwave irradiation in the functionalization of PMO materials. There are only few reports using the microwave-assisted synthesis in PMOs, most in the preparation of the PMO material.[8–10] Smeulders *et al.*[8] demonstrated that this unconventional fast heating approach kept unchanged the structure of this kind of hybrid materials during the hydrothermal step synthesis. Additionally, when compared with the conventional synthesis, the usage of microwave irradiation promoted narrower distribution of pore sizes, higher surface area and larger pore volumes.[8]

Due to the dielectric heating, chemical reactions under microwave radiation generally occur much faster.[11] Molecules possessing a permanent dipole moment tend to become aligned with the microwave electromagnetic field and, during this motion, they suffer frictions and collisions, with consequent heat generation. The efficiency of microwave heating is strongly dependent on the dielectric properties and on the relaxation times of the reaction components (namely reactants, functional groups and solvents).[12–14] Additionally, as the majority of the microwave ovens work at 2.45 GHz, the molecules exposed to this radiation are able to generate a strong internal heat with a heating rate up to 10 °C per second. Using conventional heating, the temperature of the surface of the reaction vessel becomes higher than its internal temperature and the transfer of the heating is made *via* thermal conduction. Therefore, the microwave radiation is a non-contact heating source allowing a more selective and effective heating than the conventional sources. Reaction vessels can be chosen to permit the microwave energy to go through it and heat only the reactants. Specific microwave effects

can also occur during the reaction due to the presence of polar molecules in the mixture or if the polarity of the transition state is higher than the polarity of the ground state.[15,16]

This work combines the know-how obtained from the organic and inorganic chemistry to develop the PMO materials that even after one decade of research remains largely underexploited. A microwave-assisted reaction used in organic synthesis for the monoalkylation of aniline[17] is adapted to the functionalization of $NH_2PhC_{18}PMO$ to achieve the *N*-alkylation of the amine group as depicted in Figure 5.1.1.

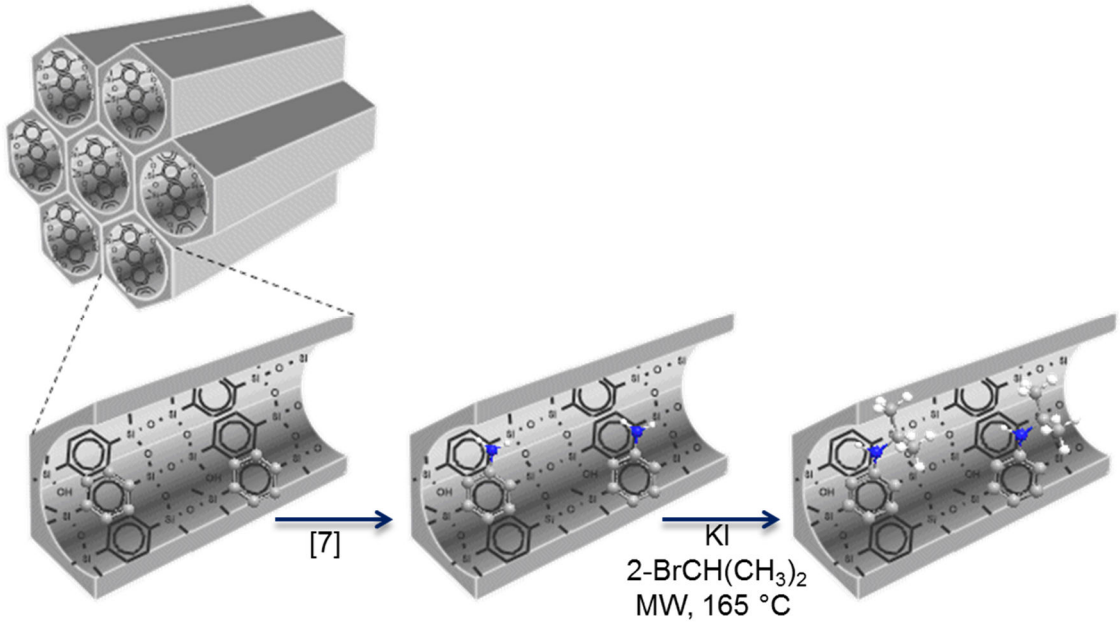

Figure 5.1.1. Schematic representation of the synthesis of *i*PrNHPhC_{18}PMO_C2.

5.1.2 Experimental details

Materials synthesis

The phenylene PMO ($PhC_{18}PMO$) was obtained following the literature procedures[18–20] by hydrolysis and condensation of home-made BTEB precursor[21] in the presence of octadecyltrimethylammonium bromide surfactant template (C_{18}-TMA). After synthesis the template was extracted by an ethanol/HCl solution. The incorporation of functional amino groups into the phenylene rings was achieved upon treatment with very strong acid solutions of HNO_3–H_2SO_4 and $SnCl_2$–HCl using the same procedure of Inagaki *et al.*[7] The final material is denoted $NH_2PhC_{18}PMO$. The *N*-alkylation of $NH_2PhC_{18}PMO$ was carried out by two reaction cycles under microwave irradiation. To a suspension of $NH_2PhC_{18}PMO$ (278 mg) in acetonitrile (3 mL), 2-bromopropane (285 mg) and KI (40 mg) were added. A

vial containing the previous mixture was then sealed and heated at 170 °C for 20 minutes in a CEM Discovery SP microwave. The reacted powder was filtered, washed successively with CH_2Cl_2 (20 mL), $NaHCO_3$ (aqueous saturated solution), brine and dried overnight at 60 °C. The dried powder was collected and subjected to a second reaction cycle in the same conditions as the first one but only with 70% of the initial 2-bromopropane quantity. The alkylated samples are denoted *i*PrNHPhC_{18}PMO_C1 or *i*PrNHPhC_{18}PMO_C2 after cycle 1 or cycle 2, respectively.

Materials characterization

The physical, textural and chemical properties of the prepared PMO materials were evaluated by N_2 sorption isotherms, TEM, FTIR, ^{29}Si MAS and CP-MAS NMR, ^{13}C CP-MAS and ^{15}N CP-MAS NMR spectroscopies. The thermal stability of materials was evaluated by TGA. Description of the experimental conditions is presented at Chapter 2 and the data obtained by PXRD, TEM, N_2 sorption isotherms, ^{29}Si MAS and CP-MAS NMR and FTIR spectroscopies and TGA and EA analyses are presented in Appendix C.

5.1.3 Results and discussion

The structural order and the textural physical properties before and after functionalization were evaluated by PXRD, TEM and -196 °C N_2 adsorption-desorption isotherms. PXRD patterns of PhC_{18}PMO, NH_2PhC_{18}PMO and *i*PrNHPhC_{18}PMO_C2 (Figure C1.1, Appendix C) reveal for all materials the first strong low-angle (100) reflection and the two much less intense (110) and (200) peaks, all characteristic for a two-dimensional hexagonal symmetry (*p6mm*) lattice. The characteristic low angle diffraction peaks at d = 4.48 nm (in the pristine PhC_{18}PMO material) and at d = 4.53 nm (after functionalization) (Table C1.1, Appendix C) allowed the calculation of the lattice parameter a ($a = 2d_{100}/\sqrt{3}$), which is 5.17 nm and 5.23 nm for the as-synthesized and functionalized PhC_{18}PMOs, respectively. The peaks at d = 7.58 nm are due to the molecular-scale crystal-like structure. Both meso- and molecular-scale periodicities are preserved after amination and monoalkylation under microwave conditions and high temperatures. The TEM images (Figure C1.2, Appendix C) support the order along the channel for all materials. The inset in Figure C1.2d shows the hexagonal arrangement of pores corroborating the 1D hexagonal structure of the *N*-alkylated PhC_{18}PMO. The -196 °C N_2 adsorption–desorption isotherms and PSD curves (Figure C1.3,

Appendix C) also confirm type IV isotherms (IUPAC classification) for all materials with narrow distribution of pore sizes as typically observed for conventional mesoporous materials such as MCM-41. The pore size profiles (Figure C1.3 and Table C1.1, Appendix C) suffer from a maximum shifting from 3.55 to 3.41 nm with the introduction of the isopropyl group into the amine.

The ^{13}C CP-MAS NMR spectra (Figure 5.1.2) support the amination of the $PhC_{18}PMO$ and the *N*-alkylation of amine moieties in $NH_2PhC_{18}PMO$. The pure $PhC_{18}PMO$ display the typical resonance at 134 ppm of the aromatic carbons as reported in literature (Figure 5.1.2a).[3,20] Small peaks can be observed in the region 0 to 50 ppm that are related to the presence of some non-extracted template.

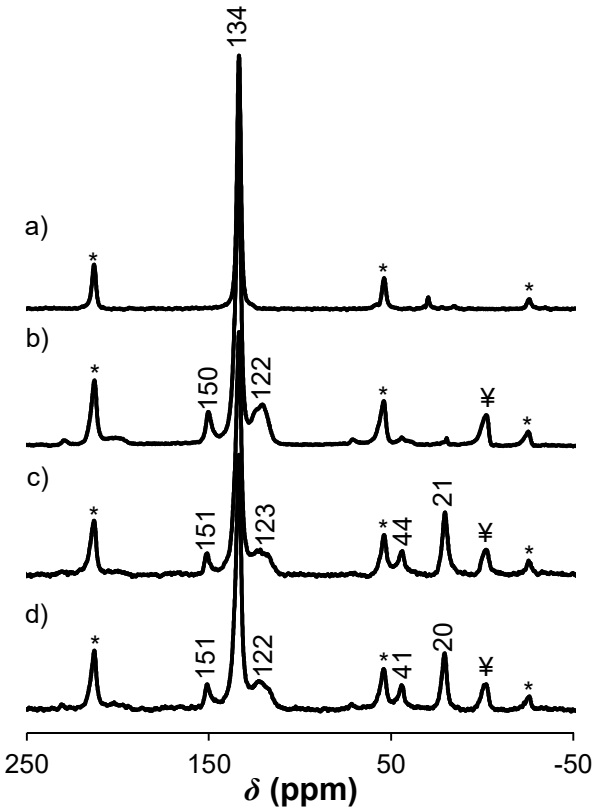

Figure 5.1.2. ^{13}C CP-MAS NMR spectra of a) $PhC_{18}PMO$, b) $NH_2PhC_{18}PMO$, c) *i*$PrNHPhC_{18}PMO$_C1 and d) *i*$PrNHPhC_{18}PMO$_C2. Signal marked ¥ are due to silicone grease. * denotes spinning sidebands. ppm referenced from TMS ((tetramethylsilane).

The ^{13}C CP-MAS NMR spectrum of $NH_2PhC_{18}PMO$ displays resonances at *ca.* 122, 134 and 150 ppm assigned to the sp^2 carbons from the phenylene group in agreement with the results reported before (Figure 5.1.2b).[7] The subsequent *N*-alkylation reaction results in chemical shift changes of the previously identified resonances in $NH_2PhC_{18}PMO$ and the

presence of two new peaks at *ca.* 41 and 20 ppm (Figure 5.1.2d) corresponding, respectively, to the CH and CH_3 carbons from the isopropyl group linked to the amine (-NHCH(CH_3)$_2$. The *N*-alkylation is also confirmed by ^{15}N CP-MAS NMR (Figure 5.1.3). The ^{15}N NMR spectrum of $NH_2PhC_{18}PMO$ (Figure 5.1.3a) presents a single peak at *ca.* -325 ppm, which corresponds to the primary amine group (NH_2).

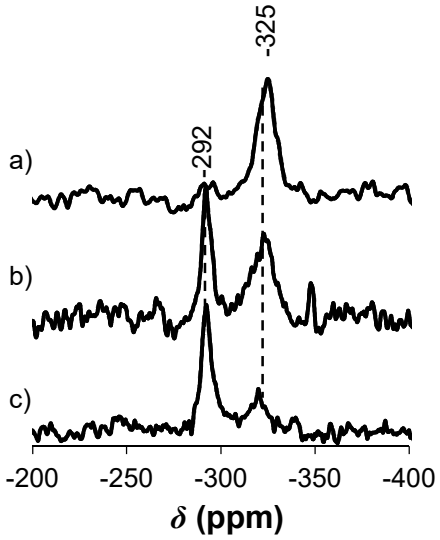

Figure 5.1.3. ^{15}N CP-MAS NMR spectra of a) $NH_2PhC_{18}PMO$, b) *i*PrNHPhC_{18}PMO_C1 and c) *i*PrNHPhC_{18}PMO_C2.

After one cycle of *N*-alkylation, a new ^{15}N resonance arises at *ca.* -292 ppm, associated to the partial formation of secondary amine groups (Figure 5.1.3b). In a second cycle of alkylation, the ^{15}N resonance at *ca.* -325 ppm is almost vanished, while the peak of the secondary amine (-292 ppm), comparatively, increases in intensity (Figure 5.1.3c).

The ^{29}Si MAS and CP-MAS NMR spectra of all materials are shown in Figure C1.4 (Appendix C). The parent $PhC_{18}PMO$ exhibits peaks at *ca.* 81, 71 and 61 ppm assigned to T^3, T^2 and T^1 [T^m = $RSi(OSi)_m(OH)_{3-m}$] organosiliceous species, respectively, as described in the literature[3,20]. The assignment of the faint T^1 peak observed in the ^{29}Si MAS NMR spectrum was further supported by the ^{29}Si CP-MAS NMR spectrum where it appears enhanced. The amination of $PhC_{18}PMO$ produces significant changes in the spectra. The T^1 peak almost disappears and the intensity of T^2 decreases with respect to T^3 sites. This means that the high acid treatment promotes the further condensation of the free silanol groups. After *N*-alkylation of $NH_2PhC_{18}PMO$, a faint resonance in the region of the Q^n species [Q^n = $Si(OSi)_n(OH)_{4-n}$] is observed in the ^{29}Si spectra of *N*-alkylated materials, which indicates a small amount of carbon-silicon bond cleavage during the *N*-alkylation reaction

under microwave conditions. The functionalization of the $PhC_{18}PMO$ material was also followed by FTIR spectroscopy (Figure C1.5, Appendix C). The presence of amine functionalized $PhC_{18}PMO$ aromatic rings is confirmed by the C-N stretching band displayed at 1267 cm^{-1} and the in plane N-H bending vibration ("*scissoring" mode*) near 1633 cm^{-1}, typical of an aromatic primary amine. This later band is overlapped with the band of H–O–H bending vibrations. The band at 1633 cm^{-1} decreases intensity when the amine is alkylated, which corroborates the partial transformation of primary to secondary amine as secondary amines do not show a band in this region. The N-H stretching modes of aromatic primary amines appear at 3408 and 3367 cm^{-1}. The aromatic C-H stretching bands appear in the parent $PhC_{18}PMO$ at 3070 cm^{-1} and at ~3100 cm^{-1} in the NH_2-PMO and *N*-alkylated materials. With the *N*-alkylation, the C-H stretching vibrations for saturated aliphatic species occur at 2980 cm^{-1}.

Elemental analysis results are presented in Table C1.2 (Appendix C). $NH_2PhC_{18}PMO$ has an amino group density close to 2 $mmol \cdot g^{-1}$ (3.2% of NH_2), indicating that 47% of phenylene bridges were functionalized with the amine group. Using this technique it was confirmed that about 87% of $NH_2PhC_{18}PMO$ was converted into *i*$PrNHPhC_{18}PMO$_C2. The isopropyl group appears with a density close to 0.52 $mmol \cdot g^{-1}$.

The TGA curves (Figure C1.6, Appendix C) exhibit a first weight loss below 100 °C due to desorption of physisorbed water. From 100 to 300 °C a 2% weight loss occurs in the case of pure $PhC_{18}PMO$ due to the small quantity of non-extracted template. The parent $PhC_{18}PMO$ material has a thermal stability up to 550 °C. Above this value the decomposition and release of the organic moieties from the framework takes place. The introduction of the amine group and the alkylation of the amine led to an expected decrease of the thermal stability. For example, the *i*$PrNHPhC_{18}PMO$_C2 is only stable up to 350 °C.

5.1.4 Conclusion

It was demonstrated that well-ordered amine functionalized periodic mesoporous phenylene-silica can be modified into the monoalkylated counterpart, by a simple microwave-assisted reaction, maintaining its structural integrity. This work proves that it is possible to extend typical homogeneous phase reactions to hybrid material design with potential to open an avenue toward new applications.

5.2 Microwave-assisted *N,N*-dialkylation of amine-functionalized periodic mesoporous phenylene-silica

Adapted from:

Mirtha A. O. Lourenço, Maria J. G. Ferreira, Mariana Sardo, Luís Mafra, José R. B. Gomes and Paula Ferreira

Microwave-assisted N,N-dialkylation of amine-functionalized periodic mesoporous phenylene-silica: An easy and fast way to design materials

Submitted for publication, **2016**

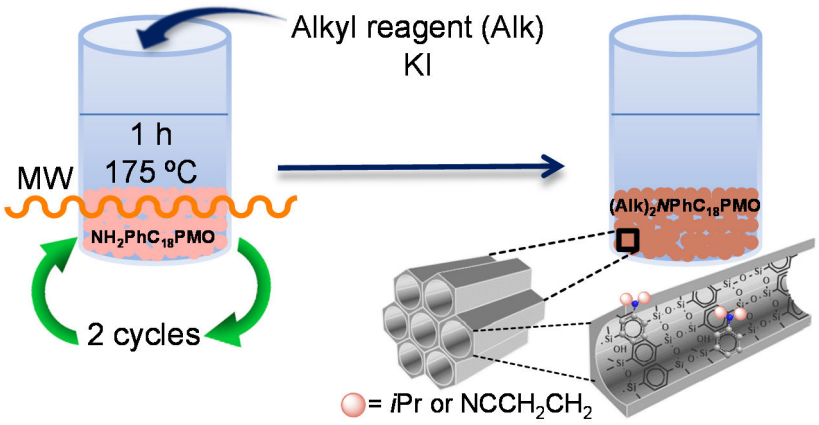

My direct contribution:

I declare that I have prepared and characterized all the PMO materials described in this Sub-chapter. This work was made in collaboration with Luís Mafra, Mariana Sardo and Maria João Ferreira, who were responsible for the ^{15}N solid-state NMR experiments.

5.2.1 Motivation

As demonstrated in Sub-chapter 5.1, microwave-assisted synthesis is a fast and simply way to modify the amine-phenylene-C_{18}PMO with preservation of both meso- and molecular-scale periodicities. In the present Sub-chapter, it is used the microwave-assisted synthesis to manipulate the amine-phenylene moieties in the NH_2PhC_{18}PMO as a versatile approach to introduce new physical and chemical properties into PMOs. Novel functional groups may be added to the PhC_{18}PMOs by this methodology, which would be unreachable by conventional synthetic approaches. Hence, the *N*,*N*-dialkylation of NH_2PhC_{18}PMO with two different alkyl agents is made in order to obtain *N*,*N*-dialkylated amine materials with different features: i) the $(i\text{Pr})_2NPhC_{18}$PMO; and ii) the $(NCCH_2CH_2)_2NPhC_{18}$PMO materials. The latter material is especially interesting since there is the possibility to convert the CN moieties into other functional groups for creating novel PMOs with on-demand properties to be considered mainly in catalysis and adsorption applications.

5.2.2 Experimental details

PMO synthesis

The PhC_{18}PMO[3,20] and the NH_2PhC_{18}PMO[7] were prepared according to the literature procedures as described in Sub-chapter 5.1.2.

The microwave-assisted *N*,*N*-dialkylation on the NH_2PhC_{18}PMO was performed in a CEM Discovery SP microwave. The reaction procedure starts with the addition of 1.107 g (9.00×10^{-3} mol) of 2-bromopropane and 0.155 g (9.34×10^{-4} mol) of KI to a suspension of 300 mg of NH_2PhC_{18}PMO in 3 mL of acetonitrile. The vial is then closed and heated at 175 °C for 1 hour. The reaction mixture was filtered, washed sequentially with CH_2Cl_2 (20 mL), $NaHCO_3$ (aqueous saturated solution) and brine. Finally, the obtained powder was dried overnight at 60 °C. The material was exposed to a second reaction cycle in the same conditions, being denoted hereafter as $(i\text{Pr})_2NPhC_{18}$PMO. The same procedure was applied to the *N*,*N*-dialkylation of the NH_2PhC_{18}PMO with 3-chloropropionitrile, using the same stoichiometry. The obtained material was denoted $(NCCH_2CH_2)_2NPhC_{18}$PMO.

The $(HOOCCH_2CH_2)_2NPhC_{18}$PMO was prepared by gentle addition of 20 mL of HCl to 200 mg of $(NCCH_2CH_2)_2NPhC_{18}$PMO. The reaction was stirred during 4 h at 45 °C. The

reaction mixture was washed with $NaHCO_3$ (aqueous saturated solution), filtered-off and further washed with distilled water. The final powder was dried at 60 °C.

An additional sample, the *i*PrNHPhC_{18}PMO, was prepared to demonstrate the possibility to obtain this material in a single cycle only. In this way, 6.82×10^{-3} mol of 2-bromopropane and 5.89×10^{-4} mol of KI were added to the previous NH_2PhC_{18}PMO and acetonitrile suspension. The microwave-assisted reaction was performed at 165 °C during 20 min. The same procedure previously described was used to wash and to dry the obtained material.

Materials characterization

The samples prepared were characterized by PXRD, -196 °C N_2 adsorption-desorption isotherms, TGA, EA, FTIR, ^{29}Si MAS and CP-MAS NMR, ^{13}C CP-MAS NMR and ^{15}N CP-MAS NMR spectroscopies. The experimental parameters used for each characterization technique are described in Chapter 2 and the data of -196 °C N_2-sorption isotherms, ^{29}Si NMR, FTIR, TGA and EA techniques are presented in Appendix C.

5.2.3 Results and discussion

N,*N*-dialkylated amine-PMOs can be obtained from NH_2PhC_{18}PMO by nucleophilic aliphatic substitution of an alkyl halide under microwave irradiation. Figure 5.2.1 shows the synthetic paths used in this work to prepare (*i*Pr)$_2$NPhC_{18}PMO, (NCCH_2CH_2)$_2$NPhC_{18}PMO and the (HOOCCH_2CH_2)$_2$NPMO materials.

The physical and textural features of the prepared PMOs were evaluated by PXRD, N_2-sorption isotherms and TEM. Figure 5.2.2 shows the PXRD patterns of the synthetized PhC_{18}PMO materials. It is possible to observe in Figure 5.2.2 that the parent PhC_{18}PMO presents a 2D hexagonal symmetry (*p6mm*) lattice characterized by the presence of the strong (100) reflection at low-angle range (with a *d*-spacing of 4.46 nm) followed by two less intense (110) and (200) reflections (Figure 5.2.2a). A medium range reflection at $d \sim 0.76$ nm is also detected which means that the PhC_{18}PMO also has molecular-scale periodicity as reported in the literature.[7] The post-functionalization of the phenylene moieties of the PhC_{18}PMO material leads to the preparation of functionalized PhC_{18}PMOs with (100) reflections that can be compatible with preservation of the 2D hexagonal symmetry (*p6mm*) lattice, Figure 5.2.2. The NH_2PhC_{18}PMO is prepared by amination of the phenylene moieties of the PhC_{18}PMO and presents a *d*-spacing of 4.41 nm (Figure 5.2.2b

and Table C2.1 Appendix C). The *N*,*N*-dialkylation with isopropyl group or with the propionitrile alkyl agent led to the preparation of the $(i\text{Pr})_2\text{NPhC}_{18}\text{PMO}$ and $(\text{NCCH}_2\text{CH}_2)_2\text{NPhC}_{18}\text{PMO}$ materials with *d*-spacings of 4.55 and 4.65 nm, respectively (Figure 5.2.2c-d and Table C2.1).

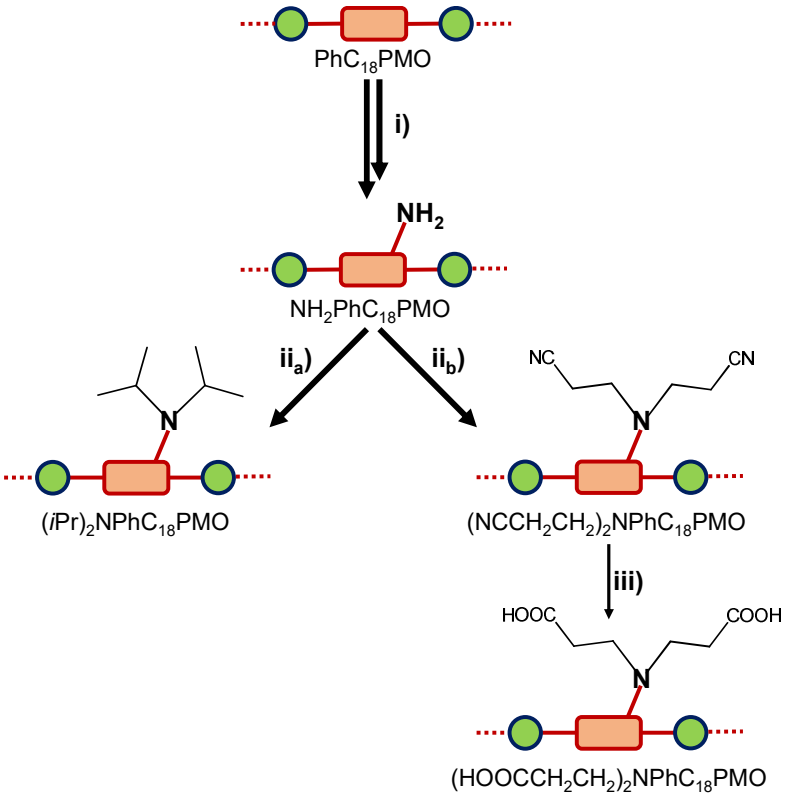

Figure 5.2.2. Schematic representation of the preparation of *N*,*N*-dialkylated amine-C_{18}PMOs by microwave-assisted reaction: i) amine functionalization of the phenylene moieties of PMO; ii) dialkylation of the amine group with a) 2-bromopropane or b) 3-chloropropionitrile; and iii) hydrolysis of nitrile group.

Then, the hydrolysis of the nitrile group on the $(\text{NCCH}_2\text{CH}_2)_2\text{NPhC}_{18}\text{PMO}$ was carried out in order to synthetize the $(\text{HOOCCH}_2\text{CH}_2)_2\text{NPhC}_{18}\text{PMO}$ to show the possibility of converting the nitrile species into other functional groups. The mesopore-order of the latter material is maintained after acid treatment and displays a *d*-spacing of 4.50 nm (Figure 5.2.2e and Table C2.1). Additionally, it is possible to observe in Figure 5.2.2 a reduction of intensity of the (100) reflection of the functionalized materials. This result may be associated to the insertion of functional groups into the pores of the $\text{PhC}_{18}\text{PMO}$, which causes a reduction of the X-ray scattering contrast between the organosilica walls and the added functional groups.[22] The prepared materials also show a reflection at $d \sim 0.76$, which indicates molecular-scale periodicity typically observed in this type of PMOs and demonstrating that

the reaction conditions used on the *N*,*N*-dialkylation of $NH_2PhC_{18}PMO$ leave unaffected the periodicity along the channel direction.

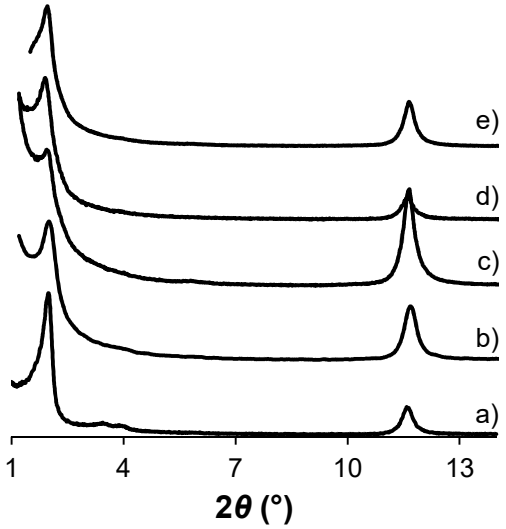

Figure 5.2.2. X-ray diffraction patterns of a) $PhC_{18}PMO$, b) $NH_2PhC_{18}PMO$, c) $(i\text{Pr})_2NPhC_{18}PMO$, d) $(NCCH_2CH_2)_2NPhC_{18}PMO$ and e) $(HOOCCH_2CH_2)_2NPhC_{18}PMO$.

The N_2 adsorption-desorption measurements and the PSD curves of functionalized amine-$PhC_{18}PMO$ are depicted in Figure C2.1 (Appendix C). The synthetized PMOs exhibit a type IV isotherm, suggesting the presence of mesopores. The PSD curves confirm a narrow distribution of the pore diameter. The *N*,*N*-dialkylation of the $NH_2PhC_{18}PMO$ with the isopropyl group leads to a reduction of the S_{BET}, from 658 to 552 $m^2 \cdot g^{-1}$. The V_p and d_p were found to decrease from 0.65 to 0.56 $cm^3 \cdot g^{-1}$, and from 3.24 to 3.18 nm, respectively. These results prove the insertion of the bulk functional groups into the pores (Figure 5.2.2a and Table C2.1, Appendix C). The use of 3-chloropropionitrile as alkyl halide agent gave also rise to the reduction of the S_{BET} and V_p, corroborating the successful alkylation of the amine functionalities of the $NH_2PhC_{18}PMO$ (Figure C2.1b and Table C2.1, Appendix C). The hydrolysis of the nitrile functional group in the $(NCCH_2CH_2)_2NPhC_{18}PMO$ to obtain the carboxylic acid functional group promotes again a decrease on the S_{BET}, V_p and d_p, as can be explained by the much bulkier nature of this group relatively to that of nitrile (Figure C2.1b and Table C2.1).

Solid-state ^{13}C CP-MAS NMR spectrum (Figure 5.2.3a) of the $NH_2PhC_{18}PMO$ shows four typical resonances at *ca.* 122, 124, 133 and 151 ppm, assigned to the sp^2 aromatic carbons bonded to the amine group as reported in the literature.[7] The *N*,*N*-dialkylation reactions led either to slight changes in the chemical shifts or to the presence of additional resonances

when compared to the parent material. The *N*,*N*-dialkylation of $NH_2PhC_{18}PMO$ with isopropyl groups yielded two additional peaks at *ca.* 21 and 44 ppm (Figure 5.2.3b), associated to the ***C***H_3 and ***C***H carbons, respectively, which is in good agreement with results previously reported in Sub-chapter 5.1.

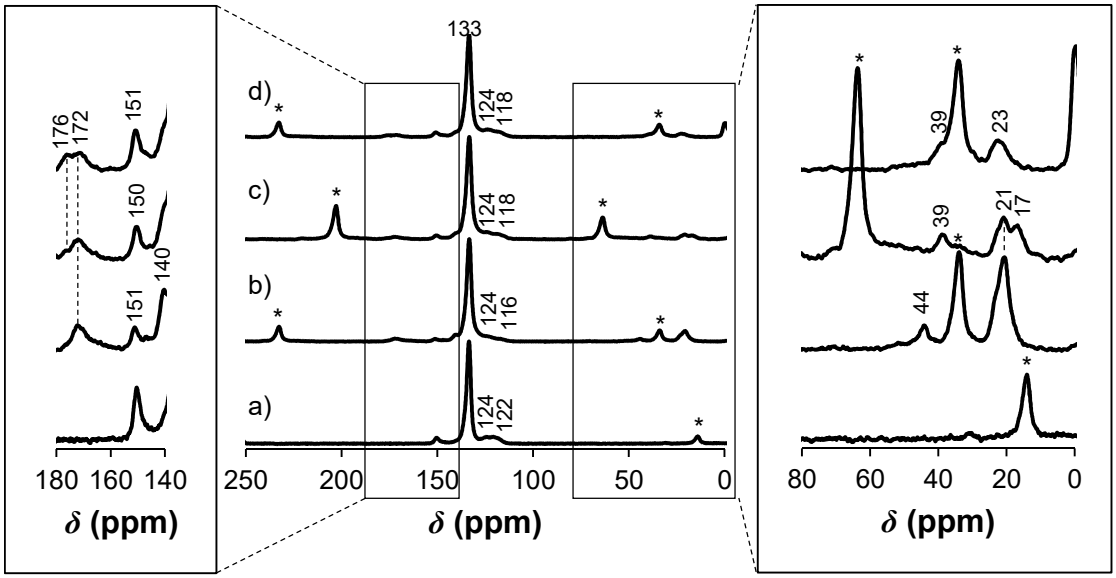

Figure 5.2.3. ^{13}C CP-MAS of a) $NH_2PhC_{18}PMO$, b) $(iPr)_2NPhC_{18}PMO$, c) $(NCCH_2CH_2)_2NPhC_{18}PMO$ and d) $(HOOCCH_2CH_2)_2NPhC_{18}PMO$. The ^{13}C CP-MAS NMR spectra were acquired with a MAS rate of 12, 10, 7 and 10 kHz, respectively. The * denotes spinning sidebands.

The reaction of the $NH_2PhC_{18}PMO$ using the 3-chloropropionitrile also promotes differences in the ^{13}C CP-MAS NMR spectrum. Two resonances are observed at 17 and 21 ppm (Figure 5.2.3c) corresponding to the NC***C***H_2CH_2- in slightly different chemical environments. The resonance associated to the CH_2 covalently bonded to the aromatic amine appears at *ca.* 39 ppm. The CN quaternary carbon is not observed in the ^{13}C CP-MAS NMR spectra, as it resonates in the same chemical shift range of the sp^2 carbons associated to the amine phenylene moieties. In order to prove the existence of the CN group in $(NCCH_2CH_2)_2NPhC_{18}PMO$, it was performed the hydrolysis of the nitrile group into COOH, which yields the $(HOOCCH_2CH_2)_2NPhC_{18}PMO$ material. The resulting carboxylic acid should be easily detected in the spectrum since it is expected to resonate at higher chemical shifts (*c.f.* > 170 ppm). This reaction brings differences to the spectrum (Figure 5.2.3d) as well, *i.e.*, the ^{13}C resonances associated to the HOOC-***C***H_2-, and to the -***C***H_2-N- functions appear at *ca.* 23 and 39 ppm. The third peak associated to the presence of COOH groups is observed at *ca.* 176 ppm. An additional resonance at *ca.* 172 ppm is only observed in the

spectra of *N*,*N*'-dialkylated samples (Figure 5.2.3b-d) and can be related to the formation of bicarbonate ions into the materials. Note that tertiary amines can remove stoichiometric amounts of CO_2 in the presence of moisture and may form bicarbonate ions as reported in the literature.[23,24]

The ^{15}N CP-MAS NMR (Figure 5.2.4) can be used to confirm if *N*-monoalkylation or complete/incomplete *N*,*N*-dialkylation occurred in $NH_2PhC_{18}PMO$. The spectrum of $NH_2PhC_{18}PMO$ shown in Figure 5.2.4a exhibits a single peak at *ca*. -321 ppm, confirming the presence of the primary amine group (NH_2). In Figure 5.2.4b, the resonance observed at *ca.* -292 ppm corresponds to the secondary amine (iPrNHPhC_{18}PMO) obtained after *N*-monoalkylation of the $NH_2PhC_{18}PMO$ with 2-bromopropane. This shift is in good agreement with the results showed in Sub-chapter 5.1. The dialkylated (iPr)$_2$NPhC_{18}PMO material presents a single resonance at -244 ppm, that corresponds to the tertiary amine. This ^{15}N resonance is shifted ~50 ppm towards higher chemical shifts when compared to secondary amines (*c.f.* Figures 5.2.4b and 5.2.4c) and indicates that the dialkylation reaction was complete.

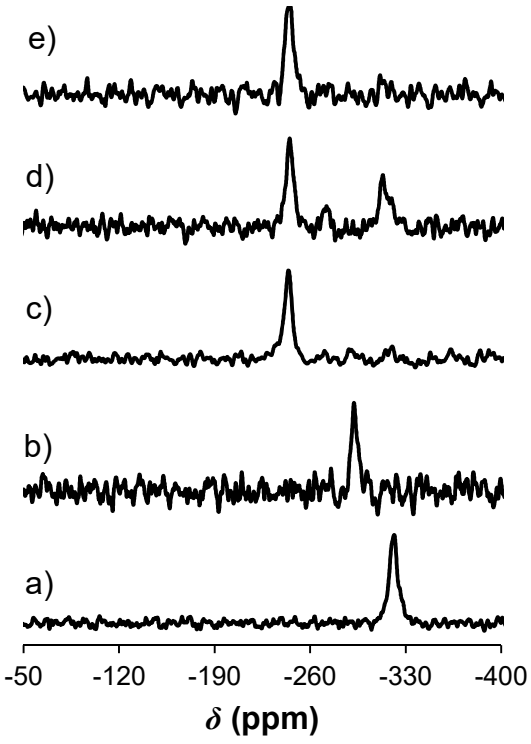

Figure 5.2.4. ^{15}N CP-MAS NMR spectra of a) $NH_2PhC_{18}PMO$, b) iPrNHPhC_{18}PMO, c) (iPr)$_2$NPhC_{18}PMO, d) (NCCH$_2$CH$_2$)$_2$NPhC_{18}PMO_C1 and e) (NCCH$_2$CH$_2$)$_2$NPhC_{18}PMO. The (NCCH$_2$CH$_2$)$_2$NPhC_{18}PMO_C1 sample corresponds to the intermediate material obtained in the first reaction cycle.

Figures 5.2.4d and 5.2.4e show the ^{15}N CP-MAS NMR spectra of the obtained material ($(NCCH_2CH_2)_2NPhC_{18}PMO$) upon reaction of 3-chloropropionitrile with $NH_2PhC_{18}PMO$, after the first and second reaction cycle, respectively. Three resonances at -320, -270 and -244 ppm are observed after the first reaction cycle, associated with primary amines (NH_2), secondary amines ($NCCH_2CH_2$-NH) and tertiary amines ($(NCCH_2CH_2)_2$-N), respectively (Figure 5.2.4d). The second reaction cycle promotes a complete conversion of the primary and secondary amines into tertiary amines, which is corroborated by the presence of a single resonance at -244 ppm (Figure 5.2.4e). The resonance related to the nitrile group is not observed in the ^{15}N CP-MAS NMR spectra. This may happen due to the absence of proton, close enough of this quaternary nitrogen, to promote the cross polarization during the acquisition of the spectrum. However, the presence of this specie in the material was proved in the ^{13}C CP-MAS NMR, presented before, by observation of the resonance associated to the carboxylic acid group whose formation occurs due to hydrolysis of the nitrile group.

The ^{29}Si CP-MAS NMR spectra (Figure C2.2, Appendix C) of the $(i\text{Pr})_2NPhC_{18}PMO$, $(NCCH_2CH_2)_2NPhC_{18}PMO$, $(HOOCCH_2CH_2)_2NPhC_{18}PMO$ show resonances at *ca.* -81, -70 and -61 ppm corresponding to T^3, T^2 and T^1 organosiliceous species [$T^m = RSi(OSi)_m(OH)_{3-m}$], respectively. The applied strong microwave conditions promoted some Si-C bond cleavages as concluded from the observed tiny peaks assigned to Q^n [$Q^n = Si(OSi)_n(OH)_{4-n}$] sites.

The *N*,*N*-dialkyaltion modification of the amine group in the $NH_2PhC_{18}PMO$ was also followed by FTIR spectroscopy (Figure C2.3, Appendix C). The $NH_2PhC_{18}PMO$ shows the C–N stretching vibration displayed at 1298 cm^{-1} and the N–H bending vibration ("scissoring" mode) near 1625 cm^{-1}, confirming the presence of the aromatic primary amine in the framework of the $PhC_{18}PMO$. The N–H stretching modes of aromatic primary amines in the $NH_2PhC_{18}PMO$ are observed at 3430-3367 cm^{-1}. The C=C stretching modes of the aromatic groups in the framework are observed at *ca*. 1600 cm^{-1}. The *N*,*N*-dialkylation of the amine groups promotes the disappearance of the band at 1625 cm^{-1}, additionally, different C=C stretching modes are observed between 1500 and 1680 cm^{-1} that are due to non-aminated phenylene groups and *N*,*N*-dialkylated phenylene moieties in the $PhC_{18}PMO$. The aromatic C–H stretching bands appear at 3050-3060 cm^{-1} in the $NH_2PhC_{18}PMO$ and *N*,*N*-dialkylated materials. The *N*,*N*-dialkylation promotes the appearance of C–H stretching vibrations bands at 2935-3000 cm^{-1} attributed to saturated aliphatic species of the

N,*N*-dialkylated PhC_{18}PMO materials. The $(HOOCCH_2CH_2)_2NPhC_{18}$PMO presents a C–O stretching peak at 1263 cm^{-1}, a C=O stretching band at 1664 cm^{-1}, and a O–H stretching band at 2963 cm^{-1}; all these bands are consistent with carboxylic acid formation from nitrile group.

The thermal stability of the *N*,*N*-dialkylated PMOs was assessed by TGA and the results are shown in Figure C2.4, Appendix C. The amine functionalized NH_2PhC_{18}PMO is stable up to 350 °C.[7] After *N*,*N*-dialkylation of the NH_2PhC_{18}PMO the thermal stability suffers a huge decrease, independently of the alkyl halide agent. The $(i\text{Pr})_2NPhC_{18}$PMO and the $(NCCH_2CH_2)_2NPhC_{18}$PMO are stable up to *ca.* 180 °C as observed in Figure C2.4. The conversion of the CN group into the COOH functionality did not affect the thermal stability of the material. The first weight loss observed in the TGA of all materials is concomitant with desorption of physisorbed water, which occurs below 100 °C. Then, the cleavage and release of the alkyl functional groups starts above 180 °C, which is followed by the cleavage and release of the amine group directly linked to the phenylene moieties of PhC_{18}PMO at *ca.* 350 °C. Finally, at about 500 °C, the decomposition and release of the phenylene bridges from the framework take place.

Table C2.2 (Appendix C) displays the EA of the NH_2PhC_{18}PMO and *N*,*N*-dialkylated NH_2PhC_{18}PMO materials. NH_2PhC_{18}PMO displays an amino group density of 1.68 $mmol \cdot g^{-1}$, which corresponds to about 40% of phenylene moieties that suffered amination. The *N*,*N*-dialkylation of NH_2PhC_{18}PMO with the isopropyl group leads to an increase in the carbon (%C) and hydrogen (%H) percentages and to a decrease in the nitrogen percentage (%N), which is in agreement with the substitution of the hydrogens of the primary amine by the isopropyl groups. The EA results indicate the conversion of 94% of primary amine groups into tertiary amines. The $(i\text{Pr})_2NPhC_{18}$PMO material displays an isopropyl density close to 1.12 $mmol \cdot g^{-1}$. The $(NCCH_2CH_2)_2NPhC_{18}$PMO shows an increase in the C, H and N density as expected once the propionitrile groups are being introduced into the NH_2PhC_{18}PMO. This material presents a propionitrile density of 1.10 $mmol \cdot g^{-1}$, corresponding to an amine conversion close to 92%. The hydrolysis of the CN group of the $(NCCH_2CH_2)_2NPhC_{18}$PMO to prepare the $(HOOCCH_2CH_2)_2$-N-PMO material is also confirmed by the EA technique, by reduction of the %N. The %C and %H also suffer a reduction, associated to the introduction of oxygen atoms into the material.

5.2.4 Conclusions

The *N*,*N*-dialkyaltion of $NH_2PhC_{18}PMO$ was explored for the first time using a microwave-assisted modification synthesis. $(iPr)_2NPhC_{18}PMO$ and the $(NCCH_2CH_2)_2NPhC_{18}PMO$ materials were achieved and fully characterized, indicating the di-alkylation of the aromatic amino groups of the PMOs, while maintaining integrity of the meso and molecular orders of the starting materials.

The nitrile group of the $(NCCH_2CH_2)_2NPhC_{18}PMO$ material can be further modified. Therefore, this work provides indication of the potential of the microwave-assisted post-synthesis modification of the organic bridges of $PhC_{18}PMO$ to introduce alternative functional groups. Hence, on-demand PMOs may be developed for a wide range of applications.

5.3 Microwave-assisted amination of the phenylene-PMO

Adapted from:

Mirtha A. O. Lourenço, José R. B. Gomes, Paula Ferreira

Optimization of the time and temperature of the microwave-assisted amination of the phenylene-PMO

RSC Adv., **2015**, 5: 9208-9216

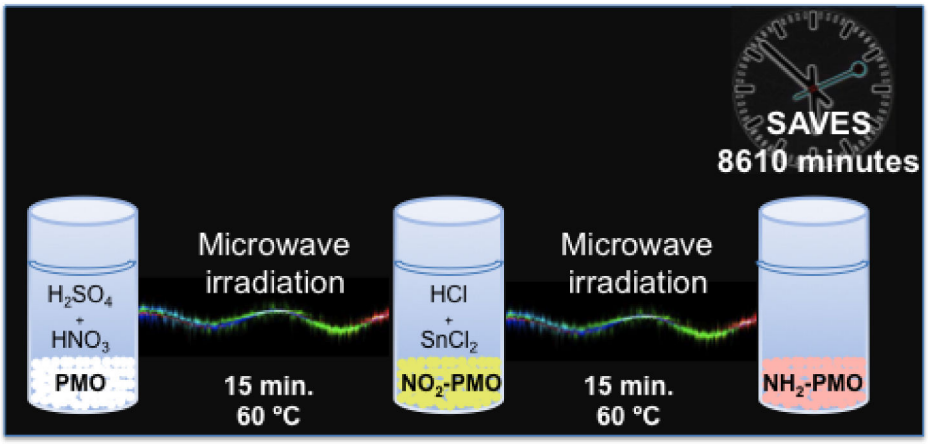

My direct contribution:

I declare that I have prepared, functionalized and characterized all PMO materials.

5.3.1 Motivation

As it was observed in Sub-chapters 5.1. and 5.2, the amine functional group of the amine-phenylene PMO bridge ($NH_2PhC_{18}PMO$)[7] can be modified with alkyl groups without destroying the meso- and molecular-scale order was achieved upon consideration of the alternative approach. In order to make these materials (*e.g.* $NH_2PhC_{18}PMO$) more competitive, it would be important to reduce their synthesis time. This functionalization reaction consists first of a strong acid treatment to introduce the nitro group in the phenyl ring, which is followed by its reduction to the amine.[7]

The effect of the temperature and time of reaction together with the microwave radiation on the quantity of nitro groups incorporated in the phenyl bridge of the PMO and their reduction to amines is an important aspect since it would make the synthesis of these materials faster and, consequently, PMOs would become more attractive for the several foreseen applications.

In this Sub-chapter, it is presented a systematic optimization study of the nitration of $PhC_{18}PMO$ at four different temperatures and different reaction times using microwave heating treatment. The effects of microwave radiation, synthesis temperature and time on the chemical and structural stability of $NO_2PhC_{18}PMOs$ were evaluated and correlated with the amount of nitro groups introduced in the phenylene moieties. The reduction reaction of the nitro group to the amine group was also made at four different temperatures during 15 minutes.

5.3.2 Experimental details

PMO synthesis

The phenylene PMO ($PhC_{18}PMO$) was synthesized according to the procedure described in Sub-chapter 4.1. The surfactant template was extracted using an ethanol/HCl solution. The nitro functional groups were incorporated into the phenylene moieties of the $PhC_{18}PMO$ by treatment with a strong acid solution of HNO_3–H_2SO_4 using a procedure from the literature[7] with subtle modifications. The $NO_2PhC_{18}PMO$ was obtained by dropping a solution of HNO_3 (0.7 mL) and H_2SO_4 (2.2 mL) into $PhC_{18}PMO$ (250 mg). Vials (10 mL) containing the previous mixtures were then sealed and heated at 37, 60, 75 and 90 °C for 15, 120 and 360 min in a CEM Discovery SP-D microwave apparatus, operating at a frequency of 2.45 GHz with continuous radiation power from 0 to 300W. By the end, the reaction mixtures

were transferred into cold distilled water (150 mL) and were then filtered and successively washed with large amounts of water. All samples were dried overnight at 60 °C. The samples obtained in this first step of the work are named "$NO_2PhC_{18}PMO\_y/T$", where *y* is the heating time expressed in minutes (min) and *T* is the heating temperature expressed in degree Celsius (°C). The reduction of the nitro to the amine group was accomplished by treatment of the different $NO_2PhC_{18}PMO\_15min/60°C$ with $HCl/SnCl_2$ solution.[7] The $NH_2PhC_{18}PMO$ was obtained by drop wise of a solution of HCl (3.13 mL) and $SnCl_2$ (0.33 g) to the $NO_2PhC_{18}PMO$ (100 mg). Vials (10 mL) having the above mixtures were then closed and heated at 37, 60, 75 and 90 °C during 15 min in a CEM Discovery SP-D microwave apparatus. The reaction mixtures were poured into distilled water (100 mL) and were then filtered, washed with large amounts of water and followed by washing with a solution of isopropylamine (2.5 mL) in ethanol (25 mL). All samples were dried overnight at 60 °C. The different samples are denoted "$NH_2PhC_{18}PMO\_15min/T$", where *T* is the heating temperature expressed in °C.

The conventional syntheses to obtain the $NO_2PhC_{18}PMO$ were performed according to Ref. [7], at room temperature during 72 h. The syntheses required additional 72 h to attain the $NH_2PhC_{18}PMO$ (total time was 8640 min). The two samples resulting from the conventional synthetic procedure are named $NO_2PhC_{18}PMO\_C$ and $NH_2PhC_{18}PMO\_C$, respectively. In order to further check the microwave effect on the nitration of the phenylene bridge of the $PhC_{18}PMO$, a conventional reaction was performed during 15 minutes at 37 °C. The material was denoted $NO_2PhC_{18}PMO\_15min/37°C\_C$.

Materials characterization

The samples prepared in this study were characterized by PXRD, TEM, SEM, -196 °C nitrogen adsorption-desorption isotherms, TGA, EA, FTIR, ^{29}Si MAS and CP-MAS NMR and ^{13}C CP-MAS NMR spectroscopies. The experimental parameters used for each technique in this study are described in Chapter 2 and some data of ^{13}C CP-MAS NMR, ^{29}Si NMR, FTIR, PXRD, -196 °C N_2-sorption isotherms, TGA, SEM techniques are presented in Appendix C.

5.3.3 Results and Discussion

The nitration of phenylene bridges in $PhC_{18}PMO$ and the subsequent nitro reduction to the amine groups under microwave irradiation were successfully accomplished after reaction during a total time of only 30 min at 60 °C as confirmed by ^{13}C CP-MAS NMR (Figures 5.3.1 and C3.1, Appendix C) and FTIR (Figures 5.3.2, 5.3.6, C3.2 and C3.3) spectroscopies. The ^{13}C CP-MAS NMR spectrum of the parent $PhC_{18}PMO$ displays one peak at 133.5 ppm assigned to the sp^2 carbons from the phenylene bridge.

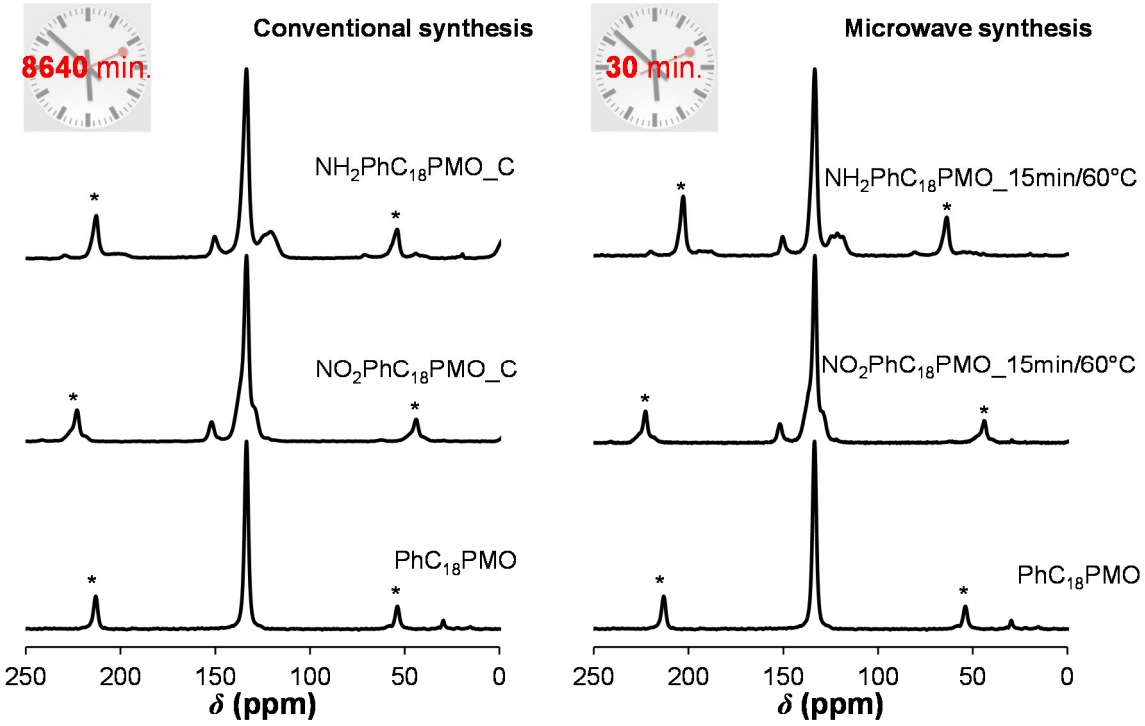

Figure 5.3.1. ^{13}C CP-MAS NMR spectra of the $PhC_{18}PMO$, $NO_2PhC_{18}PMO\_15min/60°C$ and $NH_2PhC_{18}PMO\_15min/60°C$.

The nitration reaction changes the chemical environment of the carbons of the phenylene group. In this way, the $NO_2PhC_{18}PMO\_15min/60°C$ presents four peaks at *ca.* 151, 137, 133 and 129 ppm. The reduction of the nitro group to the amine group is also accompanied by changes in the ^{13}C CP-MAS NMR spectrum. Thus, the $NH_2PhC_{18}PMO\_15min/60°C$ exhibits five resonance peaks at 150, 133, 124, 122 and 119 ppm that are assignable to the carbons in the phenylene moieties with amine groups linked. Thus, when compared with the conventional synthesis, microwave heating opens an avenue for faster functionalization of the phenylene moieties of $PhC_{18}PMO$ materials with nitro or amine groups. Using the microwave procedure, with only 15 min of reaction for each step at 60 °C, it was possible to

achieve the same degree of amine functionalization as that obtained after six days of the conventional synthesis, *c.f.* Table 5.3.1.

The $NO_2PhC_{18}PMO\_y/T$ materials were also characterized by FTIR spectroscopy to corroborate the nitro functionalization of $PhC_{18}PMO$, Figures 5.3.2 and C3.2. The $PhC_{18}PMO$ presents overtones of phenyl vibrations between 1300-2000 cm^{-1}, absorption modes assigned to the silanol stretching bands at 3200-3800 cm^{-1} and C-H aromatic stretching bands at 3028 and 3066 cm^{-1}. These values are similar to those described previously for $PhC_{18}PMO$.[7]

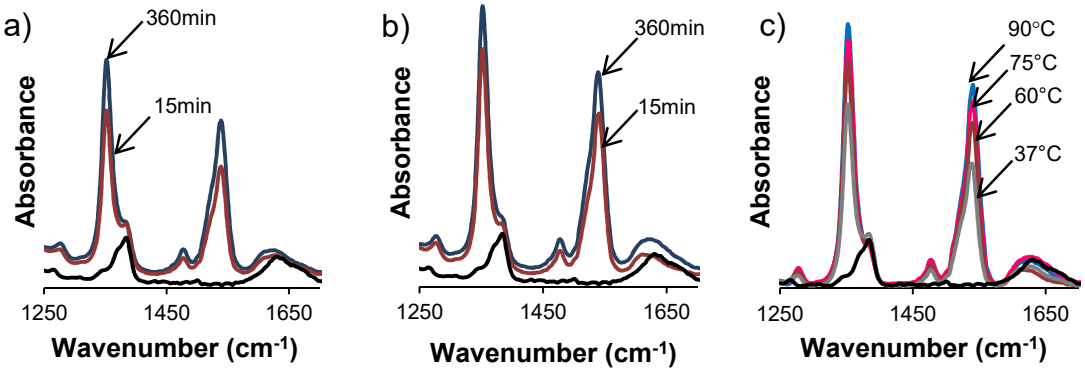

Figure 5.3.2. FTIR (ATR) spectra of $NO_2PhC_{18}PMO\_y/T$ at a) 37 °C and b) 60 °C for two different reaction times and c) $NO_2PhC_{18}PMO\_15min/T$ at different temperatures. The region of 1250 – 1700 cm^{-1} was chosen to better observe the main bands of functionalization. Black curves are for the parent $PhC_{18}PMO$ material.

Some changes in the FTIR spectra of $PhC_{18}PMO$ appear after the nitration reaction. The presence of nitro groups in the aromatic rings of the $PhC_{18}PMO$ is confirmed by the C-N stretching mode displayed at 1267 cm^{-1}, and by the appearance of strong bands due to N-O symmetrical and asymmetrical stretchings at 1352 and 1541 cm^{-1}, respectively. These two NO stretching bands are more intense in the case of nitrated PMOs with time reaction of 360 min than in the materials functionalized during 15 min. It is seen that the spectrum for NO_2 $PhC_{18}PMO\_15min/60°C$, presents NO stretching bands with similar intensities to that of the $NO_2PhC_{18}PMO\_360min/37°C$ material, *c.f.* Figures 5.3.2a and 5.3.2b. The nitrated $PhC_{18}PMO$ with NO stretching bands with the highest intensities corresponds to that obtained with the largest reaction time and temperature, *i.e.*, 360 min and 60 °C. Figure 5.3.2c displays the FTIR spectra of $NO_2PhC_{18}PMO\_15min/T$ materials in which it is possible to observe the increase of intensity of the two NO stretching bands with increasing temperature. Consequently, the increase of the number of nitrated phenylene moieties is

directly correlated with the increase of temperature and in turn it can be correlated with the injection of microwave irradiation power. The microwave radiation effect is observed through the comparison of the FTIR spectra of $NO_2PhC_{18}PMO$_15min/37°C and the NO_2 $PhC_{18}PMO$_15min/37°C_C, Figure C3.2d. The material prepared under microwave-assisted heating presents much intense NO stretching bands than the material prepared using conventional heating at the same temperature, which corroborates the favorable effect of the microwave irradiation on speeding up the nitration of the bissilylated phenylene bridge of the $PhC_{18}PMO$.

Table 5.3.1 shows the results of the elemental analyses for the $PhC_{18}PMO$ parent material and for the materials aminated under different reaction conditions.

Table 5.3.1. Elemental analyses, nitrogen density and percentage of aminated phenylene bridges for $PhC_{18}PMO$, $NH_2PhC_{18}PMO$_C (conventional synthesis) and NH_2 $PhC_{18}PMO$_*y*/*T* (synthesized using microwave).

Sample	%N	%C	%H	N Density mmol·g^{-1}	% Phenylene bridges aminated[a]
$PhC_{18}PMO$	0.08	38.79	2.82	-	-
$NH_2PhC_{18}PMO$_C	2.49	34.29	3.32	1.78	41.5
$NH_2PhC_{18}PMO$_15min/37°C	1.62	33.16	2.98	1.16	27.0
$NH_2PhC_{18}PMO$_120min/37°C	2.22	33.57	3.05	1.59	37.0
$NH_2PhC_{18}PMO$_360min/37°C	2.50	34.48	3.27	1.79	41.7
$NH_2PhC_{18}PMO$_15min/60°C	2.50	33.58	2.84	1.78	41.5
$NH_2PhC_{18}PMO$_120min/60°C	2.83	33.30	3.24	2.02	47.2
$NH_2PhC_{18}PMO$_360min/60°C	2.95	31.18	3.26	2.11	49.2
$NH_2PhC_{18}PMO$_15min/75°C	2.99	31.54	2.90	2.14	49.8
$NH_2PhC_{18}PMO$_15min/90°C	3.16	31.20	2.95	2.26	52.6

[a]% of phenylene bridges aminated is calculated based on %N and assuming single amination, *i.e.*, one amine group per phenylene bridge.

The $NH_2PhC_{18}PMO$ sample from conventional synthesis holds an amino group density equal to 1.78 mmol·g^{-1} (1.78% of N). Assuming an incorporation of just one amine group per phenylene bridge, this density value indicates that ~42% of phenylene bridges were successfully functionalized. Under microwave irradiation at 37 °C, such a high value of functionalization (maximum was 1.16 mmol·g^{-1}) could not be reached. It is also concluded that the irradiation time strongly influences the nitration reaction at 37 °C since an increase in the density of amine groups from 1.16 to 1.59 mmol·g^{-1} is obtained with the increase of the nitration reaction from 15 to 120 min, respectively. The increase in the density of amine groups obtained upon incrementing the time of reaction from 120 to 360 min is less evident, *i.e.*, a slight increase of 0.20 mmol·g^{-1} is found in the latter. When the synthesis is carried

out at 60 °C, the density of amine groups in the $PhC_{18}PMO$ after 15 min of reaction reaches a value of 1.76 mmol·g^{-1}, which is similar to the density in the sample obtained by conventional synthesis. This demonstrates that the reaction is extremely dependent on the temperature and heating source. Note that the microwave injected 230 W of power to achieve 60 °C, which is 140 W higher than the value required to reach 37 °C. The higher amount of amine groups introduced into the phenylene moieties may be due to the faster diffusion of the amine contents into the $PhC_{18}PMO$ at 60 °C. The increase of amine groups in the phenylene moieties takes place when the time is raised from 15 to 120 min with a difference of 0.26 mmol·g^{-1}, corresponding to a percentage of phenylene bridges nitrated close to 6%. The difference is even lower when the time is extended to 360 min, with a density of amine groups of approximately 2.11 mmol·g^{-1}, *i.e.*, an increase of only 0.09 mmol·g^{-1} when compared to the $NO_2PhC_{18}PMO$_120min/60°C material (Table 5.3.1). The use of microwave power to reach 60 °C leads to a higher nitro content than the use of conventional heating to reach the same temperature. This was observed for the synthesis of the material $NO_2PhC_{18}PMO$_C_4320min/60°C (conventional synthesis during 3 days made at 60 °C) which has similar amount of nitro groups than the material $NO_2PhC_{18}PMO$_240min/60°C. Moreover, the $NO_2PhC_{18}PMO$_C_4320m/60°C material loose the meso-scale periodicity (not shown) which is a huge disadvantaged comparing with the similar material made by using microwave heating.

Table 5.3.1 also reveals the amount of nitro groups incorporated in the phenylene moieties of the $PhC_{18}PMO$ material with the increase of the temperature for similar reaction time (15 min). The consideration of high temperature is found to promote the introduction of higher amounts of nitro groups into the $PhC_{18}PMO$ channels. Since $NH_2PhC_{18}PMO$_15min/75°C presents a nitrogen density of 2.11 mmol·g^{-1} which is similar to that for $NH_2PhC_{18}PMO$_360min/60°C, it suggests that the temperature is very important to control the nitrogen density into the $PhC_{18}PMO$ for short times of reaction. By increasing the temperature reaction to 90 °C resulted in a $PhC_{18}PMO$ material having the highest content of nitro groups linked to the phenylene bridge of the $PhC_{18}PMO$. The nitrogen density of 2.26 mmol·g^{-1} determined for $NH_2PhC_{18}PMO$_15min/90°C corresponds to a total of nitrated phenylene moieties of more than 50%.

The ^{29}Si MAS and CP-MAS NMR spectra of $PhC_{18}PMO$, NO_2-PMO_15min/37°C and $NO_2PhC_{18}PMO$_360min/60°C are shown in Figure 5.3.3. The pure $PhC_{18}PMO$ exhibits

peaks at *ca.* 81, 71.5 and 61.5 ppm, which correspond to T^3, T^2 and T^1 organosiliceous species, respectively. As expected taking into account the literature, significant changes are introduced in the ^{29}Si NMR spectra of $NO_2PhC_{18}PMO\_y/T$ materials upon the nitration reaction.[7] Peaks related with the presence of Q^n species are absent in the ^{29}Si spectra for all materials, which is a strong evidence that carbon-silicon bond cleavage is not happening during the nitration reaction under microwave conditions.

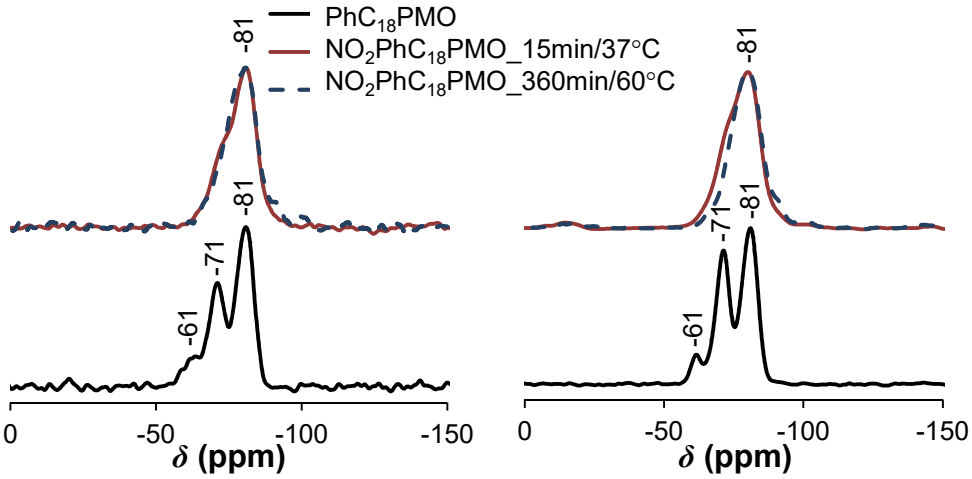

Figure 5.3.3. ^{29}Si MAS (left) and CP-MAS NMR (right) spectra of $PhC_{18}PMO$ (bottom) and $NO_2PhC_{18}PMOs\_y/T$ (top) obtained at two different reaction times and temperatures.

PXRD was used to evaluate the structural order of all materials. Figure 5.3.4 shows the PXRD patterns of the $PhC_{18}PMO$ and $NO_2PhC_{18}PMO\_y/T$ obtained at different reaction conditions (temperature and time). All prepared materials displayed an intense low angle reflection and two much less intense peaks all corresponding, respectively, to the (100), (110) and (200) reflections characteristic of the two-dimensional hexagonal symmetry (*p6mm*) lattice. The $PhC_{18}PMO$ and the two most extreme $NO_2PhC_{18}PMO$ samples, *i.e.*, $NO_2PhC_{18}PMOs$ synthesized during 15 minutes at 37 °C or during 360 min at 60 °C, exhibit the first strong characteristic low angle (100) reflections at d = 4.55 nm, 4.70 nm and 4.55 nm, respectively. From the spacing (d) of the (100) peak it can be calculated the hexagonal unit cell lattice parameter, a, which is equal to $2d_{100}/\sqrt{3}$ (Table C3.1). For the samples $PhC_{18}PMO$, $NO_2PhC_{18}PMO$_15min/37°C and $NO_2PhC_{18}PMO$_15min/60°C, the first sharp diffraction at medium-range reflection can be detected at d = 0.761, 0.762 and 0.758 nm, respectively, which is attributed to the periodic arrangement of the organic bridge within the pore walls of these materials. Thus, both meso- and molecular- scale periodicities are

preserved after nitration reaction under the conditions described and this is also valid for the other materials obtained under different conditions. Attempts were made for fast synthesis (15 min) of materials with more than 50% of phenylene moieties mono-nitrated into the $PhC_{18}PMO$ channels by increasing the temperature of the nitration reaction to 75 and 90 °C.

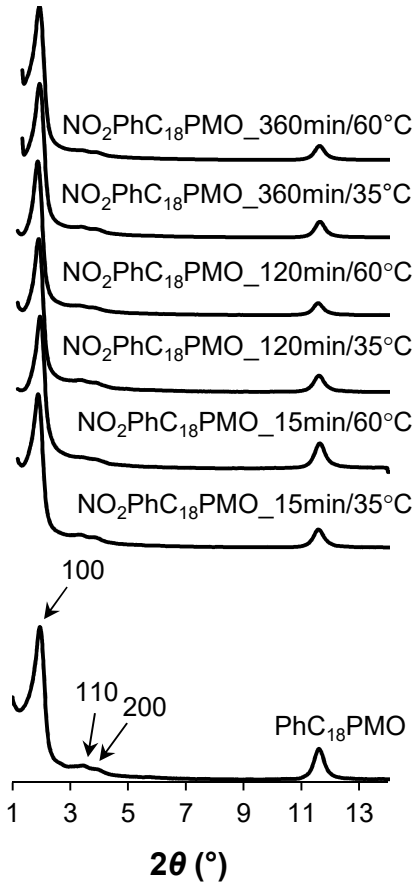

Figure 5.3.4. PXRD patterns for $PhC_{18}PMO$ and $NO_2PhC_{18}PMO\_y/T$ materials showing the typical low angle reflections characteristic of the 2D hexagonal mesoporous order and the medium-range reflection typical of the molecular-scale order in $PhC_{18}PMO$ materials.

Figure C3.4 shows PXRD patterns for the materials obtained under these conditions. The 2D hexagonal symmetry (*p6mm*) lattice is attained for all the materials as supported by the observation of the first strong peak corresponding to the (100) reflection and two less intense peaks corresponding to the (110) and (200) reflections. The $PhC_{18}PMO$ and the $NO_2PhC_{18}PMO$s synthesized at 37, 60, 75 and 90 °C exhibit the first strong characteristic low angle (100) reflection at d = 4.55 nm, 4.70 nm, 4.70 nm, 4.82 nm and 4.82 nm, respectively, Table C3.1. From the d_{100} peaks it can be calculated the hexagonal unit cell parameter $a = (2d_{100}/\sqrt{3})$ = 5.25 nm for the $PhC_{18}PMO$ and a values between 5.20 nm and 5.57 nm were obtained for the nitrated $PhC_{18}PMO$ (Table C3.1).

TEM images obtained for the material $NO_2PhC_{18}PMO\_15min/60°C$ (Figure 5.3.5) show the order along the channel and the hexagonal arrangement of pores.

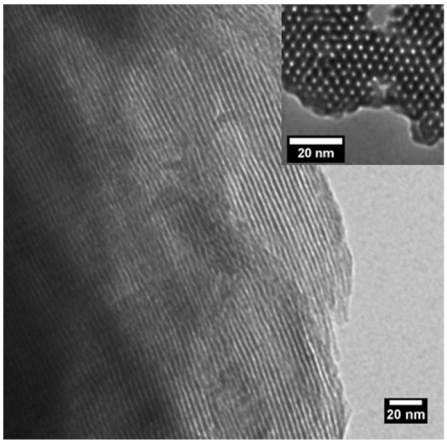

Figure 5.3.5. TEM micrographs of $NO_2PhC_{18}PMO\_15min/60°C$. The inset displays a micrograph perpendicular to the pores where it is clear their 2D hexagonal arrangement.

The -196 °C N_2 sorption isotherms and PSD curves (Figure C3.5) confirm the characteristic type IV isotherms (IUPAC classification) and narrow distribution of pore sizes for the pure $PhC_{18}PMO$ and NO_2 $PhC_{18}PMO\_y/T$ materials commonly seen in mesoporous materials.[3] A decrease of the S_{BET} and V_p upon increase of the temperature and reaction times is consistent with the enhancement of the degree of functionalization with nitro groups. The S_{BET} of the materials synthetized at 37 °C decreases with the increase of the reaction time. The increase in the reaction temperature from 37 to 60 °C is also accompanied by a decrease of the S_{BET}. The N_2 sorption isotherms display the increase of the S_{BET} with the increase of the reaction time for the nitrated materials prepared at 60 °C (Table C3.1), which is the opposite of what is expected. This can be attributed to the splitting of the large aggregates into small particles due to the microwave irradiation as observed before by Smeulders *et al.*[8] in the microwave-assisted synthesis of $PhC_{18}PMO$ under long reaction times.

Figure C3.6 shows the TGA curves for $PhC_{18}PMO$ and $NO_2PhC_{18}PMO$ at 37 and 60 °C for two different time extremes. The first weight loss for all materials corresponds to desorption of physisorbed water occurring below 100 °C. The $PhC_{18}PMO$ material presents a thermal stability up to 550 °C. Above this temperature, all materials suffer decomposition due to the degradation of the phenylene bridges from the framework. The nitro group introduction in the phenylene moieties decreases the thermal stability of all materials and a new weight loss,

corresponding to the cleavage of nitro group in the phenylene bridge of the material, is observed at approximately 400 °C.

SEM images for $NO_2PhC_{18}PMO$ materials obtained using different synthetic conditions are shown in Figure C3.7. The SEM images reveal the high order along the channels for all materials. The particle size of the different materials as a function of the reaction conditions could not be determined due to formation of ordered aggregates.

The reduction of the nitro groups is a very important step for obtaining the aminated compounds and the decrease of the reaction time will have obvious implications for the consideration of these materials in catalysis and adsorption applications.

The nitro to amine reduction was followed by ATR-FTIR spectroscopy, Figure 5.3.6. Upon treatment with $SnCl_2$–HCl, the N–O stretching vibrations disappeared completely in the case of reaction at 60 °C while new bands attributable to the bending and stretching modes of N–H appeared at 1633 and 3340–3487 cm^{-1}, respectively. It was also possible to observe the importance of the microwave heating in this reaction.

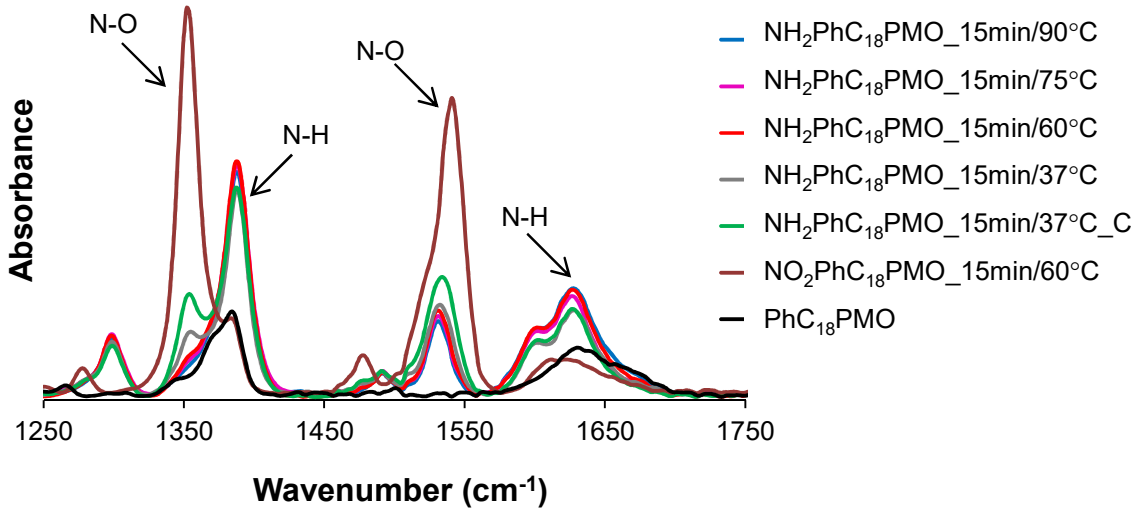

Figure 5.3.6. FTIR (ATR) spectra in the 1250 – 1700 cm^{-1} region of $PhC_{18}PMO$, $NO_2PhC_{18}PMO\_15min/60°C$ and the $NH_2PhC_{18}PMO\_15min/T$.

The reduction of the nitro to the amine groups at 37 °C was made using microwave and conventional heating and the samples were labelled $NH_2PhC_{18}PMO\_15min/37°C$ and $NH_2PhC_{18}PMO\_15m/37°C\_C$, respectively. The use of microwave heating promotes the reduction of a larger content of nitro groups, which causes a significant diminution of the intensity of the N–O stretching vibrations bands.

The ^{29}Si MAS and CP-MAS NMR spectra of the $NH_2PhC_{18}PMO\_15min/60°C$ sample are presented in Figure C3.8. The peaks at *ca.* -81, -71 and -61 ppm are assigned to the T^3, T^2 and T^1 organosiliceous species of the $NH_2PhC_{18}PMO$ material. The ^{29}Si NMR spectrum also shows that no Si-C bond cleavage is observed.

Figure 5.3.7a shows PXRD patterns for $PhC_{18}PMO$, $NO_2PhC_{18}PMO\_15min/60°C$ and $NH_2PhC_{18}PMO\_15min/T$. All materials display the first strong peak corresponding to the (100) reflection and two less intense peaks corresponding to the (110) and (200) reflections corresponding to the 2D hexagonal symmetry (*p6mm*) lattice. The intensities of these two peaks decreased with the reduction of the nitro groups. The molecular periodicity is preserved with the increase of the reaction temperature.

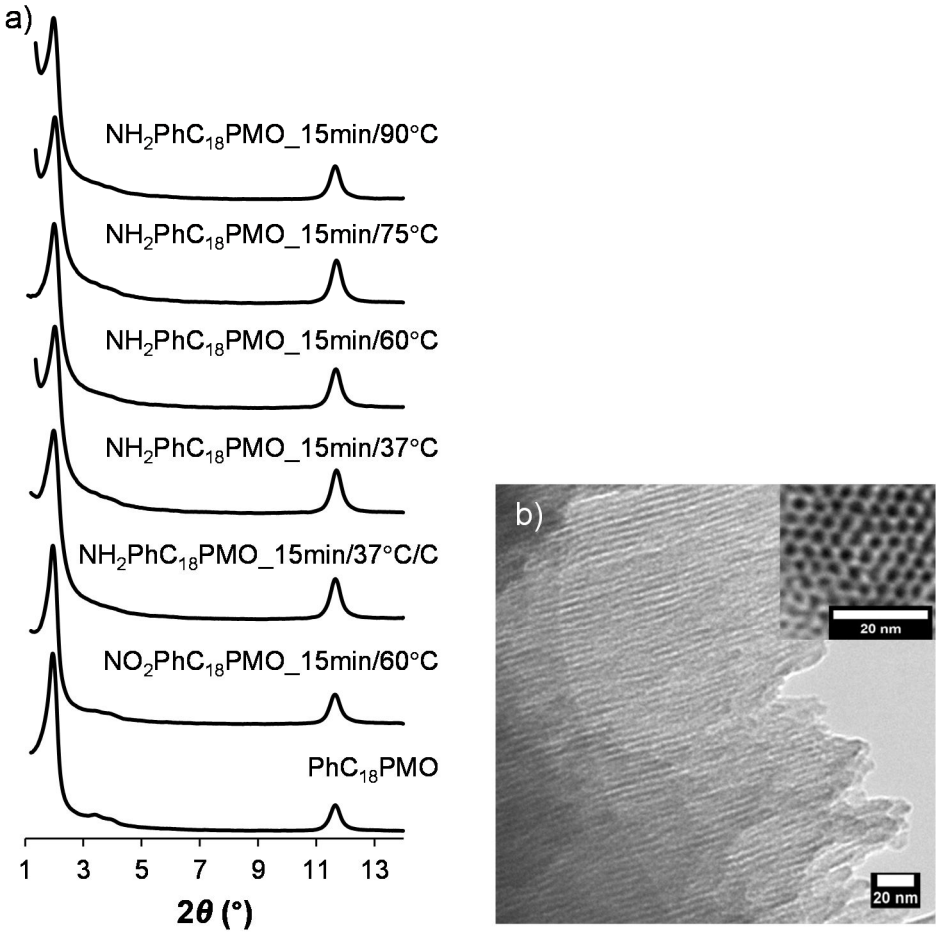

Figure 5.3.7. a) X-ray diffraction patterns for $PhC_{18}PMO$, $NO_2PhC_{18}PMO\_15min/60°C$ and $NH_2PhC_{18}PMO\_15m/T$ and b) TEM images of $NH_2PhC_{18}PMO\_15min/60°C$.

The TEM images observed in Figure 5.3.7b support the preservation of the order along the channels and also the 2D hexagonal arrangement of the pores of the $NH_2PhC_{18}PMO\_15min/60°C$ material.

The $PhC_{18}PMO$ and the $NH_2PhC_{18}PMO$_15min/*T* synthesized at 37, 60, 75 and 90 °C exhibit the first strong characteristic low angle (100) reflection at *d* = 4.55, 4.37, 4.41, 4.37 and 4.46 nm, respectively, Table C3.2.

The -196 °C N_2 sorption isotherms shown in Figure C3.9 confirm the type IV isotherms for the synthetized $NH_2PhC_{18}PMO$_15min/*T* materials and PSD curves confirms the narrow distribution of pore sizes.

The thermal stability of the amine $PhC_{18}PMO$ is similar to that of the $PhC_{18}PMO$ nitrated, Figure C3.10. The cleavage of the amine group in the phenylene bridge of the aminated material, is observed at approximately 400 °C. The thermal stability of the $NH_2PhC_{18}PMO$ is not affected by the use of different reaction temperatures using the microwave heating. The thermal stability is similar to that of the aminated $PhC_{18}PMO$ material prepared conventionally.[7]

5.3.4 Conclusions

This study shows that the time and the temperature of reaction are essential factors in the nitration of phenylene moieties of $PhC_{18}PMO$ materials and subsequent reduction of the nitro groups to amines. The information gathered from different experimental techniques, namely elemental analysis, TGA, and ^{13}C CP-MAS NMR, ^{29}Si CP-MAS NMR and FTIR spectroscopies, shows that changing the time and temperature of the nitration reaction under microwave irradiation has a huge influence on the amount of nitro groups incorporated into the $PhC_{18}PMO$ without cleavage of the Si-C bond. Both meso- and molecular-scale periodicities are preserved after strong acid treatment under microwave heating (observed by PXRD patterns and TEM images).

The temperatures used in the microwave heating (37 and 60 °C) are accompanied by different behaviors of the kinetic profiles. It was possible to find a clear dependence of the amount of nitro groups incorporated into the $PhC_{18}PMO$s with the reaction time (up to 120 min) for reactions carried out at 37 °C comparing with reactions made at 60 °C. SEM does not show differences on the particles of parent and functionalized materials. A significant reduction in the time required for the nitration of phenylene bridges in $PhC_{18}PMO$ was observed upon microwave irradiation. Characterization with several different techniques suggests that nitration occurs without modification of the structural properties of the parent $PhC_{18}PMO$. Importantly, in some cases, *e.g.* microwave-assisted reaction at *T* = 60 °C and

y = 120 min, the nitro groups content incorporated into the $PhC_{18}PMO$ channels was larger than that achieved under conventional conditions (3 days at room temperature), while similar contents between microwave-assisted and conventional heating were found when the synthesis used microwave irradiation during 15 min at 75 °C. Furthermore, the nitration reaction carried out at 90 °C during 15 min resulted in a content of nitrated phenylene moieties above 50%.

The microwave synthesis method presents clear advantages when compared with the conventional synthesis approaches, both in time and in the amount of nitro groups incorporated in the phenylene moieties of the $PhC_{18}PMO$ material. The use of the microwave heating promotes a high control of the nitro groups incorporated into the phenylene moieties of the $PhC_{18}PMO$ material. Additionally, the reduction of the nitro to the amine groups was also successfully achieved after treatment with $SnCl_2$/HCl under microwave irradiation with preservation of the structural order.

The use of microwave heating speeds up the nitration of the phenylene-$C_{18}PMO$ probably due to the presence of polar intermediate species, such as nitronium ion and water molecules. Moreover the transition state of the material should be more reactive under microwave irradiation when compared to thermal heating due to the specific microwave absorption by the polar reactants. In addition, it is believed that the diffusion of the reactant species through the mesochannels of the phenylene-$C_{18}PMO$ is improved using the microwave irradiation, allowing a fast access of the nitronium ion to the phenylene bridges for the nucleophilic attack, which is a determinant rate step.

Although phenylene-$C_{18}PMO$ is considered an apolar substance, *i.e.* being a weaker microwave irradiation absorber, it must be considered that the silanols and the delocalization of the electrons by the approximation of the positive nitronium ion can play a beneficial role in the local heating. In the amination step, the nitro groups attached to the phenylene bridges are also important for the generation of local heating which will speed-up the reaction.

5.4 Bibliography

1 M. MacLachlan, T. Asefa, G. Ozin, Writing on the wall with a new synthetic quill. *Chemistry*. **2000**, 6: 2507–2511.

2 N. Mizoshita, T. Tani, S. Inagaki, Syntheses, properties and applications of periodic mesoporous organosilicas prepared from bridged organosilane precursors. *Chem Soc Rev*. **2011**, 40: 789–800.

3 S. Inagaki, S. Guan, T. Ohsuna, O. Terasaki, An ordered mesoporous organosilica hybrid material with a crystal-like wall structure. *Nature*. **2002**, 416: 304–307.

4 T. Kamegawa, T. Sakai, M. Matsuoka, M. Anpo, Preparation and characterization of unique inorganic-organic hybrid mesoporous materials incorporating arenetricarbonyl complexes [-$C_6H_4M(CO)_3$-] (M = Cr, Mo). *J Am Chem Soc*. **2005**, 127: 16784–16785.

5 A.C. Coelho, S.S. Balula, S.M. Bruno, J.C. Alonso, N. Bion, P. Ferreira, M. Pillinger, A.A. Valente, J. Rocha, I.S. Gonçalves, Grafting of molecularly ordered mesoporous phenylene-silica with molybdenum carbonyl complexes: efficient heterogeneous catalysts for the epoxidation of olefins. *Adv Synth Catal*. **2010**, 352: 1759–1769.

6 A.C. Coelho, S.S. Balula, M.M. Antunes, T.I. Gerganova, N. Bion, P. Ferreira, M. Pillinger, A.A. Valente, J. Rocha, I.S. Gonçalves, Chemical complexation of crystal-like mesoporous phenylene-silica with $Cr(CO)_3$ and catalytic performance in the oxidation of cyclooctene. *J Mol Catal A Chem*. **2010**, 332: 13–18.

7 M. Ohashi, M.P. Kapoor, S. Inagaki, Chemical modification of crystal-like mesoporous phenylene-silica with amino group. *Chem Commun*. **2008**, 7: 841–843.

8 G. Smeulders, C.J. Van Oers, K. Van Havenbergh, K. Houthoofd, M. Mertens, J.A. Martens, S. Bals, B.U.W. Maes, V. Meynen, P. Cool, Smart heating profiles for the synthesis of benzene bridged periodic mesoporous organosilicas. *Chem Eng J*. **2011**, 175: 585–591.

9 B.E. Grabicka, M. Jaroniec, Microwave-assisted synthesis of periodic mesoporous organosilicas with ethane and disulfide groups. *Micropor Mesopor Mater*. **2009**, 119: 144–149.

10 S. Yoon, W. Son, K. Biswas, W. Ahn, Synthesis of periodic mesoporous organosilica by microwave heating. *Bull Korean Chem Soc*. **2008**, 29: 609–614.

11 A. Procopio, G. De Luca, M. Nardi, M. Oliverio, R. Paonessa, General MW-assisted grafting of MCM-41: Study of the dependence on time dielectric heating and solvent. *Green Chem*. **2009**, 11: 770–773.

12 J. Jacob, Microwave assisted reactions in organic chemistry: A review of recent advances. *Int J Chem*. **2012**, 4: 29–43.

13 C.O. Kappe, Controlled microwave heating in modern organic synthesis. *Angew Chem*. **2004**, 43: 6250–6284.

14 C. Gabriel, S. Gabriel, E. H. Grant, B. S. J. Halstead, D. Michael P. Mingos, Dielectric parameters relevant to microwave dielectric heating. *Chem Soc Rev*. **1998**, 27: Synthesis of periodic mesoporous organosilica by microwave heating 213–224.

15 R.N. Gedye, F.E. Smith, K.C. Westaway, The rapid synthesis of organic compounds in microwave ovens. *Can J Chem*. **1988**, 66: 17–26.

16 L. Perreux, A. Loupy, A tentative rationalization of microwave effects in organic synthesis according to the reaction medium, and mechanistic considerations. *Tetrahedron*. **2001**, 57: 9199–9223.

17 J.L. Romera, J.M. Cid, A.A. Trabanco, Potassium iodide catalysed monoalkylation of

anilines under microwave irradiation. *Tetrahedron Lett*. **2004**, 45: 8797–8800.

18 T. Asefa, M.J. MacLachlan, N. Coombs, G.A. Ozin, Periodic mesoporous organosilicas with organic groups inside the channel walls. *Nature*. **1999**, 402: 867–871.

19 S. Inagaki, S. Guan, Y. Fukushima, T. Ohsuna, O. Terasaki, Novel mesoporous materials with a uniform distribution of organic groups and inorganic oxide in their frameworks. *J Am Chem Soc*. **1999**, 121: 9611–9614.

20 N. Bion, P. Ferreira, A. Valente, I.S. Gonçalves, J. Rocha, Ordered benzene-silica hybrids with molecular-scale periodicity in the walls and different mesopore sizes. Synthesis of periodic mesoporous organosilica by microwave heating *J Mater Chem*. **2003**, 13: 1910–1913.

21 R.J.P. Corriu, J.J.E. Moreau, P. Thepot, M.W.C. Man, New mixed organic-inorganic polymers: hydrolysis and polycondensation of bis(trimethoxysilyl)organometallic precursors. *Chem Mater*. **1992**, 4: 1217–1224.

22 B. Marler, U. Oberhagemann, S. Vortmann, H. Gies, Influence of the sorbate type on the XRD peak intensities of loaded MCM-41. *Microporous Mater*. **1996**, 6: 375–383.

23 F.A. Chowdhury, H. Yamada, T. Higashii, K. Goto, M. Onoda, CO_2 capture by tertiary amine absorbents: A performance comparison study. *Ind Eng Chem Res*. **2013**, 52: 8323–8331.

24 Y.G. Ko, S.S. Shin, U.S. Choi, Primary, secondary, and tertiary amines for CO_2 capture: Designing for mesoporous CO_2 adsorbents. *J Colloid Interf Sci*. **2011**, 361: 594–602.

Chapter 6: General conclusions and outlook

This final Chapter presents the general conclusions of the work developed in the framework of this PhD Thesis. It is proposed a list of possible research lines that may be followed in the future aiming the improvement of the properties of PMO materials, not only in adsorption and separation applications, but also in catalysis.

6.1. General Conclusions

In this PhD Thesis, the synthesis and modification of several PMO materials were successfully accomplished using different synthetic approaches. Figure 6.1 summarizes the work performed over the last 4 years and presents the main conclusions.

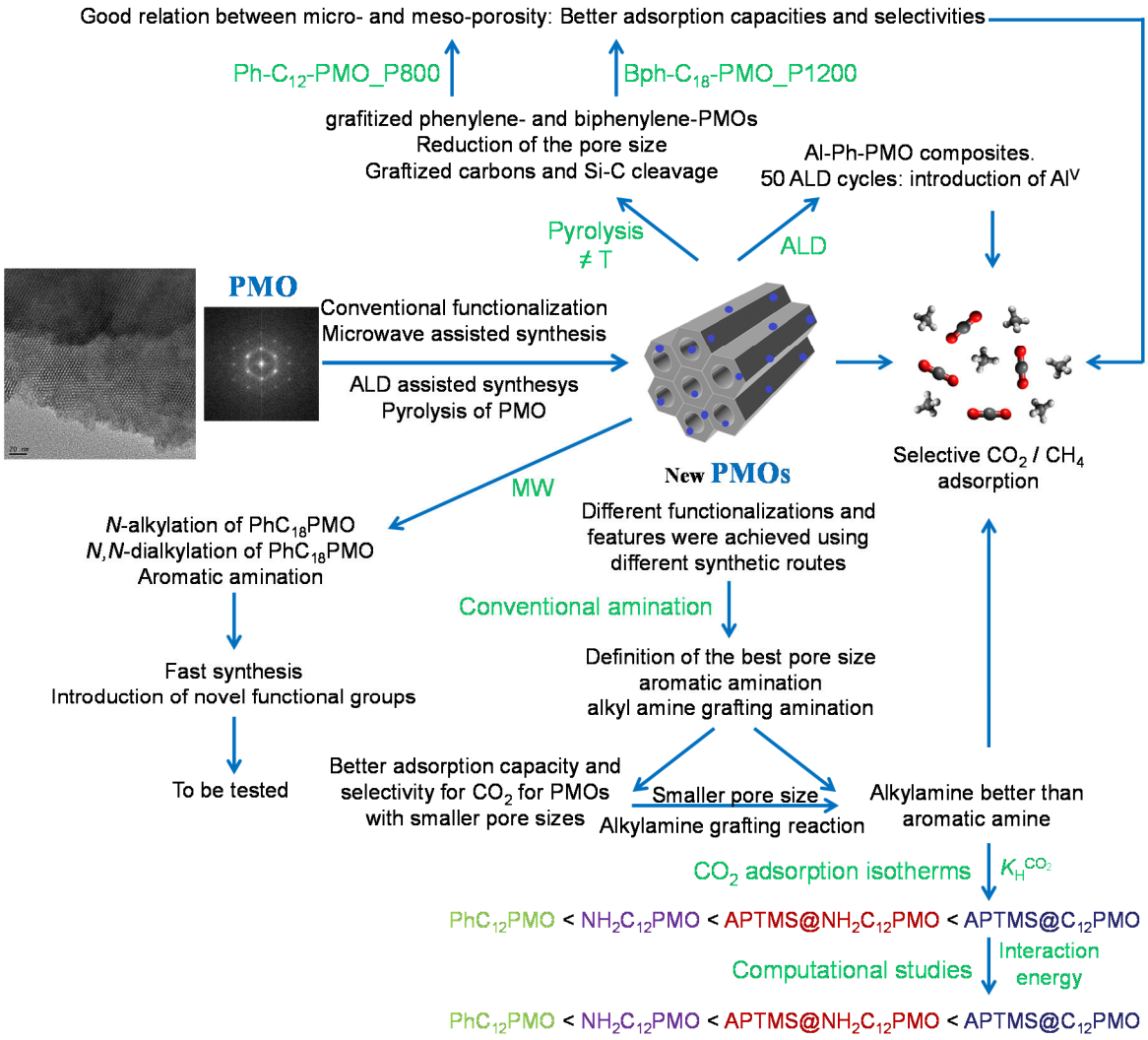

Figure 6.1. Preparation of novel PMOs using different synthetic strategies and their main physical or chemical characteristics for the CO_2 and CH_4 separation.

The materials were fully characterized; they showed two-dimensional hexagonal symmetry (*p6mm*) lattice and molecular-scale periodicities as observed by PXRD and TEM. Most of the prepared materials were tested in the CO_2 and CH_4 adsorption/separation at 35 or 25 °C (Chapters 3 and 4). All tested materials are selective for CO_2, *i.e.*, they are able to adsorb much larger amounts of CO_2 than of CH_4 and, therefore, they can be considered as promising candidates for the separation of mixtures of these two gases. In fact, the amount

of adsorbed methane in all the materials tested was found to be very low. Additionally, DFT modelling was performed for the materials presenting mainly amino groups in order to understand how the surfaces of the pristine and modified materials interact with the CO_2 and CH_4 molecules (Chapter 3). In the case of the synthetized amine-modified phenylene PMOs having different pore sizes, a direct correlation between the amounts of CO_2 adsorbed and the pore sizes or the specific surface areas of the PMO materials was not found. However, the differences in the adsorbed quantities of CO_2 could be related with the percentage of T^2_{SMP} silanol species, providing a good prediction of the experimental Henry's law constants for pure CO_2 adsorption on each material (Sub-chapter 3.1). Thus, the best adsorbent properties are correlated with the largest degrees of silica condensation. The amination of the phenylene moieties of the PhC_nPMO was more effective on materials displaying smaller pore size, which was accompanied by the concomitant increase of the K_H for the CO_2.

The grafting of the alkyl amines to the materials with smaller pore size to offer APTMS@PhC_{12}PMO and APTMS@NH_2PhC_{12}PMO adsorbents improved the adsorption of CO_2 without increasing the adsorption of CH_4 (Sub-chapter 3.2). It was observed that the introduction of amines into the PhC_{12}PMO material is in general accompanied by an increase of the quantity of adsorbed CO_2 over the studied pressure range. The Henry's constants for CO_2 adsorption were significantly increased, growing in the order PhC_{12}PMO < NH_2PhC_{12}PMO < APTMS@NH_2PhC_{12}PMO < APTMS@PhC_{12}PMO, *i.e.*, the APTMS@PhC_{12}PMO material has more affinity for CO_2 than any other amine-modified PMO material (with a K_H for CO_2 of 1.83×10^{-2} $mmol \cdot g^{-1} \cdot kPa^{-1}$). The results suggested that the type of amine presents a dominant effect on the CO_2 sorption affinity, more than the nitrogen content in the PMO channels, demonstrating that alkyl amines interact more favorably with CO_2 than aromatic amines. Periodic DFT calculations confirmed the behavior observed for the amino-functionalized PhPMO presented above on the CO_2 and CH_4 adsorption. Furthermore, the strengths of the adsorbate-adsorbent interactions were found to correlate well with the Henry's constants from the experimental adsorption studies.

The Al-PhC_{18}PMO#50 material (Chapter 4) showed acidic Al^V aluminium oxide species that are probably responsible for the observed increase in the CO_2/CH_4 separation selectivity.

The pyrolysis of phenylene- and biphenylene- PMO families resulted in carbonized PMO materials with differences in both the chemistry and the textural properties of the materials (Chapter 4). The reduction of pore size to micro-pores was the most significant difference observed when compared with the starting materials, leading to an improvement of the CO_2 adsorption capacity and the selectivity for CO_2/CH_4 separation. The highest selectivity on the CO_2/CH_4 separation was observed for materials with the highest microporosity. The most interesting material for CO_2/CH_4 separation is the biphenylene-PMO pyrolysed at 1200 °C, presenting the highest K_H for the CO_2 (2.34×10^{-2} mmol·g^{-1}·kPa^{-1}) observed in this PhD study (Chapters 3 and 4), which is remarkable for a material without further amine functionalization and showing that the relation between micro- and meso-porosity plays an important role in the adsorption of CO_2 and CH_4.

Table 6.1 presents a comparison of the materials prepared in this PhD Thesis and tested in the CO_2 and CH_4 adsorption.

Table 6.1. Capacities of different PMO adsorbents in the CO_2/CH_4 separation at 1 bar and their molar selectivity ratios.

Chapter	Materials	CO_2 capacity (mmol·g^{-1})	CH_4 capacity (mmol·g^{-1})	Ratio CO_2/CH_4	Temperature (°C)
3.1	$PhC_{18}PMO$	0.36	0.07	5.14	35
	$NH_2PhC_{18}PMO$	0.31	0.07	4.43	
	$PhC_{12}PMO$	0.40	0.08	5.00	
	$NH_2PhC_{12}PMO$	0.46	0.08	5.75	
3.2	$PhC_{12}PMO$	0.37	0.08	4.62	25
	$NH_2PhC_{12}PMO$	0.40	0.07	5.71	
	APTMS@$PhC_{12}PMO$	0.72	0.07	10.29	
	APTMS@$NH_2PhC_{12}PMO$	0.50	0.06	8.33	
4.1	$PhC_{18}PMO$	0.49	0.11	4.45	
	Al-$PhC_{18}PMO$#2	0.51	0.10	5.10	
	Al-$PhC_{18}PMO$#50	0.47	0.05	9.40	
4.2	$PhC_{12}PMO$_P800	0.65	0.18	3.61	
	$BphC_{18}PMO$_P1200	0.93	0.17	5.47	

As it is possible to observe in Table 6.1, the materials with the best CO_2 adsorption properties are the APTMS@$PhC_{12}PMO$ and the $BphC_{18}PMO$_P1200, with CO_2 adsorption capacities of 0.72 and 0.93 mmol·g^{-1}, respectively, but the materials with the best behaviour for the CO_2/CH_4 separation are the APTMS@$PhC_{12}PMO$ and Al-$PhC_{18}PMO$#50, showing that the relation between micro- and meso-porosity and surface chemistry features are the main characteristics leading to the enhancement of the

CO_2 adsorption without affecting the adsorption of CH_4. The presence of a good relation between micro- and meso- porosity improves the adsorption of CO_2, while the presence of alkyl amines allows a reduction of the CH_4 adsorption. Thus, the preparation of an alkyl amine grafted $BphC_{12}PMO$ material could be remarkable in the CO_2/CH_4 adsorption/separation, through creation of microporosity originated by the introduction of a significant amount of alkyl amines. The preparation of these material it was not yet possible due to difficulties found in the preparation of $BphC_{12}PMO$ material with highly ordered pores.

In order to make the PMO materials more interesting for adsorption or even catalytic applications, the microwave-assisted synthesis was utilized to introduce different kinds of amine groups into the PMOs in a fast and easy way (Chapter 5). Using this type of heating it was possible the modification of the amine moieties of the $NH_2PhC_{18}PMO$ with different alkyl groups (*i*Pr- and $NCCH_2CH_2$- groups), through *N*-monoalkylation or *N*,*N*-dialkylation, without destroying the structural integrity of the parent PMO (Sub-chapters 5.1 and 5.2) and to prepare NH_2PhC_nPMOs in 30 min. of microwave heating in a two-step amination process (Sub-chapter 5.3). Furthermore, it was proved that the nitrile group of the $(NCCH_2CH_2)_2NPhC_{18}PMO$ material remains intact on the surface of the materials, which may enable additional functionalization, as for instance, by chemical modification into carboxylic acids, amines or even transformation into amino acids. Therefore, this work provides indication of the potential of the microwave-assisted post-synthesis modification of the organic bridges of $PhC_{18}PMO$ to introduce alternative functional groups. Hence, on-demand PMOs may be developed for a wide range of applications.

6.2. Recommendations for further research

In terms of future work, it is suggested the improvement of the PMO features for the CO_2 and CH_4 adsorption. In fact, from this PhD Thesis it becomes clear that the preparation of adsorbents for biogas upgrading needs to have into account several different factors, such as, functional group loading, surface area, pore volume and pore size, distances between functional groups and distances between functional groups and silanols.

In this way, it is proposed to modify the PMO features in order to:

i) reduce even more the pore size of the aromatic-bridge PMOs (PhC_nPMO and $BphC_nPMO$ with $n < 12$);

ii) create microporosity in the PMO using bissilylated precursor with different alkyl amines by grafting reaction;

iii) prepare PMOs with amine functional groups introduced in favorable positions to connect with CO_2 molecules, *i.e.*, place functional groups at an adequate distance from each other for enhancing the chemical characteristics for CO_2 adsorption. Thus, the preparation of PMOs materials with amino acids (tyrosine, histidine, alanine, arginine, etc.), amino alcohols or pyridine and indole compounds bonded to the amines of the NH_2PhC_nPMOs is proposed, as well as, the evaluation of the resulting materials in the adsorption of CO_2 and CH_4;

iv) impregnate a fine layer of polyethyleneimine (PEI) into the pores of PMO, in order to incorporate significant amounts of alkylamines and to generate microporosity into the PMO without clogging the pores;

v) prepare selective nanocomposite-PMOs using the ALD technique. To accomplish such goal the study of surface dependency in the aluminium oxide deposition must be made (*i.e.* deposition of aluminium oxide into $BphC_nPMO$, SBA-15, MCM-41, etc). Additionally, the creation of defects in the aluminium oxide layer can improve the CO_2 adsorption; such creation of defects can be done by chemical attack of the Al-PhC_{18}PMO#50 composite. Alternatively, a different metal oxide can be inserted into the PMO materials;

vi) introduce nitrogen functional groups which are not easily labile in pyrolysis process (by preparation of pyridine- or bipyridine- PMOs or even by post-synthetic functionalization of PMO with N_2 or NH_3 cold plasma treatment);

vii) create biocomposites-PMOs with introduction of a fine layer of chitosan or chitosan and melanine into the PMO materials and to proceed to the pyrolysis of the resulting materials. This can be an interesting approach since it has been demonstrated that the pyrolysed chitosan presents interesting CO_2 adsorption properties. Also, this polymer is a cheap raw material that can be used to insert amine groups and to create microporosity into the PMOs. These chitosan-PMO composites may display electrical conductive features and can be also good candidates for the electroreduction of CO_2.

In parallel with this, it is also important to continue the computer simulation using the same approach considered in this PhD Thesis, for screening other phenylene-PMO functionalizations or of other organic bridged PMOs, with the desired characteristics for CO_2/CH_4 separation. Additionally, as the computational cost is an important factor for screening purposes, small but appropriate cluster models centered on the organic or inorganic moieties are thought to study the surface of PMO materials with large organic bridges and their interactions with CO_2 and CH_4. State-of-the-art DFT functionals need to be tested as well as the cluster size, stoichiometry and shape of the PMO cluster model.

As referred in Chapter 1, several PMO materials present intrinsic structural features for catalytic applications (Knövenagel condensation, kinetic resolution of hydrobenzoin or of 1,2-diphenylethane-1,2-diol, etc.), and adsorption of metal ions (Hg(II), Cu(II), etc.) or organic compounds (naproxen, etc.) when compared with other kinds of materials (silicas, MOFs and zeolites). It will be interesting to test the prepared PMOs in these applications.

As it is understood from this PhD Thesis, the preparation of different kinds of PMO materials, using different functionalization strategies, to change their physical, chemical and textural properties is an important way to find new remarkable materials for a wide range of applications. In this way, the search for new strategies targeting the synthesis and/or the modification of novel PMOs is a step to be explored in the future for obtaining materials with enhanced adsorptive properties.

Appendices

Appendix A

A1.1. Experimental manometric apparatus

The custom made manometric experimental setup shown in Figure S1 is composed of two gas and sample chambers allowing the analysis of two adsorbents simultaneously. Pressure and temperature are monitored and valves are controlled by a personal computer running a custom made LabVIEW program.

All valves are from ASCO (Emerson) and are pneumatic actuated. Valves 2 and 4 are normally opened valves (ref. E290A794) while the remaining are normally closed (ref. E290A791).

Valves 1 and 3 enable the introduction of the gas (from Gas Inlet) or evacuation of the system (towards the atmosphere, through valve 6, or towards the vacuum pump, through valve 7). Valves Val 2 and 4 allow the isolation of the samples of adsorbent in the sample tanks when feeding or evacuating the gas tanks.

The oven used for adsorbents activation and temperature control is a GC 1000 from Dani (Dani Instruments Spa, Milan, Italy).

Temperature sensors TS are PT-100 Resistance Temperature Detector probe (type PR-11-2-M30-300-MI-B) from Omega (Omega Engineering Ltd, Manchester, United Kingdom).

Stainless steel tubing, tanks and fittings are from Swagelok.

The pressure transducers PS (Unik 5000, PMP 5013-TB-A3-CA-HO-PA, 0-2.5 bar (A) and 0-10 bar (B), absolute) from GE are used to follow the pressure inside the tanks along the experiment.

The volume of the gas tanks (volume between valves 1 and 2) is 73.4 cm^3 and 71.3 cm^3, and the volume of the sample tanks (including free volume of the tubes until valves 2 and 4) is of 24.8 cm^3 and 26.4 cm^3 for unit 1 and 2, respectively. These volumes were determined by two independent helium picnometry experiments.

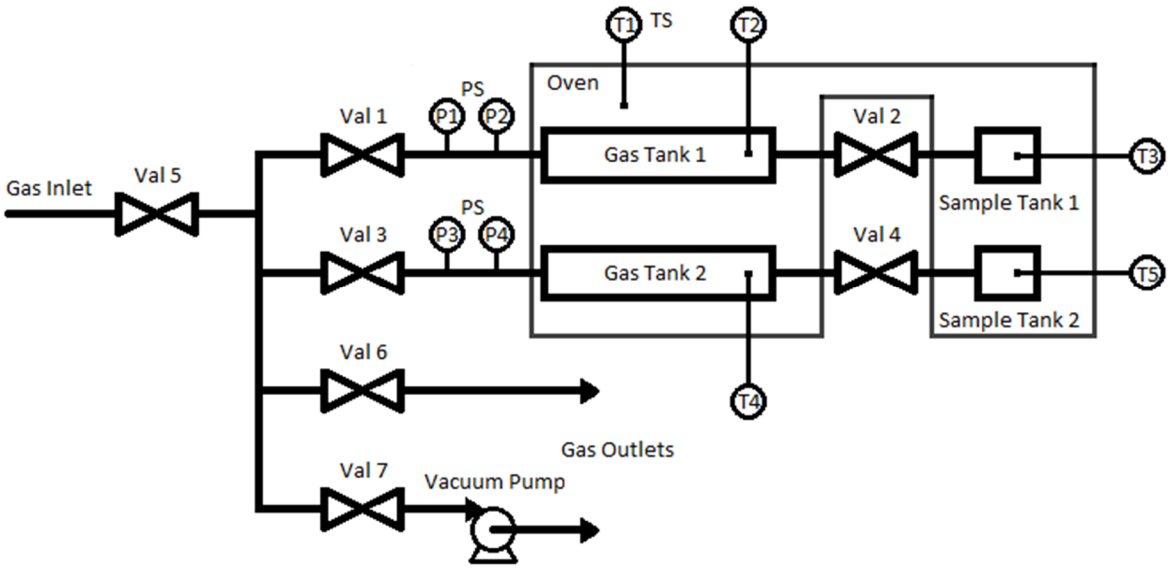

Figure A1.1. Manometric apparatus. Val: valve, PT: pressure sensors (P1-4), TS: temperature sensors (T1-5).

Sample activation.

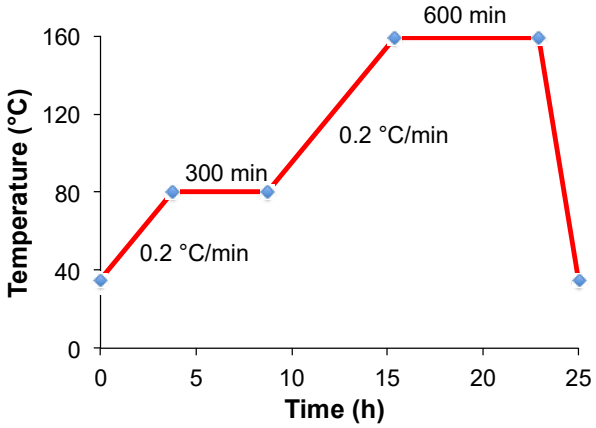

Figure A1.2. Sample activation: heating program used in this work.

A1.2. Data from the characterization of PMO materials of sub-chapter 3.1.

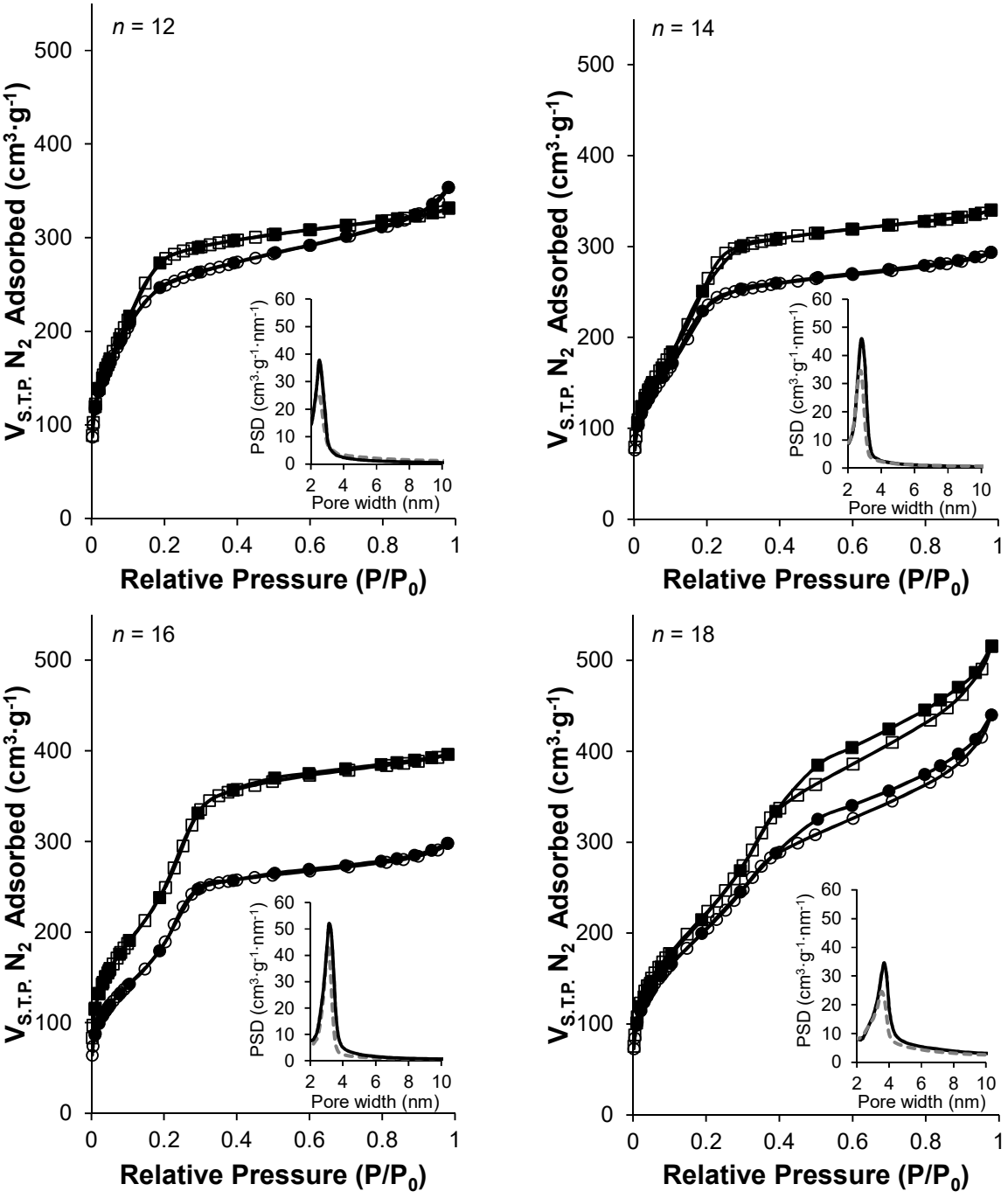

Figure A1.3. -196 °C N_2 isotherms of synthesized PMOs. The squares represent the unmodified PMOs and the spheres represent aminated PMOs. The open symbols denote adsorption and the filled symbols characterize desorption. The insets display the PSD curves of all used materials where the continuous black line corresponds to PhC_nPMOs and the dashed grey line corresponds to the NH_2PhC_nPMOs.

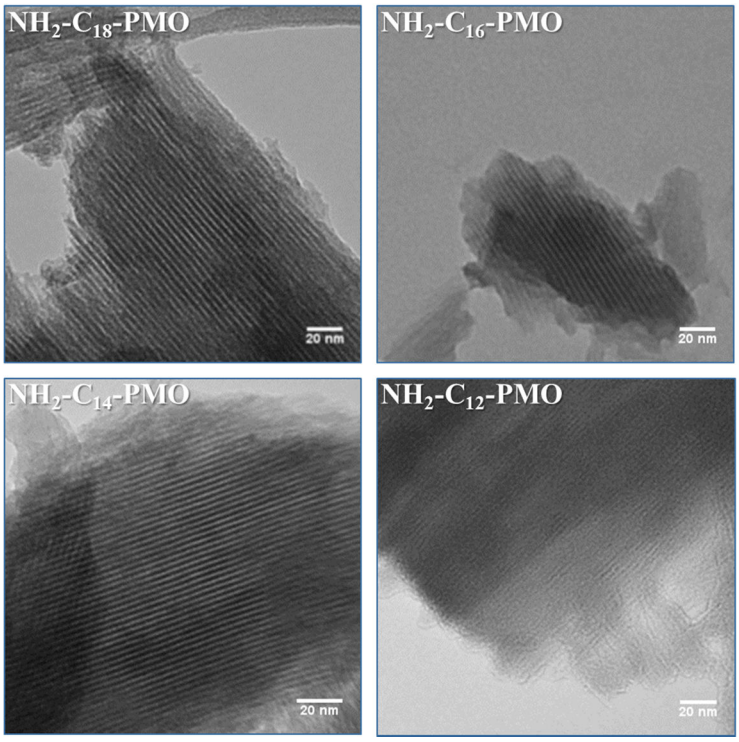

Figure A1.4a. High-resolution transmission electron microscopy image of $NH_2PhC_{12}PMO$, $NH_2PhC_{14}PMO$ $NH_2PhC_{16}PMO$ and $NH_2PhC_{18}PMO$, materials.

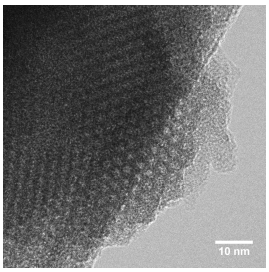

Figure A1.4b. TEM image of the edge on of the $NH_2PhC_{16}PMO$.

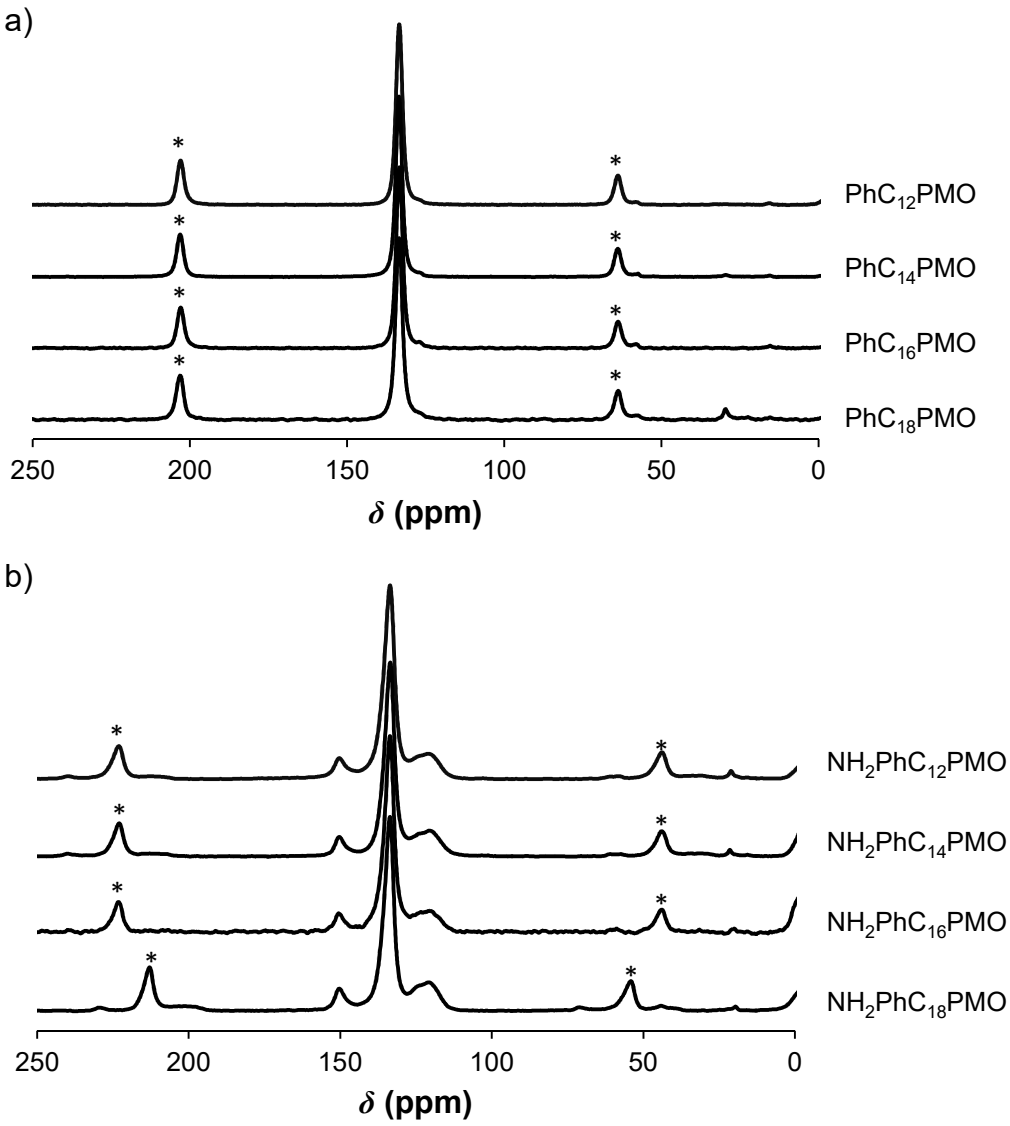

Figure A1.5. ^{13}C CP-MAS NMR spectra of a) PhC_nPMOs and b) NH_2PhC_nPMOs. The spectrum of $NH_2PhC_{18}PMO$ was collected with a spinning rate of 7 kHz. The spectra of the other materials were recorded with a spinning rate of 9 kHz.

Table A1.1. T^m species in the prepared materials calculated from the fits of the ^{29}Si MAS NMR spectra.

Materials	SiO_2OH^a %	$SiO(OH)_2^b$ %	$T^1_{NMR}{}^c$ %	$T^2_{NMR}{}^d$ %	Condensation degree[e] %	$T^1_{SMP}{}^f$ %	$T^2_{SMP}{}^g$ %
$PhC_{12}PMO$	93.97	6.03	2.02	31.40	66.58	1.22	18.92
$NH_2PhC_{12}PMO$	96.42	3.58	1.22	32.79	66.00	0.77	20.61
$PhC_{14}PMO$	92.88	7.12	2.39	31.25	66.35	1.41	18.43
$NH_2PhC_{14}PMO$	93.07	6.93	2.02	27.16	70.81	1.28	17.20
$PhC_{16}PMO$	95.24	4.76	1.57	31.48	66.95	0.96	19.26
$NH_2PhC_{16}PMO$	92.86	7.14	1.84	23.98	74.17	1.14	14.86
$PhC_{18}PMO$	93.20	6.80	1.98	27.16	70.86	1.17	15.99
$NH_2PhC_{18}PMO$	92.14	7.86	2.27	26.63	71.10	1.32	15.51

[a]Percentage of single T^2 type silanol regarding to the hydroxylated silanols calculated as $T^2/(T^1+T^2)$, where the $T^1$and T^2 are the area of the resonances at *ca.* -61 and -71 ppm, respectively. [b]Percentage of geminal T^1 type silanol regarding to the hydroxylated silanols calculated as $T1/(T^1+T^2)$. [c]Percentage of germinal T^1 type silanol regarding to all silicon species calculated as $T^1/(T^1+T^2+T^3)$ where the T^1, T^2 and T^3 are the area of the resonances at *ca.* -61, -71 and -81 ppm, respectively, obtained from the deconvolution of peaks from the fits of the ^{29}Si MAS NMR spectra. [d]Percentage of the total T^2 type silanol regarding to all silicon species calculated as $T^2/(T^1+T^2+T^3)$. [e]Percentage of the condensation degree that correspond to the percentage of T^3 type silicon species regarding to all silicon types calculated as $T^3/(T^1+T^2+T^3)$. [f]Percentage of germinal T^1 type silanol presented in the material regarding to all silicon species calculated as $(T^1/(T^1+T^2+T^3))$ x % Si-O. [g]Percentage of total T^2 type silanol presented in the material regarding to all silicon species calculated as $(T^2/(T^1+T^2+T^3))$ x % Si-O.

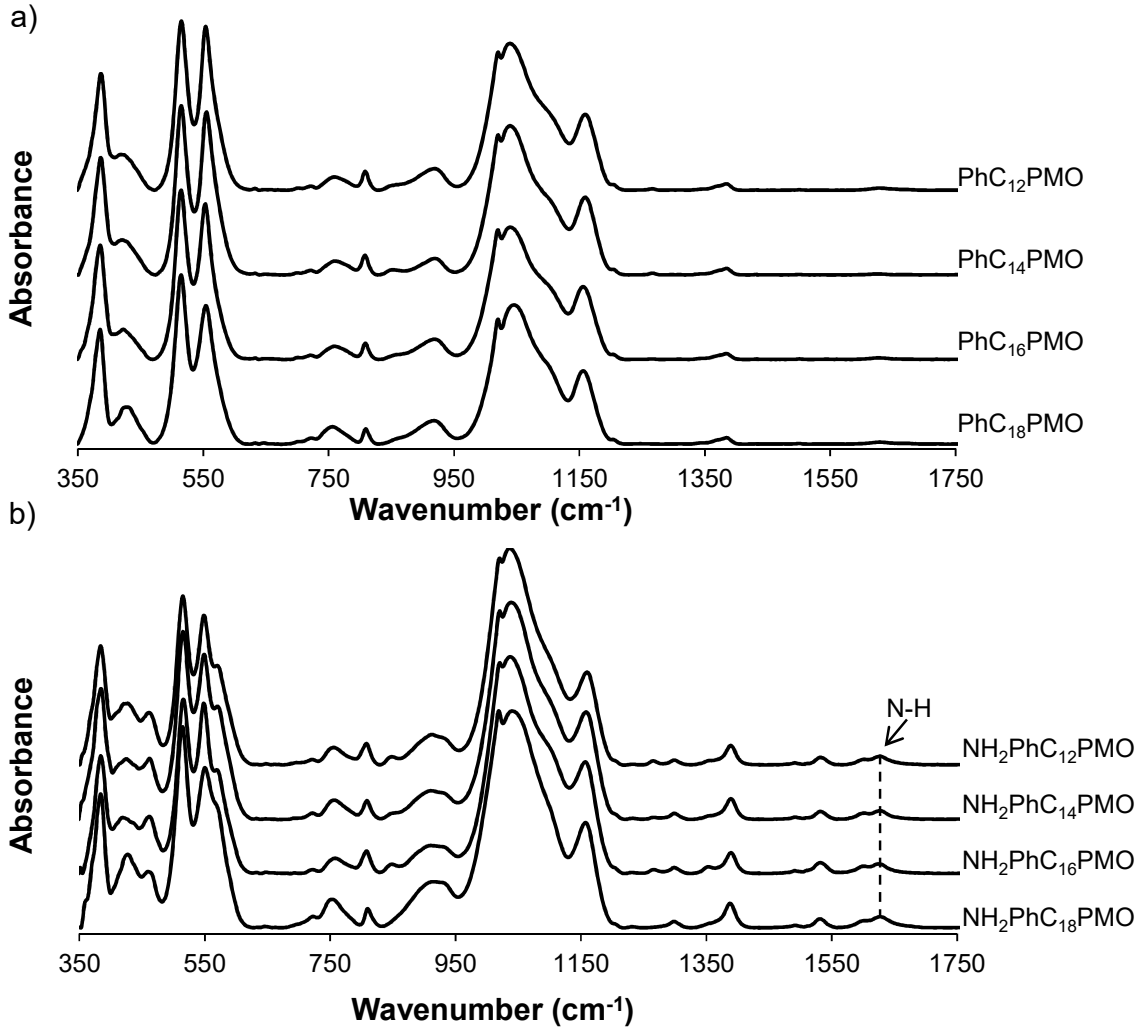

Figure A1.6. FTIR (ATR) spectra of a) PhC$_n$PMOs and b) NH$_2$PhC$_n$PMOs.

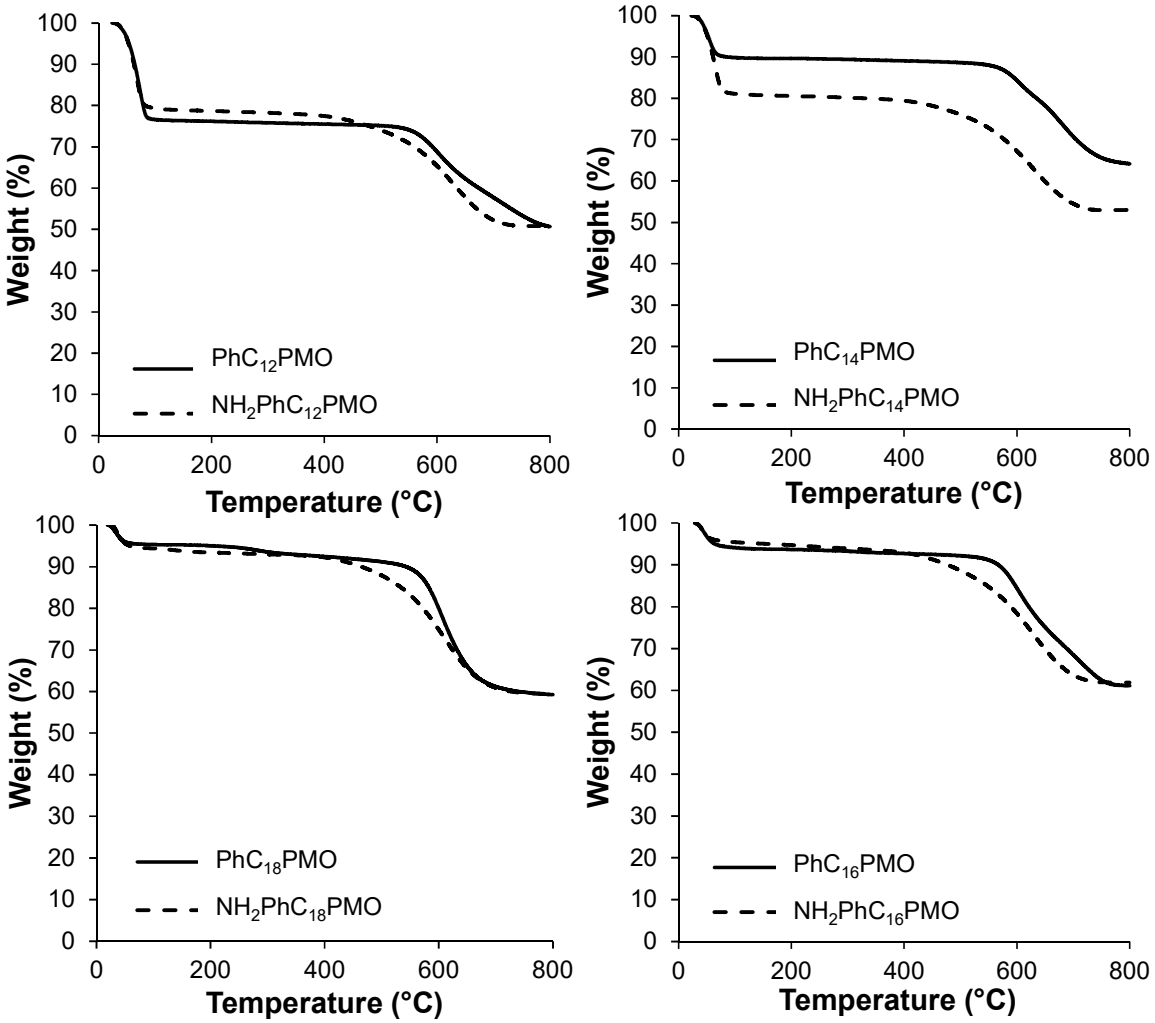

Figure A1.7. TGA PhC$_n$PMOs and NH$_2$PhC$_n$PMOs materials.

Table A1.2. Elemental analyses and nitrogen density of PhC_nPMOs and NH_2PhC_nPMOs.

Sample	%N	%C[a]	%H	%Si-O[b]	*N* density mmol·g^{-1}	*% phenylene moieties aminated*
$PhC_{12}PMO$	-	37.21	2.53	60.26	-	
$NH_2PhC_{12}PMO$	2.58	31.57	3.01	62.84	1.85	43.0
$PhC_{14}PMO$	-	38.56	2.48	58.96	-	
$NH_2PhC_{14}PMO$	2.89	31.29	2.50	63.32	2.07	48.2
$PhC_{16}PMO$	-	36.38	2.44	61.18	-	
$NH_2PhC_{16}PMO$	3.16	32.12	2.75	61.97	2.25	52.7
$PhC_{18}PMO$	-	38.39	2.75	58.86	-	
$NH_2PhC_{18}PMO$	3.03	35.81	2.92	58.24	2.16	50.5

[a]Note that the %C of carbon for the non-aminated samples can be theoretically calculated using the T^m function of % T^3, % T^2, and % T^1 silicon species in the pure PhC_nPMO material. In this way, based on the molecular formula of organosilicas $SiO_{1.5}$-R-$SiO_{1.5}$, the percentage of carbon can be calculated as $\%C = [3 \times At.Wt._C / (1.5 \times At.Wt._O + 1 \times At.Wt._{Si} + 3 \times At.Wt._C + 2 \times At.Wt._H)] \times \% T^3 + [3 \times At.Wt._C / (2 \times At.Wt._O + 1 \times At.Wt._{Si} + 3 \times At.Wt._C + 3 \times At.Wt._H)] \times \% T^2 + [3 \times At.Wt._C / (2.5 \times At.Wt._O + 1 \times At.Wt._{Si} + 3 \times At.Wt._C + 3 \times At.Wt._H)] \times \% T^1$, where At.Wt. stands for the atomic weights of the elements and % T^3, % T^2 and % T^1 are the percentages of T^m silanol species reported in Table A1.1. For instance, in the case of the C_{12}-PMO material, the formula above gives $\%C = [3 \times 12.011 / (1.5 \times 15.999 + 1 \times 28.085 + 3 \times 12.011 + 2 \times 1.008)] \times 66.58 + [3 \times 12.011 / (2 \times 15.999 + 1 \times 28.085 + 3 \times 12.011 + 3 \times 1.008)] \times 31.40 + [3 \times 12.011 / (2.5 \times 15.999 + 1 \times 28.085 + 3 \times 12.011 + 3 \times 1.008)] \times 2.02 = 38.70$ %. The % C for the remaining samples are 38.68 %, 38.73 % and 38.39 %, respectively for $PhC_{14}PMO$, $PhC_{16}PMO$ and $PhC_{18}PMO$. The maximum difference observed between theoretical and experimental %C is 2.35 % for $PhC_{16}PMO$. The good qualitative agreement supports the consideration of the % T^3, % T^2 and % T^1 for providing a quantitative measurement of the T^m environments in each sample, which is essential to support the function described by equation 3.1.4. [b]The percentage of Si-O was determined by the equation % Si-O = 100 % - % C - % H - % N.

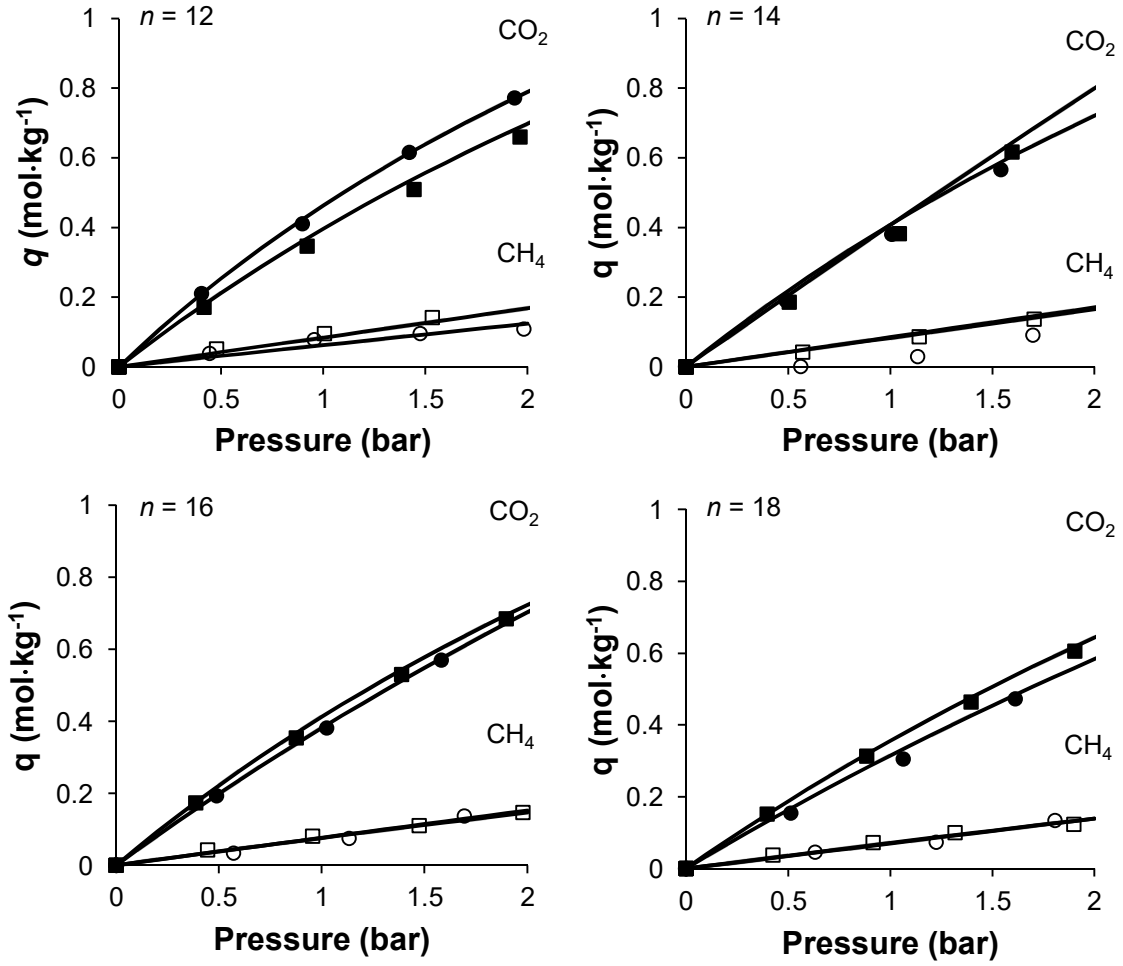

Figure A1.8. Adsorption equilibrium isotherms of pure CO_2 (closed symbols) and CH_4 (open symbols) molecules in the as-synthesized (squares) and amine functionalized (spheres) PhC_nPMOs. Solid lines represent the fits to Langmuir model.

Table A1.3. Langmuir parameters of PhC_nPMOs and NH_2PhC_nPMOs for CO_2.

Sample	***qs*** mmol·g^{-1}	***b*** bar^{-1}
$PhC_{12}PMO$	2.95	0.16
$NH_2PhC_{12}PMO$	2.67	0.21
$PhC_{14}PMO$	2.35	0.17
$NH_2PhC_{14}PMO$	3.10	0.15
$PhC_{16}PMO$	2.96	0.16
$NH_2PhC_{16}PMO$	4.53	0.09
$PhC_{18}PMO$	3.36	0.12
$NH_2PhC_{18}PMO$	4.01	0.09

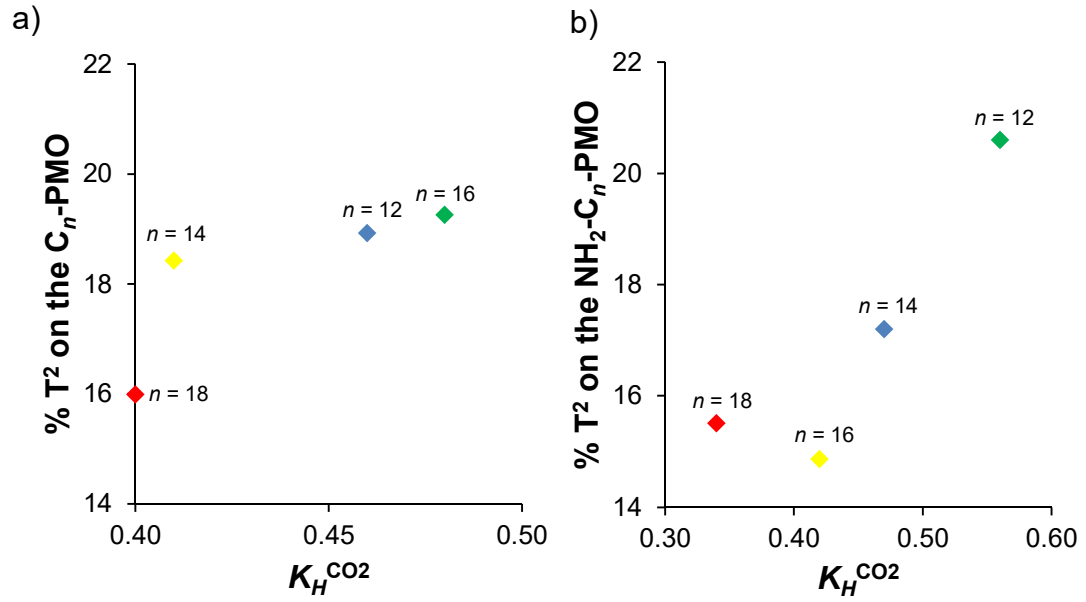

Figure A1.9. Correlation between the percentage of T^2_{SMP} silanols species presented on the material and the Henry constant of CO_2 on a) PhC_nPMOs and b) NH_2PhC_nPMOs.

A2.1. Data from the characterization of PMO materials of sub-chapter 3.2.

Table A2.1. Physical properties of $PhC_{12}PMO$, $NH_2PhC_{12}PMO$, APTMS@$PhC_{12}PMO$ and APTMS@$NH_2PhC_{12}PMO$.

Sample	d_{100} nm	a[a] nm	S_{BET} $m^2 \cdot g^{-1}$	V_P $cm^3 \cdot g^{-1}$	d_P[b] nm	b[c] nm
$PhC_{12}PMO$	3.59	4.14	1004	0.69	2.54	1.60
$NH_2PhC_{12}PMO$	3.63	4.19	924	0.70	2.41	1.78
APTMS@$PhC_{12}PMO$	3.34	3.92	634	0.43	2.24	1.68
APTMS@$NH_2PhC_{12}PMO$	3.50	4.04	305	0.27	2.23	1.81

[a]Unit cell parameter calculated as ($2d_{100}/\sqrt{3}$) . [b]Pore width obtained from the BJH method with the corrected Kelvin equation, i.e. KJS–BJH method at the maximum of pore size distribution calculated on the basis of adsorption data. [c]Pore wall thickness calculated as ($2d_{100}/\sqrt{3}$ - d_P), where the first term is the unit cell parameter.

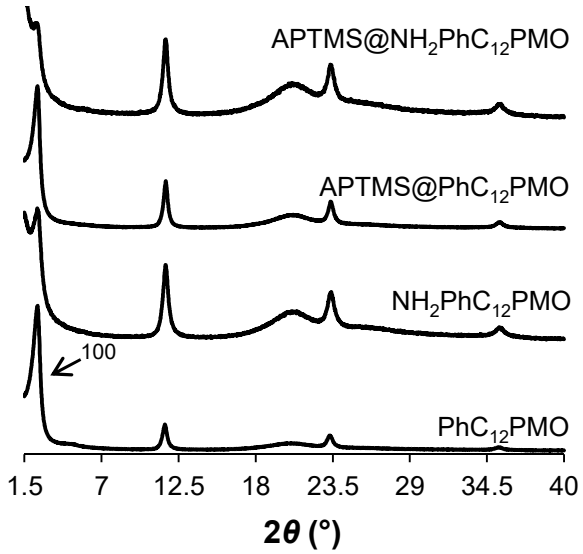

Figure A2.1. Powder X-ray diffraction patterns of $PhC_{12}PMO$, $NH_2PhC_{12}PMO$, APTMS@$PhC_{12}PMO$ and APTMS@$NH_2PhC_{12}PMO$.

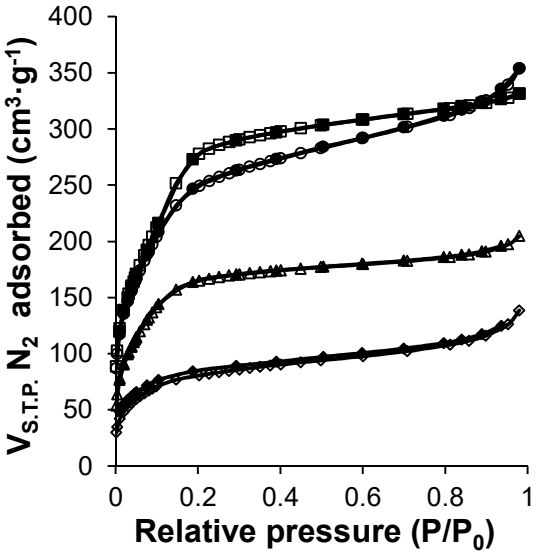

Figure A2.2. -196 °C N_2 isotherms of a) $PhC_{12}PMO$ ((□) adsorption, (■) desorption)); $NH_2PhC_{12}PMO$ ((○) adsorption, (●) desorption)); APTMS@$PhC_{12}PMO$ ((Δ) adsorption, (▲) desorption)) and APTMS@$NH_2PhC_{12}PMO$ ((◊) adsorption, (♦) desorption)).

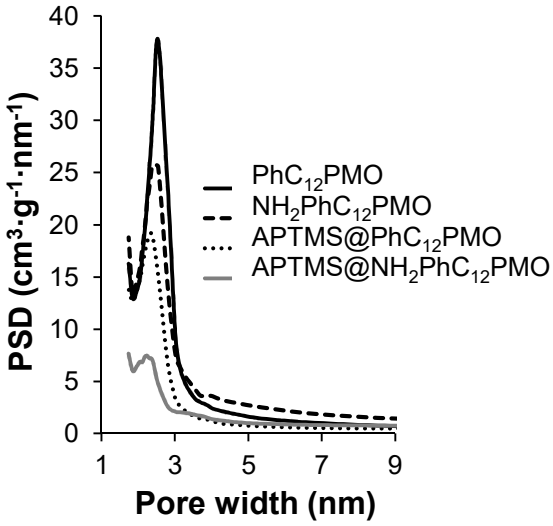

Figure A2.3. Pore Size Distribution curves of $PhC_{12}PMO$, $NH_2PhC_{12}PMOs$, APTMS@$PhC_{12}PMO$ and APTMS@$NH_2PhC_{12}PMO$.

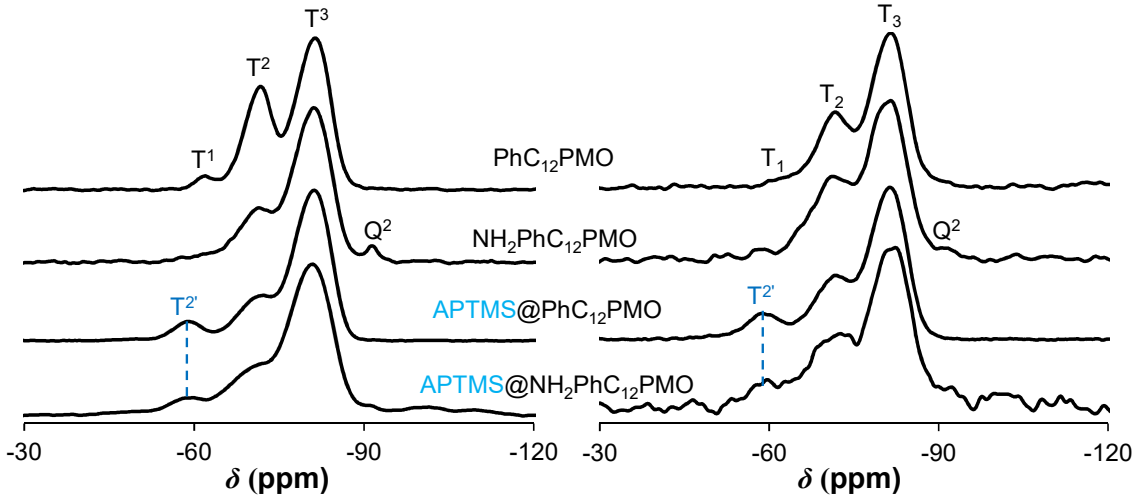

Figure A2.4. ^{29}Si CP-MAS (left) and MAS (right) NMR spectra of $PhC_{12}PMO$, $NH_2PhC_{12}PMO$, APTMS@$PhC_{12}PMO$ and APTMS@$NH_2PhC_{12}PMO$. Chemical shifts referenced from TMS.

Table A2.2. Percentage of T^m silanol species calculated from the fits of the ^{29}Si MAS NMR spectra.

PMO	% T^1	% T^2	% T^3	%$T^{2'}$[a]
$PhC_{12}PMO$	2.02	31.40	66.58	-
$NH_2PhC_{12}PMO$	1.22	32.79	66.00	-
APTMS@$PhC_{12}PMO$	-	28.76	61.80	9.44
APTMS@$NH_2PhC_{12}PMO$	-	34.73	58.22	7.05

[a]percentage of T^2 silanols in the APTMS group.

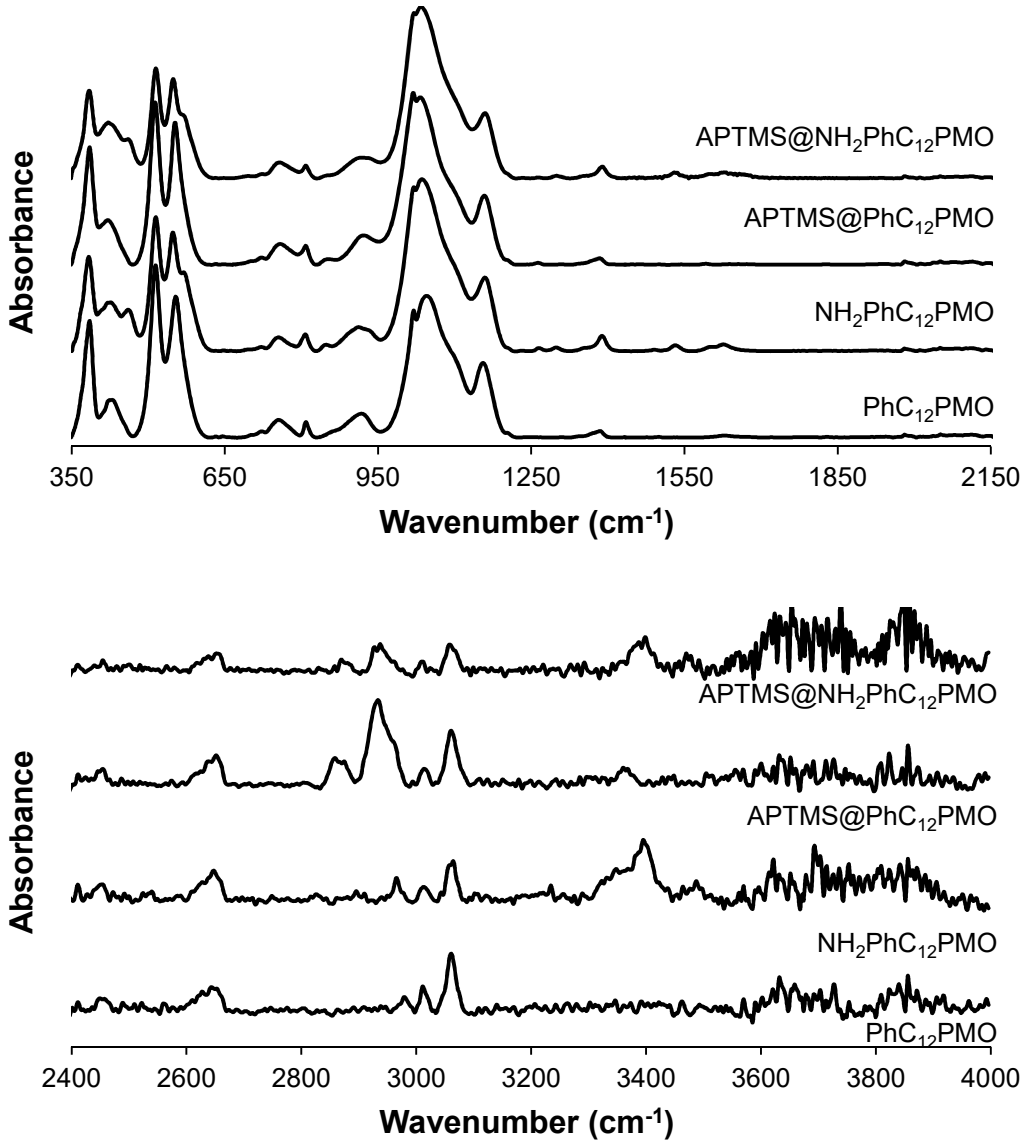

Figure A2.5. FTIR (ATR) spectra of $PhC_{12}PMO$, $NH_2PhC_{12}PMO$, APTMS@$PhC_{12}PMO$ and APTMS@$NH_2PhC_{12}PMO$.

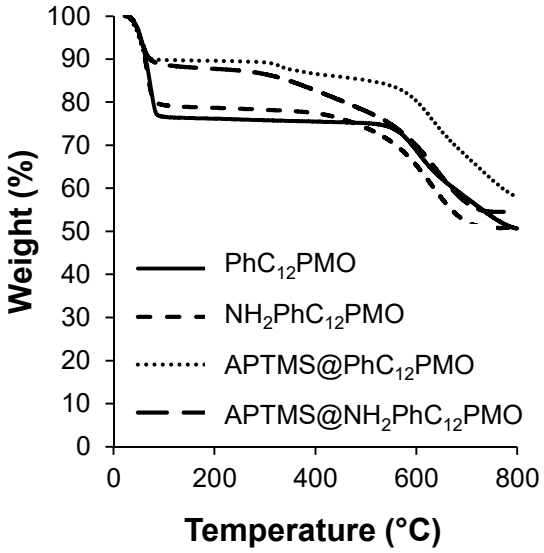

Figure A2.6. TGA of $PhC_{12}PMO$, $NH_2C_{12}PMO$, $APTMS@PhC_{12}PMO$ and $APTMS@NH_2PhC_{12}PMO$.

Table A2.3. Elemental analyses and nitrogen density of $PhC_{12}PMO$, $NH_2PhC_{12}PMO$, $APTMS@PhC_{12}PMO$ and $APTMS@NH_2PhC_{12}PMO$.

Sample	%N	%C	%H	***N* density** mmol·g^{-1}
$PhC_{12}PMO$	-	37.21	2.53	-
$NH_2PhC_{12}PMO$	2.58	31.57	3.01	1.85
$APTMS@PhC_{12}PMO$	1.93	34.08	3.38	1.39
$APTMS@NH_2PhC_{12}PMO$	3.64	32.53	3.51	2.60

A2.2. CO_2 and CH_4 adsorption in the PMOs: experimental and computational studies

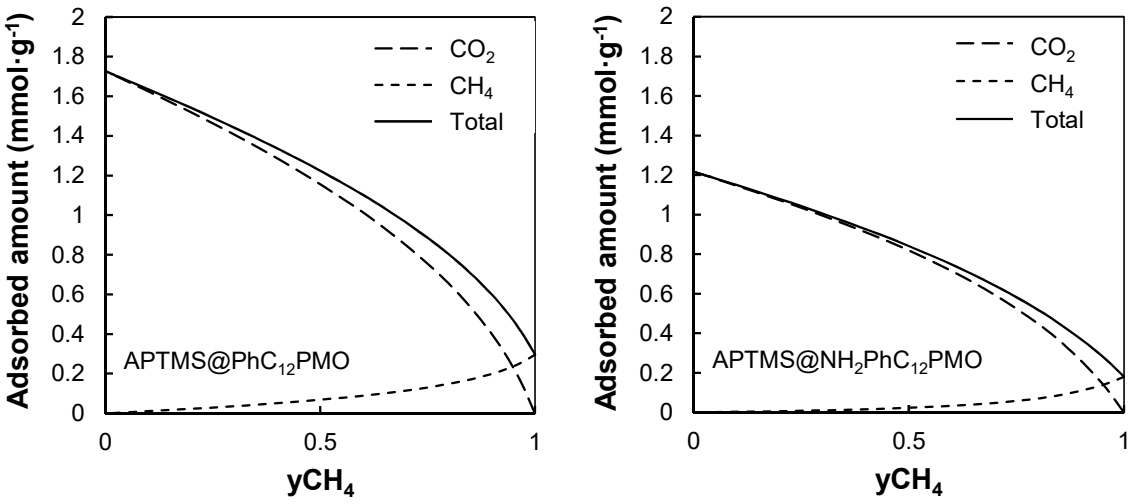

Figure A2.7. Adsorbed amounts of the CO_2/CH_4 mixture as a function of the CH_4 molar fraction in the gas phase, at 500 kPa and 25 °C, for APTMS-PMO materials.

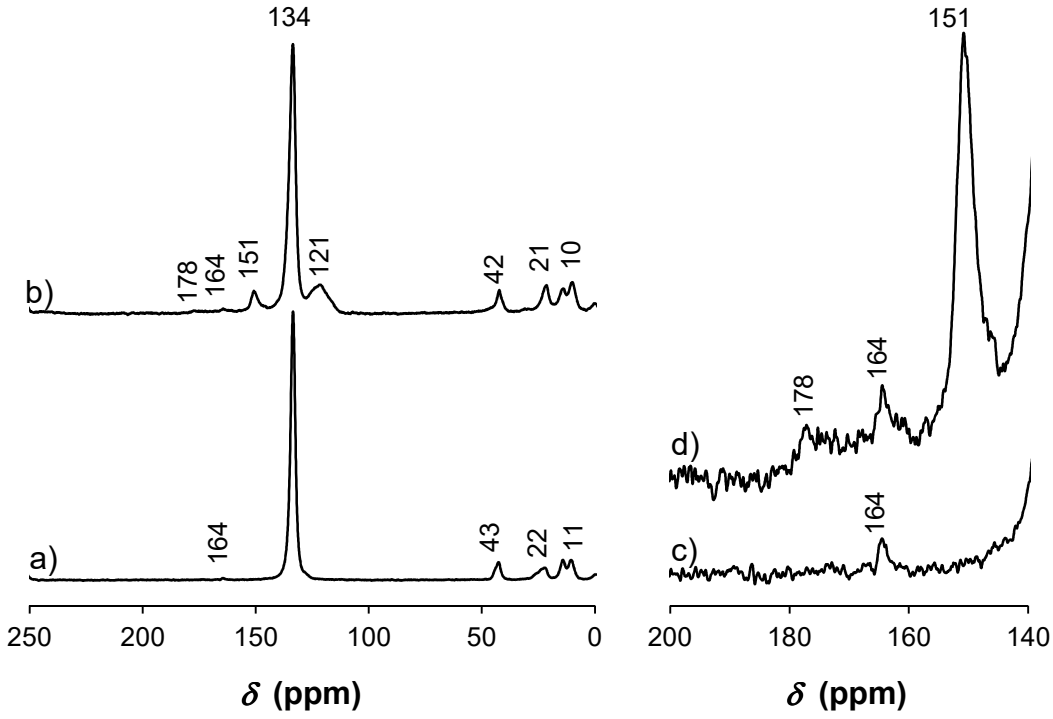

Figure A2.8. a) ^{13}C CP-MAS NMR spectra of a) APTMS@PhC_{12}PMO and b) APTMS@NH_2PhC_{12}PMO after material degassing; c) and d) correspond to the magnified 140-200 ppm region of APTMS@PhC_{12}PMO and APTMS@NH_2PhC_{12}PMO, respectively.

Table A2.4. Virial coefficients (C_1, C_2 and C_3) and Henry constants (K_H) for the adsorption at 25 °C and 35 °C of methane and carbon dioxide on APTMS@PhC$_{12}$PMO.[a]

Gases	Temperature	K_H	C_1	C_2	C_3
	°C	(mmol·g^{-1}·kPa^{-1}) x 10^{-2}	g·mmol^{-1}	(g·mmol^{-1})^2	(g·mmol^{-1})^3
CH$_4$	35	0.08	1.230		
	25	0.07	0.797		
CO$_2$	35	1.80	2.812	-1.197	
	25	1.83	1.647	-0.476	0.048
Ratio CO$_2$/CH$_4$	35		22.50		
	25		26.1		

[a]Obtained by the nonlinear least-squares the virial equation to the adsorption data

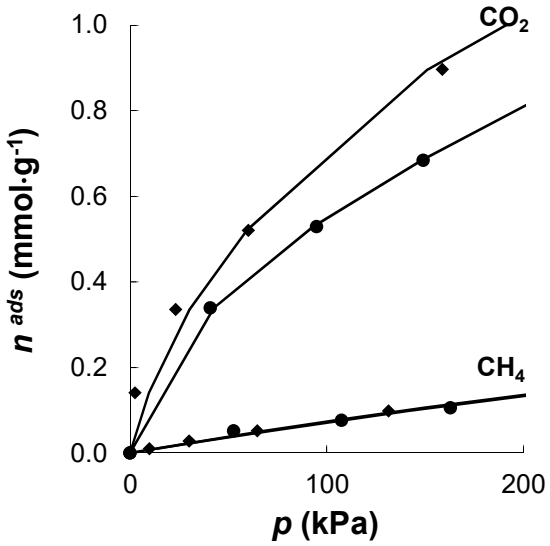

Figure A2.9. Adsorption equilibrium isotherms of CO_2 and CH_4 at 25 and 35 °C. Solid lines represent the fits to the Virial model. ● corresponds to the APTMS@PhC$_{12}$PMO materials measured at 35 °C (1st utilization of the material) and ♦corresponds to the APTMS@PhC$_{12}$PMO measured at 25 °C (2nd utilization of the material).

Table A2.5. Selected distances between atoms in the CO_2 and CH_4 adsorbates and in the parent and aminated PhPMO adsorbents.

	R'@RPhPMO[a]		Atomic distances (Å)							
			CO_2			CH_4				
			O_9	C_{10}	O_{11}	C_{12}	H_{13}	H_{14}	H_{15}	H_{16}
R'- Functionalized RPhPMO Materials	-H / -H	H_1					3.61			
		H_2				3.33		3.12		
		H_3	3.80	4.33				3.07		
		Si-O_6-H_5	2.28				5.43			
		Si-O_7-Si			3.90				3.15	
		Si-O_8-Si		3.81						
	-H / -NH_2	N-H_{17}			2.60			2.36	2.42	
		N_{18}		4.12	3.24	3.44				
		N-H_{19}			3.19	2.62		2.65		
		H_1	2.87	2.66			3.97			
		Si-O_6-H_5	2.45				4.84			
		Si-O_7-Si			4.68				2.74	
		Si-O_8-Si		2.96					2.74	
	-APTMS / -H	H_1			5.32		5.15	4.94		
		H_2							4.56	
		H_3	7.02		7.53			6.72		
		Si-O_7-Si							5.59	
		H_{20}	2.75						2.64	
		H_{21}	3.41						3.09	
		H_{22}					3.16			
		H_{25}			3.18					
		N-H_{26}	4.14							3.85
		N_{27}		2.99		3.37				
		N-H_{28}			2.58			2.58		2.75
		Si-O-H_{29}	3.23	3.66			2.93			
	-APTMS / -NH_2	H_1	3.57							
		H_2		3.19				3.80		
		H_3	6.05							
		Si-O_7-Si			4.80					
		N-H_{17}	4.51					5.71		
		N_{18}		5.04						
		N-H_{19}	4.78		4.54					
		H_{20}			2.62					
		H_{21}			2.76					
		H_{22}					3.98			
		H_{25}	3.25						3.64	
		N-H_{26}			4.75					
		N-H_{28}			4.21				3.59	
		Si-O-H_{29}	2.45	2.74			2.66	2.14		
		Si-O-H_{30}	4.60				4.91			

[a]The reference atom for measuring the atomic distances appears in black.

Table A2.6. Selected atomic distances between CO_2 or CH_4 and the **R**-functionalized PhPMOs.

	RPhPMO[a]		Atomic distances (Å)							
			CO_2			CH_4				
			O_9	C_{10}	O_{11}	C_{12}	H_{13}	H_{14}	H_{15}	H_{16}
R - Functionalized PhPMO Materials	$-NO_2$	N-O_{31}		3.30	3.30			2.74		
		N_{32}		4.57				3.26		
		N-O_{33}			4.44			3.76		
		H_1	2.86			3.07	2.25			
		H_2	4.07	3.50	3.29	3.37		2.65		
		Si-O_6-H_5	2.34				2.38			
		Si-O_7-Si	4.21						3.44	
		Si-O_8-Si							3.30	
	$-NH$-*i*-Pr	N-H_{34}			2.81				2.87	
		N_{35}		3.66						
		NH-C-H_{36}		3.58	3.36				2.75	
		CH-C-H_{37}	3.49					3.48		
		CH-C-H_{38}			2.78			2.19		3.16
		CH-C-H_{39}	2.50				2.55			
		CH-C-H_{40}			3.14		2.19			
		H_1	2.62	3.50						4.20
		Si-O_6-H_5	3.37				4.91			3.00
		Si-O_7-Si		2.87					2.28	
	$-CH_2NH_2$	C-H_{41}			3.16					2.99
		CH-N-H_{42}			2.26				2.77	2.60
		H_1	3.86				4.26			
		H_2	3.01				2.38			2.88
		Si-O_6-H_5	2.38				2.54			
		Si-O_7-Si	3.25						3.30	
		Si-O_8-Si		3.11					2.28	
	$-SO_3H$	S-O_{43}		3.10	3.18			2.43		
		S-O_{44}			4.76					
		S-O_{45}H			3.38			3.15		
		H_1	3.58				3.48			
		H_2	3.86				4.38			
		Si-O_6-H_5	2.72		4.38		2.95			
		Si-O_7-Si	3.71							
		Si-O_8-Si		4.03					3.03	

[a]The reference atom for measuring the atomic distances appears in black.

Appendix B

B1.1 Data from characterization of PMO materials of sub-chapter 4.1

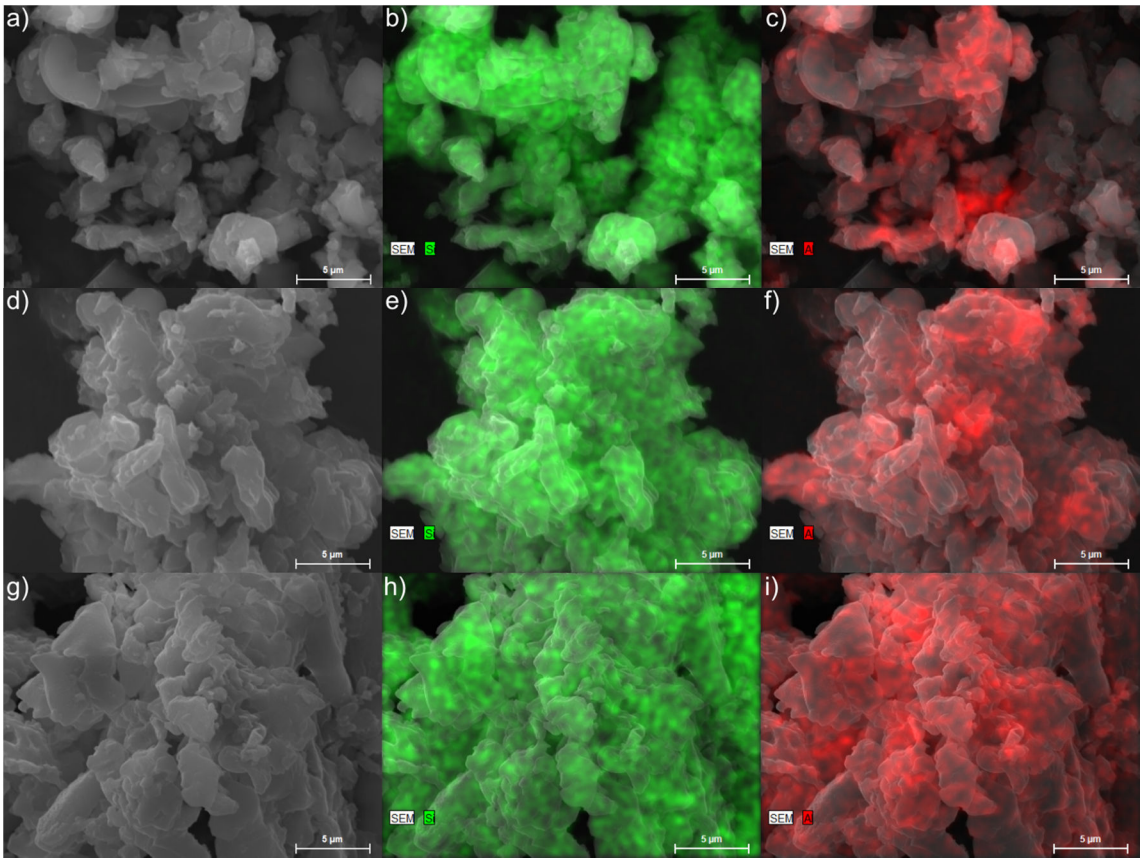

Figure B1.1. SEM and EDS mapping images of Al-PhC$_{18}$PMO#10 (a), b), and c)), Al-PhC$_{18}$PMO#20 (d), e), and f)) and Al-PhC$_{18}$PMO#100 (g), h), and i)).

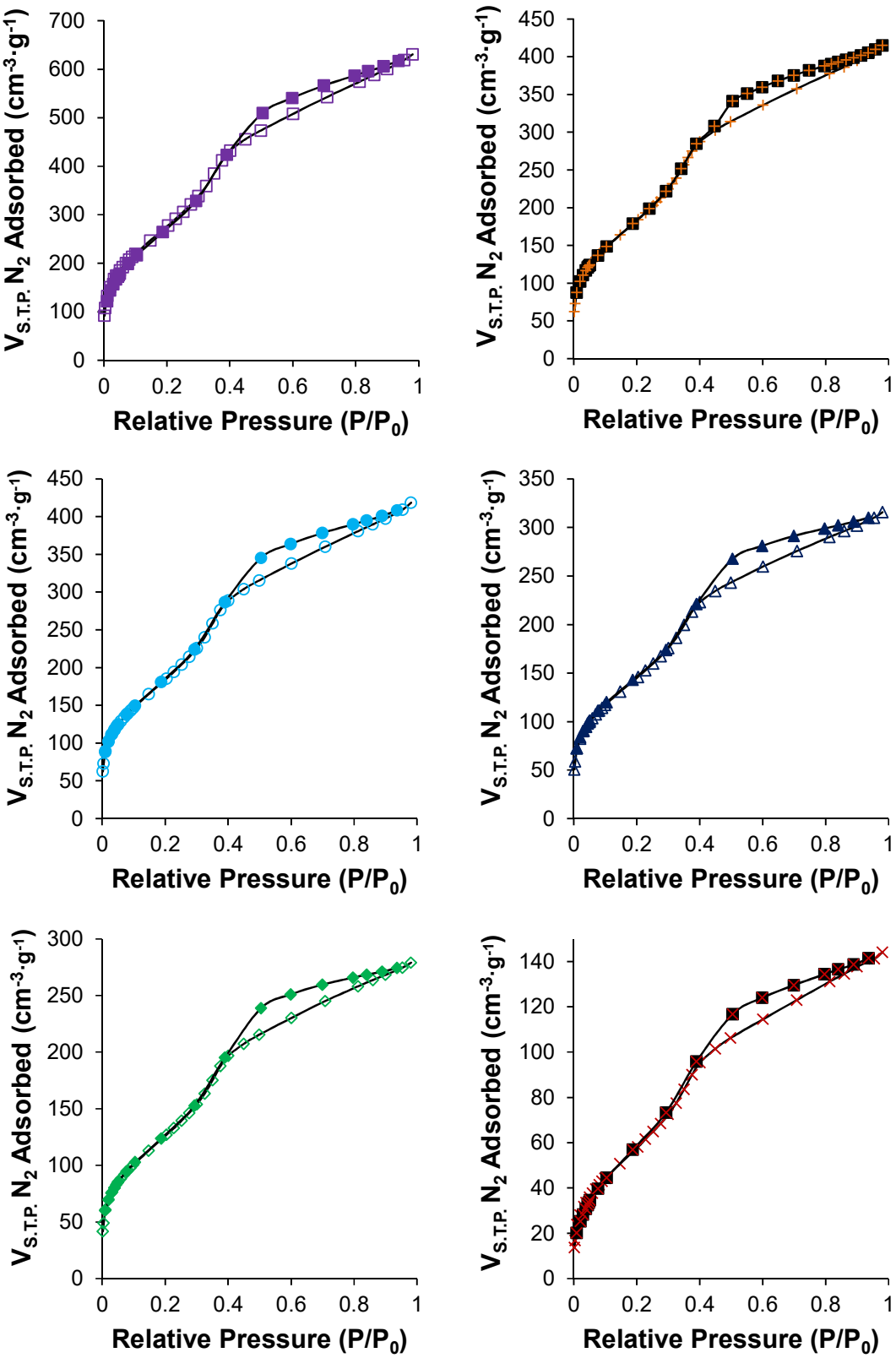

Figure B1.2. -196 °C N_2 adsorption desorption isotherms of $PhC_{18}PMO$ (□), Al-$PhC_{18}PMO$#2 (+), Al-$PhC_{18}PMO$#10 (○), Al-$PhC_{18}PMO$#20 (Δ), Al-$PhC_{18}PMO$#50 (◊) and Al-$PhC_{18}PMO$#100 (x). Empty symbols correspond to the adsorption and fully symbols correspond to desorption.

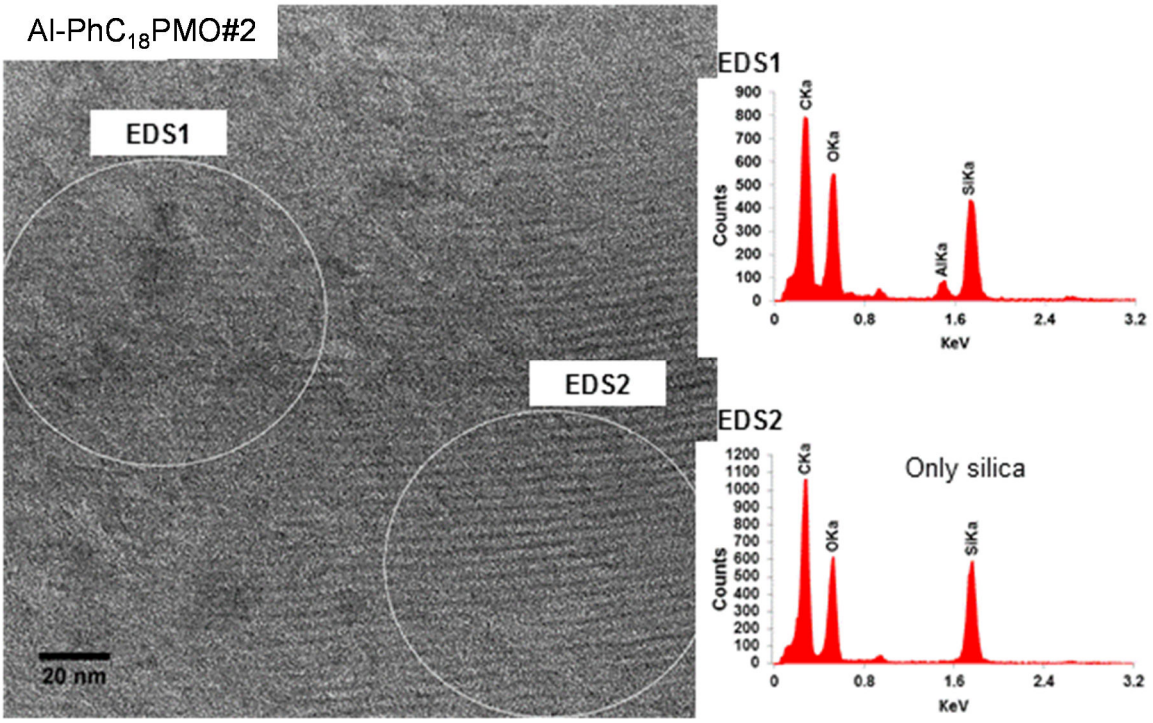
Al-PhC18PMO#2
EDS1
EDS2
20 nm
EDS1
Counts
CKa
OKa
AlKa
SiKa
KeV
EDS2
Only silica
Counts
CKa
OKa
SiKa
KeV

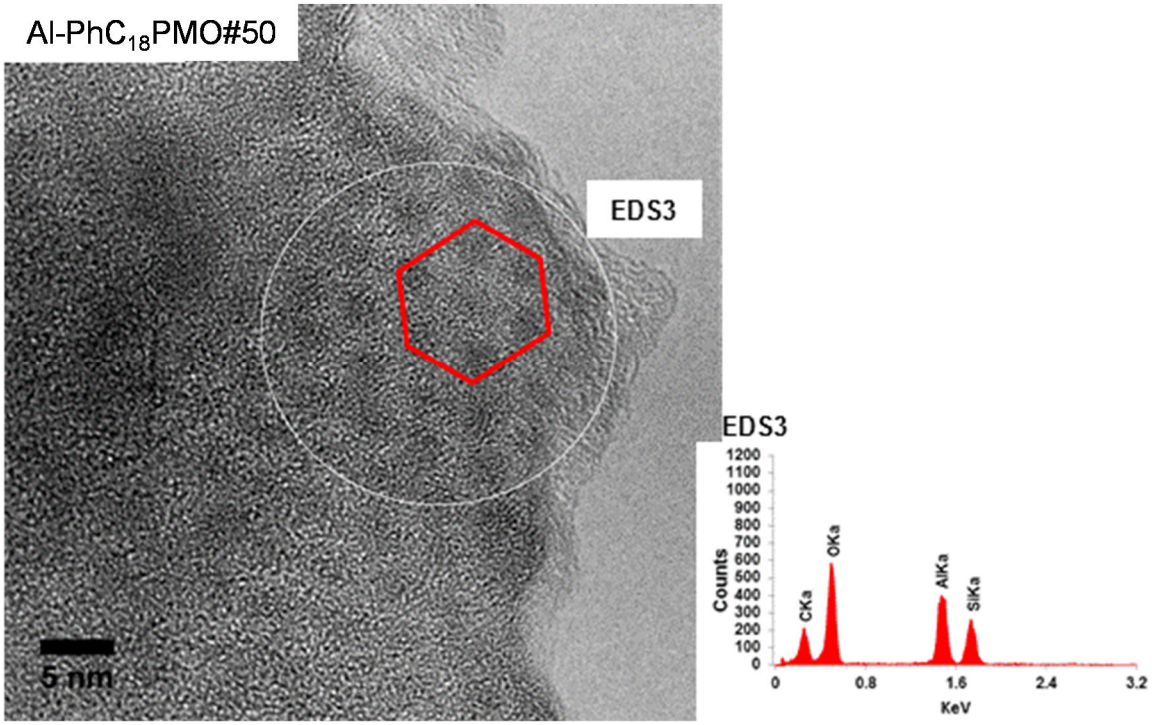
Al-PhC18PMO#50
EDS3
5 nm
EDS3
Counts
CKa
OKa
AlKa
SiKa
KeV

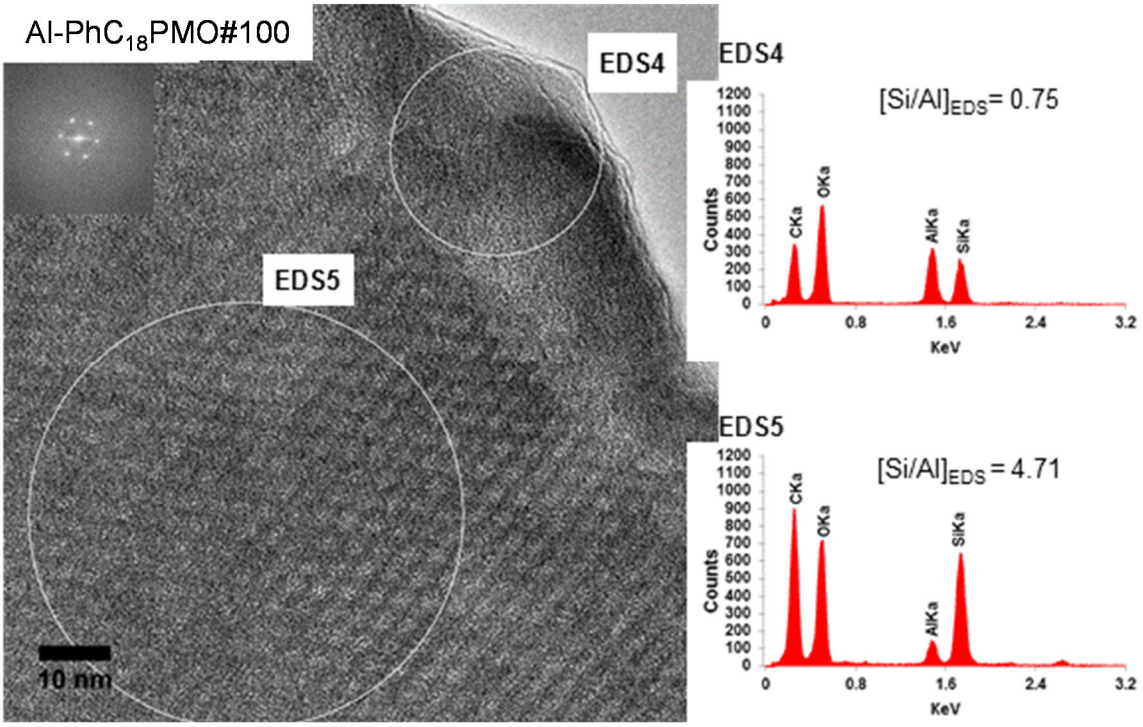

Figure B1.3. TEM images and EDS analyses of Al-PhC$_{18}$PMO#2, Al-PhC$_{18}$PMO#50 and Al-PhC$_{18}$PMO#100 composites.

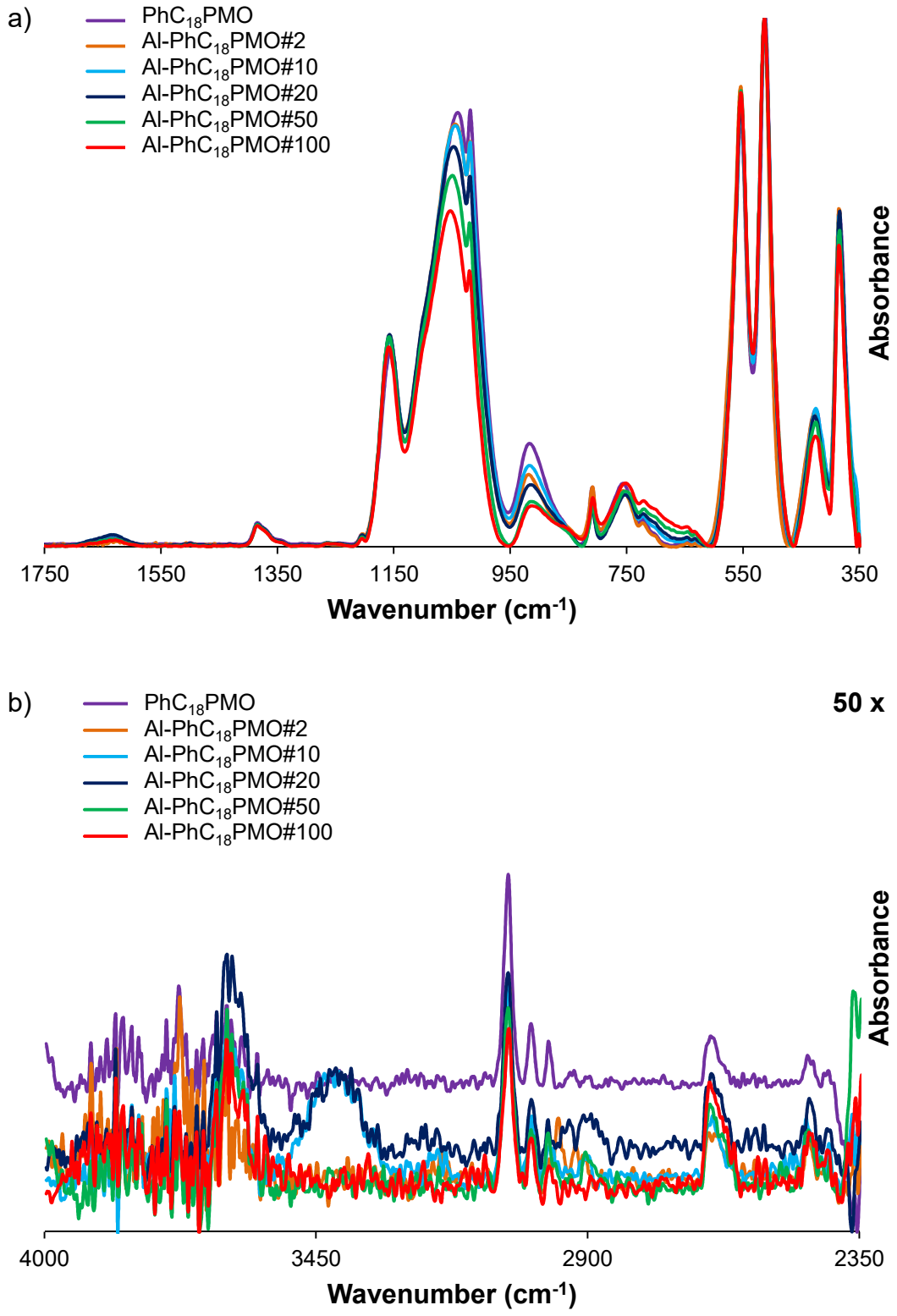

Figure B1.4. FTIR (ATR) spectra of $PhC_{18}PMO$, Al-$PhC_{18}PMO$#10, Al-$PhC_{18}PMO$#20, Al-$PhC_{18}PMO$#50 and Al-$PhC_{18}PMO$#100 in the range of a) 350-1750 cm^{-1} b) 2350-4000 cm^{-1}.

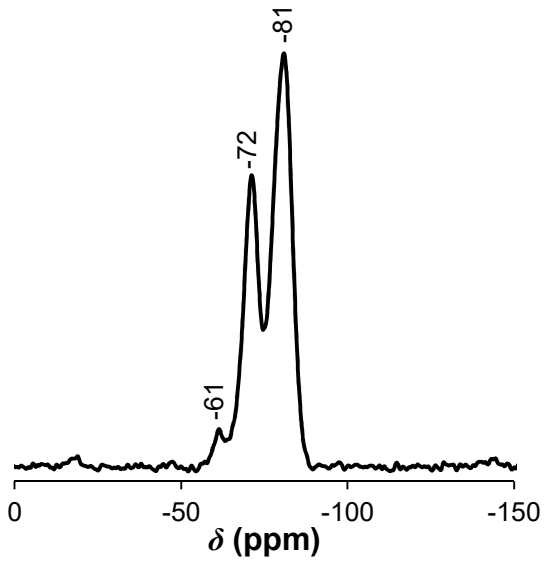

Figure B1.5. ^{29}Si CP-MAS NMR spectra of Al-PhC_{18}PMO#50.

Table B1.1. Percentage of T^m silanol species calculated from the fits of the ^{29}Si MAS NMR spectra.

PMO	% T^1	% T^2	% T^3
PhC_{18}PMO	3.89	37.31	58.80
Al-PhC_{18}PMO#50	3.38	33.10	63.52

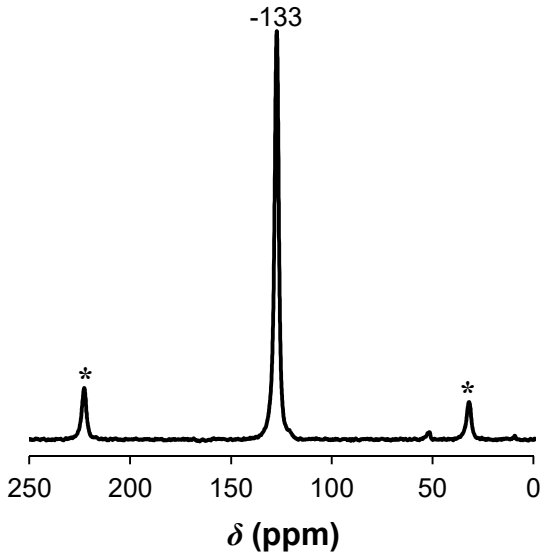

Figure B1.6. ^{13}C CP-MAS NMR spectra of Al-PhC_{18}PMO#50.

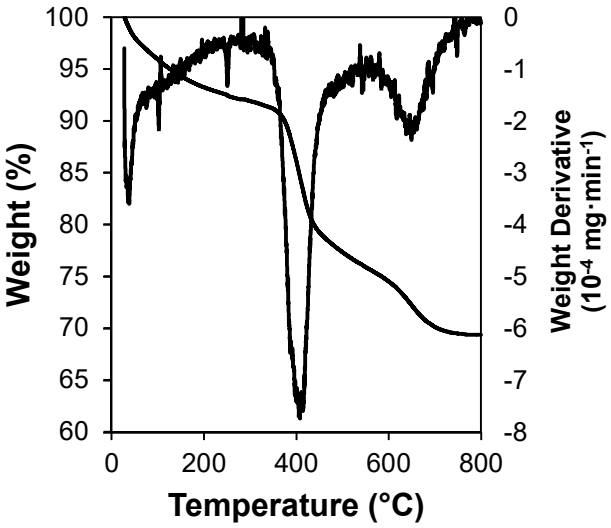

Figure B1.7. TGA of Al-PhC$_{18}$PMO#50 composite.

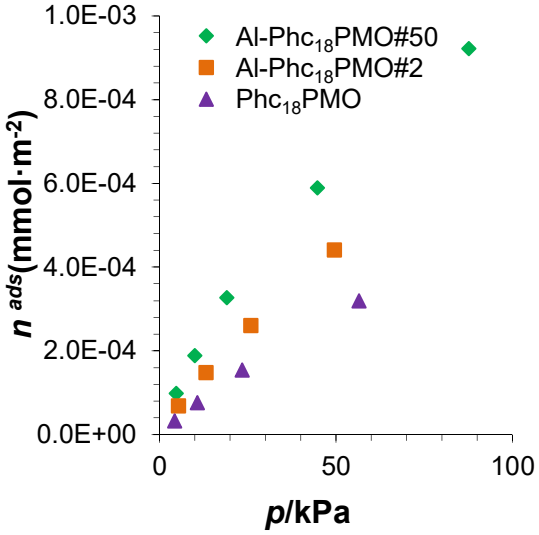

Figure B1.8. Carbon dioxide adsorption isotherms at 25 °C on the PhC$_{18}$PMO, Al-PhC$_{18}$PMO#2 and Al-PhC$_{18}$PMO#50, expressed by surface area (S_{BET}) of the material.

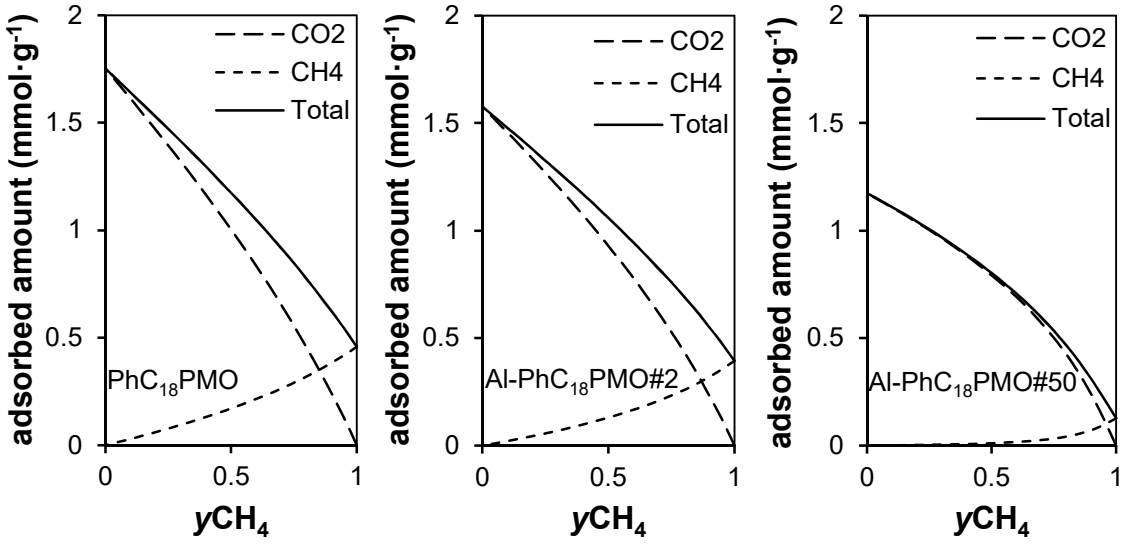

Figure B1.9. Adsorbed amounts of the CO_2/CH_4 mixture as a function of the CH_4 molar fraction in the gas phase, at 500 kPa and 25 °C, for $PhC_{18}PMO$ samples.

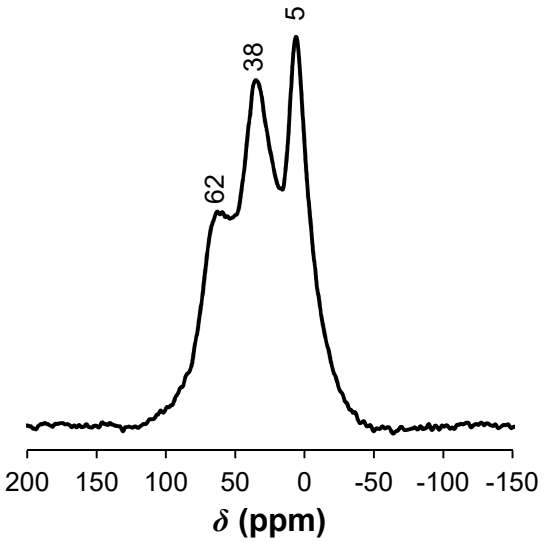

Figure B1.10. ^{27}Al MAS NMR spectrum of $PhC_{18}PMO+Al_2O_3$_a material mixture.

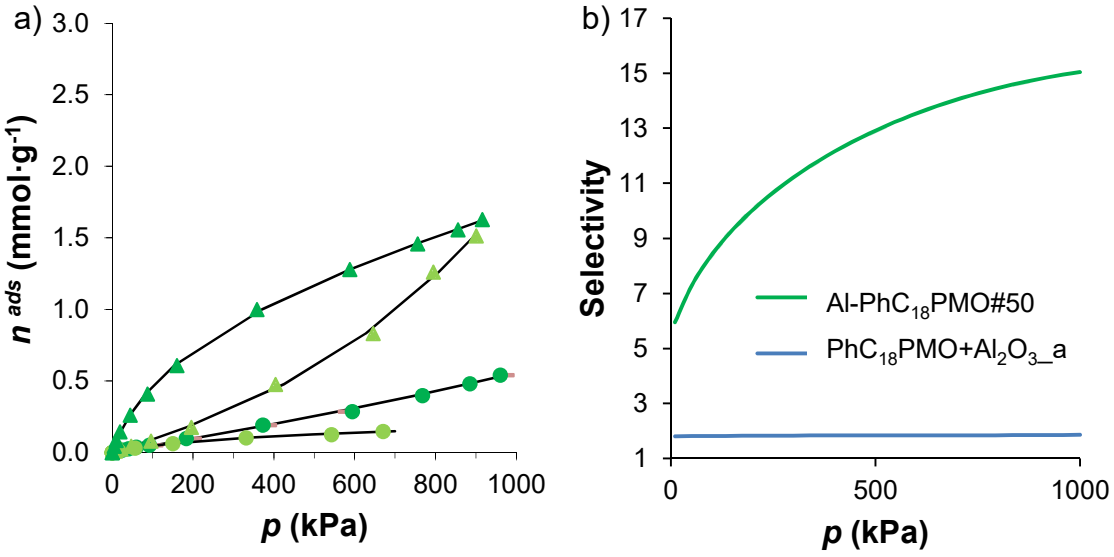

Figure B1.11. a) Carbon dioxide (triangles) and methane (circles) adsorption isotherms at 25 °C on the Al-PhC$_{18}$PMO#50 (dark green) and PhC$_{18}$PMO+Al$_2$O$_3$_a (light green). The lines represent the fitting of the virial equation. b) Average selectivity for the CO$_2$/CH$_4$ separation on the Al-PhC$_{18}$PMO#50 and PhC$_{18}$PMO+Al$_2$O$_3$_a.

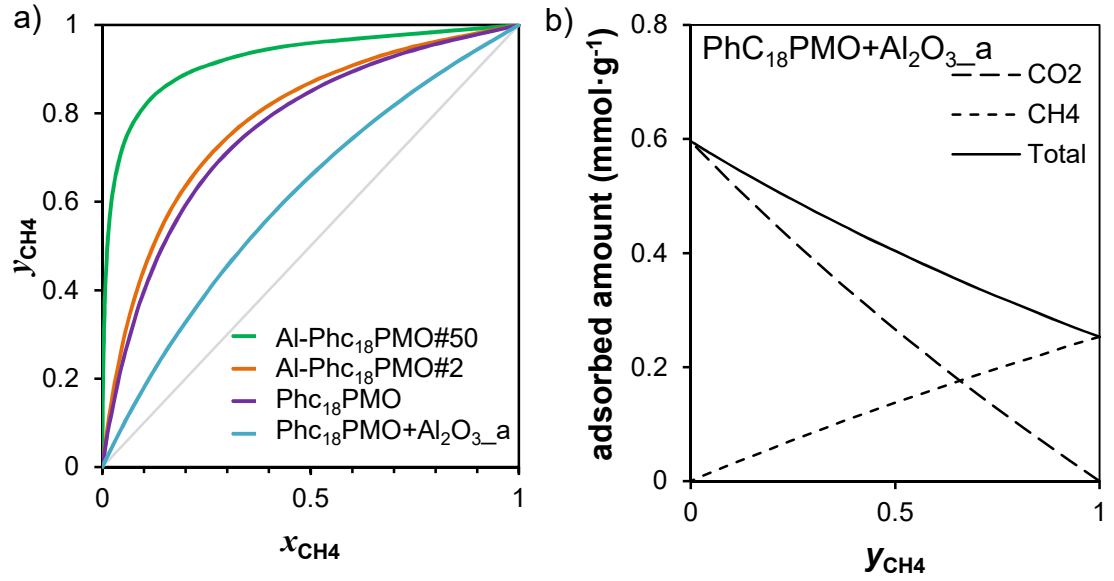

Figure B1.12. a) Isothermal (25 °C), isobaric (500 kPa) *xy* phase diagrams of the CO$_2$/CH$_4$ mixtures on the PhC$_{18}$PMO+Al$_2$O$_3$_a. y_{CH4} is the molar faction of methane in the gas phase; x_{CH4} is the molar faction of methane in the adsorbed phase and b) adsorbed amounts of the CO$_2$/CH$_4$ mixture as a function of the CH$_4$ molar fraction in the gas phase, at 500 kPa and 25 °C, for PhC$_{18}$PMO+Al$_2$O$_3$_a sample.

B2.1 Data from characterization of PMO materials of sub-chapter 4.2

Table B2.1. Physical properties of pyrolysed PMO materials.

Sample	d_{100} nm	S_{BET} $m^2 \cdot g^{-1}$	V_P $cm^3 \cdot g^{-1}$	V_{micro} $cm^3 \cdot g^{-1}$	d_P[a] nm
$PhC_{18}PMO$	4.65	782	0.68	-	3.70
$PhC_{18}PMO\_P800$	4.09	771	0.66	-	3.02
Pyrolysed phenylene-PMOs					
$PhC_{12}PMO$	3.59	1004	0.14	-	2.54
$PhC_{12}PMO$-AS_P800	3.29	830	0.48	0.14	2.11
$PhC_{12}PMO\_P800$	3.27	772	0.45	0.16	2.18
$PhC_{12}PMO\_P1200$	-	668	0.48	0.09	-
$NH_2PhC_{12}PMO\_P800$	3.25	606	0.31	0.14	-
Pyrolysed phenylene-PMOs					
$BphC_{18}PMO$	4.96	756	0.78	-	3.27
$BphC_{18}PMO$-AS_P800	4.12	711	0.48	0.01	2.54
$BphC_{18}PMO\_P800$	4.20	803	0.56	0.003	2.54
$BphC_{18}PMO$-H_2SO_4_P800	4.43	695	0.46	0.04	2.54
$BphC_{18}PMO\_P1200$	4.01	751	0.48	0.06	2.41

[a]Pore width obtained from the BJH method with the corrected Kelvin equation, *i.e.* KJS–BJH method at the maximum of Pore Size Distribution calculated on the basis of adsorption data.

Sample	Lateral view of the channels	Top view of the channels
Pyrolised phenylene-PMOs		
PhC$_{18}$PMO_P800	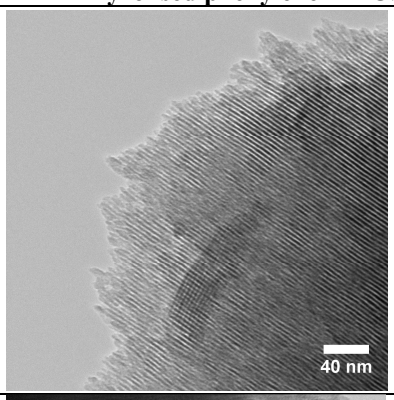	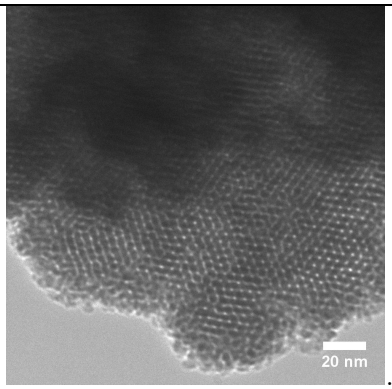
PhC$_{12}$PMO_AS_P800	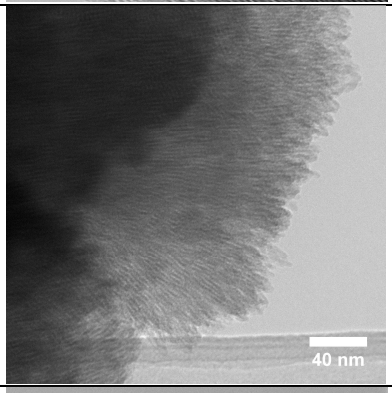	No evidences found
PhC$_{12}$PMO_P800	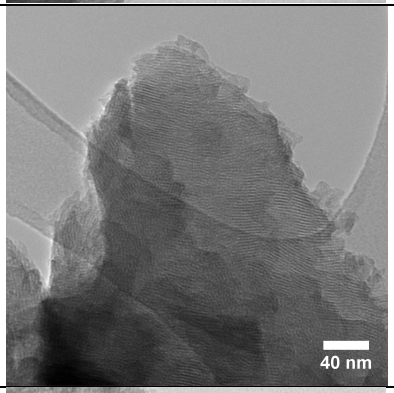	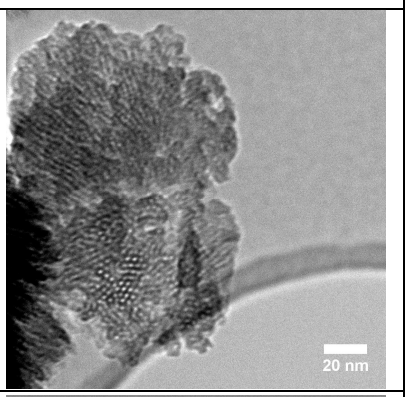
PhC$_{12}$PMO_P1200	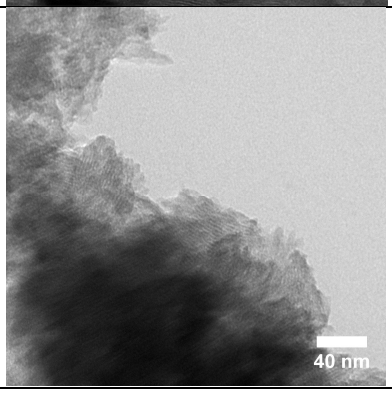	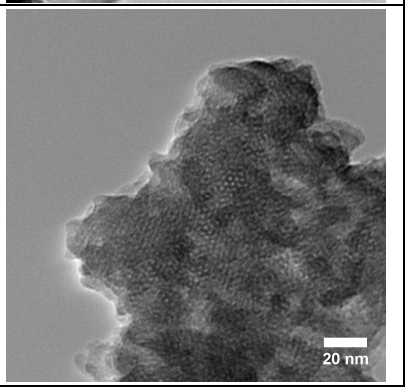

$NH_2PhC_{12}PMO\_P800$	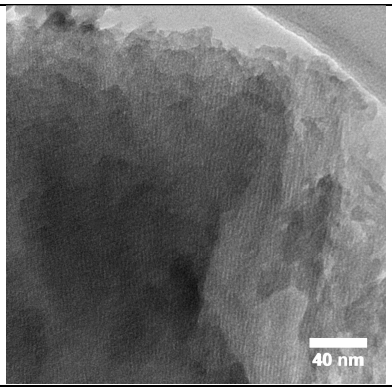	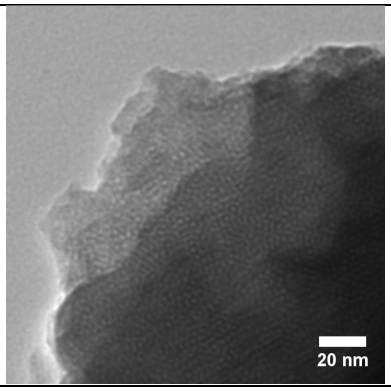
Pyrolysed biphenylene-PMOs		
$BphC_{18}PMO\_AS\_P800$	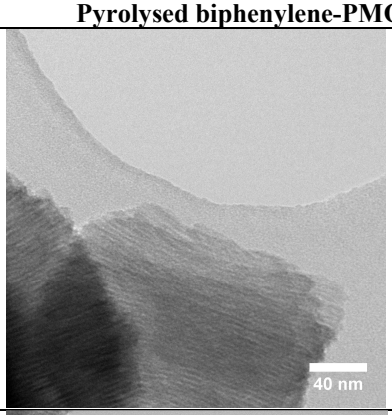	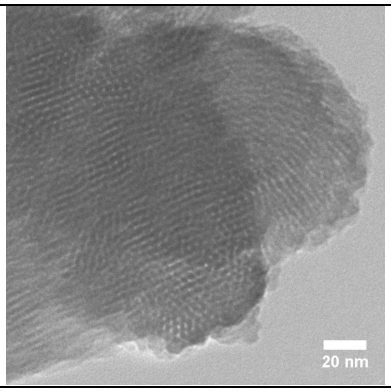
$BphC_{18}PMO\_P800$	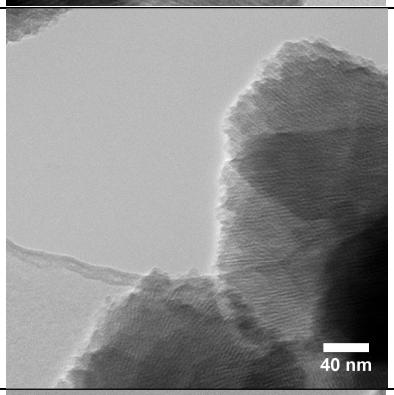	No evidences found
$BphC_{18}PMO\text{-}H_2SO_4\_P800$	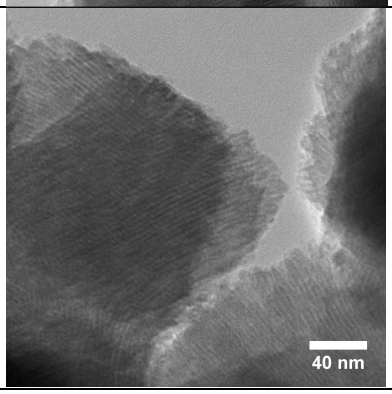	No evidences found

BphC$_{18}$PMO_P1200	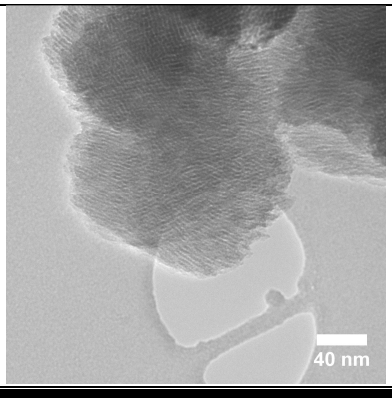	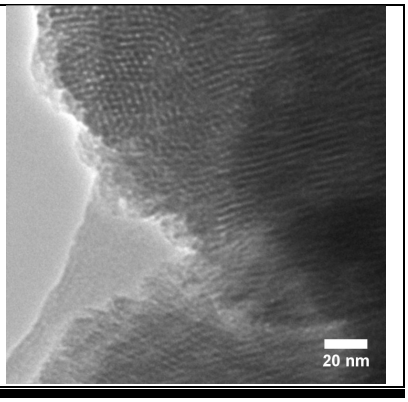

Figure B2.1. TEM images of carbonized PMO materials.

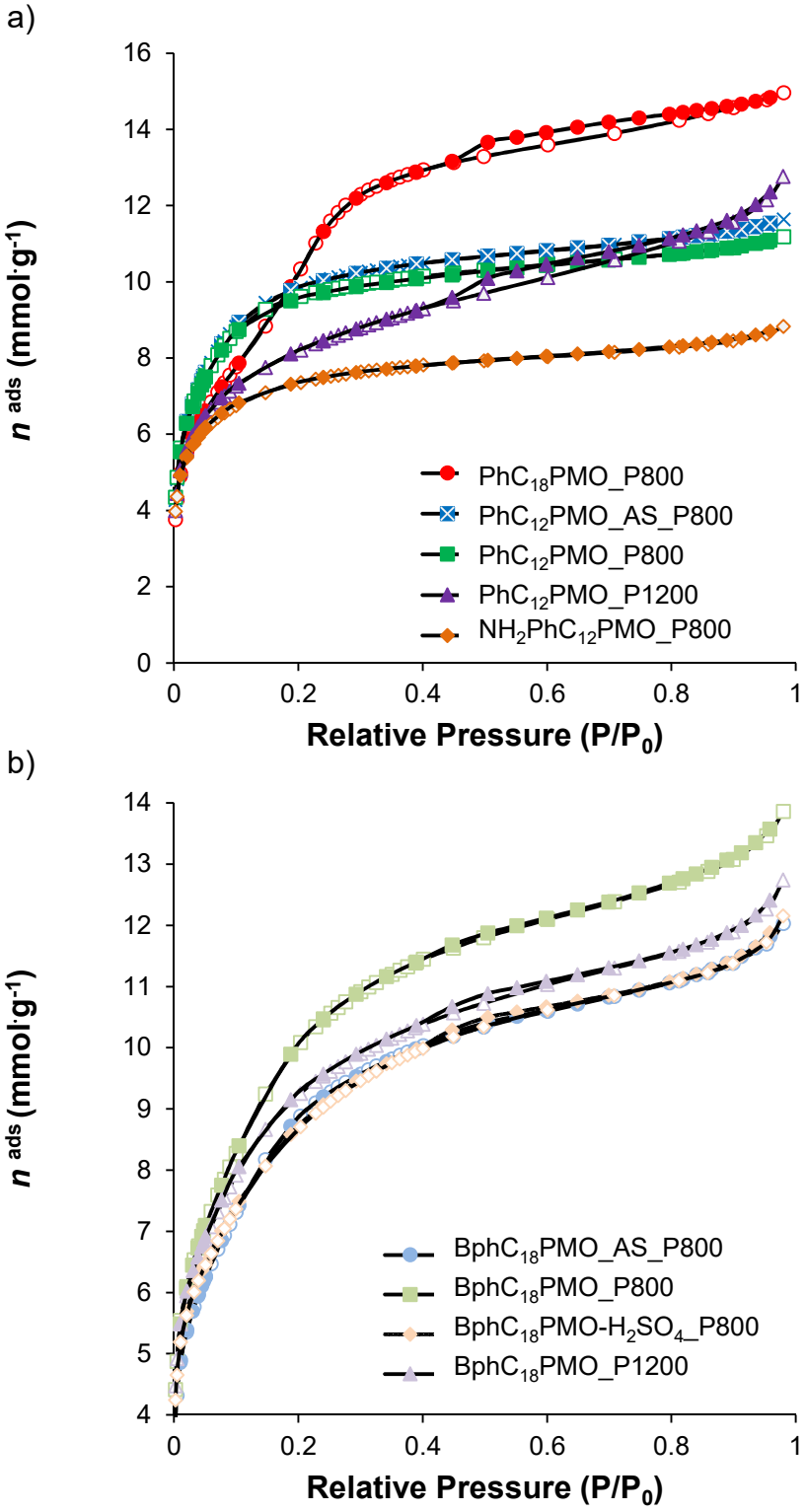

Figure B2.2. -196 °C N_2 adsorption-desorption isotherms of carbonized PMOs (adsorption – empty symbol; desorption – fully symbol)).

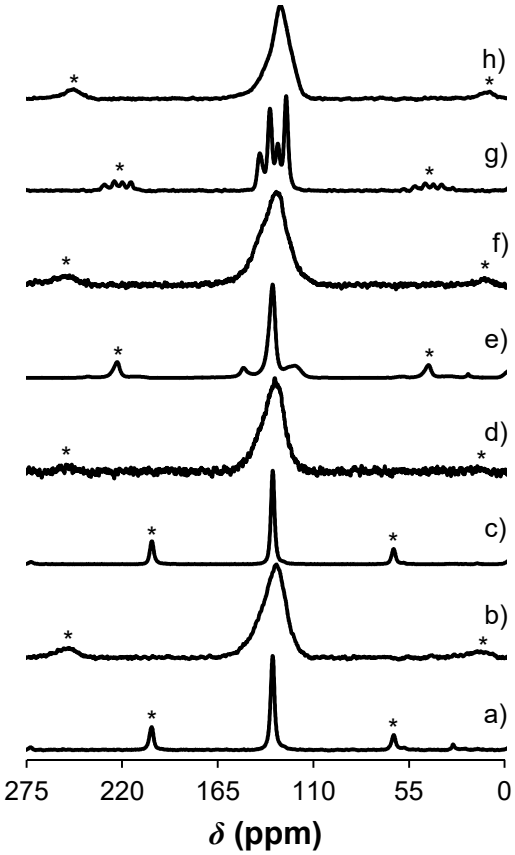

Figure B2.3. ^{13}C CP-MAS NMR spectra of carbonized adsorbents: a) $PhC_{18}PMO$, b) $PhC_{18}PMO\_P800$, c) $PhC_{12}PMO$, d) $PhC_{12}PMO\_P800$, e) $NH_2PhC_{12}PMO$, f) $NH_2PhC_{12}PMO\_P800$, g) $BphC_{18}PMO$ and h) $BphC_{18}PMO\_P800$. Asterisks represents the lateral side bands.

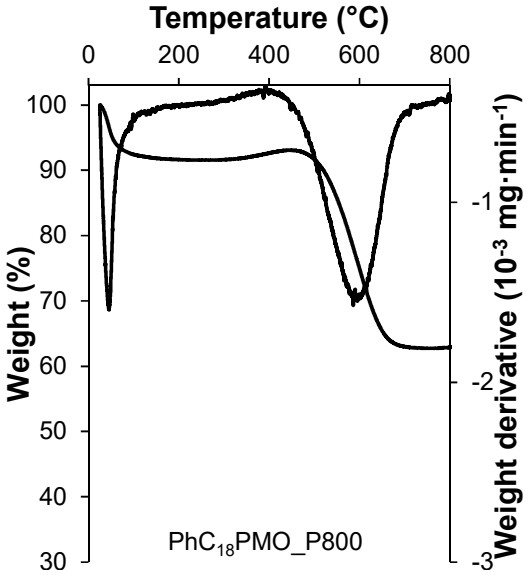
Temperature (°C)
0
200
400
600
800
Weight (%)
100
90
80
70
60
50
40
30
Weight derivative (10^{-3} mg·min^{-1})
-1
-2
-3
$PhC_{18}PMO\_P800$

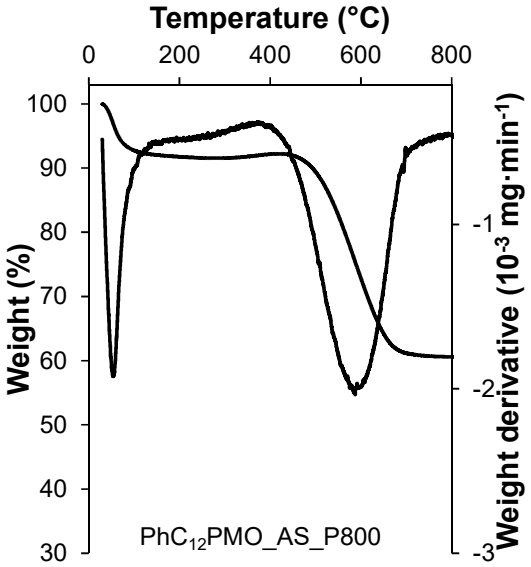
Temperature (°C)
0
200
400
600
800
Weight (%)
100
90
80
70
60
50
40
30
Weight derivative (10^{-3} mg·min^{-1})
-1
-2
-3
$PhC_{12}PMO\_AS\_P800$

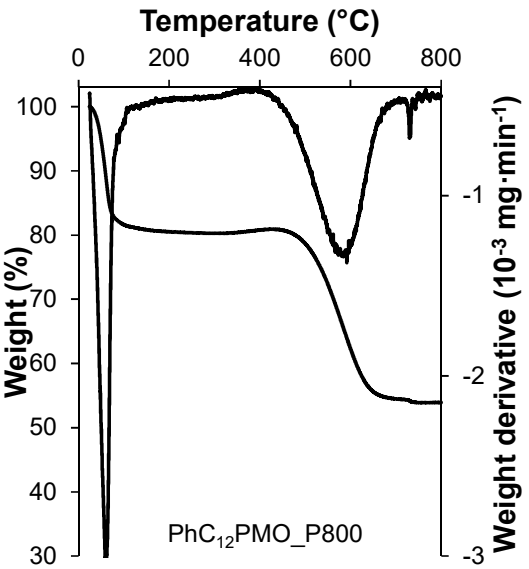
Temperature (°C)
0
200
400
600
800
Weight (%)
100
90
80
70
60
50
40
30
Weight derivative (10^{-3} mg·min^{-1})
-1
-2
-3
$PhC_{12}PMO\_P800$

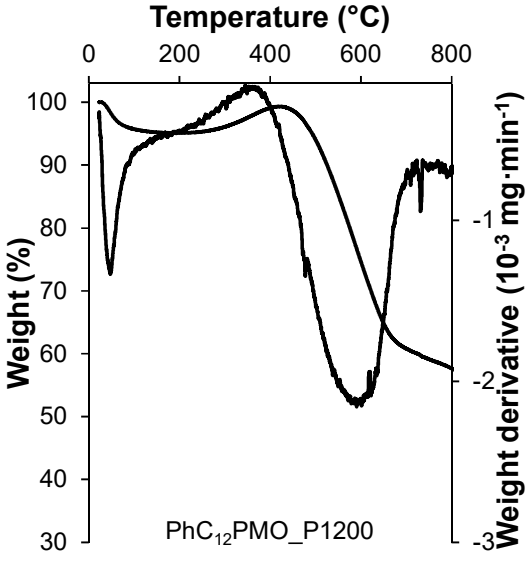
Temperature (°C)
0
200
400
600
800
Weight (%)
100
90
80
70
60
50
40
30
Weight derivative (10^{-3} mg·min^{-1})
-1
-2
-3
$PhC_{12}PMO\_P1200$

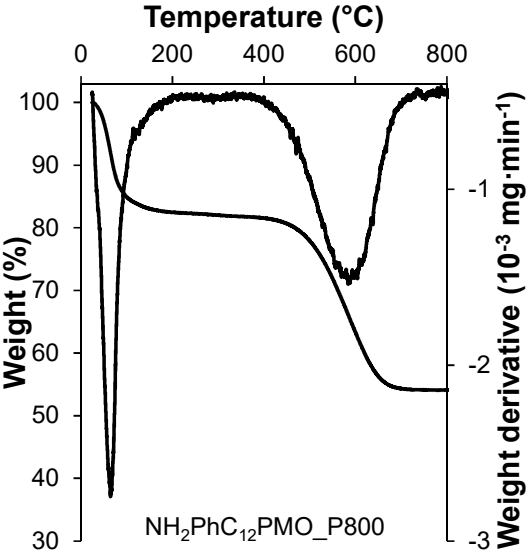
Temperature (°C)
0
200
400
600
800
Weight (%)
100
90
80
70
60
50
40
30
Weight derivative (10^{-3} mg·min^{-1})
-1
-2
-3
$NH_2PhC_{12}PMO\_P800$

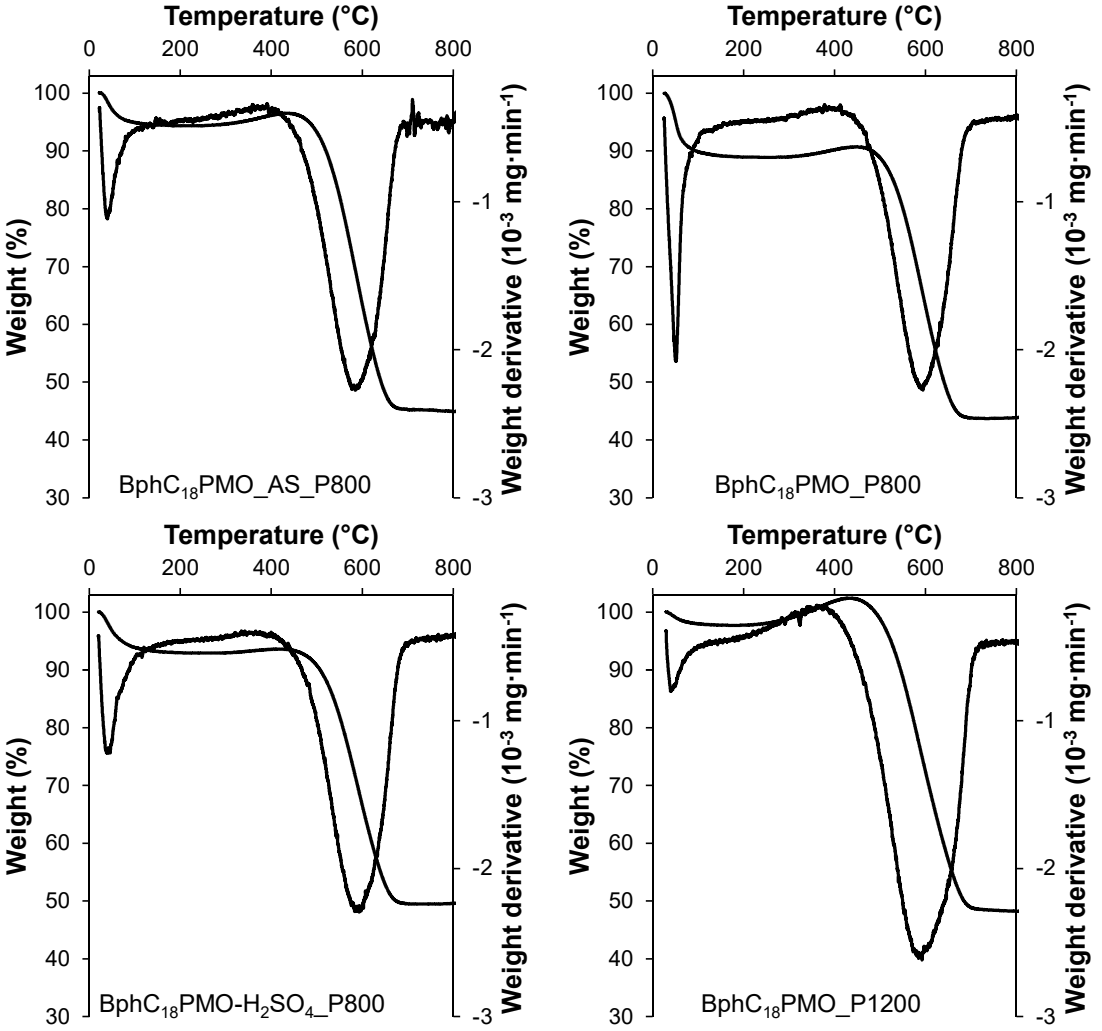

Figure B2.4. TGA analyses of pyrolysed PMO materials.

Table B2.2. Elemental analyses of pyrolysed PMOs.

	Sample	% C	% H	% N
Pyrolysed phenylene-PMOs	$PhC_{18}PMO\_P800$	32.43	0.71	-
	$PhC_{12}PMO\_AS\_P800$	27.97	3.20	0.01
	$PhC_{12}PMO\_P800$	30.48	0.52	-
	$PhC_{12}PMO\_P1200$	29.85	2.64	-
	$NH_2PhC_{12}PMO\_P800$	25.25	2.53	1.19
Pyrolysed biphenylene-PMOs	$BphC_{18}PMO\_AS\_P800$	44.19	2.75	0.02
	$BphC_{18}PMO\_P800$	47.70	1.04	-
	$BphC_{18}PMO\text{-}H_2SO_4\_P800$	41.50	1.11	-
	$BphC_{18}PMO\_P1200$	45.55	2.72	-

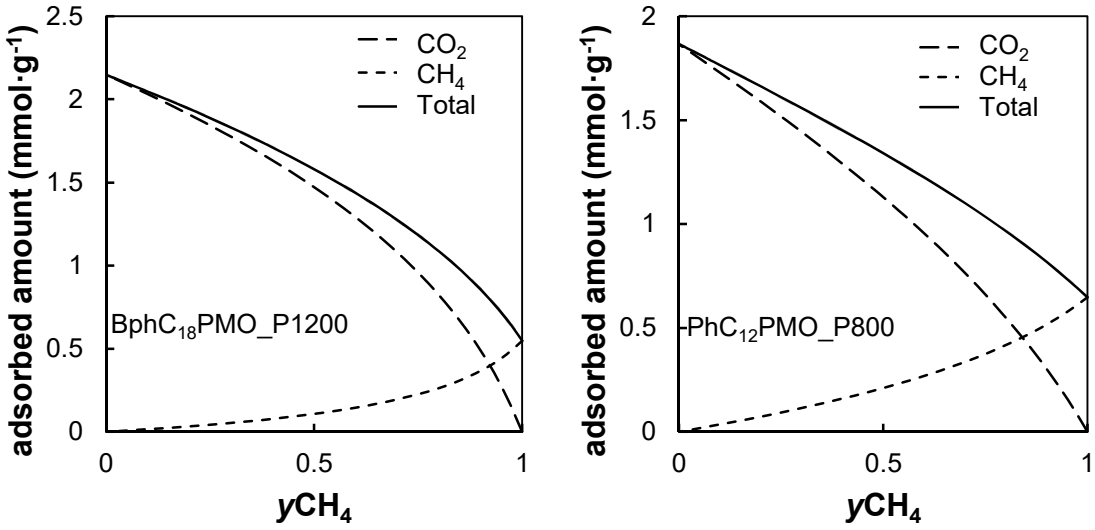

Figure B2.5. Adsorbed amounts of the CO_2/CH_4 mixture as a function of the CH_4 molar fraction in the gas phase, at 500 kPa and 25 °C, for carbonized PMO materials.

Appendix C

C1.1 Data from characterization of PMO materials of sub-chapter 5.1

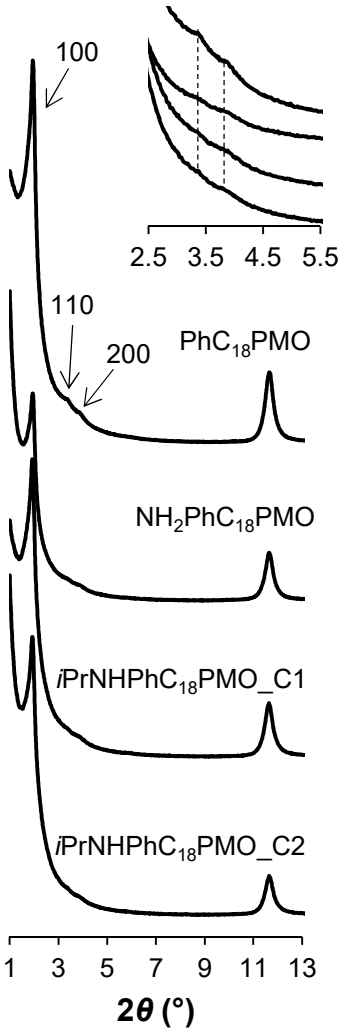

Figure C1.1. X-ray diffraction patterns of $PhC_{18}PMO$, $NH_2PhC_{18}PMO$, *i*$PrNHPhC_{18}PMO$_C1 and *i*$PrNHPhC_{18}PMO$_C2. The inset displays the magnified patterns in the 2θ region from 2.5 to 5.5°.

Table C1.1. Physical properties of PMO, NH_2-PMO, *i*Pr-NH-PMO_int and *i*Pr-NH-PMO.

Sample	d_{100} (nm)	S_{BET} ($m^2 \cdot g^{-1}$)	V_P ($cm^3 \cdot g^{-1}$)	d_P[a] (nm)	b[b] (nm)
$PhC_{18}PMO$	4.48	782	0.63	3.55	1.62
$NH_2PhC_{18}PMO$	4.53	719	0.51	3.55	1.68
***i*$PrNHPhC_{18}PMO$_C1**	4.53	693	0.50	3.41	1.82
***i*$PrNHPhC_{18}PMO$_C2**	4.53	698	0.53	3.41	1.82

[a]Pore width obtained from the maximum on the BJH pore size distribution calculated on the basis of adsorption data. [b]Pore wall thickness calculated as ($2d_{100}/\sqrt{3} - d_P$), where the first term is the unit cell parameter.

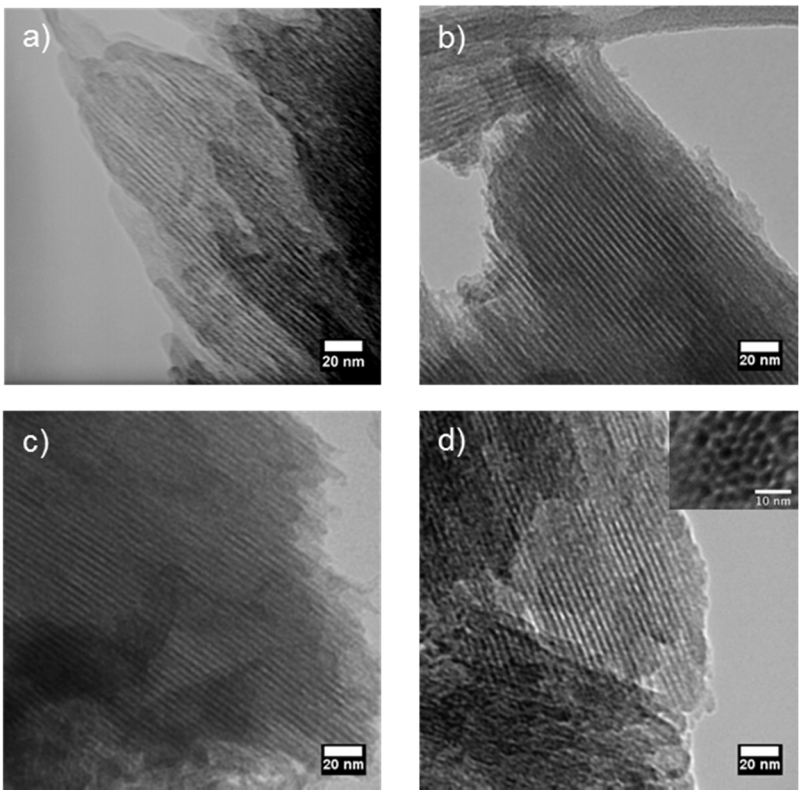

Figure C1.2. TEM micrographs of: a) $PhC_{18}PMO$, b) $NH_2PhC_{18}PMO$, c) *i*$PrNHPhC_{18}PMO$_C1 and d) *i*$PrNHPhC_{18}PMO$_C2 (the inset displays a micrograph where the hexagonal arrangement of pores can be seen).

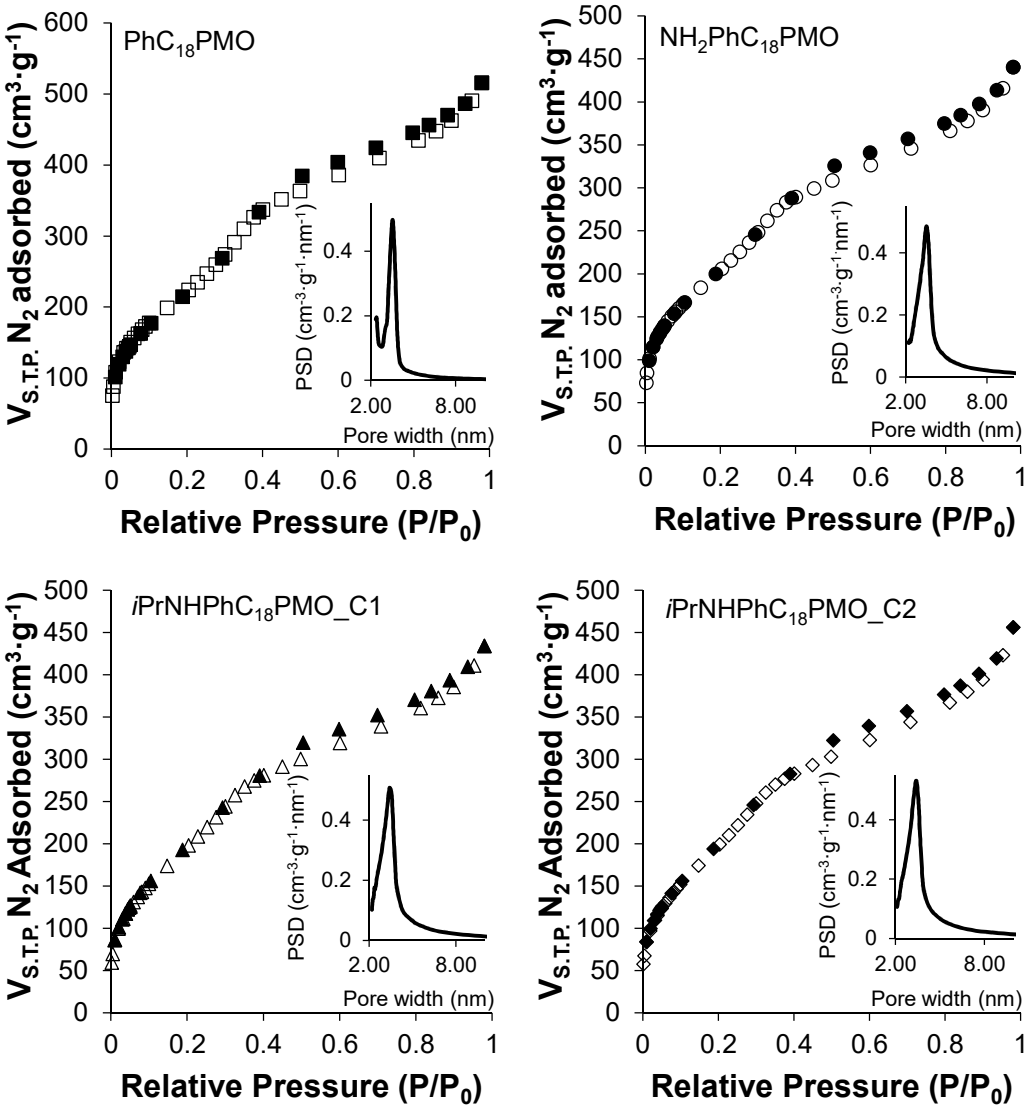

Figure C1.3. -196 °C N_2 isotherms of $PhC_{18}PMO$ ((□) adsorption; (■) desorption)), $NH_2PhC_{18}PMO$ ((○) adsorption; (●) desorption)), *i*PrNHPhC$_{18}$PMO_C1 ((Δ) adsorption; (▲) desorption)) and *i*PrNHPhC$_{18}$PMO_C2 ((◊) adsorption; desorption (♦)).

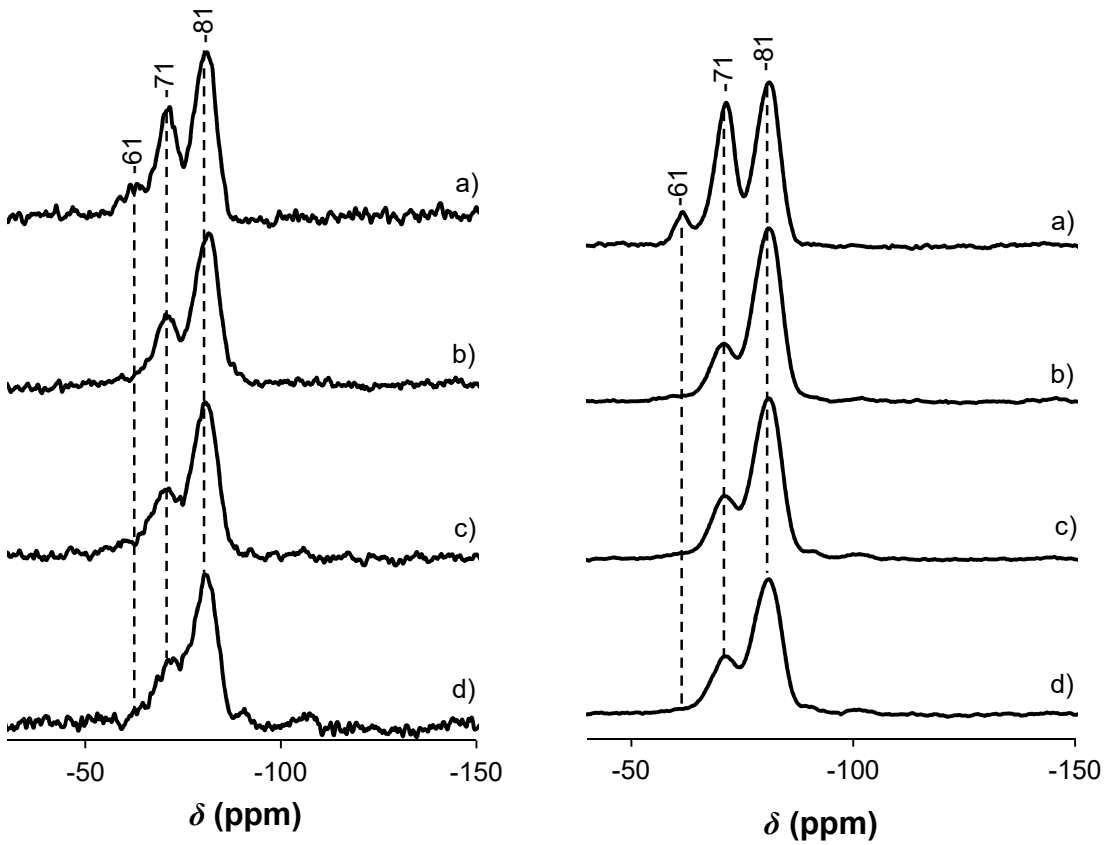

Figure C1.4. ^{29}Si MAS (left) and CP-MAS (right) NMR spectra of a) $PhC_{18}PMO$, b) $NH_2PhC_{18}PMO$, c) *i*PrNHPhC_{18}PMO_C1 and d) *i*PrNHPhC_{18}PMO_C2.

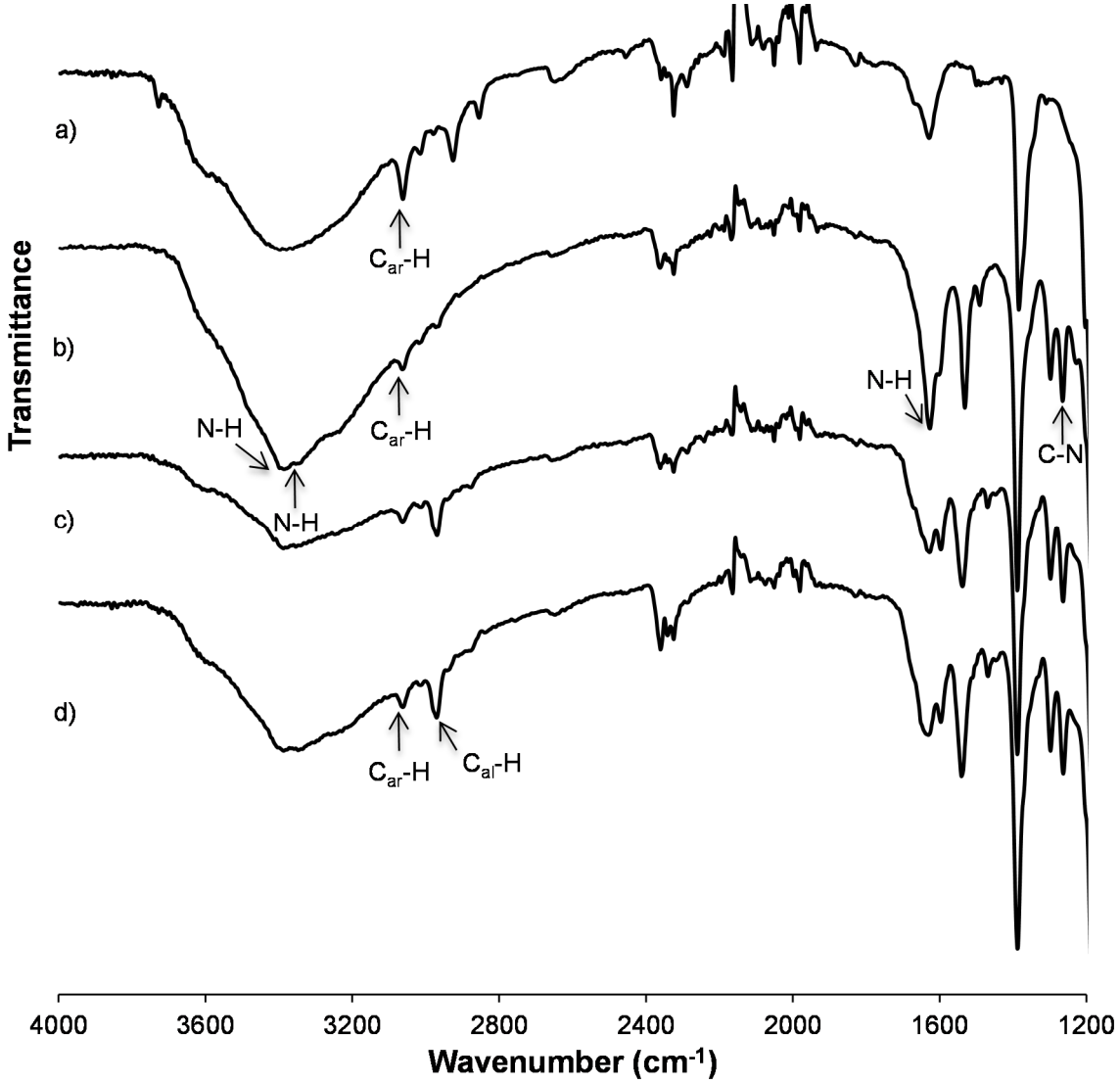

Figure C1.5. FTIR (ATR) spectra of a) $PhC_{18}PMO$, b) $NH_2PhC_{18}PMO$, c) *i*$PrNHPhC_{18}PMO$_C1 and d) *i*$PrNHPhC_{18}PMO$_C2 in the range of 1200 - 4000 cm^{-1} (C_{ar} and C_{al} despite for aromatic and aliphatic carbons, respectively).

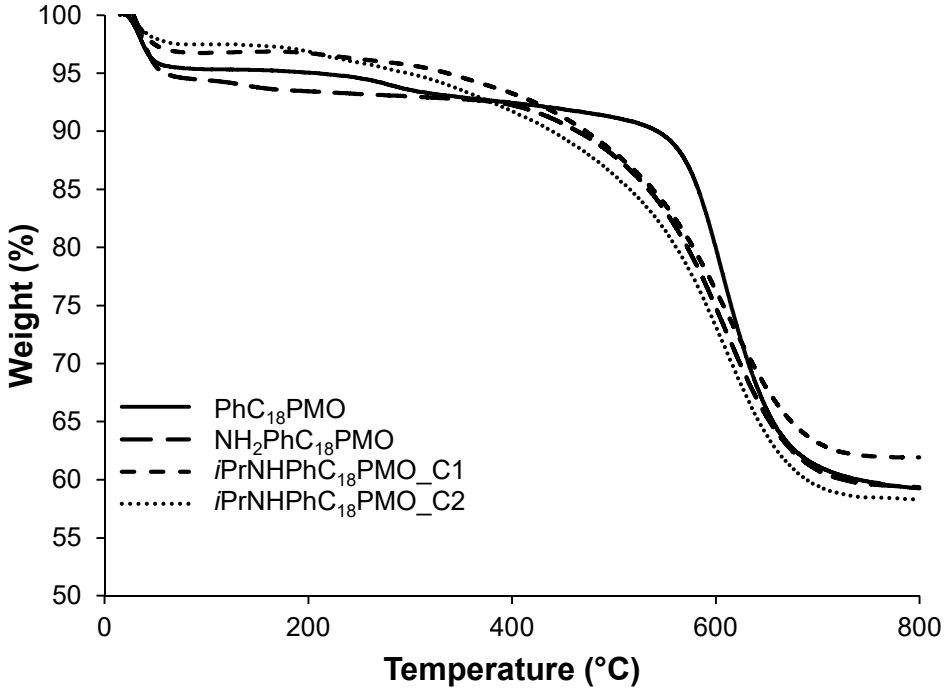

Figure C1.6. TGA of $PhC_{18}PMO$, $NH_2PhC_{18}PMO$, *i*PrNHPhC_{18}PMO_C1 and *i*PrNHPhC_{18}PMO_C2.

Table C1.2. Elemental analyses of $PhC_{18}PMO$, $NH_2PhC_{18}PMO$, *i*PrNHPhC_{18}PMO_C1 and *i*PrNHPhC_{18}PMO_C2.

Sample	% N	% C	% H
$PhC_{18}PMO$	0.10	38.89	2.75
$NH_2PhC_{18}PMO$	3.03	35.81	2.92
***i*PrNHPhC_{18}PMO_C1**	2.96	37.50	3.37
***i*PrNHPhC_{18}PMO_C2**	3.00	38.05	3.44

C2.1 Data from characterization of PMO materials of sub-chapter 5.2

Table C2.1. Physical properties of $PhC_{18}PMO$, $NH_2PhC_{18}PMO$ and alkylated $PhC_{18}PMO$ materials.

Sample	d_{100} (nm)	S_{BET} ($m^2 \cdot g^{-1}$)	V_P ($cm^3 \cdot g^{-1}$)	d_P[a] (nm)
$NH_2PhC_{18}PMO$	4.41	658	0.65	3.24
$(iPr)_2NPhC_{18}PMO$	4.55	552	0.56	3.18
$(NCCH_2CH_2)_2NPhC_{18}PMO$	4.65	575	0.61	3.24
$(HOOCCH_2CH_2)_2NPhC_{18}PMO$	4.50	524	0.59	3.18

[a]Pore width obtained from the BJH method with the corrected Kelvin equation, i.e. KJS–BJH method at the maximum of pore size distribution calculated on the basis of adsorption data.

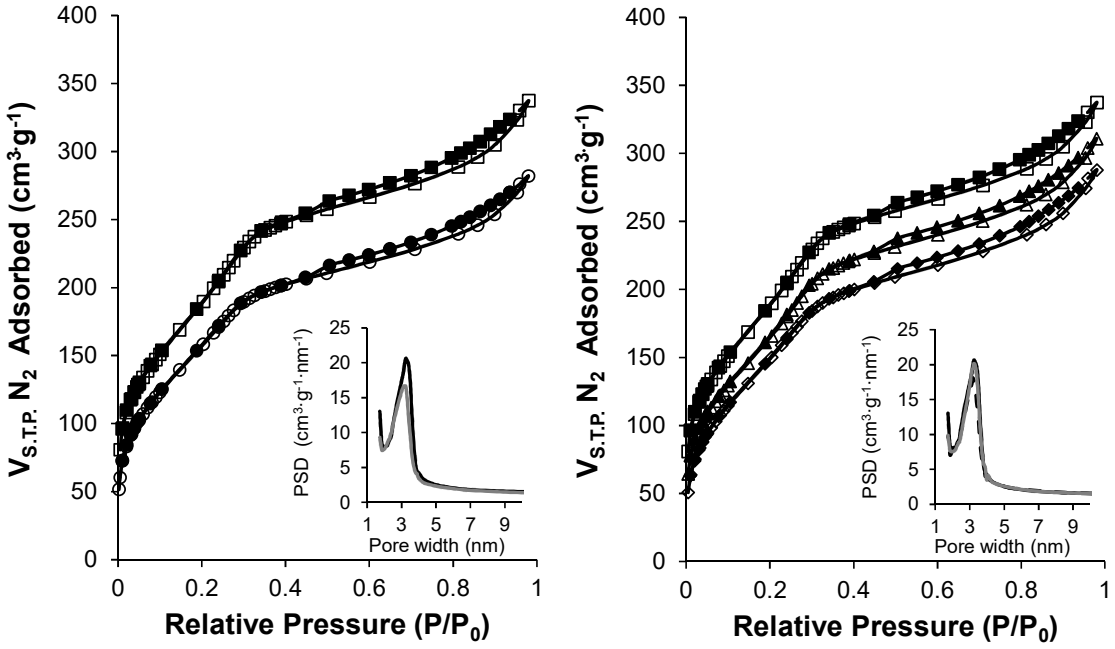

Figure C2.1. -196 °C N_2 isotherms of $NH_2PhC_{18}PMO$ ((□) adsorption; (■) desorption)), $(iPr)_2NPhC_{18}PMO$ ((○) adsorption; (●) desorption)), $(NCCH_2CH_2)_2NPhC_{18}PMO$ ((Δ) adsorption; (▲) desorption)) and $(HOOCCH_2CH_2)_2NPhC_{18}PMO$ ((◊) adsorption; desorption (♦)). The insets display the characteristic narrow PSD curves of PMO materials: $NH_2PhC_{18}PMO$ (black line), $(iPr)_2NPhC_{18}PMO$ and $(NCCH_2CH_2)_2NPhC_{18}PMO$ (grey line) and $(HOOCCH_2CH_2)_2NPhC_{18}PMO$ (dashed grey line).

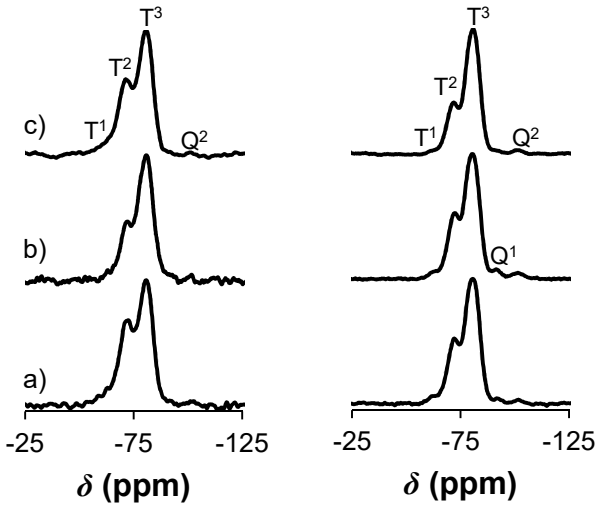

Figure C2.2. ^{29}Si MAS (left) and CP-MAS (right) NMR spectra of a) (iPr)$_2$NPhC$_{18}$PMO, b) (NCCH$_2$CH$_2$)$_2$NPhC$_{18}$PMO and c) (HOOCCH$_2$CH$_2$)$_2$NPhC$_{18}$PMO.

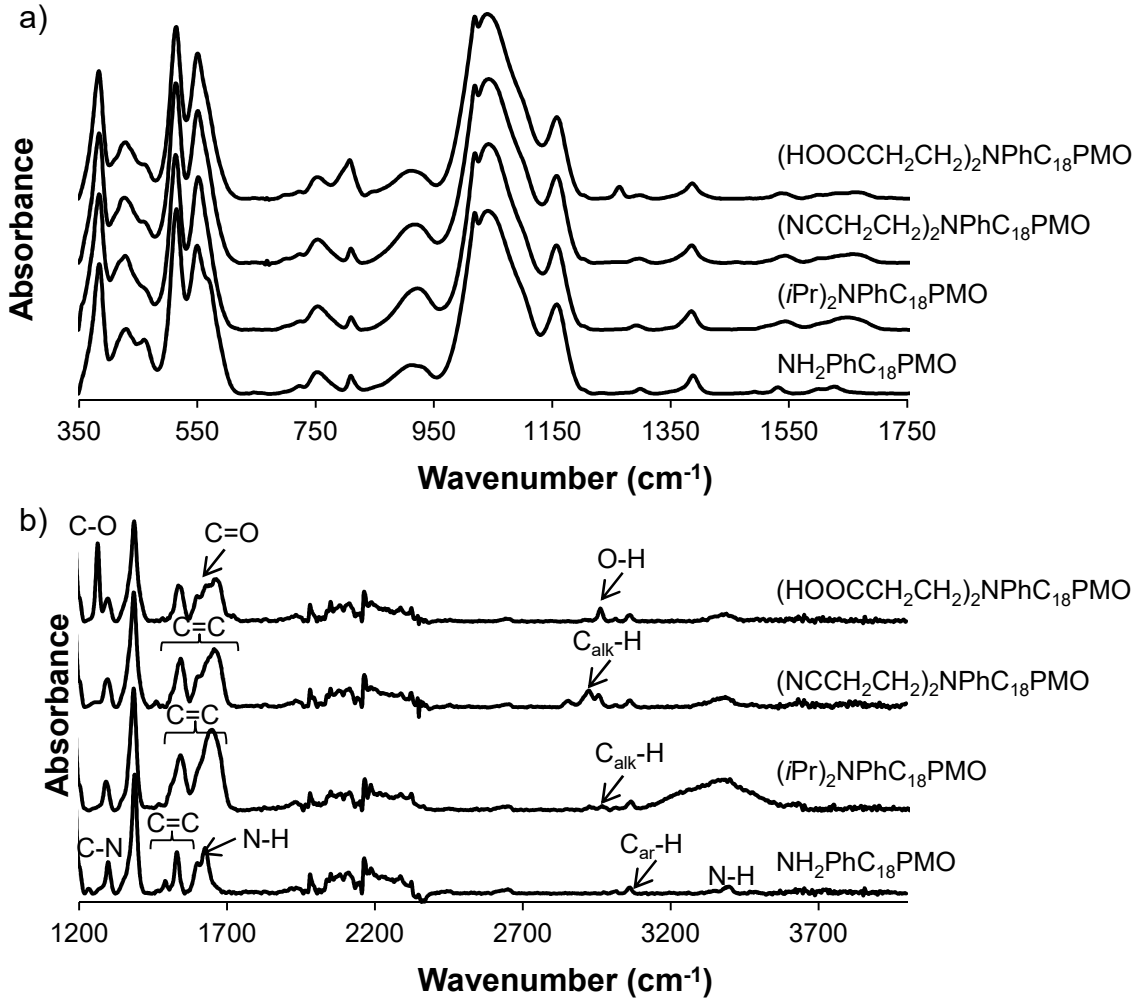

Figure C2.3. FTIR (ATR) spectra of $PhC_{18}PMO$, $NH_2PhC_{18}PMO$, (*i*Pr)$NHPhC_{18}PMO$, (*i*Pr)$_2NPhC_{18}PMO$, $(NCCH_2CH_2)_2NPhC_{18}PMO$ and $(HOOCCH_2CH_2)_2NPhC_{18}PMO$ in the range a) 350-1750 cm^{-1} and b) 1200-4000 cm^{-1}.

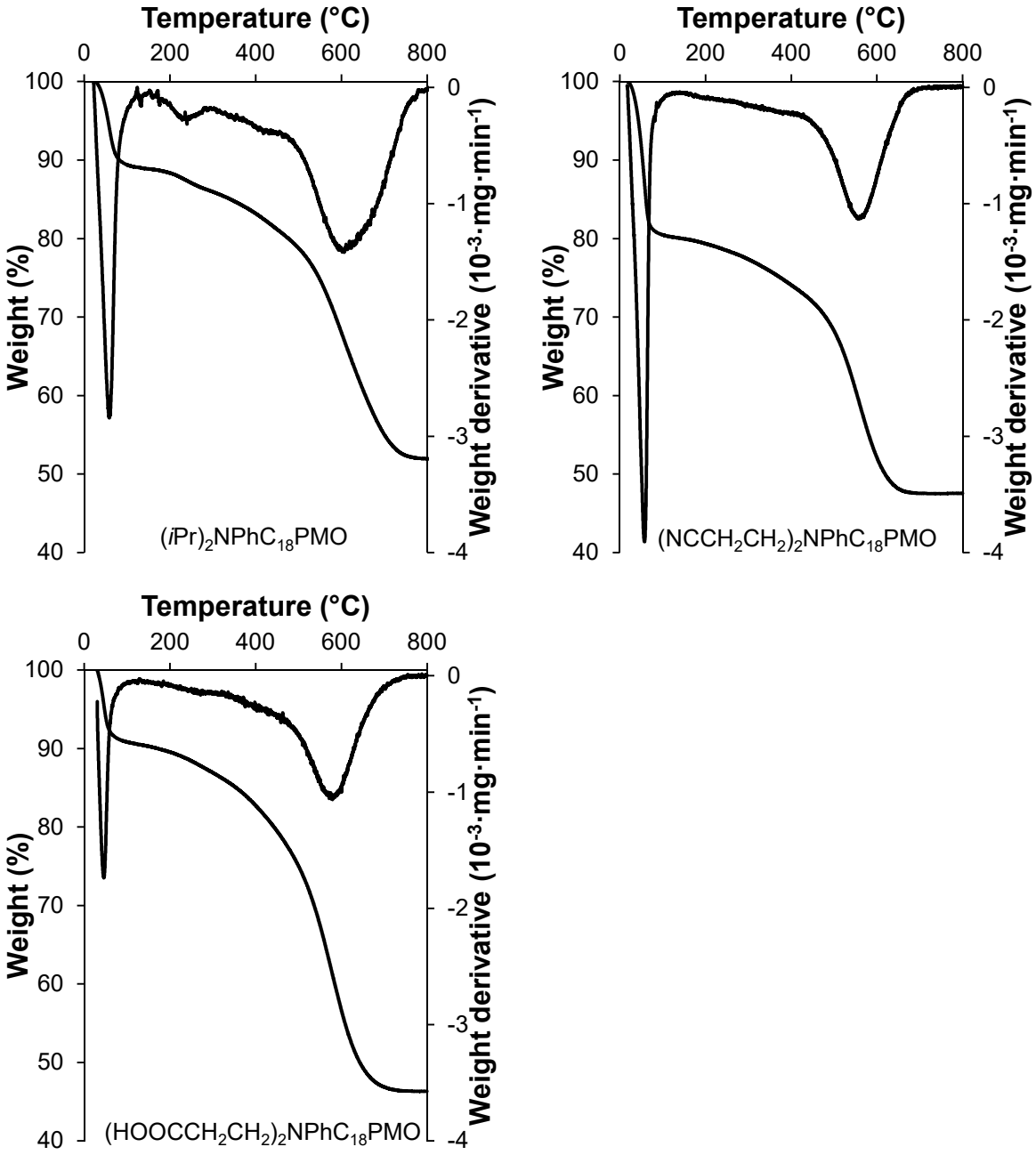

Figure C2.4. TGA of $(i\text{Pr})_2\text{NPhC}_{18}\text{PMO}$, $(\text{NCCH}_2\text{CH}_2)_2\text{NPhC}_{18}\text{PMO}$ and $(\text{HOOCCH}_2\text{CH}_2)_2\text{NPhC}_{18}\text{PMO}$.

Table C2.2. Elemental analyses of $PhC_{18}PMO$, $NH_2PhC_{18}PMO$, $(iPr)_2NPhC_{18}PMO$, $(NCCH_2CH_2)_2NPhC_{18}PMO$ and $(HOOCCH_2CH_2)_2NPhC_{18}PMO$.

Sample	% N	% C	% H
$NH_2PhC_{18}PMO$	2.54	35.32	2.60
$(iPr)_2NPhC_{18}PMO$	2.37	39.39	3.23
$(NCCH_2CH_2)_2NPhC_{18}PMO$	2.84	40.34	3.11
$(HOOCCH_2CH_2)_2NPhC_{18}PMO$	2.30	36.13	3.05

C3.1 Data from characterization of PMO materials of sub-chapter 5.3

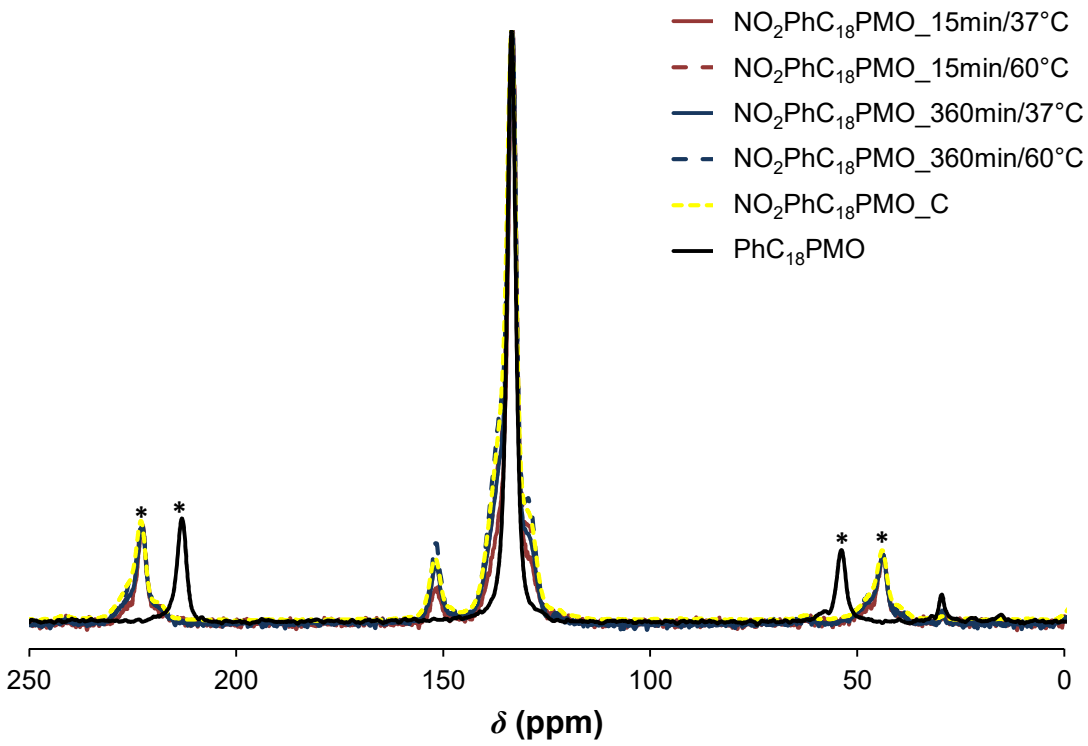

Figure C3.1. ^{13}C CP-MAS NMR spectra for $PhC_{18}PMO$ and $NO_2PhC_{18}PMO\_y/T$ samples obtained under different synthetic conditions. * denotes spinning sidebands.

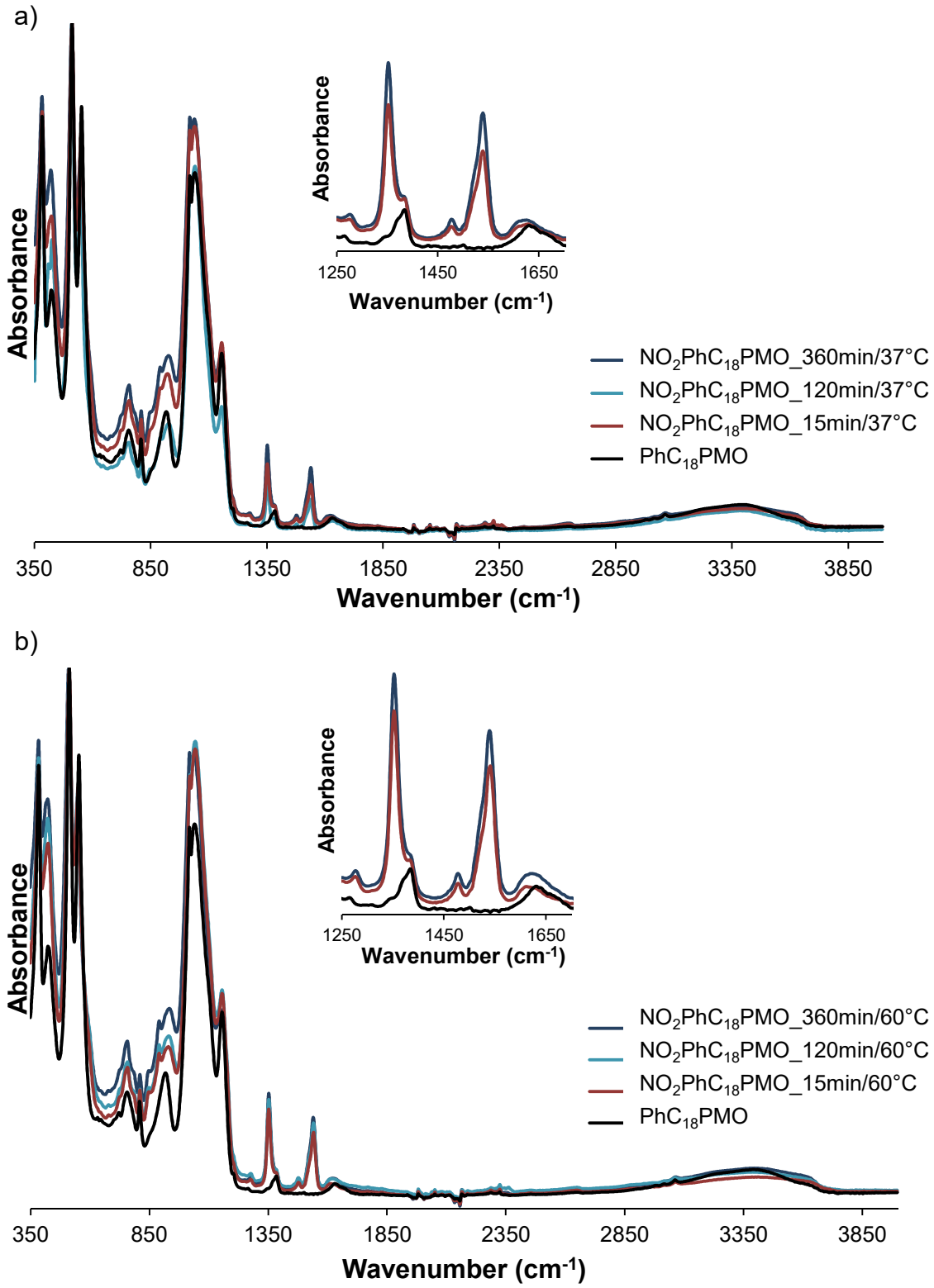
a)
Absorbance
Wavenumber (cm-1)
1250
1450
1650
NO2PhC18PMO_360min/37°C
NO2PhC18PMO_120min/37°C
NO2PhC18PMO_15min/37°C
PhC18PMO
350
850
1350
1850
2350
2850
3350
3850
b)
Absorbance
Wavenumber (cm-1)
NO2PhC18PMO_360min/60°C
NO2PhC18PMO_120min/60°C
NO2PhC18PMO_15min/60°C
PhC18PMO

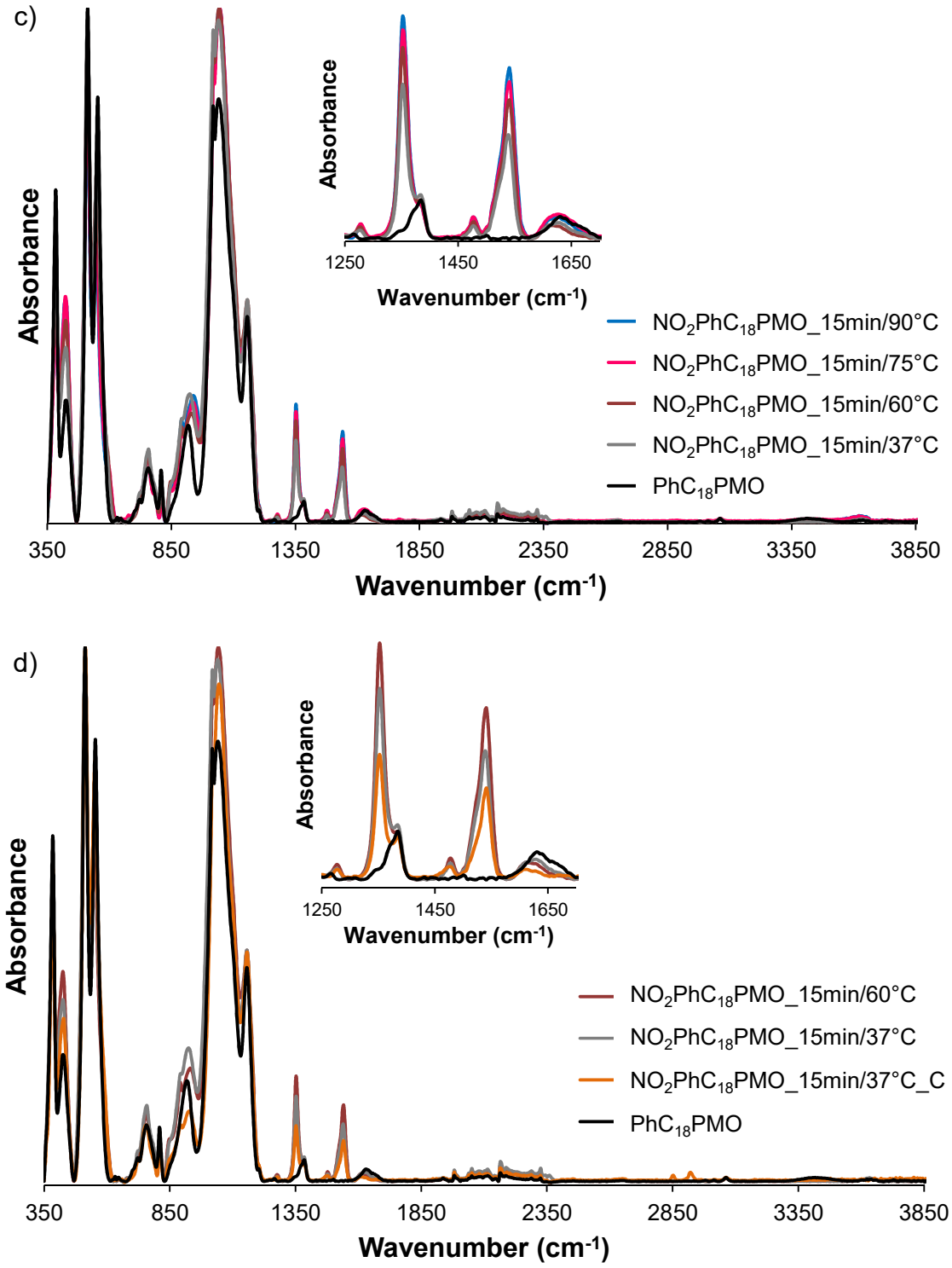

Figure C3.2. FTIR (ATR) spectra of $PhC_{18}PMO$, $NO_2PhC_{18}PMO\_y/T$ at a) 37 °C and b) 60 °C for different reaction times, c) $NO_2PhC_{18}PMO\_15min/T$ at different temperatures and d) $NO_2PhC_{18}PMO\_15min/T$ at different temperatures using microwave and conventional heating. The insets display the region 1250 – 1700 cm^{-1} magnified.

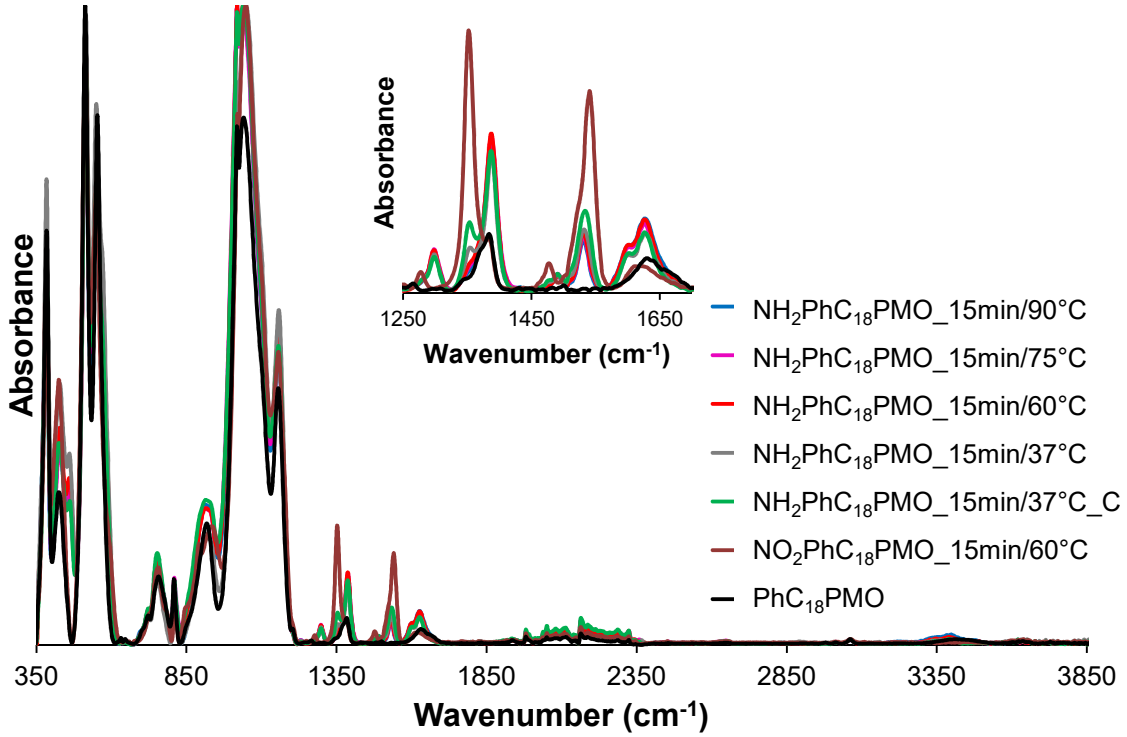

Figure C3.3. FTIR (ATR) spectra of $PhC_{18}PMO$, $NO_2PhC_{18}PMO$_15min/60°C and $NH_2PhC_{18}PMO$_15min/*T* at different temperatures. The insets display the region 1250 – 1700 cm^{-1} magnified.

Table C3.1. Textural parameters and physical properties of $PhC_{18}PMO$ and $NO_2PhC_{18}PMOs$_*y*/*T*.

Sample	d_{100} (nm)	a^a (nm)	S_{BET} ($m^2 \cdot g^{-1}$)	V_P ($cm^3 \cdot g^{-1}$)	$d_p{}^b$ (nm)	b^c (nm)
$PhC_{18}PMO$	4.55	5.25	920	0.66	3.58	1.67
$NO_2PhC_{18}PMO$_15min/37°C	4.70	5.42	788	0.62	3.58	1.84
$NO_2PhC_{18}PMO$_120min/37°C	4.50	5.20	757	0.58	3.51	1.69
$NO_2PhC_{18}PMO$_360min/37°C	4.65	5.36	626	0.49	3.51	1.85
$NO_2PhC_{18}PMO$_15min/60°C	4.70	5.42	698	0.57	3.54	1.88
$NO_2PhC_{18}PMO$_120min/60°C	4.55	5.25	743	0.57	3.51	1.74
$NO_2PhC_{18}PMO$_360min/60°C	4.55	5.25	808	0.63	3.51	1.74
$NO_2PhC_{18}PMO$_15min/75°C	4.82	5.57	730	0.61	3.69	1.88
$NO_2PhC_{18}PMO$_15min/90°C	4.82	5.57	776	0.65	3.55	2.02

[a]Unit cell parameter calculated as($2d_{100}/\sqrt{3}$). [b]Pore width obtained from the BJH method with the corrected Kelvin equation, *i.e.* KJS–BJH method at the maximum of pore size distribution calculated on the basis of adsorption data. [c]Pore wall thickness calculated as ($2d_{100}/\sqrt{3} - d_P$), where the first term is the unit cell parameter.

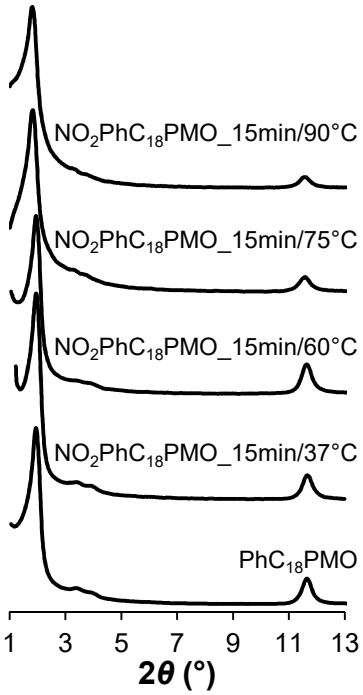

Figure C3.4. X-ray diffraction patterns of $PhC_{18}PMO$ and $NO_2PhC_{18}PMO\_15min$ synthesized at different reaction temperatures during 15 minutes.

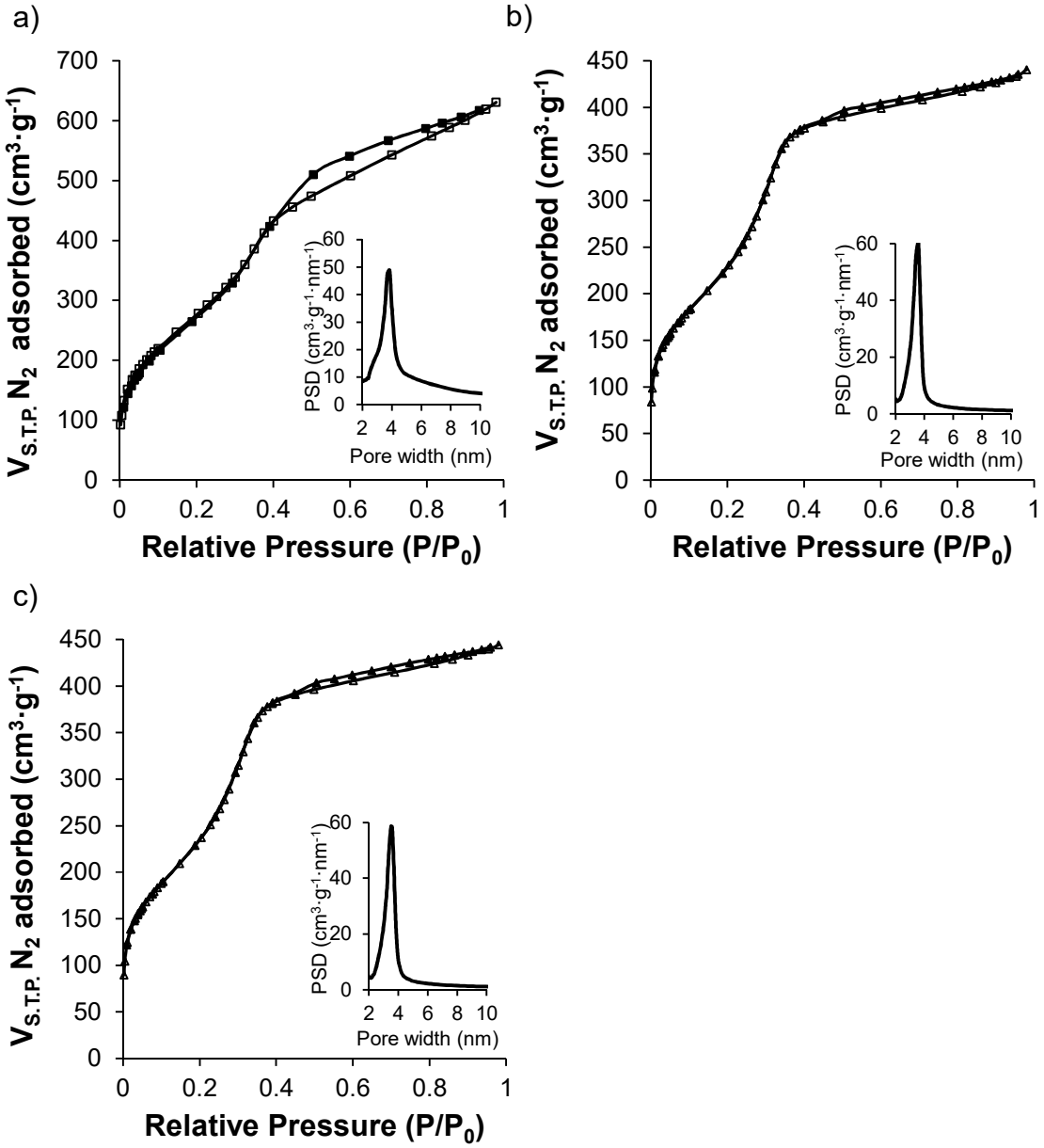

Figure C3.5. -196 °C nitrogen type IV isotherms of: a) $PhC_{18}PMO$; b) $NO_2PhC_{18}PMO$_15min/37°C and c) $NO_2PhC_{18}PMO$_360min/60°C. Empty/filled symbols correspond to adsorption/desorption. The insets display the characteristic narrow PSD curves of PMO materials.

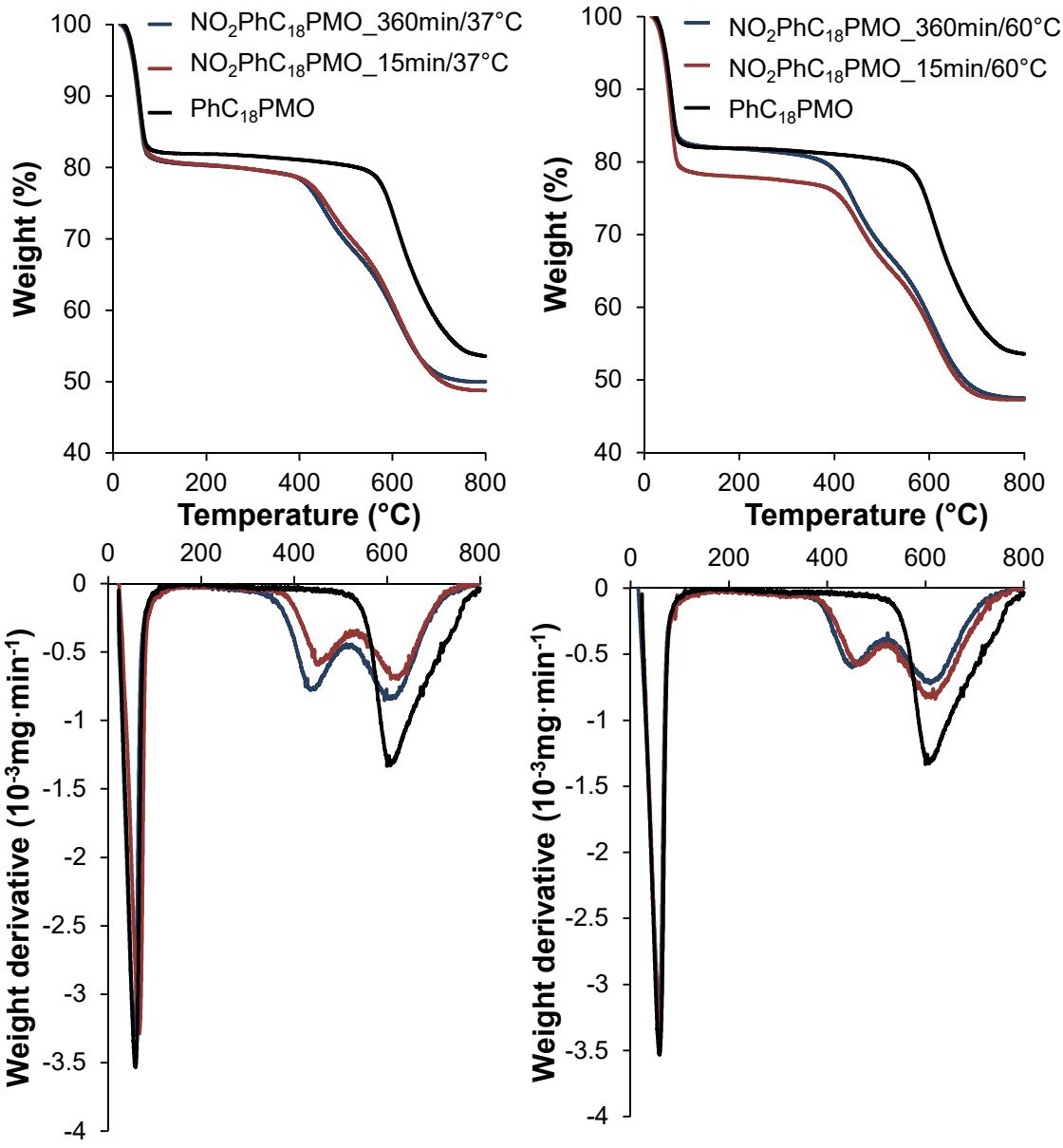

Figure C3.6. Weight loss curves (up) and weight loss derivatives (down) for $PhC_{18}PMO$ and $NO_2PhC_{18}PMO$.

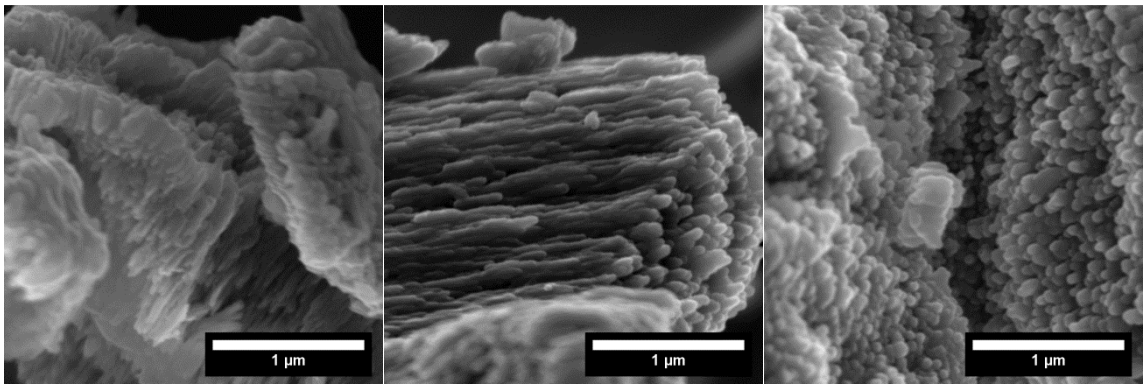

Figure C3.7. Scanning electron microscopy images for $NO_2PhC_{18}PMO\_C$ (left), $NO_2PhC_{18}PMO\_15min/37°C$ (middle) and $NO_2PhC_{18}PMO\_360min/60°C$ (right).

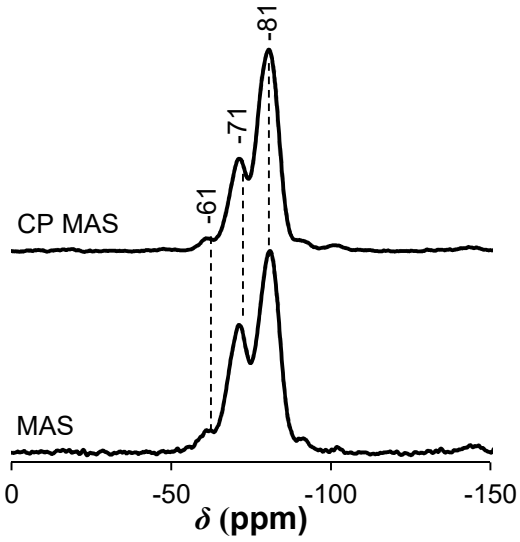

Figure C3.8. ^{29}Si MAS and CP-MAS NMR spectra of the $NH_2PhC_{18}PMO\_15min/60°C$.

Table C3.2. Physical properties of $PhC_{18}PMO$, $NO_2PhC_{18}PMO\_15min/60°C$ and $NH_2PhC_{18}PMO\_15min/T$ materials.

Sample	d_{100} nm	a [a] nm	S_{BET} $m^2 \cdot g^{-1}$	V_P $cm^3 \cdot g^{-1}$	d_p [b] nm	b [c] nm
$PhC_{18}PMO$	4.55	5.25	920	0.66	3.58	1.67
$NO_2PhC_{18}PMO\_15min/60°C$	4.70	5.42	698	0.57	3.54	1.88
$NH_2PhC_{18}PMO\_15min/37°C\_C$	4.46	5.15	752	0.44	3.27	1.88
$NH_2PhC_{18}PMO\_15min/37°C$	4.37	5.05	722	0.44	3.40	1.65
$NH_2PhC_{18}PMO\_15min/60°C$	4.41	5.10	699	0.44	3.40	1.70
$NH_2PhC_{18}PMO\_15min/75°C$	4.37	5.05	688	0.43	3.40	1.65
$NH_2PhC_{18}PMO\_15min/90°C$	4.46	5.15	686	0.44	3.54	1.61

[a]Unit cell parameter calculated as$(2d_{100}/\sqrt{3})$. [b]Pore width obtained from the BJH method with the corrected Kelvin equation, *i.e.* KJS–BJH method at the maximum of pore size distribution calculated on the basis of adsorption data. [c]Pore wall thickness calculated as $(2d_{100}/\sqrt{3} - d_P)$, where the first term is the unit cell parameter.

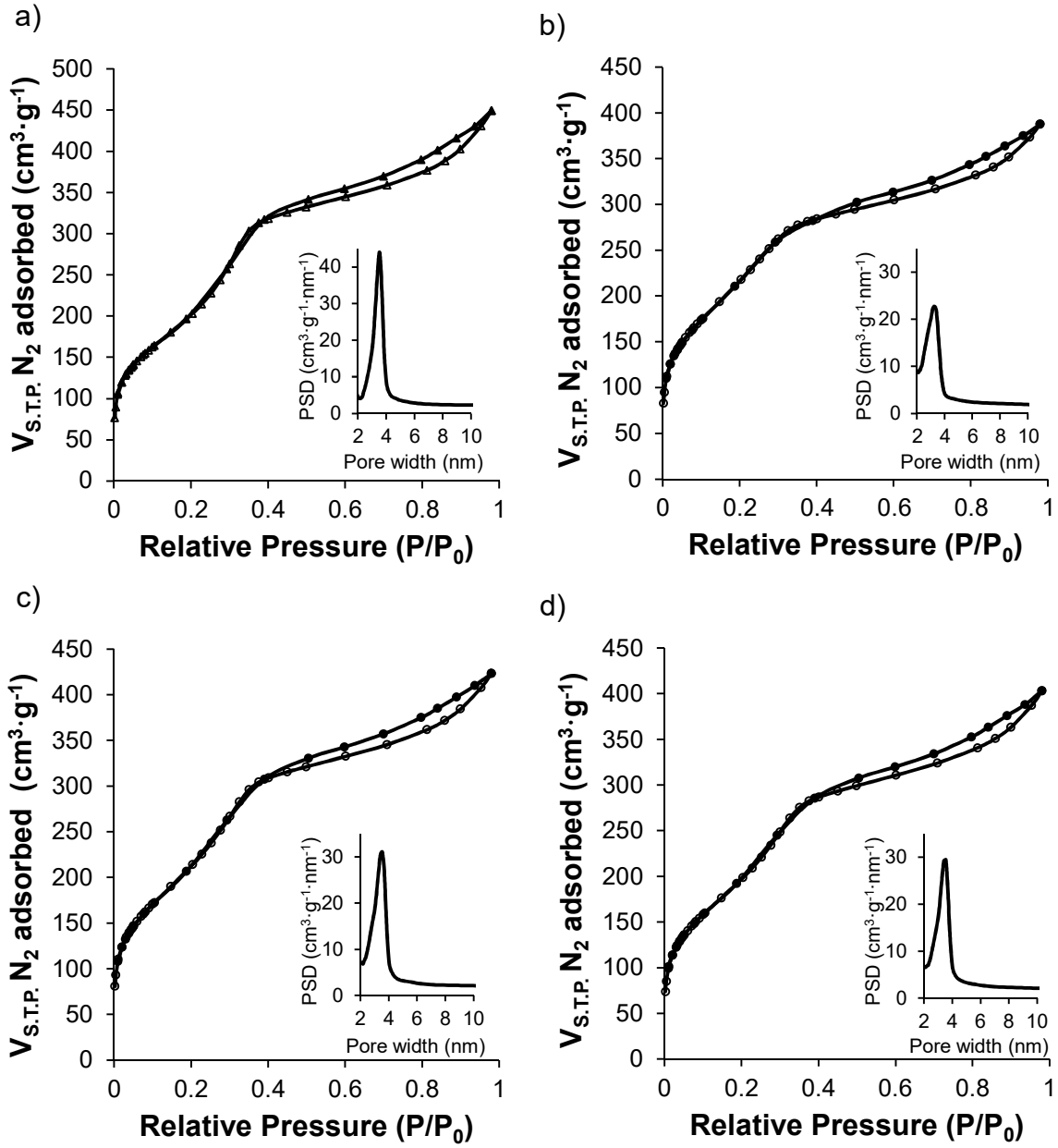

Figure C3.9. -196 °C N_2 isotherms of a) $NO_2PhC_{18}PMO\_15min/60°C$ (triangles); b) $NH_2PhC_{18}PMO\_15min/37°C\_C$ (circles); c) $NH_2PhC_{18}PMO\_15min/37°C$ (circles) and d) $NH_2PhC_{18}PMO\_15min/90°C$ (circles). Empty/full symbols correspond to adsorption/desorption. The insets display PSD curves.

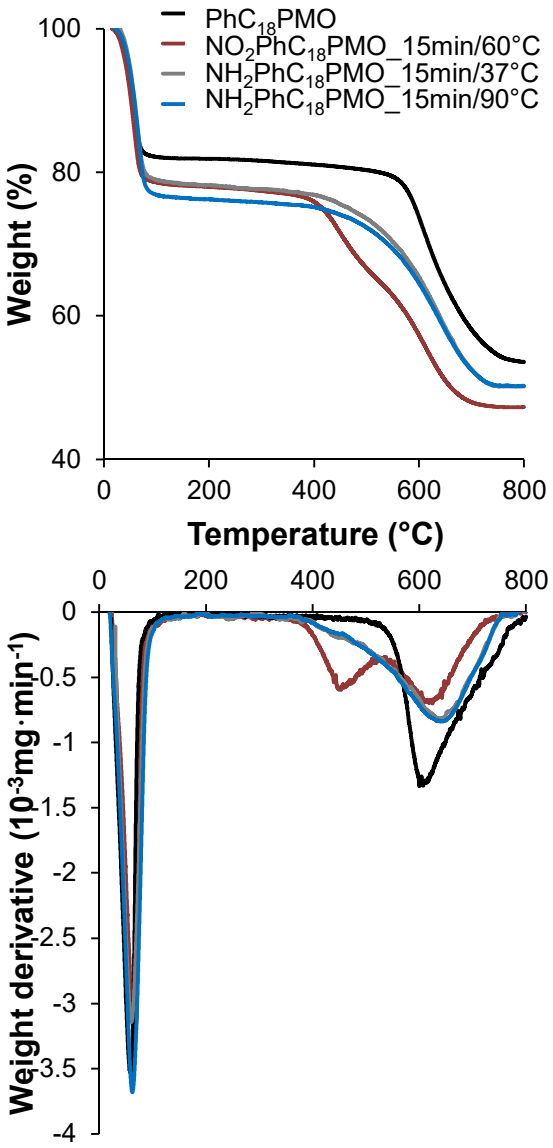

Figure C3.10. Weight loss curves (up) and weight loss derivatives (down) for $PhC_{18}PMO$, $NO_2PhC_{18}PMO$_15min/60°C, $NH_2PhC_{18}PMO$_15min/37°C and $NH_2PhC_{18}PMO$_15min/90°C.